University of Zurich UZH

Department of Geography
Physical Geography
Glaciology & Geomorphodynamics Group (3G)

Evolution of a moraine-breaching landslide in the recently deglaciated area of the Findelengletscher

GEO 511 Master's Thesis

Submitted by
Christine Schärer
11-722-790

Supervised by
Prof. Dr. Andreas Vieli
Dr. Isabelle Gärtner-Roer
Nico Mölg

Faculty representative
Prof. Dr. Andreas Vieli

Submission: 30. April 2018

Abstract

Mountain glaciers are retreating due to the recent climate change and exposing new landscapes to geomorphological processes. The transition from glacial to non-glacial conditions is associated with hydrological, cryospheric and geomorphological changes leading to an intense morphodynamic in those areas through the availability and instability of sediments.

This study investigated the evolution of a moraine-breaching landslide in the recently deglaciated area of the Findelengletscher based on multi-temporal digital elevation models (DEMs). According to the available DEM data the temporal scale was set from 2005 to 2017, covered by seven DEMs. The aim was to quantify the evolution of the area on the one hand by elevation differences and image correlation for a spatially distributed approach and on the other hand, by tracking of prominent boulders as well as the evolution along profiles. The study area consisted of the glacier, the lateral moraine and the landslide, which breached the lateral moraine and partially deposited on the glacier.

Each features could be recognized in the performed analyses by their unique pattern in the horizontal or vertical changes. The landslide was characterized by the down-slope moving with maximal magnitudes higher than 22m/a, whereas the lateral moraine showed small down-slope displacements together with elevation loss through the melt out of dead-ice. The glacier was identifiable by high negative elevation change, which were increasing during the observation periods. The mound showed smaller elevation loss than the glacier due to the debris cover and was moving in South-Western direction. Up-glacier from the landslide a debris covered glacier part could be detected through the consistent west-movement, whereas the rest of the moraine shows downslope movements.

Acknowledgment

First of all, I would like to thank my supervisors Andreas Vieli, Isabelle Gärtner-Roer and Nico Mölg for their help developing this thesis and for their support and inputs during the process. The discussions with them were always helpful and encouraging. Especially, I want to thank Andreas Vieli and Nico Mölg for searching and providing me with the data necessary for the thesis. A special thanks goes to Nico Mölg for the support in planning and conducting the fieldwork, especially regarding the planning and processing of the drone flight.

Further, I want to thank Sarah Giezendanner and Alexandra Kessler for proofreading the thesis and supporting me through the process of writing this thesis, especially during motivation crises and other problems. My final thank goes to my parents for enable my academic studies at the University of Zurich during all these years as well as encouraging and supporting me through the process of this thesis.

Contents

List of Figures

List of Tables

1. Introduction

1.1 Motivation

High mountain environments are highly sensitive to climate change and therefore have been changing rapidly (Abermann et al., 2010; Heckmann et al., 2016; Müller et al., 2014b). A known sensitive and visible indicator of the climate change are the fluctuations of mountain glaciers (Fischer et al., 2015; IPCC, 2013). In the recent decades a rapid recession of mountain glaciers can be documented (Fischer et al., 2015; IPCC, 2013; Lane et al., 2017). Since the Little Ice Age (LIA) glacier termini retreated several kilometers accompanied by a loss of ice volume (Carrivick and Heckmann, 2017). These glacier changes are well reported through glacier inventories (change of the glacier area) and through glacier mass balance data (Fischer et al., 2015; IPCC, 2013; WGMS, 2018; Zemp et al., 2007).

The glacier recession exposes new landscapes, which are vulnerable to a variety of geomorphological processes (Ballantyne, 2002, 2003; Carrivick and Heckmann, 2017; Curry et al., 2006). Those landscapes are in transition from glacial to non-glacial conditions, which is associated with hydrological, cryospheric and geomorphological changes (Carrivick and Heckmann, 2017; Lane et al., 2017). However, only little is known about the latter one (Lane et al., 2017). Such recently deglaciated environments are characterized by intense morphodynamics induced through, among others, the instability of rockwalls and the availability and instability of glacigenic sediments (Heckmann et al., 2016).

Different remote sensing techniques exist to receive information about the earth surface and to generate Digital Elevation Models (DEMs) (Kääb, 2005a; Müller et al., 2014b). Multi-temporal DEMs and their difference are commonly used to study landform changes (Abermann et al., 2010; Fischer et al., 2011; Müller et al., 2014b). Especially in context of monitoring glacial and periglacial systems in high mountain environments with limited accessibility, they are a useful tool to monitor and quantify environmental changes and understand mass transport systems, which is important for assessing natural hazards (Müller et al., 2014b).

For various reasons the Findelengletscher and his surrounding is selected as study site: Firstly, the area is easy to access with the infrastructure of the nearby cable cars. Secondly, the data coverage of the area is excellent with seven DEMs (including the one conducted in this thesis) over the last 12 years and the glacier data from the monitoring programme. Thirdly, the occurrence of a landslide makes this environment even more interesting in relation to processes and interactions between the glacier, moraine and the landslide.

1.2   Research Question and Objectives

The aim of this Master's thesis is to describe and quantify the changes of a recently deglaciated landscape with the example of the Findelengletscher and his surrounding. The main scope lies on the evolution of a landslide event and the interactions between the landslide and the Findelengletscher. Concretely, the following research questions (RQ) with the according objectives can be formulated:

- RQ 1: How is the evolution of the landslide since the occurrence?

    - Detect the landslide area and identify active parts

    - Quantify changes in the geometry and velocity of the movements

- RQ 2: How is the evolution of the glacier and the moraine in relation to the landslide?

    - Detect the unstable areas

    - Quantify changes in the geometry and velocity of the movements

- RQ 3: How does the landslide affect the glacier in relation to melting and moving?

    - Determine and compare the melting rate on bare ice and on from the landslide affected area (debris-covered)

    - Determine the movement of the landslide affected area (debris-covered)

For answering those research questions remote sensing techniques and glaciological field measurements are applied. On the remote sensing side multi-temporal digital elevation models (DEM) and their corresponding shaded reliefs are used to investigate the evolution of the landslide-glacier-moraine system (RQ1 and RQ2). Among the existing DEMs (2005, 2009, 2010, 2013, 2014 and 2015) a new DEM in summer 2017 is acquired within this master thesis. Multi-temporal DEMs and their difference are commonly used to study landform changes (Abermann et al., 2010; Fischer et al., 2011; Müller et al., 2014b). Further, an image matching method is applied to investigate the velocity and motion pattern of the system. To answer RQ3 glaciological field measurements are conducted during a three month period in summer 2017. Ablation stakes are used to measure melting rates and the movement.

2. Background

This chapter delineates the thematic and scientific background to this thesis. As outlined above this thesis investigate a recently deglaciated area, where glacial and mass movement processes are dominating. Therefore, the first section deals with glaciers and their dynamics followed by a section about mass movements. In the last section the scientific knowledge and research approaches about recently deglaciated areas should be explained.

2.1 Glaciers

2.1.1 Basic Terminologies

A glacier is "a perennial mass of ice and possibly firn and snow, [which] is originating on the land surface by the recrystallization of snow or other forms of solid precipitation" (Cogley et al., 2011). Sugden (1994) completes his definition with the ability of glaciers to deform and flow if snow and ice accumulates to sufficient thickness. Preconditions for the occurrence of glaciers are climate conditions and topographic characteristics that enables snow accumulation over several years and transformation into firn and further to ice (IPCC, 2013). Most glaciers consist of a mass gaining (accumulation area) and a mass losing part (ablation area). In the accumulation area the glacier is gaining mass through solid precipitation (snow) or relocation of snow (wind and avalanches). In the ablation area the glacier is losing mass through melting, evaporation and breakaway. The two parts are separated through the Equilibrium Line, where the annual accumulation equals the annual ablation. The change in the mass of a glacier (or part of the glacier) is called mass balance (Benn and Evans, 2010; Cogley et al., 2011; IPCC, 2013).

2.1.2 Classification of glaciers

Glaciers can be classified either according to their size, morphology and relationship to the topography (overview in Benn and Evans (2010)) or according to their thermal properties. The Findelengletscher is a valley glacier. Valley glaciers occur, where the ice is flowing from a cirque or a ice field into a bedrock valley. They are typically surrounded or flanked by ice-free slopes overlooking the glacier surface, which are an important source of snow and rock debris avalanches (Benn and Evans, 2010).

The thermal properties of a glacier depends mainly on the atmospheric conditions (temperature and precipitation). Figure 2.1, a schematic diagram according to which the thermal regime of a glacier (conditions at the ELA) can be defined by the temperature and the precipitation. Three thermal regimes exist: cold glaciers, temperate glaciers and the mixture of both polythermal glaciers. The thermal regime corresponds to state of the ice of which the glacier consists. Temperate ice is in the thermodynamic

equilibrium at the solid-liquid phase boundary, so the liquid and solid phase is present. The ice is at its pressure-melting point. On the other hand cold ice has a temperature below the pressure-melting point (Benn and Evans, 2010; Cuffey and Paterson, 2010).
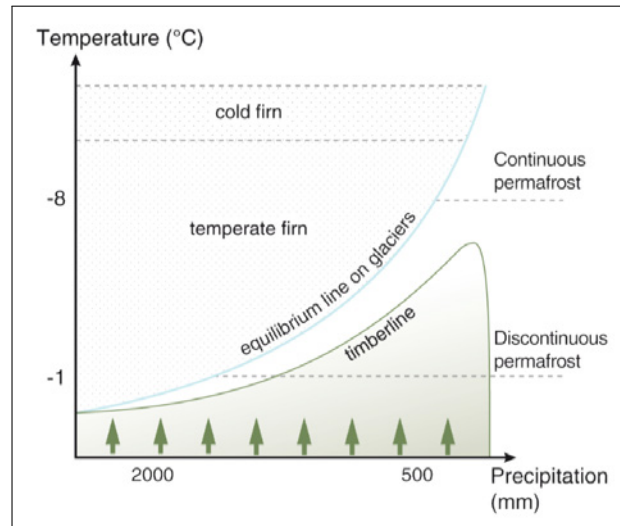
Figure 2.1: Cryosphere Diagram (Zemp et al., 2007)

Temperate glacier can be found in regions with the conditions at the temperate firn regime (Figure 2.1), which corresponds to humid-maritime climates with high precipitation and summer melt. The glacier consists of temperate ice over the entire volume (maybe except of a surface layer). Temperate glaciers are characterized by a long melting season leading to high mass turnover and rapid movements (Benn and Evans, 2010; Cogley et al., 2011). Glaciers in the cold firn zone are called cold glaciers (Figure 2.1). They are typically found in dry, continental climates, where the heat sources are limited. Cold glaciers are characterized by a low mass turnover and slow movements and they consist entirely of cold ice (maybe except of a surface layer) (Benn and Evans, 2010; Cogley et al., 2011; Zemp et al., 2007). Polythermal glaciers are a mixture of temperate and cold ice. There are different types of polythermal glacier types according to the thermal structures depending on the available warming processes. Different forms are described in Benn and Evans (2010).

2.1.3 Surface Energy Balance

The energy balance is the sum of all energy fluxes over a given time interval. Out of it one can calculate the evolution of the near-surface temperatures or the glacier ablation rates (Benn and Evans, 2010). The meteorological conditions above the glacier and the physical properties of the glacier itself are the controlling factors at the glacier-atmosphere interface. For the estimation or calculation of the melt, the different energy fluxes to and from the surface have to be assessed. Usually, energy fluxes with positive signs means an energy gain to the surface and a negative sign an energy loss. As a surface is two-dimensional (no volume), no energy can be stored (Benn and Evans, 2010; Hock, 2005). Consequently, the surface energy balance is expressed as:

$$Q_{SW} + Q_{LW} + Q_H + Q_L + Q_G + Q_R + Q_M = 0 \qquad (2.1)$$

where Q_{SW} is the net short wave radiation, Q_{LW} is the net long wave radiation, Q_H is the sensible heat flux, Q_L is the latent heat flux, Q_G is the ground heat flux, Q_R is the sensible heat flux supplied by rain and Q_M is the energy consumed during melting or released during freezing (Benn and Evans, 2010; Hock, 2005; Hubbard and Glasser, 2005; Nicholson and Benn, 2006).

The net short wave radiation Q_{SW} (Equation 2.2) is the difference between the incoming short wave radiation (also called global radiation) and outgoing/reflected short wave radiation. The outgoing short wave radiation can be determined by the albedo (a) of the surface multiplied by the incoming short wave radiation. The albedo is high for fresh snow (> 0.95) and low for debris covered and dirty ice (0.1-0.2). The incoming short wave radiation is a function of the solar constant and depends on the atmosphere conditions, the slope gradient and aspect, latitude and time of day (Benn and Evans, 2010; Hubbard and Glasser, 2005).

$$Q_{SW} = Q_{SW,in} \cdot (1 - \alpha) \tag{2.2}$$

The net long wave radiation Q_{LW} (Equation 2.3) is the difference between the incoming and outgoing long wave radiation.

$$Q_{LW} = LW_{in} - LW_{out} \tag{2.3}$$

Both terms (incoming and outgoing) can be described by the Stefan-Boltzmann-Equation (Equation 2.4), where the energy flux is the multiplication of the emissivity ε, the Stefan-Boltzmann-constant σ and the temperature of the body $T[K]$ to the power of four. At the glacier margins (especially valley glaciers) the long wave radiation tends to be high, caused by the emitted radiation from the rock surface (Benn and Evans, 2010; Hock, 2005).

$$I = \varepsilon \cdot \sigma \cdot T^4 \tag{2.4}$$

The sensible heat (Q_H) describes the energy transfer from the air to the surface through turbulent mixing. It is a function of the temperature gradient (difference between air temperature and surface temperature) and the wind speed. The higher the temperature gradient and the wind speed are, the larger is the sensible heat flux (Benn and Evans, 2010; Hubbard and Glasser, 2005).

The latent heat (Q_L) is the energy gain or loss through phase changes (evaporation/condensation & sublimation/deposition) and can be described by the vapor pressure gradient and the wind speed. If the vapor pressure gradient is positive, the latent heat flux is positive, so either condensation or resublimation occurs. Both phase changes release energy (Benn and Evans, 2010; Hubbard and Glasser, 2005).

The ground heat (Q_G) describes the energy used to change the temperature of ice or snow. Surface melting can only occur if the temperature of the ice or snow is 0°C. The ground heat depends on the density and the heat capacity of the material (ice or snow) and the temperature gradient within the cold ice or snow. For temperate ice or snow the ground heat flux is zero as the temperature of the ice or snow is already 0°C (Benn and Evans, 2010; Hock, 2005).

The sensible heat flux supplied by rain (Q_R) is mainly controlled by the precipitation intensity and the temperature difference between the rain and the surface. In most cases this heat flux can be neglected because it is small compared to the other fluxes of the surface energy balance. Only in maritime regions where storms originate from warm oceans can the sensible heat flux be a significant short-term heat

source (Benn and Evans, 2010; Hock, 2005; Hubbard and Glasser, 2005).

The last term of equation 2.1 Q_M describes the heat that is consumed during melting or released during freezing. Thus, Q_M is negative (melting) if the sum of the other fluxes is positive. In the manner that a balance is established. If the sum of the other fluxes is negative, the glacier ice gets colder (Benn and Evans, 2010; Hock, 2005; Hubbard and Glasser, 2005; Nicholson and Benn, 2006).

In many cases the equation of the surface energy budget is arranged, so that the energy available for melting can be estimated out of it (Equation 2.5). If further a surface temperature of 0°C is assumed, the ground heat flux is zero, so any surplus energy at the surface-atmosphere interface is used for melting (Hock, 2005; Hubbard and Glasser, 2005).

$$Q_M = Q_{SW} + Q_{LW} + Q_H + Q_L + Q_R \tag{2.5}$$

2.1.4 Influence of Debris Cover on the Surface Energy Balance

Supraglacial debris cover can originates from a deposition of a mass movement (debris flow, rockfalls, etc.) or from the melt-out of englacial and subglacial debris bands. Mass movement processes such as debris flow, snow avalanches, rockfalls or landslides depends on the topography, weathering and erosion rates at the location of the glacier (Benn et al., 2003). Supraglacial debris is a phenomenon that is almost only observable in the ablation area. In the accumulation area the debris would be buried in the snow pack and transferred into the glacier (Reznichenko et al., 2011). Large debris deposits (>10% of the ablation area) change the glacier dynamics in two ways: The insulating effect of the deposit reduces the ablation, which leads to a less negative or more positive net mass balance and the additional weight is provided by the deposit itself and over time by the increasing relative ice thickness is added up as well (Reznichenko et al., 2011; Shulmeister et al., 2009). The mass will increase the basal sliding of the glacier as the sliding depends on the mass of the ice per unit of bed. Theoretically, the flow velocity at a given location should increase by 20% if 10% ice depth is added (Reznichenko et al., 2011). Small debris deposits (<10% of the ablation area) influences the glacier only locally, but the overall mass balance and velocity will not be affected significantly (Reznichenko et al., 2011; Shulmeister et al., 2009).

From numerous field experiments an empirical relationship between supraglacial debris thickness and ice-melt rates is detected (Nicholson and Benn, 2006). Under a thin debris layer (< ca. 2-5cm) ablation rates increase (with respect to clean ice) and under thicker debris they decline exponentially. This pattern can be explained first by the lower albedo of rock surfaces, so they will absorb more radiation and therefore more energy for melting is available. On the other hand, the debris builds a thermal barrier between the atmosphere and the ice and as such reduces the energy flux to the ice surface. The insulating effect dominates for thick debris layers and the albedo effect for thin ones. However, the threshold whether melt rate is accelerated or inhibited varies under the influence of local climate and debris lithology as one can see on the basis of the different glaciers in Figure 2.2 (Benn and Evans, 2010; Nicholson and Benn, 2006; Pellicciotti et al., 2015; Reznichenko et al., 2011; Shulmeister et al., 2009).
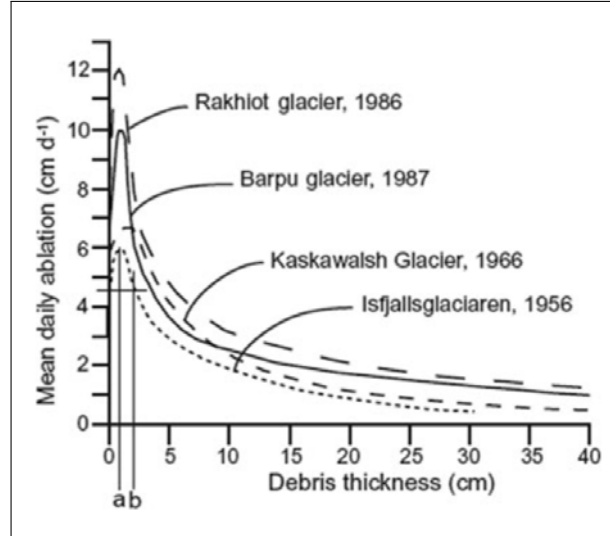
Figure 2.2: Examples of empirical measurements of the relationship between debris thickness and ice ablation rate on the sample of some glaciers (Nicholson and Benn, 2006)

The sub-debris melt rate (M) is defined as the downward energy flux at the base of the layer (Q_m) divided by the density of ice (ρ_i) and the latent heat of fusion ($L_i = 334 kJkg^{-1}$).

$$M = \frac{Q_m}{\rho_i \cdot L_i} \tag{2.6}$$

The energy flux through the debris layer is mainly given by the head conduction down a vertical temperature gradient, so Q_m is the conductive heat flux Q_c, which can be derived from:

$$Q_c = k \cdot \frac{dT}{dz} \tag{2.7}$$

where k is the thermal conductivity of the debris layer [$Wm^{-1}K^{-1}$] and T the temperature within the layer [K] at a point z within the layer [m]. If a linear temperature gradient between the upper and lower surface of the debris is assumed, Equation 2.7 can be modified as followed:

$$Q_c = k \cdot \frac{T_s - T_i}{h_d} \tag{2.8}$$

where T_s is the steady-state surface temperature [K], T_i the ice temperature [K] and h_d the debris thickness [m]. This equation is valid for the assumption that the heat stored in the debris layer is constant over time (thermal equilibrium). However, data from vertical temperature profiles showed that this assumption is not valid. As the thermal regime of the debris is dominated by the diurnal cycle under stable weather conditions. Therefore, a thermal equilibrium within the debris layer cannot be expected over time intervals of less than 24 hours (Nicholson and Benn, 2006).

Nicholson and Benn (2006) showed in their study that at the temperate glacier Chiacciaio del Belvedere a 1cm debris cover reduces the energy flux (available for melt) by 33% if the debris is dry and by 11% if the debris is wet.

Usually, supraglacial debris cover only occurs in the ablation area with an increase of the debris thickness towards the glacier terminus, which reverses the ablation gradient as the ablation rates are small on the lower parts of the glacier (Benn et al., 2003, 2012). Debris-covered glaciers commonly react on climate variations through thickening and thinning only rather combined with advance and retreat. This is caused by the large lateral-terminal moraines, which acts as barriers to glacier advance (Benn et al., 2003). As above-mentioned a debris cover insulates and protect the glacier ice from direct radiation, therefore other processes enable ablation on debris covered glaciers. Mainly four processes contributes to the ablation on debris covered glaciers: (1) Melting beneath the debris can occur, (2) clean ice close to the glacier ELA is vulnerable for melting, (3) melting of ice cliffs and (4) calving into proglacial lakes. Ice cliffs develop, where the debris slumps from slopes and exposes the ice or through the collapse of englacial voids (Benn et al., 2012; Pellicciotti et al., 2015).

2.1.5 Glacier Mass Balance and Motion

As mentioned before, the glacier mass balance describes the change in the mass of a glacier, so it is the sum of all components of accumulation and ablation (both surface, internal and basal). The measure for this change is the specific balance rate. Regarding a certain point or column (vertical section through the glacier) it is defined by

$$\dot{m} = \dot{acc}_{sfc} + \dot{abl}_{sfc} + \dot{acc}_{int} + \dot{abl}_{int} + \dot{acc}_{bas} + \dot{abl}_{bas} + \frac{q_{in} + q_{out}}{ds} \tag{2.9}$$

with *acc* referring to accumulation, *abl* to ablation and the indices *srf* to surface, *int* to internal and *bas* to basal. The last component q describes the flow of ice into and out of the column with the horizontal dimension (*ds*) (Cogley et al., 2011; Zemp et al., 2013). Glacier flowing processes can be grouped into two domains: motion within the ice mass and motion focused to near the base of the ice mass (Hubbard and Glasser, 2005). The first one refers to ice as a deformable material, deformation results from the movement between or within individual ice crystals (Benn and Evans, 2010). The second one is also called basal motion and can be divided into (basal) sliding and subglacial sediment deformation (Hubbard and Glasser, 2005). Sliding describes the slipping of the glacier on its bed. This component is important, where meltwater is present beneath the glacier. When the glacier is sliding over its bed, it can erode the glacier bed by frictional drag, which is known as deformation of the glacier bed (Benn and Evans, 2010).

Usually, the mass change of a glacier is considered over a certain time span (t_0 to t_a), often one year or a season. For a certain point on the glacier (x) the net (mass) balance is defined as the integral of the specific balance rate $\dot{m}$ over a time interval t_0 to t_a.

$$b(x) = \int_{t_0}^{t_a} \dot{m}(x,t) \cdot dt \tag{2.10}$$

For obtaining the glacier-wide mass balance (*B*), also called the total net balance, one have to integrate the point (mass) balances over the glacier area S:

$$B = \frac{1}{S} \cdot \int_S b(x) \cdot dS \tag{2.11}$$

This formulas are valid for land-terminating glaciers, balance components for ice shelves, lake and marine floating glacier tongues are not considered (Cogley et al., 2011; Cuffey and Paterson, 2010; Zemp et al., 2013). To clarify over which time span or in which measuring unit the specific balance rate, the net mass balance or the total net balance are considered, lowered letters can be used. Whereby for example a lower *a* stands for annual or a lower *w* implies that the equivalent thickness of water per unit time is considered (Cogley et al., 2011; Zemp et al., 2013).

2.1.6   Glacier observation methods

The **glaciological observation method** determines the mass balance through in situ measurements of the accumulation and ablation at individual points. With this method only the surface components of accumulation and ablation can be addressed as well as the component from the glacier motion (ablation stake moves with the glacier). Accumulation is measured in pits excavated into the snowpack or from cores. The annual increments can be identified from changes in the density, crystal size or dirt layer. The accumulation at that point can be calculated by the sum of the multiplication of the individual horizon thickness (h_i) with the density of that horizon (ρ_i).

$$acc_{point} = \sum_{1}^{i} h_i \cdot \rho_i \; [\text{m w.e.}] \tag{2.12}$$

The ablation is determined by using stakes drilled into the ice, which are used to measure the drop in the ice surface over a time span. The measured meter ice has to be multiplied by the density of ice to convert into meter water equivalent.

$$abl_{point} = \Delta h_{stake} \cdot \rho_{ice} \; [\text{m w.e.}] \tag{2.13}$$

where $h_{stake}(t_a)$ is the stake height out of the ice at t_a, $h_{stake}(t_0)$ is the stake height out of the ice at t_0 and ρ_{ice} the density of ice. To get the glacier-wide mass balance the individual point measurements have to be interpolated and extrapolated over the whole glacier area (Benn and Evans, 2010; Cogley et al., 2011; Cuffey and Paterson, 2010; Zemp et al., 2013).

Within the **geodetic observation method** the mass balance is determined by calculating the volume changes through differencing glacier surface elevations from repeated mapping. Thereby, the volume change has to be converted into a mass by multiplying with the density of ice. The mapping of the elevation can be done in many different ways such as ground surveys using theodolites or global navigation satellite systems (GNSS) or airborne and spaceborne surveys with photogrammetry, laser scanning or SAR interferometry. The volume change of a glacier can be calculated as followed:

$$\Delta V = r^2 \cdot \sum_{k=1}^{K} \Delta h_k \tag{2.14}$$

where K is the number of pixels covering the glacier at the maximum extent, Δh_k is the elevation difference of the two DEM at pixel *k* and *r* is the pixel size. The bedrock beneath the glacier is assumed to be constant and the two elevation data sets have to be co-registered (aligned and same cell size).

The glacier-wide average thickness change $\overline{\Delta h}$ is the volume change of the entire glacier divided by the mean glacier area during the time span of the measurements and can be derived from the following equation:

$$\overline{\Delta h} = \frac{\Delta V}{\bar{S}} \qquad (2.15)$$

where ΔV is the volume change (Equation 2.14) and $\bar{S}$ the average glacier area. By assuming a linear change through time, the average glacier area can be determined as the average between the two extents (t_0 and t_a) (Cogley et al., 2011; Zemp et al., 2013).

With Equation 2.14 the volume change for a glacier can be determined instead of the mass change. Therefore, a conversion from the volume change ΔV to the mass change ΔM by assuming a conversion factor $f_{\Delta V}$ is necessary (Equation 2.16) (Huss, 2013).

$$\Delta M = f_{\Delta V} \cdot \Delta V \qquad (2.16)$$

The conversion factor $f_{\Delta V}$ depends on the density of snow, firn and ice and its change over time (Huss, 2013; Zemp et al., 2013). It is possible to considered different conversion factors for different glacier parts (e.g. firn area) or an approximately density for the entire glacier can be assumed (Huss, 2013; Zemp et al., 2013). Huss (2013) suggest to use a conversion factor of $f_{\Delta V} = 850 \pm 60 \, kg/m^3$.

The geodetic observation method is useful as inaccessible and large areas can be investigated (Cuffey and Paterson, 2010; Huss, 2013; Paul et al., 2015). To asses a glacier in an ideal way both methods should be considered as they measure different components of the glacier elevation change and as their temporal resolution usually varies. Glaciological field measurements are carried out on an annual timescale, whereas the geodetic method timescales of a few years or decades are considered (Cuffey and Paterson, 2010; Zemp et al., 2013).

2.2   Mass Movements

Mass movements or mass wastings are the downward and outward movement of slope materials such as rocks, rock debris, soils or combination of these under the force of gravity. As mass movements are constraint to slopes, the term slope failures is used in the same manner (Smithson et al., 2008; Strahler and Strahler, 2009; USGS, 2004; Varnes, 1978). Often mass movements consist of a starting zone or release area, where the material is removed from, a transportation pathway, through which the material is transported and in the end deposited in a deposition or accumulation area (Zepp, 2011). Mass movements are important processes in the reworking and deposition in glacial environments due to the abundance of steep, unstable slopes around the margins of glaciers (Benn and Evans, 2010). There exists a wide range of mass movements, which can be grouped according to the type of material (rock, rock debris, soil), the mode of failure (fall, slide, flow), the rate of movement (slow, rapid) and/or the water content (dry, wet) (Benn and Evans, 2010; Smithson et al., 2008; Strahler and Strahler, 2009; USGS, 2004; Varnes, 1978). A classification schema based on the mode of failure and on the type of material is presented here (Blair, 1994; USGS, 2004; Varnes, 1978). Blair (1994) identified falls, topples, slides, flows and complex failures as important in relation to valley and moraine wall stability.

TYPE OF MOVEMENT		TYPE OF MATERIAL		
		BEDROCK	ENGINEERING SOILS	
			Predominantly coarse	Predominantly fine
FALLS		Rock fall	Debris fall	Earth fall
TOPPLES		Rock topple	Debris topple	Earth topple
SLIDES	ROTATIONAL	Rock slide	Debris slide	Earth slide
	TRANSLATIONAL			
LATERAL SPREADS		Rock spread	Debris spread	Earth spread
FLOWS		Rock flow (deep creep)	Debris flow (soil creep)	Earth flow
COMPLEX		Combination of two or more principal types of movement		

Figure 2.3: Classification of mass movements (Blair, 1994; Varnes, 1978)

The abrupt movement of geological material (rock and boulders) refers to 'falls' as mode of failure. The material is mostly falling, leaping or rolling down through the air. According to the size of the transported material it is classified as a rock fall (very coarse material) or as a debris fall (coarse material) (Benn and Evans, 2010; USGS, 2004). Debris falls frequently occur on the glacier-facing side of lateral moraines or on debris-covered valley walls. They often occur during or after wet storms as larger clasts become unstable due to the washing out of the fine matrix by the rain (Blair, 1994).

Topples are characterised through the forward rotation of a unit or units under the action of gravity and forces exerted by fluids in cracks. A toppling failure can be linked with falling or sliding depending on the geometry and orientation of the failing mass (USGS, 2004; Varnes, 1978). The forward rotation and opening of the joints is rather slow, whereas the tumble itself is rapid. Topples can be well recognized in advance due to the slow opening of joints (Blair, 1994).

A slide failure consists of a distinct zone of weakness, which separates the slide material from the underlying and stable material. Slides can further be divided in rotational slides and translational slides. Within the first-mentioned the failure-surface is concave and the movement is rotational about an axis transverse across the slide, whereas the failure-surface within the second-mentioned is planar and only little rotation is observable (USGS, 2004; Varnes, 1978). A slide can disaggregate during the transport and evolve into a debris flow (Benn and Evans, 2010).

Flows are sediment-water mixtures, which can divided according to the velocity of the movement and the water content of the material (Benn and Evans, 2010; USGS, 2004). A rapid mass movement consisting of a combination of loose soil, rock, organic matter, air and water moving downslope as a slurry is a debris flow. Debris flows are commonly triggered by intense surface-water flow caused by heavy precipitation or rapid snowmelt. Debris flow depositions are usually recognizable as debris fans beneath steep gullies, which are the source areas of debris flows. Very rapid or extremely rapid debris flows are called debris avalanches. In an earthflow or a mudflow the slope material gets liquified and runs out forming a bowl at the head. It usually occurs under saturated conditions in fine-grained materials or clay-bearing rocks on moderate slopes. The slow downward movement of soil or rock is called creep. Creeping is visible through curved tree trunks, bent fences, tilted poles or ridges. Creeping is caused by shear stress sufficient to produce permanent deformation but too small to produce shear failure (USGS, 2004; Varnes, 1978).

Lateral spreads are lateral extension caused by liquefaction and occurs on gentle slopes or even flat terrain. The failure is triggered by rapid ground motion such as earthquake (USGS, 2004; Varnes, 1978).

Often, slope movements involve a combination of the above-mentioned mass movements. This can either be through the presence of multiple shear planes or the further development (spreading) of an initial failure (Blair, 1994; USGS, 2004; Varnes, 1978).

2.3   Terminology and Evolution of recently deglaciated Landscapes

Glacial recession exposes landscapes such as unstable rock walls, moraines and glacier forefields to geomorphological processes. Those landscapes are subject of an increasing number of studies due to three reasons: First, they are unique natural laboratories, where the development of soil and vegetation and their interactions with geomorphological processes can be studied. Second, those areas are suitable for testing and developing application of mapping and measurement methods to quantify and to document changes. Third, they are sources of potential hazards such as debris flows and lake outbursts (Carrivick and Heckmann, 2017; Heckmann et al., 2016).

2.3.1   Basic Terminologies: Proglacial, Paraglacial and Periglacial

In the context of cold and/or glaciated environments and their surrounding are the terms proglacial, paraglacial and periglacial common. The meaning of those three terms is essential while investigating recently deglaciated landscapes.

Periglacial environments are determined by the dominant processes present in such environments like freezing and thawing and/or permafrost related processes. Through the intense frost activity breaking down bedrock and cryogenic weathering distinctive landscape forms are established. The forming occurs in situ as the processes are not effective in evacuating sediments. Periglacial landscapes exists in (i) the polar deserts and semi-deserts of the high Arctic, (ii) the tundra zone, (iii) the boreal forest zone, (iv) the maritime and continental sub-arctic and (v) mid- and low latitude alpine regions (Slaymaker, 2011).

Proglacial environments are defined through their ice-marginal location, immediately in front of glaciers, ice caps or ice sheets. Carrivick and Heckmann (2017) for example use the Little Ice Age (LIA) moraines and the current glacier extent as boundary of a proglacial system. The dominant processes are glacifluvial, glacilacustrine and glacimarine processes (Slaymaker, 2011). Benn et al. (2003) add aeolian processes, which redistribute glacigenic sediments, to this list of processes. Proglacial rivers have a distinct seasonally and diurnally pattern. Common erosional forms are drainage diversions and spillways and common depositional forms are sander and outwash fans with distinctive facies (Slaymaker, 2011). Through the instability of deglaciated rockwalls and the availability and instability of glacigenic sediments are proglacial environment considered to be rapidly changing (Heckmann et al., 2016).

Paraglacial environments are transitional landscapes, which are recovering from the disturbance of glaciation. As such they cannot be defined by certain processes or a certain location, but by a temporal component (Carrivick and Heckmann, 2017; Slaymaker, 2011). The term was firstly introduced and defined by Church and Ryder (1972) as "non-glacial processes that are directly conditioned by glaciation". Ballantyne (2002) added the landforms, landsystems and landscapes that are directly conditioned by glaciation to his definition of the paraglacial concept. He identified six landsystems: Rock slopes, sediment/drift-mantled slopes, glacier forelands, alluvial landsystems, lacustrine landsystems and coastal landsystems (Ballantyne, 2002, 2003). In context of valley glaciers the focus lies on the paraglacial

modification of rock slopes and sediment-mantled slopes. The time period, over which the glaciogenic sediments are stabilized or exhausted, is called paraglacial period. The response after deglaciation and the time scale of recovery varies in each landscapes according to the processes or the spatial extent (Ballantyne, 2002, 2003; Slaymaker, 2011).

The above-mentioned remarks show the difference between the three terms periglacial, proglacial and paraglacial. Whereas periglacial and proglacial environments can be clearly defined either through the dominant processes or through the location, paraglacial environments are more difficult to define. Paraglaical describes transitional landscapes, which are recovering from glaciation and as such the spatial and temporal scale is very variable (Carrivick and Heckmann, 2017; Slaymaker, 2011). Figure 2.4 shows the transition from glacial to non-glacial conditions with the terms . Landforms within proglacial areas are rapidly changing and represent a platform for paraglacial re-working processes (Carrivick and Heckmann, 2017).
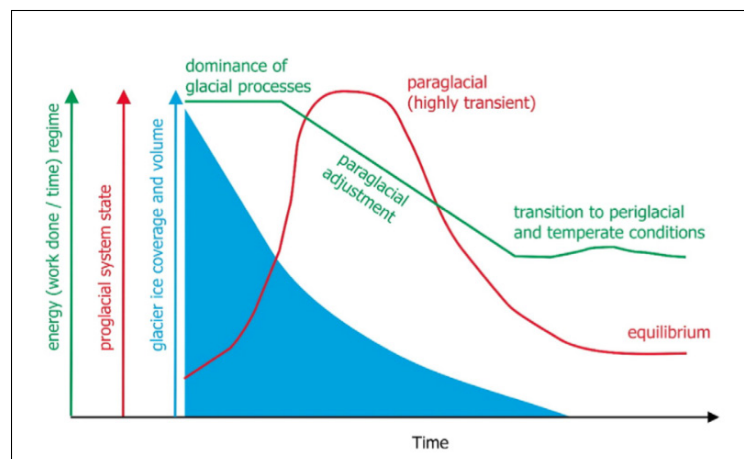
Figure 2.4: Conceptual model of proglacial system transition from domination by glacial processes, through paraglacial period towards a periglacial or temperate landscape (Carrivick and Heckmann, 2017)

2.3.2 Components, Processes and their evolution

Glacier recession exposes unconsolidated material to geomorphological re-working processes, whereby three main sediment sources exist. First, sediments originate from glacial erosion and subglacial sediment storage, which is controlled by the thermal state of the glacier and the lithology of the underlying bedrock. Second, debris introduced by weathering and instability of rockwalls steepened by glacial erosion. Third, glacigenic debris covering hillslopes or accumulated as lateral or terminal moraines. Such debris-mantled slopes are re-worked through deformation, different mass movements and fluvial incision (Carrivick and Heckmann, 2017). Several studies (Ballantyne, 2002, 2003; Curry et al., 2006) identified debris flows as the dominant sediment transport on sediment-mantled slopes. An individual debris flow can be identified by the deposition of parallel levées in the upper part and by one or more lobes of debris in the lower part (Ballantyne, 2002, 2003) (Figure 2.6). The often intersecting gullies, which incise the lateral moraine, are the conspicuous sign of a paraglacial landscape. For intense gully building the lat-

eral moraine has to stand up at least 120m above the valley floor and a slope gradient bigger than 30° is necessary (Curry et al., 2006).

In some cases re-working processes can even cause failure of moraine walls as observed along the flanks of Tasman Glacier, New Zealand (Blair, 1994) (Figure 2.6, Stage II/III). Especially, ice-cored lateral moraines are vulnerable to failure because the underlying ice melting is reducing the strength of the sediment. Further, extensive gully building favor instabilities of the moraines (Ballantyne, 2003; Blair, 1994; Curry et al., 2006).

From a sediment cascading point of view, proglacial landscape can be divided into three main parts: the glacier, the hillslopes and the proglacial channel network (Figure 2.5). The sediment connectivity describes the degree to which such system components are connected in relation to the sediment transfer. When two system parts are coupled, sediments can flow from one to another, whereas between decoupled parts sediment transfer is prevented. Within this point of view lateral moraines play a special role as on one hand they act as as a barrier between the areas within the moraines and the adjacent hillslopes (Carrivick and Heckmann, 2017; Cossart and Fort, 2008). But on the other hand the lateral moraines their-self are a source for sediment transfer (Ballantyne, 2002; Curry et al., 2006). In a proglacial system the sediment transfer can be either be lateral or longitudinal. The lateral fluxes originate from the hillslopes (e.g. lateral moraines), whereas the longitudinal fluxes are supplied by the glacier and its meltwater (Figure 2.5).
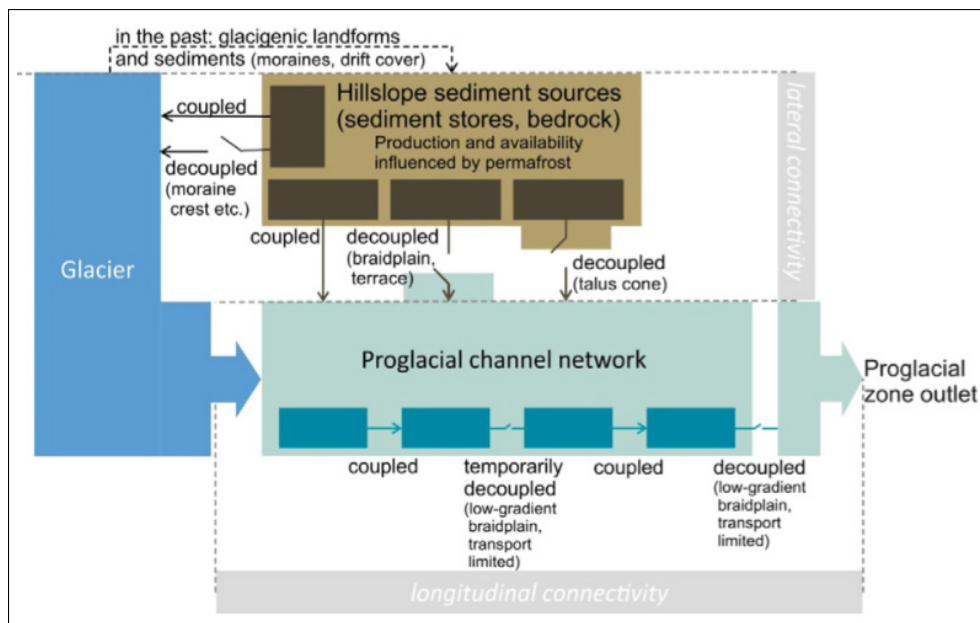
Figure 2.5: Conceptual model of sediment transfer through a proglacial system, highlighting the role of sediment connectivity between hillslopes, channels and the glacier (lateral connectivity) and along the channel network (longitudinal connectivity) (Carrivick and Heckmann, 2017)

In this context proglacial rivers play an important role whether sediments are evacuated from the proglacial area or deposited in it. Therefore, they have been in focus of proglacial research from a geomorphological or hydrological point of view (Carrivick and Heckmann, 2017; Staines et al., 2015). The discharge of proglacial rivers is characterized by the meltwater input from the glacier, which implies

a high temporal variability on a daily and seasonal scale. Another characteristic feature of glacially formed landscapes are proglacial lakes. Such lakes act as a buffer for meltwater discharge and as a trap for sediments, which affect geomorphological activities within proglacial areas (Carrivick and Heckmann, 2017).
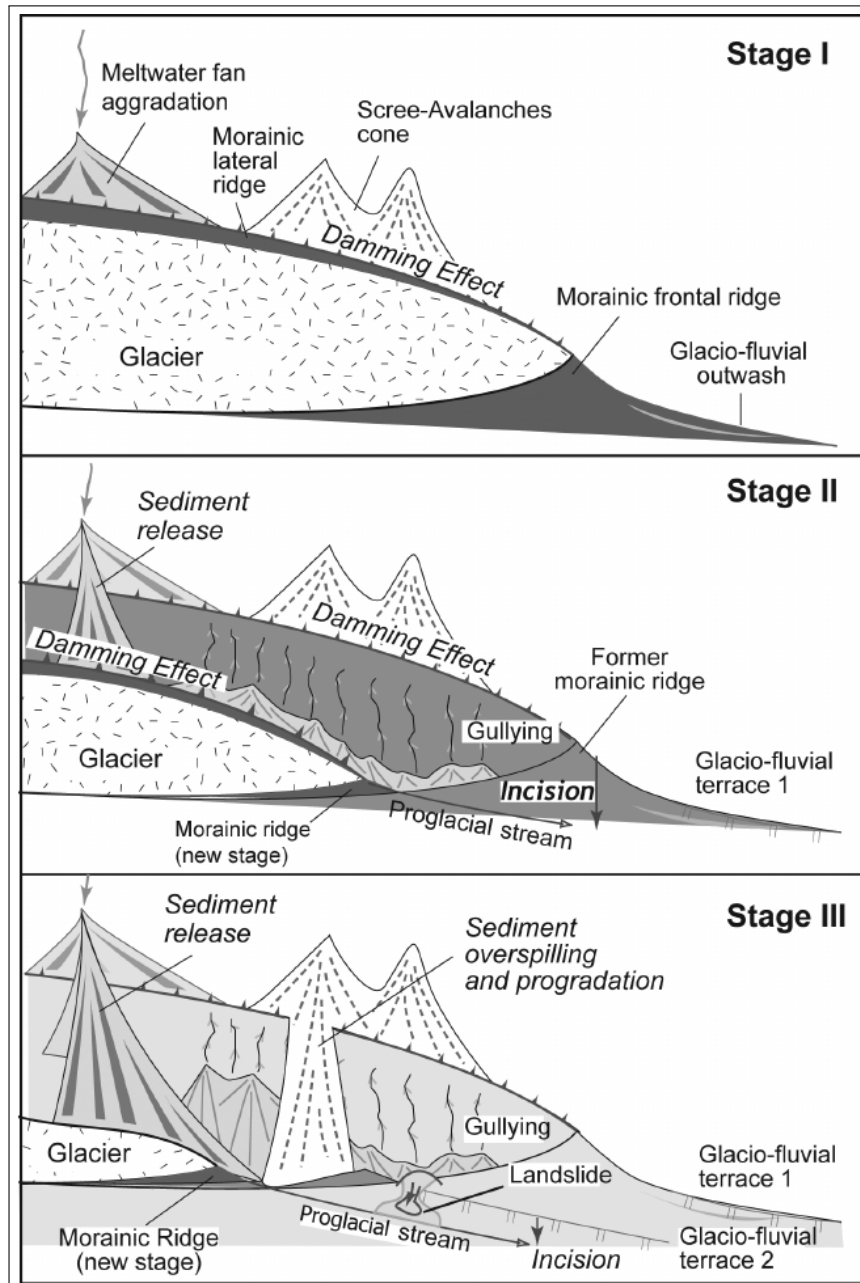
Figure 2.6: Sketch showing the geomorphic evolution of recently deglaciated glacial margins. The presence of moraines creates a damming effect, hence a fragmentation of the cascade sedimentary system. The duration of such damming effects depends on the number, volume and cohesion of moraines and the erosion processes at work on the moraine (Cossart and Fort, 2008)

Figure 2.6 shows the geomorphic evolution of a recently deglaciated glacial margin. In Stage I the glacier is present in its full extent forming a lateral moraine, which acts as a dam for any debris coming from behind the moraine. In Stage II the glacier has retreated and the lateral moraine is exposed to geomorphological processes causing the building of gullies and probably the breaching of the lateral moraine. If and how the moraine is breaching depends on the one hand on the volume of the aggregated sediments behind the moraine and on the other hand on the erosional processes acting on the lateral moraines from both sides. On the valley floor the proglacial stream incises into the glacio-fluvial depositions. With ongoing glacier retreat the lateral moraine may collapse further partially caused by the continuing gullying. The incision of the proglacial stream progresses as well (Cossart and Fort, 2008).

2.3.3 Quantifying and Analyzing

To analyze proglacial areas different methods can be used. In one way or another the forms from different states in time have to be captured. This can either be through geomorphological mapping or remote sensing techniques such as orthoimages or laser scanning. By comparing the different states, it is possible to detect and quantify the changing features.

Horizontal movements can be investigated by image cross-correlation, which have already been applied to glacier surfaces, landslides, rock glacier surfaces, soil creep and debris flows. Further, interferometry has been used to analyze glacier surface motion, river planforms, permafrost creep and rockslides. The synthetic aperture radar (SAR) can either be stationed on a satellite or on a ground-based platform (Carrivick and Heckmann, 2017).

By quantifying elevation changes between different states erosion and deposition of hillslope processes can be identified. This can be done either with differential Global Positioning Systems (dGPS), where only some point of interest can be investigated, or with fully-spatially-distributed methods such as photogrammetry/Structure-from-motion or laser scanning, where Digital Elevation Models (DEM) are generated (Carrivick and Heckmann, 2017; Staines et al., 2015). The association of erosion and deposition towards elevation change in proglacial areas is problematic as elevation change can also be the result of dead-ice/permafrost degradation/melting or aggradation (Carrivick and Heckmann, 2017). However, the analysis of elevation changes is widely used to assess changes in a landscape (Carrivick and Heckmann, 2017; Kociuba, 2017; Lane et al., 2017; Sailer et al., 2012; Staines et al., 2015)

Within geomorphological studies the determination of sediment volumes and budgets are common to understand the landscape evolution (Müller et al., 2014a; Otto et al., 2009). However, the determination of different sediment sources, fluxes and storages within a proglacial area is challenging because of the high temporal variability of proglacial areas as well as the different processes overlaying each other (Carrivick and Heckmann, 2017).

As already implied above the main challenge in the quantification and analyses of proglacial areas is to cover the spatial and temporal scale of the features and processes. Further, processes are interacting and overwriting each other. The presence of buried or dead-ice bodies complicate the identification of processes and features as well. Especially when surface lowering or lifting (DEM Differences) are considered, where elevation changes can occur through erosion/depostion or through dead-ice/permafrost degradation/aggradation (Carrivick and Heckmann, 2017).

2.4   Digital Elevation Models

Remote sensing techniques to study glaciated and high mountain environments are widely used among others due to the difficult access of such landscapes. Generally, these methods can be classified according to (1) the basic sensor types, (2) the location of the platform and (3) the section of the electromagnetic spectrum they cover. There exist two basic sensor types: active (sending and receiving) and passive (receiving) systems. The platform itself can either be located in space, in the air or on the ground. Further, the remote sensing system concentrate their observation in a certain range within the electromagnetic spectrum (visible, near infrared, etc.). The remote sensing techniques are in most cases used to derive digital elevation models (DEM) or other data about the surface (movement or surface cover) (Kääb, 2005b).

2.4.1   Definition

Digital elevation models are quantitative and digital models of a surface, such as the earth surface. There exist different ways to represent such a continuous surface in a GIS: as a regular grid (Altitude matrices) or as a triangular irregular network (TINs). The first mentioned is the most common form and is considered in this thesis (Burrough and McDonnell, 2005). Therefore, the definition for digital elevation models can be concretezed as it represents the elevation of part or all of the Earth's surface within a fixed spacing in two horizontal coordinate directions. The elevation value can either be a sample or an average within one grid cell (Cogley et al., 2011).

2.4.2   Generation techniques

As mentioned above, there exist a wide range of remote sensing techniques and therefore several methods can be used to derive a DEM. An overview can be found in Kääb (2005a). In the following the methods applied to generate the DEMs used in this master's thesis are shortly explained.

Airborne Laser Scanning

Airborne laser scanning (ALS) is an active remote-sensing technique, which uses a laser beam fixed on an aircraft or helicopter to sample a surface (Albertz, 2009; Bossard, 2014). A LiDAR (= light detection and ranging) system measures the distance to the target by calculating the elapsed time between the emitted and the received return signal. Among the LiDAR system an ALS needs further a global navigation satellite system (GNSS) and an inertial navigation system (INS) (also called Inertial measurement units IMU) to determine the position and orientation of the platform. Finally, a control and data recording unit is necessary to preserve the measurements (Albertz, 2009; Deems and Painter, 2006; Lilesand et al., 2008). An advantage of LiDAR remote sensing systems is the ability to detect multiple returning pulses and therefore the possibility to map vegetation or building heights (Deems and Painter, 2006; Lilesand et al., 2008).
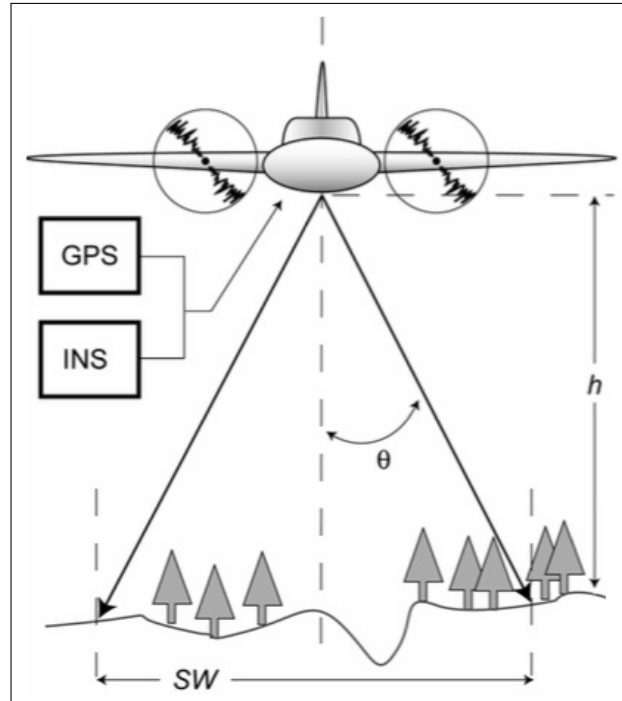
Figure 2.7: Airborne Laser Scanning (ALS) principle
with acquisition parameters scan angle, platform height,
swath width, GNSS and INS (Deems and Painter, 2006)

The laser scanning system considers two optical beams - the emitted laser beam and the returned signal of the respective beam. The emitted laser beams are directed by an oscillating mirror. Among the current angle of the mirror, the position (GNSS and INS) of the platform and the laser time range (time between the emitted and the received return signal) needs to be known for the determination of the position (x, y and z) of an object. A characteristic parameter to describe and compare ALS campaigns is the average point density, which depends on scan angle, the scanning frequency, the flying height above ground, the measuring frequency and the aircraft ground speed (Deems and Painter, 2006; Lilesand et al., 2008; Wehr and Lohr, 1999). Further, the parameters of the used laser beam (wavelength and beam divergence) are needed to know for comparing ALS campaigns (Bossard, 2014). The result of an ALS campaign is a point cloud with x, y and z values for each point. Such point clouds are commonly simplified to a raster grid for further analysis (Hugenholtz et al., 2013; Joerg et al., 2012).

Photogrammetry and Structure from Motion
Photogrammetry describes the science and technology to obtain spatial measurements from photographs. The photographs must overlap and can either be analogue (hardcopy) or digital. Among other products digital elevation models can be generated with photogrammetry (Lilesand et al., 2008). A wide range of satellite images or aerial photographs can be used to generate DEMs with Photogrammetry (Kääb, 2002; Micheletti et al., 2015). For the 3-D reconstruction of a scene the 3-D location and pose of the camera(s) and/or the 3-D location of some control points need to be known (Westoby et al., 2012).

With the recent development in computer technologies digital photogrammetry has advanced. With 'Structure from Motion (SfM)' a new approach emerged within digital photogrammetry. Structure from

motion applies the basic principles of photogrammetry (3-D reconstruction from a series of partially overlapping images) to images obtained by low-cost and non-metric cameras. Often such cameras are fixed on unmanned aerial vehicles (UAVs or drones). There is no knowledge about the camera position or the location of ground control points (GCP) necessary, which is the main difference towards the 'conventional' photogrammetry. These parameters are reconstructed simultaneously through the identification of matching features in multiple images. With Structure from Motion a 3-D point cloud is generated in a 'fictive' space/coordinate system. To align this point cloud to a real-world coordinate system, some ground control points (GCPs) with known real-world coordinates need to be identifiable within the point cloud. Such GCPs can be determined after the images were taken or in advance. Structure from Motion is most suitable for areas with minimal vegetation coverage and relatively complex, heterogeneous topography (meso- and micro-scale) (Westoby et al., 2012).

3. Study Site and Data

3.1 Study Site

3.1.1 Location and Area of Interest

This thesis investigates the Findelengletscher (also called Findelgletscher) and its surrounding area. The Findelengletscher is a temperate valley glacier located in the Swiss Alps in the Canton Valais (46°00' N, 7°52' E), close to Zermatt (Figure 3.1). It covers an area of about 13 km^2 and has a length of about 6.7 km (2010) (Joerg et al., 2012). The elevation span ranges from 2600 to 3900 m a.s.l.. The glacier is facing west and has a well-defined outline with a distinct tongue. Since the end of the Little Ice Age the glacier has retreated and separated from his former tributary Adlergletscher (Joerg et al., 2012; Maisch et al., 2000).
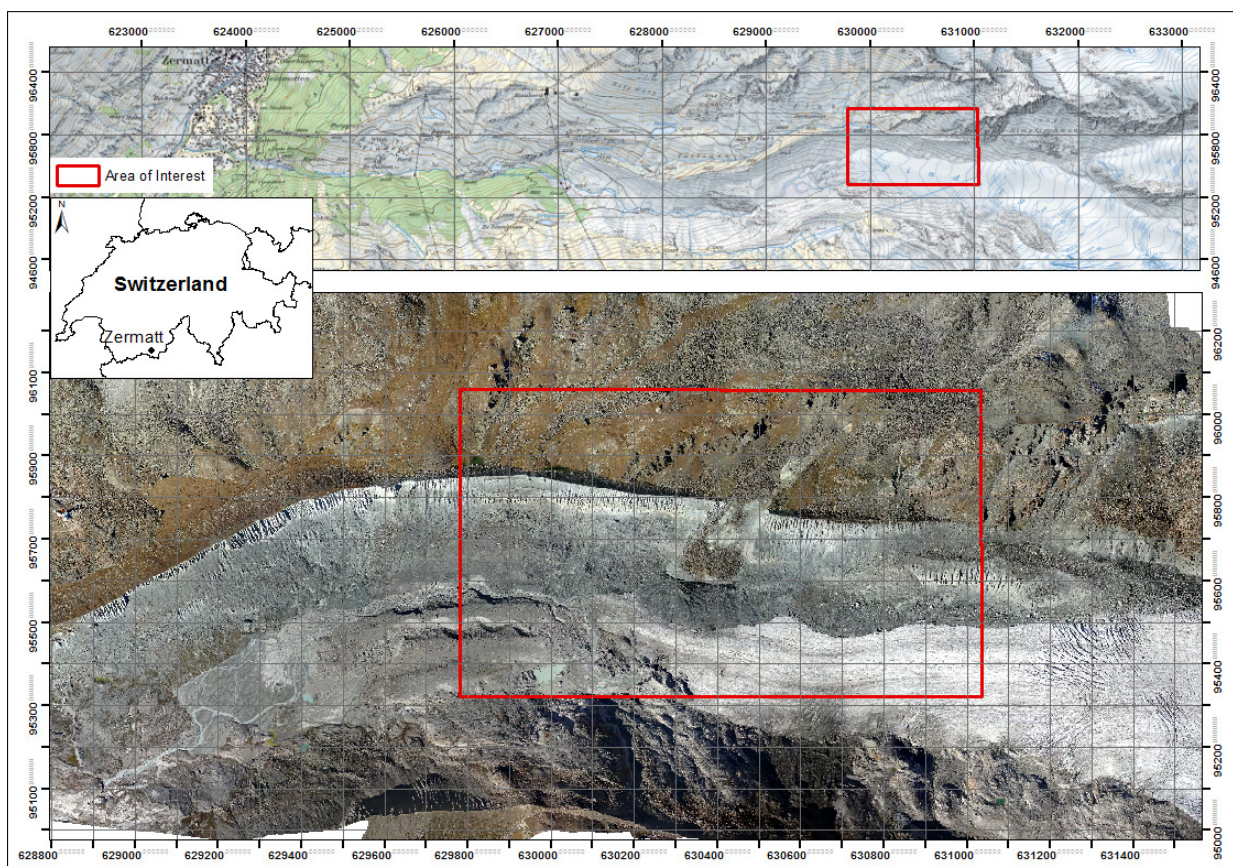
Figure 3.1: Location of the study area with the area of interest (Background: Swisstopo, Orthophoto 2017)

The glacier forefield and the frontal part of the glacier tongue are flanked by two prominent lateral moraines, which are approximately 3km long and stand up to 140m above the valley floor. The glacier-facing side of the moraines are steep (41-64°, locally 80°) and vulnerable to ongoing reworking, whereas the glacier-averted side is less steep and vegetated (Figure 3.1) (Lukas et al., 2012). This study focus on the right (northern) lateral moraine and the frontal part of the glacier tongue, where a landslide broke through the lateral moraine and partially deposited on the glacier (Figure 3.1).

On the basis of the field campaign in summer 2017 and the initial sighting of the available data the investigation area is divided into different zones for each observation year (Figures A.13-A.19, Appendix). Figure 3.2 shows the orthophoto from 2017 with the different zones and an overview about the location of the applied research methods. The evolution of the different zones is covered in Section 5.3. In Figure 3.3 one can see two profiles of 2017 through the lateral moraine: once down-glacier from the landslide (Figure 3.3a) and once through the landslide (Figure 3.3b) with the different zones indicated. The zone 'Glacier' covers the debris-free ice-body of the glacier tongue (light blue in Figures 3.2 & 3.3). The moraine is divided into two parts. The moraine top goes with landscape beyond as it is more or less stable over the observation periods. The 'Moraine-Foot' zone covers the lower part of the moraine starting beneath the gullies towards the glacier margin respectively the valley floor (orange in Figures 3.2 & 3.3a). Further, the zone 'Slide-Area' is defined as the landslide area, which covers the area from the release area towards the deposits of the landslide (red in Figures 3.2 & 3.3).
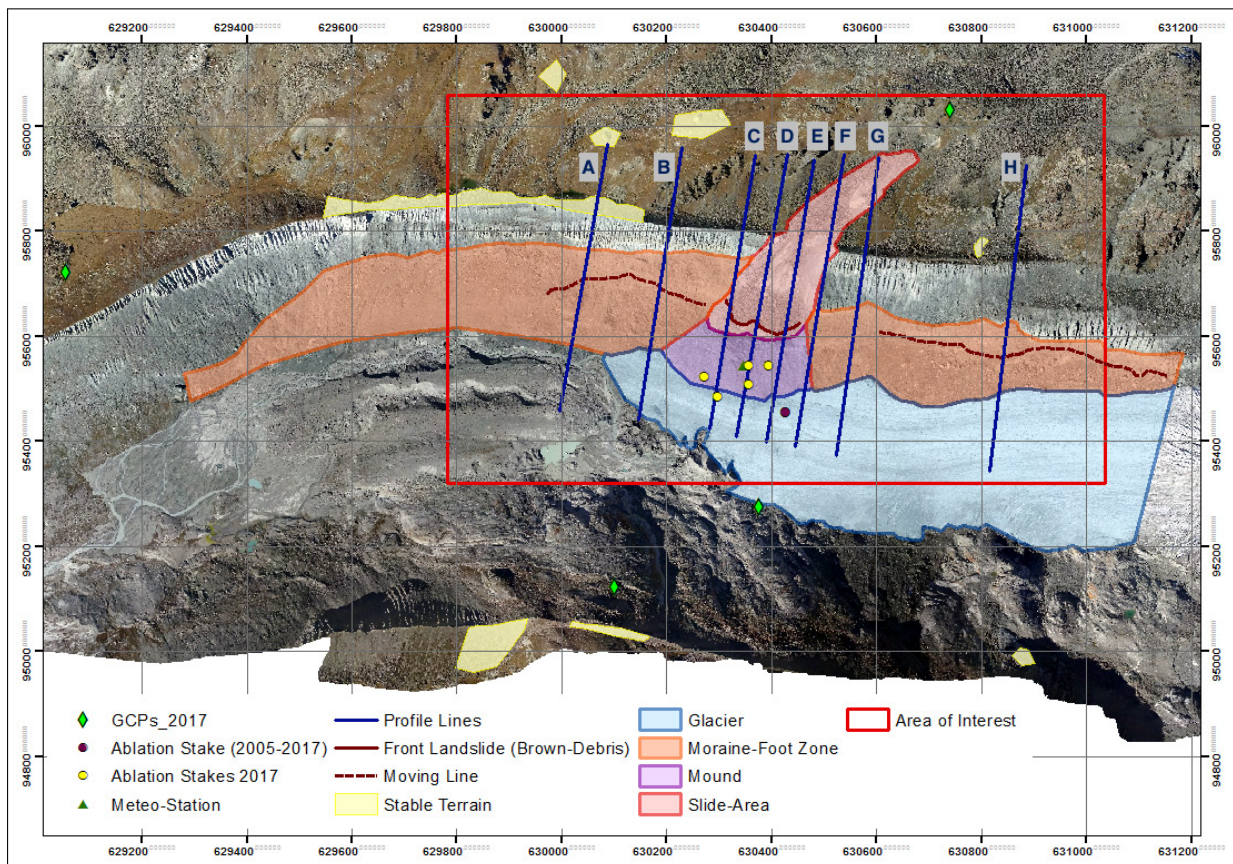
Figure 3.2: Orthophoto from 2017 with the different zones and the location of the applied research methods

(a) Profile with the zones Glacier and Moraine-Foot   (b) Profile with the zones Glacier, Mound and Slide-Area
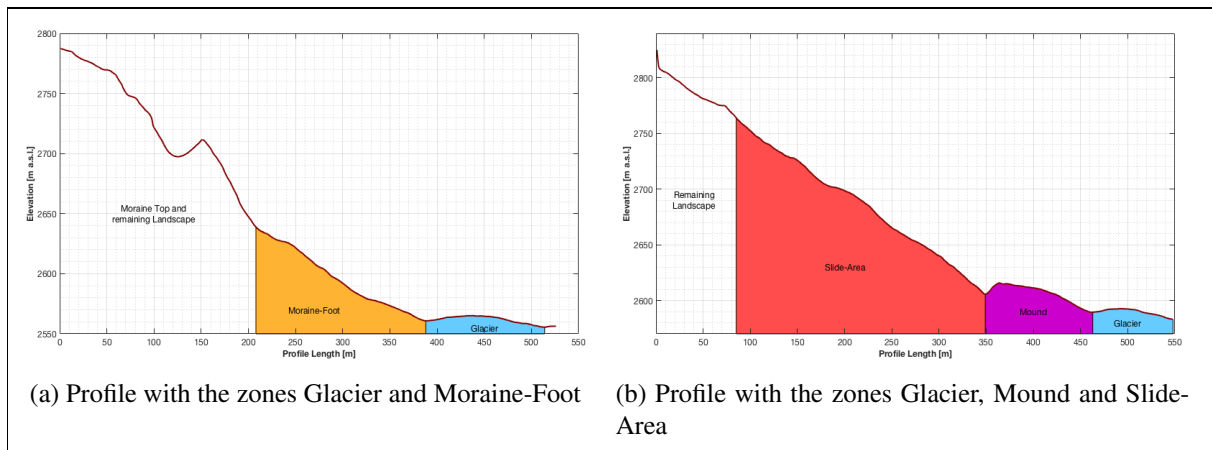
Figure 3.3: Profile through the right lateral moraine beside the landslide (a) and through the landslide (b) with the corresponding zones

3.1.2 Previous Research on Findelengletscher - an Overview

The Findelengletscher has been the subject of a few research projects concerning different aspects of glacier releated research fields. Length variation measurements have been available since 1885 (GlaciologicalReports, 2017) and since 2004 direct glaciological mass balance measurements have been conducted. The resulting data are reported to the Swiss Glacier Monitoring Network (GLAMOS) and the World Glacier Monitoring Service (WGMS). For the time period 2004/05 - 2009/10 a mean annual mass balance of -0.38 m w.e. were reported (Joerg et al., 2012; Rastner et al., 2016). Other studies investigated the volumetric changes of the glacier (Bossard, 2014; Joerg and Zemp, 2014; Joerg et al., 2012; Kääb, 2005a) or the glacier surrounding (Ruff, 2015) on the basis of different digital elevation models. Rastner et al. (2016) analyzed and visualized the retreat of the Findelengletscher between 1859 and 2010. The spatial distribution of winter snow on the glacier was explored by Machguth et al. (2006) and Sold et al. (2013). Lukas et al. (2012) examined the morphology, genesis and preservation potential of the lateral moraines. Further studies investigated the hydrology and discharge of the Findelengletscher area (Huss et al., 2014; Uhlmann et al., 2013a,b).

The large amount of studies is mainly based on three reasons: (1) the Findelengletscher's surface has a nearly constant slope and is almost debris-free, (2) the big elevation range (2600 - 3900 m a.s.l.) is the basis for a strong melt over multiple decades and (3) the nearby cable car and helicopter-base allows an easy access to the glacier (Joerg et al., 2012).

3.1.3 Settings at Findelengletscher

Glacier history and Moraine formation

As mentioned-above, the glacier length change of the Findelengletscher is reported since 1885 (GlaciologicalReports, 2017) and Rastner et al. (2016) analyzed the retreat of the glacier using old topographic maps and new digital elevation models. Figure 3.4 shows the reported length change. Since the beginning of the length measurements, the position of the glacier termini has retreated more than 2.5km (GlaciologicalReports, 2017). Three periods (1890-1909,1920-23 and 1988-1995) show a glacier advance (GlaciologicalReports, 2017; Rastner et al., 2016). For two of those periods Rastner et al. (2016)

also determined a thickness gain. Further, Rastner et al. (2016) animated the evolution of the Findelen-gletscher according to their findings, which is available as supplementary material of their study.
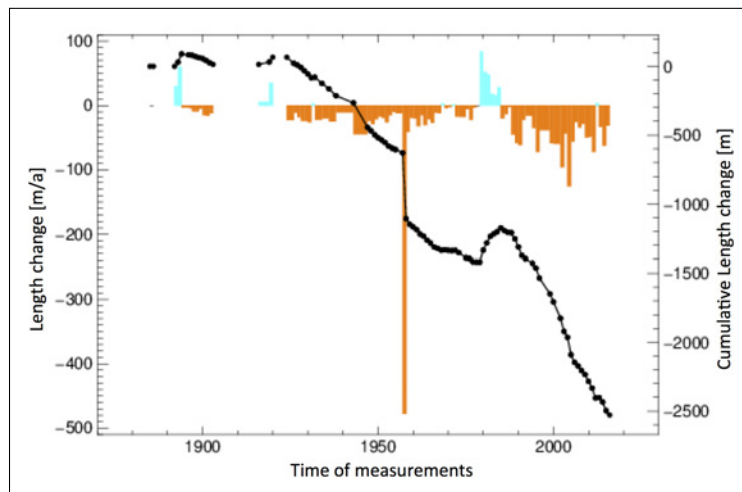
Figure 3.4: Length change of the Findelengletscher since 1885. The orange bars mark glacier retreat and the light blue ones mark glacier advance. The black line is the cumulative length change since 1885 (GlaciologicalReports, 2017)

Lukas et al. (2012) investigated the moraines and the forefield of the Findelengletscher. Among other things they found evidence of debris transport (subglacial or englacial origin) to the glacier surface at the glacier margin and observed dead-ice within the moraine formed during the glacier retreat after the 1979/1980 advance. Within their investigation period the dead-ice reached a maximum height of 30m above the valley floor. The dead-ice is visible, where the overlaying debris sediments were reworked. According to their findings at Findelengletscher Lukas et al. (2012) developed a conceptual model of lateral moraine formation in the Alps (Figure 3.5). Sub- and englacial debris is transported along debris bands and is melting out on the glacier surface (Figure 3.5a). When the glacier is retreating ablation on the bare ice is bigger than under the debirs-covered part causes the formation of debris cones (Figure 3.5b). With further recession of the glacier dead-ice zones could be established in the lower part of the moraine (Figure 3.5c). The upper part of the moraine is exposed to paraglacial processes (gullying) and in the lower part the dead-ice melt-out is forming debris fans (Figure 3.5d) (Lukas et al., 2012).
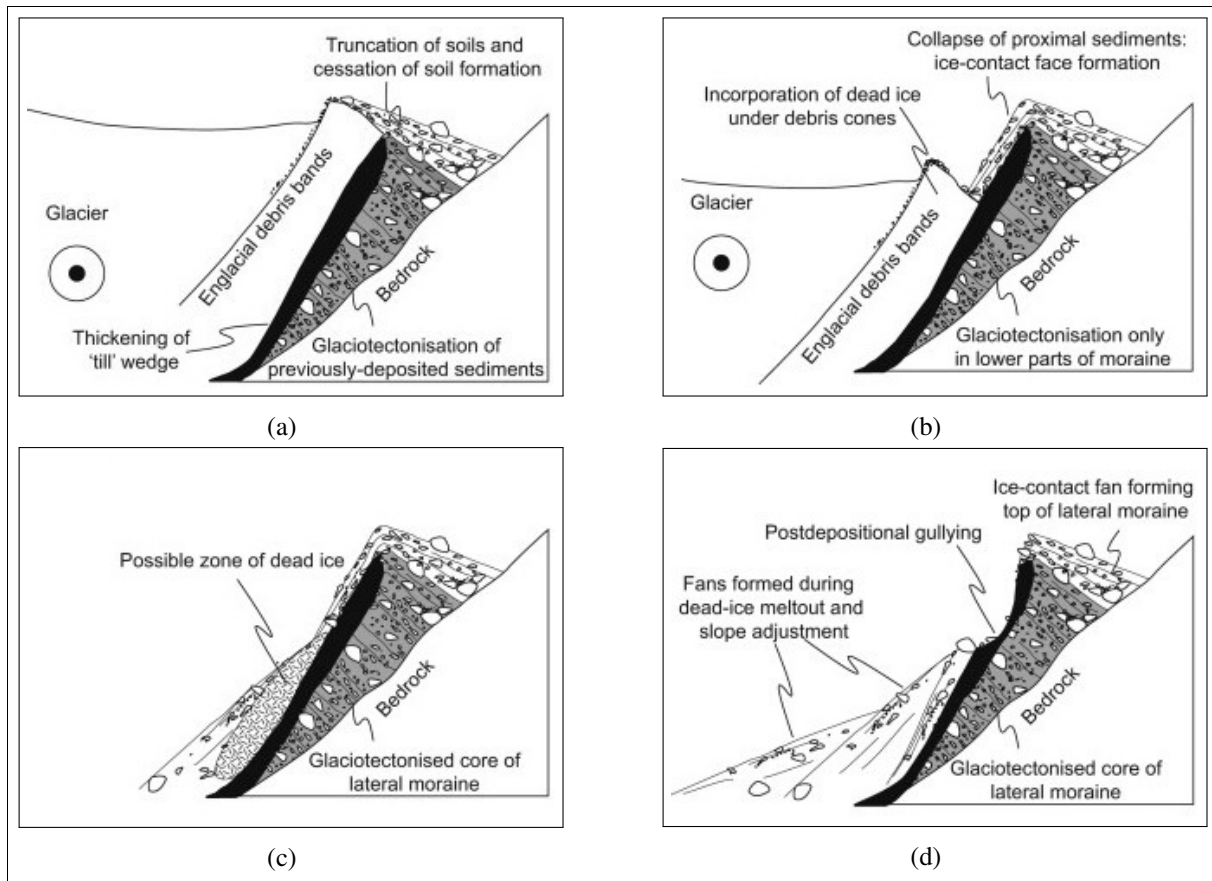
Figure 3.5: Schematic diagram showing the conceptual model of lateral moraine formation (Lukas et al., 2012)

Landslide event

The above-mentioned landslide is first recognizable in the data from 2009 (see Figure A.7, Appendix). To find out the approximate timing of the landslide other remote sensing data were considered (to fill the gap between 2005 and 2009). First, google earth was examined but there were no data available for this time period. Second, Landsat respectively the U.S. Geological Survey (USGS) was considered. In Figure 3.6 one can see the available data for the questionable time period, but the resolution is too coarse. So it is not possible to determine when the landslide event occurred exactly between 2005 and 2009.

(a) 18th June 2006

(b) 21st July 2006

(c) 06th September 2006

(d) 22nd September 2006
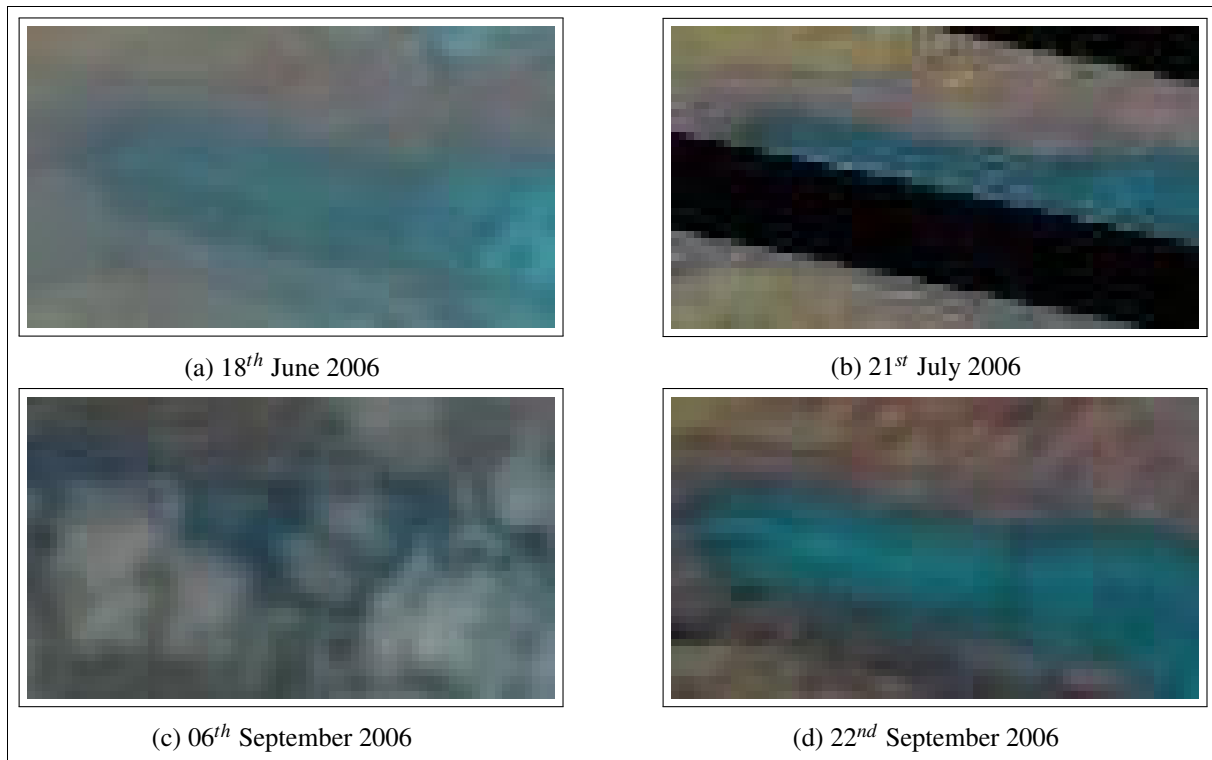
Figure 3.6: Landsat Images from the U.S. Geological Survey (USGS) (Access: 30.November 2017)

In Figure 3.1 and in Figure 3.7 it is visible that the whole landslide can be divided according to the color of the material. The brown material originates from the upper part of the release area (hillslope behind the moraine), whereas the grey material has been part of the moraine. In Figure 3.7 one can see that the landslide (mainly brown material) slides down and pushes the moraine material (grey material) in front of it. Regarding the size of the landslide material it is visible that all kind of stone sizes and grain sizes are present (Figure 3.8b). Sometimes even a whole body of soil and stones are dislocated as a whole block.

Within the landslide area one can see that in some parts the bedrock is visible, which means the whole overloading moraine has been dislocated (Figure 3.8). Further, a layer of fine material on the bedrock is recognizable (Figure 3.8d), which probably acted as a sliding horizon.
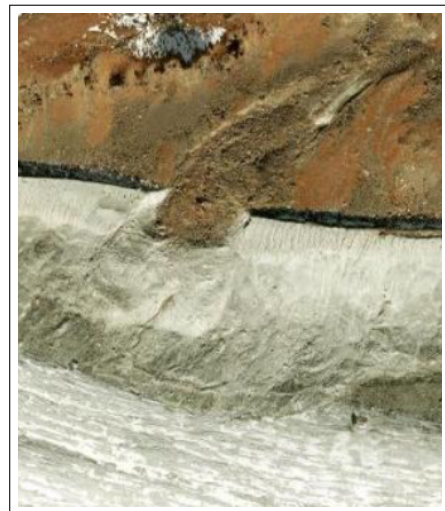
Figure 3.7: Map showing the landslide in 2009 (GoogleMaps, Access: 26.January 2018)

(a) Landslide viewed from the opposite lateral moraine (2017)

(b) Landslide Area viewed from below (2017)

(c) Uncovered bedrock within the sliding area (Photo: A.Vieli, 2015)

(d) Layer consists of fine material overlaying the bedrock (Photo: A.Vieli, 2015)

Figure 3.8: Photographs of the landslide area

3.2 Data

In this thesis data sets from different providers are used (Table 3.1). This section emphasizes on showing an overview over the data, their acquisition purpose and processing standard.

Name Abbr.	Acquisition Date	Acquisition Method	Research Project	Raster Resolution	Product
2005	28./29.Oct 2005	Airborne Laser Scanning	GLAXPO	1m	DEM
2009	4.Oct 2009	Airborne Laser Scanning	GLAXPO	1m	DEM
2010	29.Sept 2010	Airborne Laser Scanning	GLAXPO	1m	DEM
2013	No information	Arial photos (Photogrammetry)	GLAMOS	1m	DEM
2014	No information	Arial photos (Photogrammetry)	GLAMOS	1m	DEM
2015	No information	Arial photos (Photogrammetry)	GLAMOS	1m	DEM
2016	*No information*	*Arial photos*	*GLAMOS*	*1m*	*Aerial Photos*
2015 Sept	*08.Sept 2015*	*eBee Drone (Structure-from-Motion)*	*GIUZ*	*0.14m*	*Orthophoto/ DEM*
2017	21.Sept 2017	eBee Drone (Structure-from-Motion)	GIUZ	0.3m	Orthophoto/ DEM

Table 3.1: Remote Sensing Data: Orthophoto and Digital Elevation Models (DEM). *italic* written data was available but only partially used within this thesis

As in Table 3.1 marked, some of the available data were only considered for a part of the analyses. The data for 2016 is only used in the Tracking of large boulders (Section 4.3.2). For the observation year 2015 the data from the GLAMOS is used because this data is already at a 1m resolution. In the following the data sets are named after their year of acquisition.

3.2.1 GLAXPO

Four DEMs were acquired by airborne laser scanning (ALS) through BSF-Swissphoto in October 2005, in October 2009 and in September 2010 within the Glacier Laserscanning Experiment Oberwallis (GLAXPO). GLAXPO was a project of the University Zürich in collaboration with AXPO Holding AG. The data cover the whole Findelen- and Adlergletscher and their surrounding. The highest point density was obtained in September 2010 (14.3 Pt/m^2) and the lowest in October 2005 (1.1 Pt/m^2). The received point clouds were interpolated into rasters with 1m resolution (Joerg and Zemp, 2014; Joerg et al., 2012). Joerg et al. (2012) assigned a mean systematic uncertainty of 0.15m and a maximal stochastic uncertainty of 0.1m to the data from 2005. The uncertainties for the other data sets are smaller due to the higher point densitiy. For detailed information about the data acquisition parameters, data preparation and uncertainty assessment see Joerg et al. (2012) and Joerg and Zemp (2014).

3.2.2   GLAMOS

The data for the years 2013-2015 (2016) were obtained by the 'Schweizerisches Gletschermessnetz' (GLAMOS), which gather measurements for the glaciers in the Swiss Alps. The network is operated by the ETH Zurich and the Universities Fribourg and Zurich. In this context arial photographs are taken ever year from which Digital Elevation Models are acquired by photogrammetry (GLAMOS, 2018).

3.2.3   GIUZ

The Department of Geography (GIUZ) owns an eBee drone, which is a professional mapping drone developed by senseFly. The drone captures high-resolution arial photos that can be transformed into orthomosaics and 3D models (SenseFly, 2017). Within this thesis a drone flight in 2017 was planned and conducted by Nico Mölg. For more information about eBee and the acquisition of a DEM with eBee see Section 4.1.4.

4. Methods

4.1 Field Measurements

4.1.1 Ablation Measurements

On the 13th July 2017 ablation stakes are installed on the debris-covered mound (Stakes 1-4) respectively on the bare glacier tongue (Stake 5). Stake 6 is from the Glacier Monitoring Program and is used as an additional data source. The installed ablation stakes are distributed over the mound (two on the top, two on the flank) and at varying debris thickness (15cm, 25cm and 30cm) (Figure 4.1 and Table 4.1). For the stakes without or only thin debris cover four meter holes are drilled (Stake 1,2,5), whereas at the sites with thicker debris cover only two meter holes are used (Stake 3,4). As the holes cannot be perfectly drilled, some offsets can occur describing whether the stake is beneath or above the surface (Table 4.1, Column4). For the installation the debris cover has to be removed, so that it is possible to drill the hole with the Kovacs Ice Driller. After the drilling and the inserting of the ablation stake, the debris is rearranged as originally as possible.

	Debris Thickness [m]	Stake Length [m]	Offset Installation [m]	h_{t_0} [m]
Stake 1	0.15	4	-0.05	4.05
Stake 2	0.15	4	0.05	3.95
Stake 3	0.3	2	0.1	1.90
Stake 4	0.25	2	0.06	1.94
Stake 5	0	4	-0.05	4.05

Table 4.1: Overview of the installed ablation stakes with the stake height (h_{t_0}) in the last column

On the 23rd August and on the 21st September 2017 the melt can be determined by measuring the length out of the ice/debris. As the ice melt rate is usually expressed in units of water equivalent one have to multiply it with the density of ice.

Uncertainties mainly occur through errors in the height determination due to sinking or floating of the ablation stakes or reading/measurement errors (Zemp et al., 2013). Further, the movement of debris boulder or the ice can cause tilting or in the worst case breaking of the ablation stakes, which also introduces errors (Nicholson and Benn, 2006).
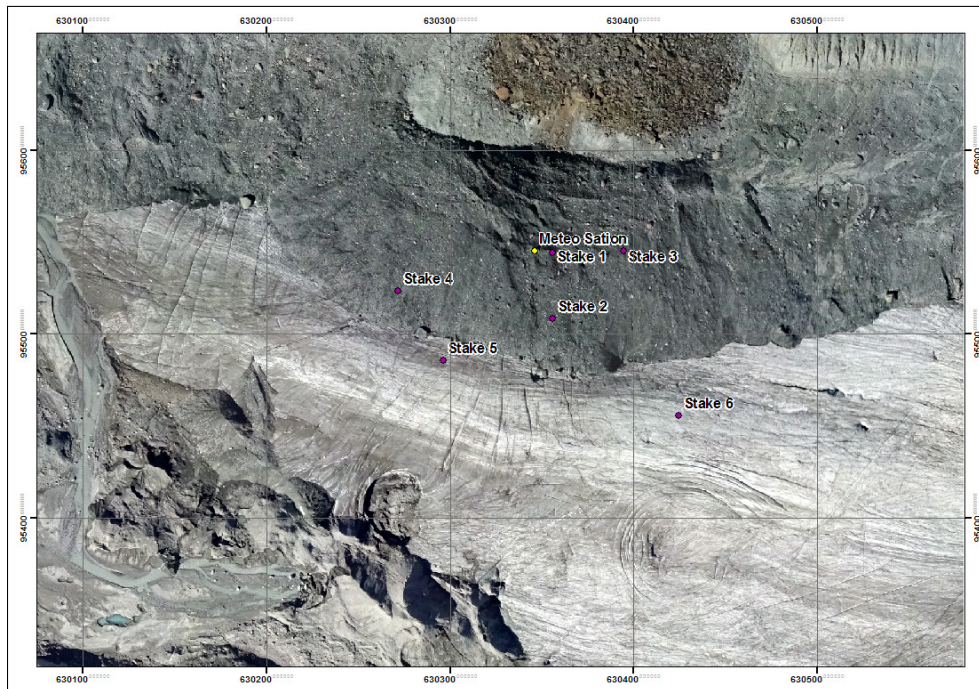
Figure 4.1: Location of the ablation stakes and the Meteo-Station (Stake 1-5 within the field campaign of this thesis, Stake 6 part of the Findelengletscher Monitoring Program)

4.1.2 Stake Displacements

Within the field measurement campaign four ablation stakes were placed on the mound in the study site. The position of the stakes is measured with the differential GPS (dGPS) on the day of the installation (13th July 2017) and on the 21st September 2017, when the stakes are pulled out.

The Differential Global Positioning System (dGPS) is an enhancement to the Global Positioning System (GPS) using fixed ground-based reference station with known coordinates to enhance the accuracy of the location measurement (Figure 4.3). Through the difference between the known position of the reference station and the measured position by the satellites, the atmospheric disturbance at this point can be determined. This is then used to correct the GPS Measurement of the Rover (mobile GPS-receiver). This differential procedure can be made in real time if there is any kind of a radio connection (radio, mobile network, etc.) between the reference station and the rover. There are 31 reference station in Switzerland and one of them is located in Zermatt (Bergstation Furi) (Swisstopo, 2017b). These reference

Figure 4.2: dGPS in the field (measuring a ground control point for the Drone)

stations work with the new Swiss reference system (LV95 LHN95), which conditioned a coordinate transformation as this thesis uses the old swiss reference system (LV03 LN02). The transformation is done with the REFRAME online tool provided by swisstopo (Swisstopo, 2017a).
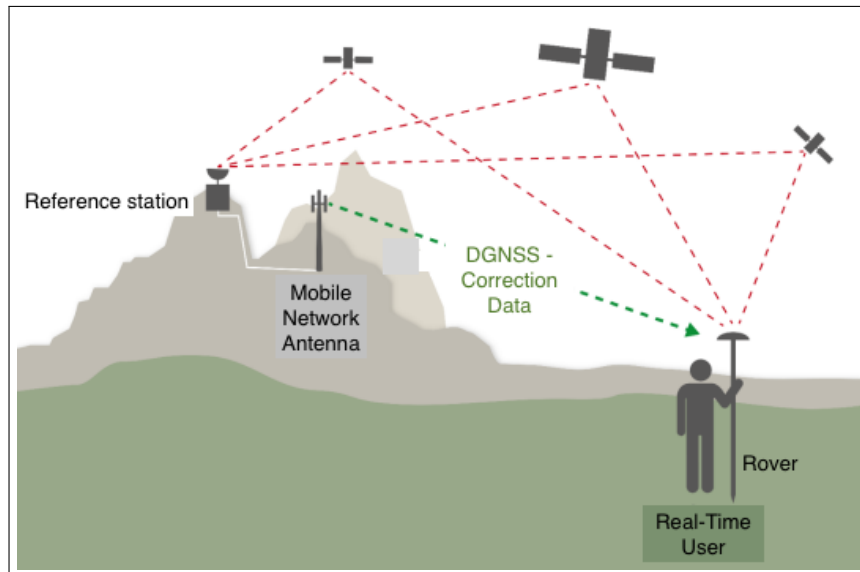
Figure 4.3: Schematic sketch of the functional principle of a dGPS (Swisstopo modified)

A dGPS surveying equipment consists of three parts: the antenna with a tripod, the GNSS/GPS receiver and the controller. The antenna is installed on the top of the tripod and the tripod is set to a length of 1.5m. The antenna and the GNSS/GPS receiver are connected with a cable. (Figure 4.2). The bubble level on the dGPS antenna helps to aligne it upright. The receiver and the controller communicate over radio, so no further cable is necessary. On the controller each measurement can be named and stored in a surveying project. The antenna height (1.5m in this case) has to be entered before the measurement.

4.1.3 Meteorological Data

Among the ablation stakes a small Meteo Station, which measures the air temperature and the solar radiation, has been installed to relate the obtained melt measurements to the local weather conditions. The measuring devices are installed at a pole, which then is fixed on a large boulder on the mound (Figure 4.4 and Figure 4.1).
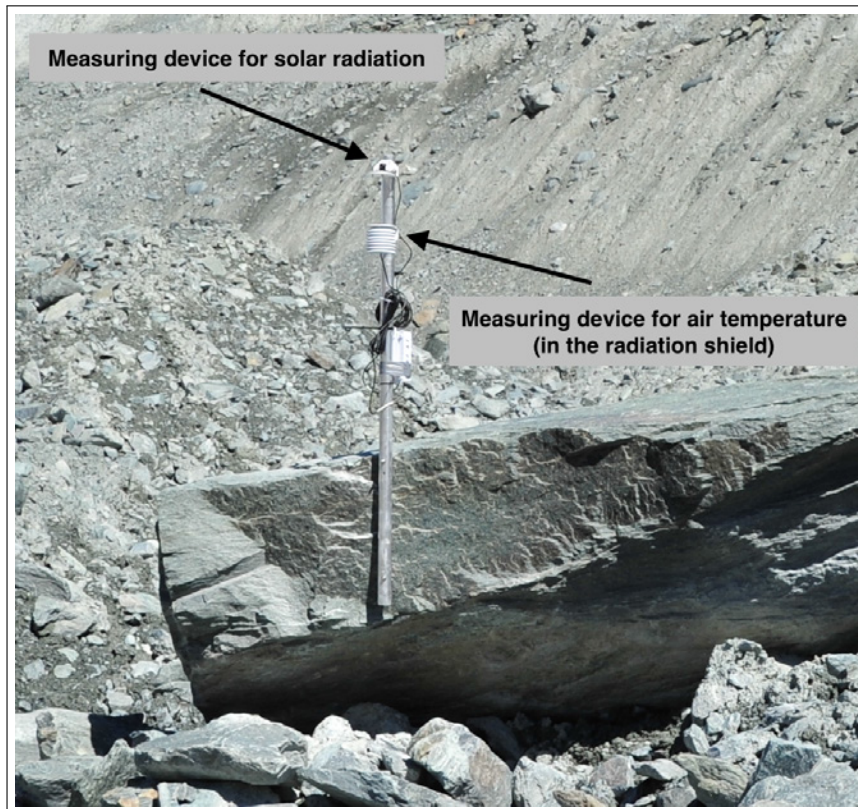
Figure 4.4: Meteo Station

4.1.4 Acquisition of a DEM with eBee drone

The eBee drone (Figure 4.5) is a professional mapping drone developed by senseFly. The drone captures high-resolution aerial photos that can be transformed into orthomosaics and 3D models. The drone consists of two wings and the main body. The main body provides the place for the camera and battery. The propeller is attached to the main body as well. The drone (inclusive the camera) has a wingspan of 96cm and is approximately 700g heavy (SenseFly, 2017).

Flight Planning and Procedure

The Software eMotion, provided by senseFly upon the acquisition of the eBee drone, is used for the flight planning. The software can be used to plan, simulate, monitor and control the flight mapping.

In the beginning the user can choose or import a background map and define the region of interest. In the next step the desired ground resolution and image overlap can be defined. The Software will than automatically generate a flight plan, which includes the calculation of the required flying altitude. The flight tra-

Figure 4.5: eBee Drone

jectories and waypoints are displayed over the background map. After the flight plan is uploaded to the drone and the battery levels are checked, the drone is ready for launching.

To start the drones motor, the drone has to be shaken three times and the drone can just be thrown into the air. The drone rises (in loops) as in the flight plan defined and follows the planned flight trajectories. In the eMotion software the flight parameters, battery level and image acquisition are displayed in real time (SenseFly, 2017). To cover the study site of this thesis two 20 minutes drone flights were required. The aim was to get an orthphoto and DEM with a resolution of 30cm. The flight was planned and performed by Nico Mölg.

Data Processing

With the eMotion Software the flight images can be organized and pre-processed. For the production of a georeferenced orthomosaic raster and digital surface models the Software Agisoft PhotoScan Pro (Agisoft LLC, 2018) was used. In advance of the flight some Ground Control Points (GCPs) were marked with color (big enough to be captured in the photographs of the drone) and their position is determined by the dGPS (Figure 4.2). Agisoft PhotoScan Pro works in three processing steps. In the first step unique features are identified and matched in the different images with an algorithm. Afterwards, they are used to determine the camera orientation (internal and external) from which a three-dimensional point cloud is created. These two steps are repeated in an iterative process until the optimal point cloud is found. In the last step the GCPs comes into play with which the generated point cloud is georeferenced (Agisoft LLC, 2018).

4.2 Pre-Processing and Uncertainties

For the DEM processing and analyzing three different software packages are used: ArcGIS Desktop version 10.0 (ESRI, Inc.), MATLAB (The MathWorks, Inc) and Microsoft Excel 2011/2016 (Microsoft, Inc). The first-mentioned is used to perform tasks related to analyzing, comparing and visualizing. With MATLAB (The MathWorks, Inc) calculations and visualization are done. In Microsoft Excel 2011/2016 (Microsoft, Inc) the Solver Add-In is used to do the co-registration.

4.2.1 Pre-Processing

The pre-processing includes all work steps that are necessary to be able to compare the different DEMs, which includes three tasks: Coordinate Transformation, Resampling to the same cell size and the Co-Registration.

Coordinate Transformation

The coordinate system of the different DEMs have to be homogenized. The reference system used in this thesis is the old swiss reference system (CH1903 LV03 LN02). Therefore, all the DEMs with another reference system or no further information about the reference system have to be reprojected and transformed with the Project Raster Tool in ArcGIS.

Resampling

In Table 3.1 one can see that the available data sets do not have the same raster resolution. In order to compare them, it is necessary to have the same cell size. The aim is to work with a raster resolution of 1x1m, so the Drone DEM have to be resampled. The resampling is performed in ArcGIs with the Resampling tool with the bilinear option. This method determines the new value of a cell based on a weighted distance average of the four nearest input cell centers and is useful for continuous data as it will case a smoothing of the data (ESRI, 2017).

Co-Registration

The last step of the pre-processing is the co-registration, whereby the DEMs (slaves) are aligned to one DEM (master). The DEM of 2015 is selected as the master DEM. The co-registration ensures that the pixels for each DEM represent the same location on the Earth's surface. Nuth and Kääb (2011) provide a framework for assessing and correcting DEMs to quantify glacier elevation changes. In their approach three potential biases over stable terrain (e.g. off glacier) are identified: (1) geo-location of the data (x, y and z matrices), (2) elevation dependent bias and (3) biases related to the acquisition geometry of the data. The main interest of this thesis lies in the systematic uncertainties and shifts resulting from the first potential bias (Nuth and Kääb, 2011).
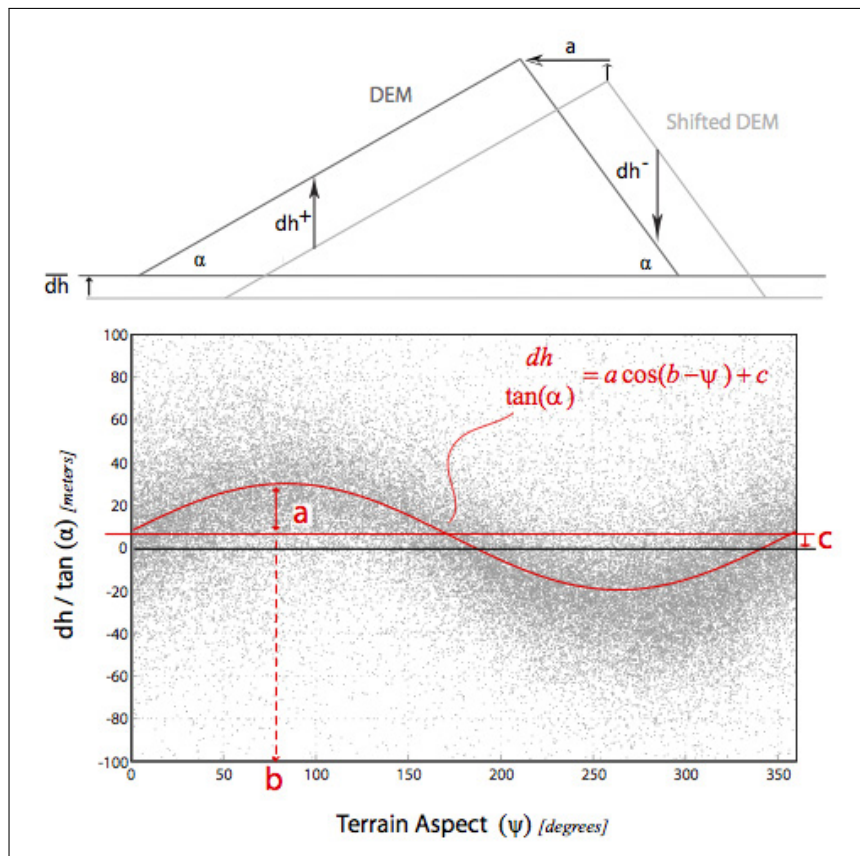
Figure 4.6: Top: 2-D scheme of elevation differences induced by a DEM shift. Bottom: The scatterplot of elevation differences between two DEMs, showing the relationship between the vertical deviations normalized by the tangent of the slope (y-axis) and the terrain aspect (x-axis) (Nuth and Kääb, 2011)

Two DEMs that are not perfectly aligned show a characteristic relationship between elevation differences and the direction of the terrain (aspect) that is related to the x- and y-shift vector between the two DEMs. A schematic drawing and a real example were one DEM is shifted to another is shown in Figure 4.6. The elevation difference is related to the magnitude (a) of the shift vector and the tangent of the slope of the terrain (α) (Equation 4.1). This means that the elevation differences are larger on steeper terrain:

$$\tan(\alpha) = \frac{dh}{a} \tag{4.1}$$

Further, the elevation differences (dh) are positive on eastern slopes and negative on western slopes because the terrain aspect (Ψ) is usually defined circular form the north (azimuth). So the direction of the shift can be modeled as the cosine of the difference between the aspect (Ψ) and the horizontal directional component of the shift vector. By combining this relation and Equation 4.1 a full analytical solution can be derived by relating the elevation differences to the elevation derivatives slope (α) and aspect (Ψ):

$$dh = a \cdot \cos(b - \Psi) \cdot \tan(\alpha) + \overline{dh} \tag{4.2}$$

where dh is the individual elevation difference, a is the magnitude of the horizontal shift, b is the

direction of the shift vector, α is the terrain slope, Ψ is the terrain aspect and $\overline{dh}$ is the overall elevation bias between two DEMs. To get a clean sinusoidal relationship between elevation difference and aspect (Figure 4.6), the vertical deviations are normalized by dividing by the tangent of the slope. So equation 4.2 can be transformed to:

$$\frac{dh}{\tan(\alpha)} = a \cdot \cos(b - \Psi) + c \tag{4.3}$$

where

$$c = \frac{\overline{dh}}{\tan(\overline{\alpha})} \tag{4.4}$$

The graphical description of the three cosine parameters (a, b and c) is shown in Figure 4.6 and they can be solved using least squares minimization. As the terrain, which is not an analytical surface, is used to solve this analytical relationship, the first solution may not be the final solution. So iterations of the process are necessary to achieve the final solution. The iterations can be stopped for example after the improvement of the standard deviation is less than 2% or if the magnitude of the solved shift vector is less than 0.5m (Nuth and Kääb, 2011).

For the determination of the mean elevation bias (dh) equation 4.4 can be rearranged and an estimation of the mean terrain slope is used. The x- and y-components of the shift vector can be determined from the magnitude (a) and direction (b) with the following basic trigonometric relations:

$$\begin{aligned} \Delta x &= a \cdot \sin(b) \\ \Delta y &= a \cdot \cos(b) \end{aligned} \tag{4.5}$$

For the co-registration unglaciated and stable areas with equal distribution of the aspect (to detect horizontal shifts in every direction) and over the study site are selected. The chosen areas are shown in Figure 3.2. For these areas the following variables are extracted:

- Elevation difference (dh)

- Slope (α) > 5° of the master DEM

- Aspect (Ψ) of the master DEM

The extracted values are insert into Microsoft Excel, where the Solver Add-In is used to fit the curve and find an analytic solution. The co-registration has been performed with the help of a tutorial from Ph. Rastner (Rastner, 2015).

4.2.2 Estimation of the uncertainties

The uncertainties can be divided in systematic uncertainties and stochastic and random uncertainties. Systematic uncertainties describe offsets or biases within measurements, whereas stochastic or random uncertainties are caused unpredictable changes best described as noise.

Systematic uncertainties

To assess the systematic uncertainty between two elevation data sets the mean elevation bias over stable terrain can be considered (Rastner et al., 2016). The mean elevation bias over stable terrain (*MED*) is calculated as followed, where x_i is the difference between the individual pixel and the corresponding pixel in the reference DEM.

$$MED = \bar{x} = \frac{1}{n} \cdot \sum_{i=1}^{n} x_i \tag{4.6}$$

Stochastic uncertainties

The variability in elevation over stable terrain can be used to estimate the stochastic uncertainty between two elevation data sets. To measure the variability, a few statistical measures exist such as the standard deviation or the standard error (Rastner et al., 2016). Both mentioned measures are used (Equations 4.7 & 4.8).

$$STDV = \sqrt{\sum_{i=1}^{n} (x_i - \bar{x})} \tag{4.7}$$

$$SE = \pm \frac{STDV}{\sqrt{n}} \tag{4.8}$$

n in Equation 4.8 refers to the number of independent raster cells. In spatial data this assumption is not given due to autocorrelation (Koblet et al., 2010; Rastner et al., 2016; Zemp et al., 2013). To achieve for the autocorrelation a threshold distance for the autocorrelation has to be defined and the DEM needs to be resampled with the according grid size. Koblet et al. (2010) used a distance of 100m, where the autocorrelation gets insignificant. As Bossard (2014) a less conservative threshold distance of 10m is used in this thesis as a small scale study area is investigated and high resolution DEMs are used.

4.3 Spatially discrete Analyses

The quantitative analyses can be divided into spatially discrete and distributed methods. The profile lines and the point tracking contribute to the spatially discrete analysis.

4.3.1 Profile Lines

The profile lines are vertical to the lateral moraine and are used to get an idea of the reworking processes and mass movements along the lateral moraine. The profile lines are created in ArcGIS manually by drawing lines. Afterwards the tool Stack Profile is used to extract the elevation values along the profile lines for all the available DEMs. The result is a large table for each profile with all the elevation data in it. For the analysis and visualization the data tables are transferred to MATLAB. Five profiles (C-G) capture the landslide, two profiles are down-glacier from the landslide area (A,B) and one is up-glacier from it (H).

4.3.2 Point Tracking

The simplest way of measuring horizontal displacements in such a small area with high availability of high resolution DEM (shaded reliefs) and orthophotos is to track down prominent (large) boulders. It is further good to get an idea about the magnitude of the movements for the setting the parameters in the image correlation.

In ArcGIS the different shaded reliefs and orthophotos are viewed and compared with the help of the Swipe tool. The position of prominent boulders are marked in each shaded relief/orthophoto, which results in a point dataset, where each point represents the position at certain time. Coordinates are added to the points with the add x-,y- coordinates tool. The data tables are than exported for the further analysis with MATLAB. With the coordinates the shift in x and y direction as well as the resulting shift vector and its direction are calculated. For the visualization the data sets are imported back to ArcGIS.

4.4   Spatially distributed Analyses

Among the spatially discrete methods also spatially distributed analyses are conducted with the DEM differences and the image correlation (CIAS).

4.4.1   Digital elevation model differencing and Volume change

The DEM differences are calculated with the Raster Calculator tool in ArcGIS. In advance all the DEM are clipped to the extent close to the Area of Interest with the extract by mask tool. From the elevation difference the Volume change can be calculated by considering the raster cell size.

4.4.2   Image Correlation (CIAS)

Automatic matching of images from different times is a common method to derive glacier surface velocities, rock glacier surface velocities or landslide velocity fields (Heid and Kääb, 2012; Kääb, 2002; Kääb and Vollmer, 2000). In this thesis the Open Source Correlation Image Analysis Software (CIAS) firstly developed by Kääb and Vollmer (2000) and further improved by Kääb (2002). The Software can be downloaded from the Homepage of A.Kääb (University of Oslo) and it is written in IDL (University of Oslo, 2017).

Background

The schematic workflow of the image matching is shown in Figure 4.7. In the image1 a section, called 'reference block', with enough contrast is chosen. His counterpart, called 'test block', is than searched in a sub-area (called 'test area' or 'search area') of the image2. For identifying the corresponding image blocks the normalized cross-correlation (NCC) as given by equation 4.9 is used.

$$CC(i,j) = \frac{\sum_{k,l}(s(i+k,j+l) - \mu_s) \cdot (r(k,l) - \mu_r)}{\sqrt{\sum_{k,l}(s(i+k,j+l) - \mu_s)^2 \cdot \sum_{k,l}(r(k,l) - \mu_r)^2}} \tag{4.9}$$

where (i,j) represents the position in the search area, (i,j) the position in the reference area, r is the pixel value of the reference chip, s the pixel value of the search chip, μ_r the average pixel value of the reference chip and μ_s the average pixel value of the search chip. The horizontal displacement between image 1 and 2 is given by the difference between the central pixel of the reference block and the successfully determined test block (Heid and Kääb, 2012; Kääb and Vollmer, 2000). The cross-correlation is normalized because different illumination conditions can be better compared and the correlation coefficients from different attempts can be compared (Heid and Kääb, 2012).
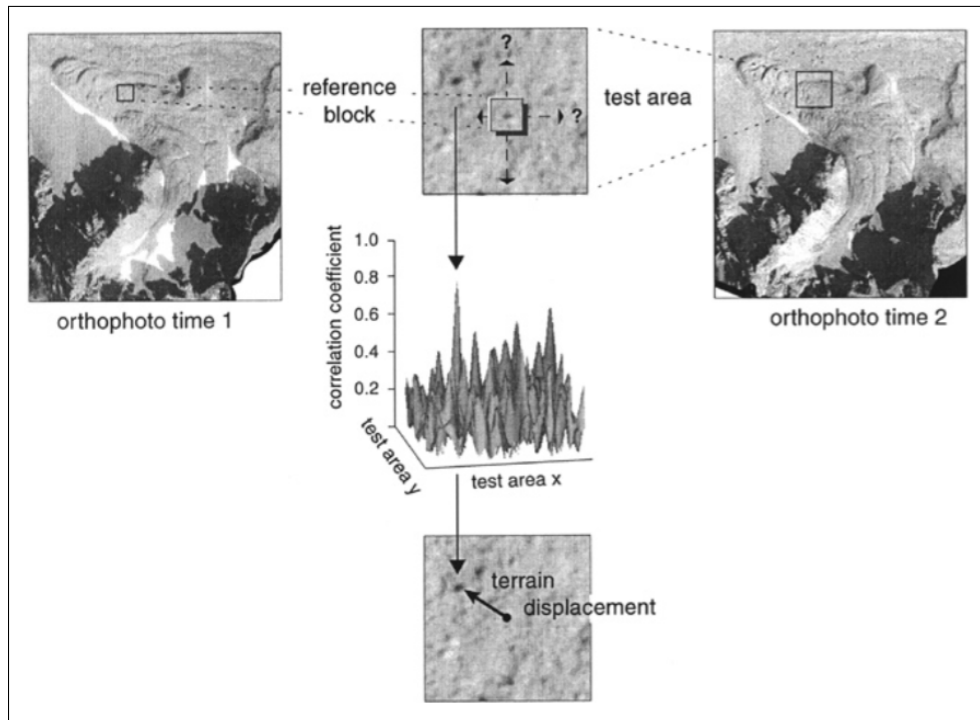
Figure 4.7: Scheme of measuring surface displacements from repeated digital orthoimages (or shaded reliefs) by block-correlation techniques. A reference-block in the image at time 1 is searched for in a test area in the image at time 2. Applying the image georeference, the horizontal shift between the reference-block location and the corresponding test block directly gives the horizontal surface displacement (Kääb, 2002; Kääb and Vollmer, 2000)

Application of CIAS

To run the Software CIAS ENVI IDL was used. CIAS is user-friendly and requires as input two co-registered images in geotiff or tiff-world format. The images have to be single channel (gray-scale) and need the same resolution. With a polygon function the area of interest can be chosen in the images. Further, the reference block size, the search area size and the grid distance, with which the drawn polygon should be analyzed, have to specified. To determine this parameters it is important to have an idea about the magnitude of the expected movements. The reference block needs to be big enough to have a unique and identifiable contrast-signature and the search area has to be big enough to cover the expected movement magnitudes.

After some attempts the reference block size was set to 20x20 pixel, so 20x20m as the pixel-size is 1m. The grid size (according to which the study area is investigated) is set to 10m, so that the reference blocks are overlapping. According to the point tracking data the expected magnitude of the movement is around 25m/a-30m/a. Kääb and Vollmer (2000) suggest a search area size of twice the expected movement according to which a search area size of 60x60 pixels was chosen. This is valid for the one-year timescales. The search area has to be extended for the two-years, three-years and four-years observation periods as the image correlation determine the total movement (not the annual movement). For the two-year period a search area size of 100x100 pixel was chosen, for the three-year period one of 150x150 pixel and for the four-year period one of 200x200 pixel.

The result of the image correlation (CIAS) is a point-data set with an ID and the X-/Y-Coordinates of

the pixel and values for the Δx, the Δy, the total length, the direction, the maximum correlation-coefficient and the average correlation-coefficient. To assess the quality of the received correlation results the Signal-to-Noise Ratio (SNR) is calculated, which is the maximum correlation-coefficient divided by the average correlation-coefficient.

Post-Processing

As mentioned-above the SNR is calculated to assess the quality of the determined correlation. Therefore, the SNR values are classified into three classes: insufficient, sufficient and good. The thresholds for the classes are determined according to the mean SNR plus/minus one standard deviation. For the three one-year observation period the thresholds are averaged. The cells classified as insufficient are excluded in the analysis of the magnitude and the direction of the movement. CIAS determined the total Magnitude of the Movement between the two observation years. As a consequence the annual magnitude has to be calculated to comparing the different time periods. To visualize the result arrows are used to indicate the orientation of the movement and different colors to refer to the magnitude of the movement.

5. Results

5.1 Field Measurements

5.1.1 Ablation Measurements

The ablation stakes have been installed on the 13th July followed by measurements of the melt on the 23rd August and on the 21st September 2017. As mentioned before the stakes 1-5 have been installed within the field campaign of this thesis, whereas stake 6 is part of the glacier monitoring program at the Findelengletscher. In Table 5.1 the debris thickness (Column 1) at the stake sites, the measured stake heights for the three measurement times (Column 2-4) and the calculated melt between the different measurement times (Column 5-7) are visible. One can see that over all time periods the melt on the bare ice (Stakes 5 & 6) is the highest and the smallest at Stake 3 with the thickest debris cover. Over the whole measurement period a melt of -4.05m at Stake 5 is measured and only a melt of -0.9m at Stake 3. Comparing Stake 1 and 2 with the same debris thickness, it is remarkable that the melt over the whole measurement period is quite different (difference of approximately 0.5m). One explanation could be that Stake 2 have been heavy tilted during the measurement period by down-rolling stones. The melt at Stake 4 with 25cm debris thickness is in the same magnitude as the melt at Stake 1 and 2 with only 15cm debris thickness.

	Debris Thickness [m]	h_{t_0} [m]	h_{t_1} [m]	h_{t_2} [m]	Melt Δt_{01} [m]	Melt Δt_{12} [m]	Melt Δt_{02} [m]
Stake 1	0.15	4.05	2.65	1.67	-1.40	-0.98	-2.38
Stake 2	0.15	3.95	2.62	2.08	-1.33	-0.54	-1.87
Stake 3	0.30	1.90	1.30	1.00	-0.60	-0.30	-0.90
Stake 4	0.25	1.94	0.79	0.03	-1.15	-0.76	-1.91
Stake 5	0	4.05	1.21	0	-2.84	-1.21	-4.05
Stake 6	0	-	3.02	2.00	-	-1.02	-

Table 5.1: Measured stake heights ($t_0 = 13^{th}$ July, $t_1 = 23^{th}$ Aug and $t_2 = 21^{st}$ Sep) and the calculated melt ($\Delta t_{01} \widehat{=} t_0 - t_1$, $\Delta t_{12} \widehat{=} t_1 - t_2$ and $\Delta t_{02} \widehat{=} t_0 - t_2$). Stakes 1-5 were installed within this thesis, Stake 6 belongs to the measurement network of the Findelengletscher

In Table 5.2 the calculated melts are shown as percentages from the melt on bare ice (Stake 5). At Stake 2 and 3 one can see that the percentage stays more or less the same, which means the melt reduction through the debris cover is the same over the whole observation period. For Stake 2 an overall average of 45.88% can be calculated and one of 22.71% at Stake 3. In contrast, at Stake 1 and 4 quite different

percentage values are visible. They vary from 49.30% to 80.99% at Stake 1 and from 40.49% to 62.81% at Stake 4. For the whole observation period (13th July - 21st September) one can see that a 30cm debris cover reduces the melt to 22% towards the melt on bare ice. A debris cover of 15cm and 25cm lead to more or less half of the melt towards the melt on bare ice.

	Debris Thickness [m]	Melt Δt_{01} [%]	Melt Δt_{12} [%]	Melt Δt_{02} [%]
Stake 1	0.15	49.30	80.99	58.77
Stake 2	0.15	46.83	44.63	46.17
Stake 3	0.3	21.13	24.79	22.22
Stake 4	0.25	40.49	62.81	47.16
Stake 5	0	100	100	100

Table 5.2: Melt beneath the debris cover expressed in percentages of the melt on bare ice within the same time periods ($\Delta t_{01} \mathrel{\widehat{=}} t_0 - t_1$, $\Delta t_{12} \mathrel{\widehat{=}} t_1 - t_2$ and $\Delta t_{02} \mathrel{\widehat{=}} t_0 - t_2$)

Figure 5.1 shows the relation between the observed melt and the debris thickness at the stake sites. The different colors indicate the different time periods: *black* represents the melt between the 13th July and the 23rd August, *red* the melt between the 23rd August and the 21st September and *blue* the melt over the whole time period (13th July - 21st September). It can be said that the difference in melt between bare ice and debris covered ice gets bigger with increasing period of time.
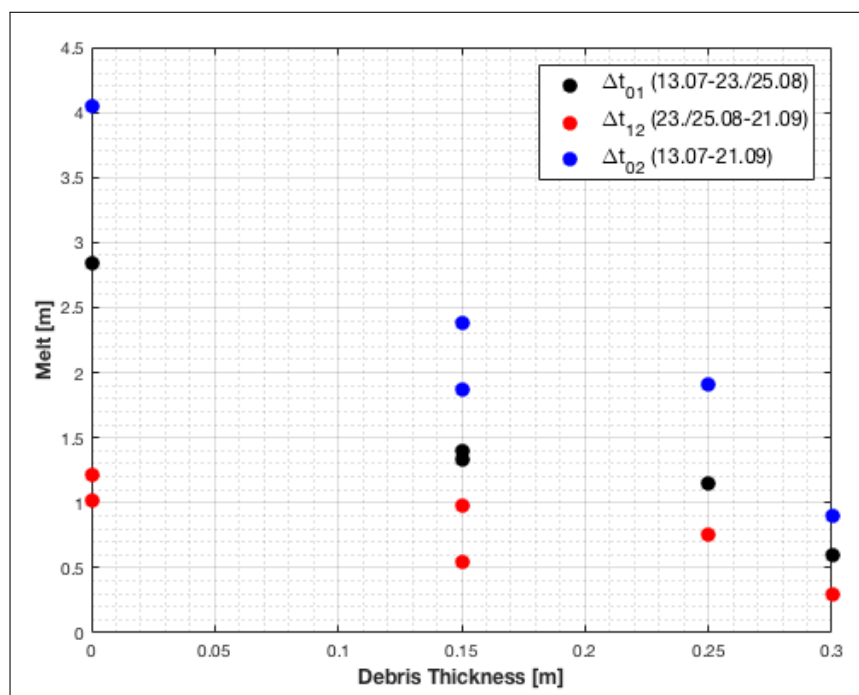
Figure 5.1: Relation between the observed melt and the debris thickness at the different stake sites. The different colors represent different observation time periods

5.1.2 Stakes Displacements

The positions of the ablation stakes have been measured with the dGPS on the 13th July and 21st September. On the base of this measurements the horizontal and vertical displacement can be determined (Table 5.3). One can see that the largest horizontal shift occurs at Stake 2 with a displacement of 2.26m. The displacement for the other three stakes are a bit smaller with 1.97m respectively 1.92m. Further, it is visible that the displacement in x-direction (Easting) is bigger for all four stakes than the one in the y-direction (Northing). Stakes 2, 3 and 4 are shifted southwest, whereas Stake 1 is moving West. In the horizontal displacement is no trend with the location of the stakes or the debris thickness detectable. Looking at the vertical component (Δz) of the movement one can see that the biggest vertical lowering occurs at Stake 1 with -2.70m and the smallest lowering at Stake 3 with -1.58m. Within the vertical displacement a trend with the debris thickness is recognizable, the vertical displacement with thicker debris cover is smaller.

	$\Delta x[m]$	$\Delta y[m]$	Horizontal Shift [m]	Direction Shift	$\Delta z[m]$
Stake 1	-1.81	-0.62	1.92	W (251.10°)	-2.70
Stake 2	-1.78	-1.39	2.26	SW (231.91°)	-2.20
Stake 3	-1.81	-0.78	1.97	SW (246.73°)	-1.58
Stake 4	-1.60	-1.15	1.97	SW (234.11°)	-1.83

Table 5.3: Measured displacement at the ablation stakes from the 13th July to the 21st September 2017

5.1.3 Meteorological Data

A small Meteo-Station have been installed on the 13rd July with a temperature sensor and radiation measuring device. The variables are measured hourly. The station has been operational until 12:00 on the 21st September. In the first six days of the measurement period the devices are not working correctly, so that data are only available from the 19th July to the 21st September.

The measured air temperature regime is shown in Figure 5.2. The solid, red line shows the daily mean air temperature during the field campaign. To get an idea of the daily fluctuations the daily minimum and the daily maximum air temperature are also showed with the shaded area in between. Over the whole time period the mean air temperature was 7.1°C. Some warm phases (for example 01st-05thAugust or 25th-30thAugust) and some cold phases (for example 09th-12thAugust or 01st-04thSeptember) can be identified. The maximum air temperature with 18.5°C is reached on the 4th August and the minimum air temperature with -5.4°C on the 18th September.
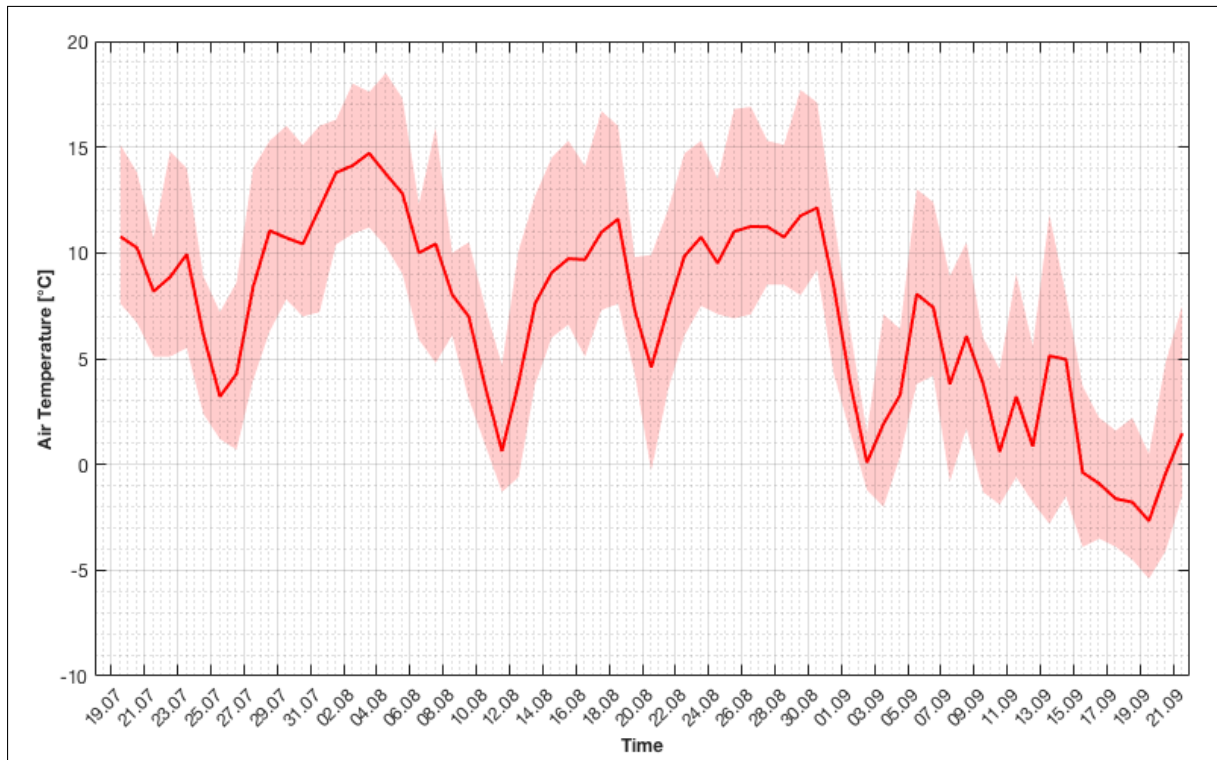
Figure 5.2: The daily mean air temperature (solid, bold line) during the field campaign. The area between the daily minimum and the daily maximum air temperature is shaded

The daily mean incoming solar radiation at the Meteo-Station is shown in Figure 5.3. The highest daily mean solar radiation is measured on the 17th August with 335W/m^2. On 15 days the daily mean solar radiation was 300W/m^2 or more. The daily mean solar radiation is smaller than 50W/m^2 on the 11th and on the 31st August. A long period with daily mean solar radiation values over 250W/m^2 is recognizable from the 12th to the 22nd August. Regarding the daily maximum solar radiation the highest value with 1055 W/m^2 is measured on the 14th August and 3rd September (Figure A.5, Appendix). The smallest daily maximum solar radiation is measured on the 11th and on the 31st August, where also the daily mean solar radiation is low.
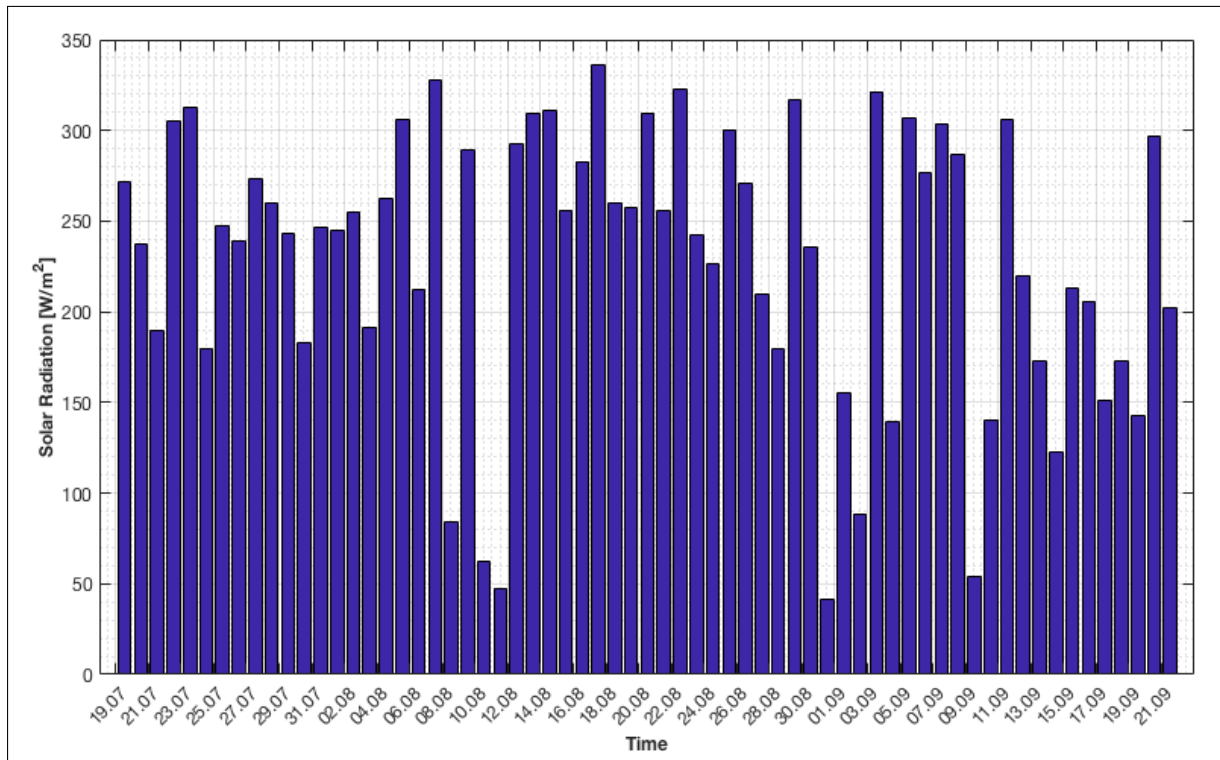
Figure 5.3: Daily mean solar radiation during the Field Campaign

5.2   Pre-Processing and Uncertainties

5.2.1   Acquisition and Processing of the data 2017

The drone flight was realized on the 21st September in the late afternoon. During the two flights 284 aerial photos were taken to cover the area. To georeference the DEM two GCPs have been measured with the dGPS in advance and are marked to be visual in the photos. Two more GCPs are selected after the flight and their coordinates are extracted from SWISSIMAGE. Further, the position of the ablation stakes (Stakes 1, 3 and 4) are used as they are also marked in the terrain. The resulting orthophoto is shown in Figure A.4 (Appendix).

5.2.2   Resampling and Co-Registration

In Table 3.1 one can see that the Airborne Laser Scanning data from the GLAXPO project and the DEMs from the GLAMOS project already have the same cell size of 1 meter. The other data sets have to be resampled to a cell size of 1 meter.

For the Co-Registration the DEM from 2015 (GLAXPO) is chosen as the master DEM. The elevation difference for each observation period towards 2015 is calculated and the stable terrain is extracted from it. Further, the slope and aspect of the DEM 2015 are used to perform the Co-Registration. Table 5.4 shows the obtained parameters from the applied co-registration method. The result of the curve fit based on the observed dependency of the normalized elevation differences and the aspect is visible in Figure 5.4. The red line indicates the theoretical sinusoidal curve.

Iteration 0				
DEMs	RMSE [m]	Δx [m]	Δy [m]	$\overline{dh}$ [m]
2005 - 2015	1.49	0.46	-0.49	-0.45
2009 - 2015	1.12	0.001	0.06	-0.17
2010 - 2015	1.11	-0.0001	-0.007	-0.18
2013 - 2015	0.56	-0.002	-0.13	0.06
2014 - 2015	0.63	0.07	-0.36	0.25
2015 - 2017	1.52	-0.66	0.33	0.46
Iteration 4				
2015 - 2017	1.29	-0.42	0.28	0.03

Table 5.4: Results of the Co-registration after iteration 0: (RMSE) is the root-mean-square error, (Δx) is the shift in x-direction (East-West), (Δy) is the shift in y-direction (North-South) and $\overline{dh}$ is the overall elevation bias of the DEMs

Regarding at the column 3-5 in Table 5.4 one can see that the shift vectors and the overall elevation bias are smaller or equal to ± 0.5m, except for the period 2015-2017. As one criteria for stopping the iterations is a shift vector less than 0.5m, further iterations are necessary for this period. After four iterations the shift vectors for the period 2015-2017 get smaller than ± 0.5m as in Table 5.4 visible.
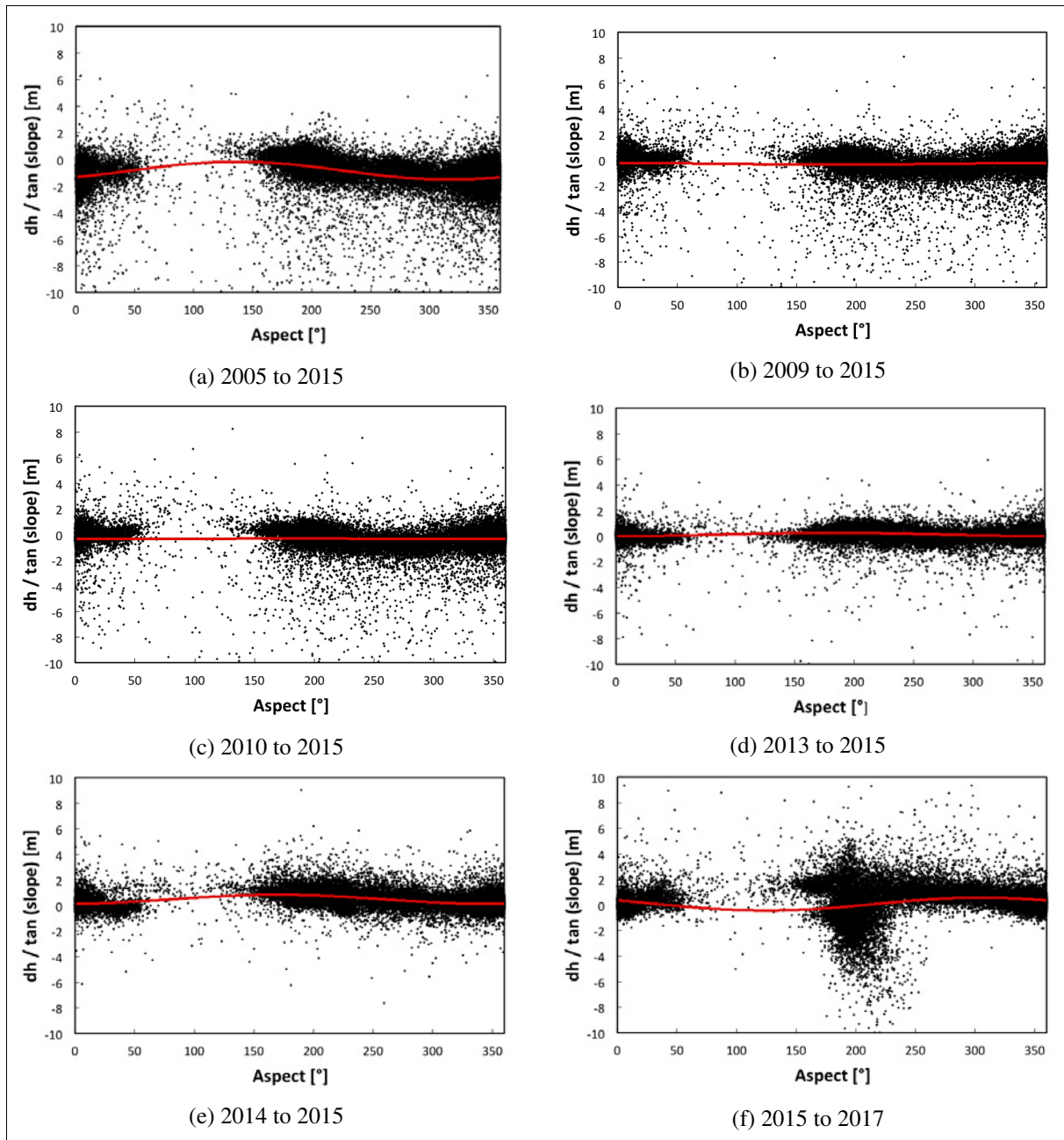
Figure 5.4: Scatterplot of the elevation differences for each time period normalized by the tangent of the slope (y-axis) and terrain aspect (x-axis); The red line shows the theoretical sinusoidal curve fit (Nuth and Kääb, 2011); For the period 2015-2017 the scatterplot after iteration 4 is shown

5.2.3 Estimation of uncertainties in the DEMs

Systematic uncertainties

The systematic uncertainties are described by the mean elevation bias over stable terrain (MED) and by the shift vectors remaining after the co-registration (Table 5.5; Column 2-5). For the MED and as well for the residual shift vectors one can see that they are the largest for the period 2005-2015 with values between 0.45 and 0.49m. In all the other periods the values for the parameters are smaller than 0.4m. The horizontal and vertical systematic uncertainties are clearly in the subpixel range, which enables detailed multi-temporal DEM analysis.

Stochastic uncertainties

The stochastic uncertainties are described by the standard deviation (STDV) and standard error (SE). To account for autocorrelation a 10m raster cell distance is considered in the calculation of the standard error (SE), which leads to 330 independent raster cells. Table 5.5 shows the STDV in column 6 and the SE in column 7. The stochastic uncertainty is the lowest for the period 2013-2015 (0.23m STDV, 0.01 SE) and the highest for the period 2015-2017 (0.59m STDV, 0.03m SE).

DEMs	Systematic Uncertainties				Stochastic Uncertainties	
	MED [m]	Δx [m]	Δy [m]	$\overline{dh}$ [m]	STDV [m]	SE [m] (n = 330)
2005 - 2015	-0.45	0.46	-0.49	-0.45	0.52	0.03
2009 - 2015	-0.12	0.001	0.06	-0.17	0.38	0.02
2010 - 2015	-0.13	-0.0001	-0.007	-0.18	0.39	0.02
2013 - 2015	0.06	-0.002	-0.13	0.06	0.23	0.01
2014 - 2015	0.20	0.07	-0.36	0.25	0.31	0.02
2015 - 2017*	0.06	-0.42	0.28	0.03	0.59	0.03

Table 5.5: Systematic and stochastic uncertainties for the DEM differences. (*Value after iteration 4)

5.2.4 Quality and Uncertainties of the Image Correlation

The SNR-values are classified into the three classes insufficient, sufficient and good. Figures A.41-A.46 (Appendix) show the distribution of those classes for each observation period. For the observation period 2009-2010 the quality of the image correlation is the best as the amount of good classified SNR is the highest. Further, one can see that for all observation periods the insufficient classified SNR are distributed over the whole area. Areas with insufficient SNR classification are characterized through a smooth surface with low contrast as in the glacier forfield, on the glacier or on the vegetated hillslopes. Areas classified with insufficient SNR-values are excluded from the further analyses of the image correlation.

5.3 Qualitative Analysis

For the qualitative comparison shaded reliefs (also called hillshades) are created for each DEM by using the ArcGIS Hillshade tool. Figures A.6-A.12 in the Appendix A show the shaded reliefs for the study site and the different years. Beside the glacier shrinking one can see the formation and evolution of the landslide from 2005 until 2017. For each year the above-mentioned zones (see Section 3.1.1) are defined (Figures A.13-A.19). The evolution of those zones as well as other recognizable features are addressed in the following.

5.3.1 Evolution of the Glacier

Figure 5.5 shows the glacier outlines of the Findelengletscher. In general, one can see that the glacier gets smaller in length and in width over the observation periods. The glacier tongue has retreated around 500m between 2005 and 2017 and a lost in width around 200m (100m on both sides) during the same period is observable. Further, it is visible that in 2005 the glacier oultines on both sides of the glacier is almost a straight line, whereas after the formation of the landslide (on the right side of the glacier) two bulges start to emerge: one right beneath the landslide-breakthrough and one bit more up-glacier. The bulges are growing towards the glacier middle with time through the retreat of the glacier on the one hand and through the push of the landslide on the other hand.

Figure 5.5: Glacier Outlines for the different observation years (Background: Shaded relief of 2017)

5.3.2 Evolution of the Slide-Area

In Figure 5.6 one can see the outlines of the Slide-Area for each time. The extent of the release area (on the hillslope behind the moraine) is determined in 2005 and set for the other periods. Only the front and with of the Slide-Area is adapted for each observation period. The downward moving of the landslide body is detectable, which is around 50-60m from 2009 to 2017. As mentioned before (see Section 3.1.3) the landslide can be divided into two parts, visible through the different color (brown versus grey) and texture of the debris. Figure 5.7 shows the front of the brown debris material on the left side and the front of the whole landslide, which equals the extent of the Slide-Area, on the right side. Looking at the front of the brown debris, it is visible that the movement between 2009 and 2010 is bigger than the movements in the other one-year-cycles (2013-2014 and 2014-2015). This decrease in the movement could indicate a settlement of the landslide. The downward moving of the whole landslide body is almost constant over the observation periods. Comparing the movement of the brown debris and the whole landslide body, one can see that the distance between 2009, 2010 and 2013 are bigger for the brown material than for the whole landslide body. This suggest that the brown material moves faster than they grey one in front of it.
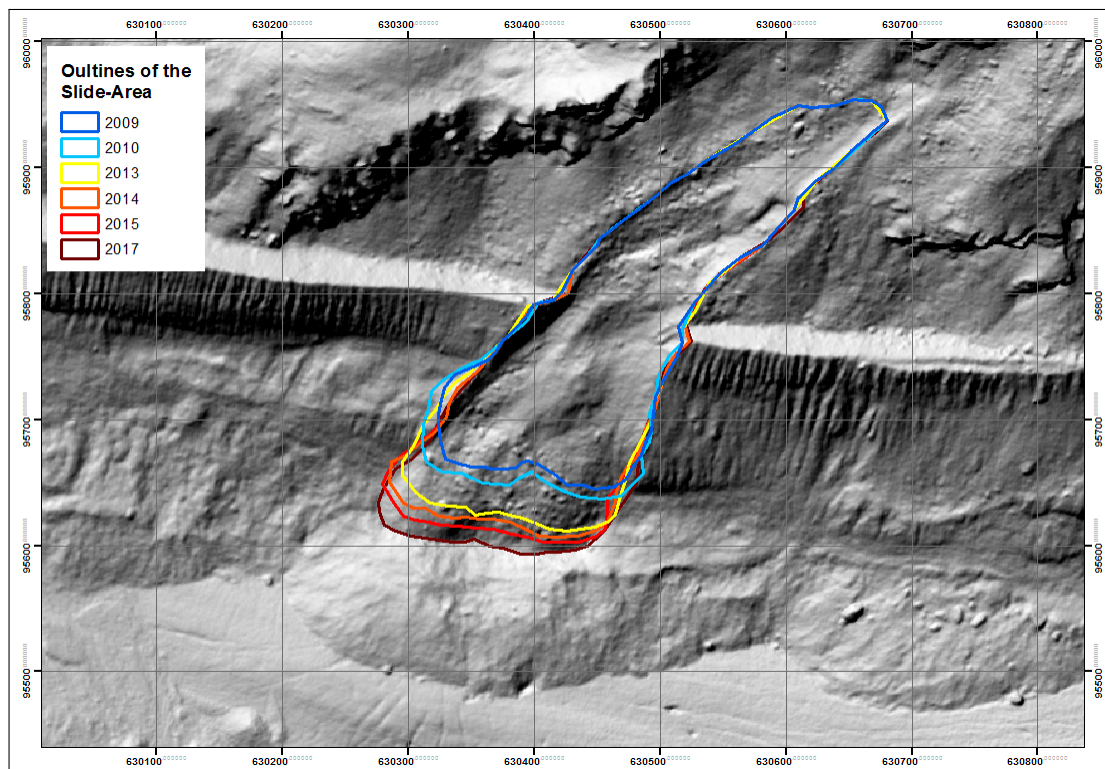
Figure 5.6: Outlines of the Slide-Area for the different observation years (Background: Shaded relief of 2017)
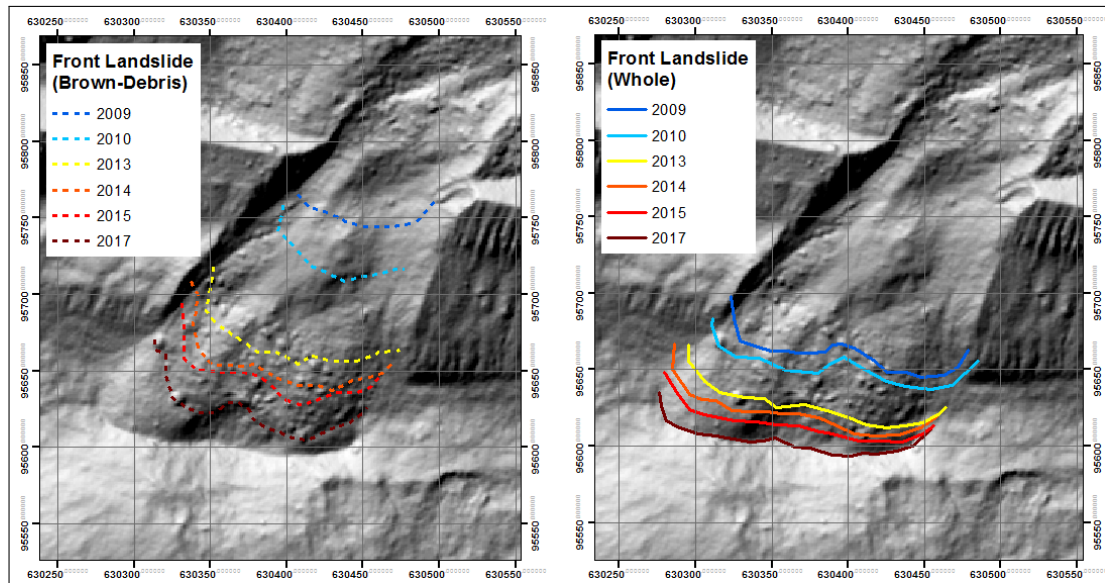
Figure 5.7: Frontline of the Brown-Debris (left) and the whole landslide body (right)

5.3.3 Evolution of the Moraine-Foot Zone

Figure 5.8 shows the Moraine-Foot zone for the different observation years. It is defined as the zone between the glacier (debris-free ice) and the steep, gullied moraine top. Therefore, the bottom (glacier-side) extent-line is evolving over time according to the retreat of the glacier, which is described above with the glacier outlines. The upper (moraine top side) extent-line is changing generally in two phases. One downward moving is visible from 2005 to 2009/2010 and a second one from 2009/2010 towards 2013-2017.
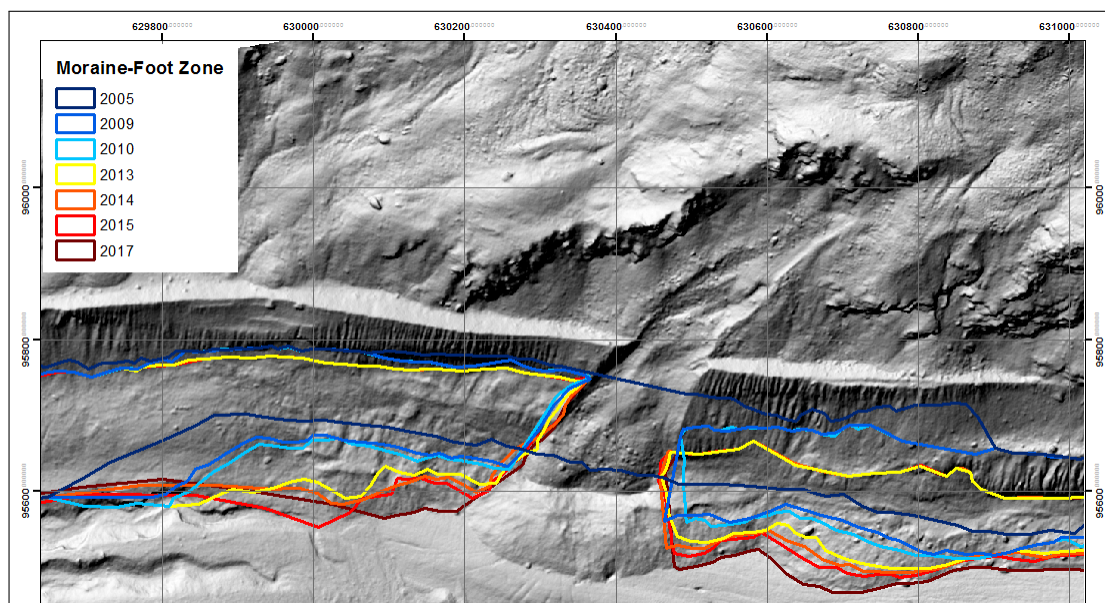
Figure 5.8: Outlines of the Moraine-Foot Zone for the different observation years (Background: Shaded relief of 2017)

Evolution of the Moving Line

The 'Moving Line' for each observation year is visible in Figure 5.9. This line is assumed to be the border between the glacier movement and the gravitative movements on the moraine flank or it can mark the extent of the buried ice beneath the debris. In the part up-glacier from the landslide the line is clearly visible, whereas it is more difficult in the part down-glacier from the landslide. Qualitatively, one can see that the changes between the different observation years are small. Only a small shift towards the glacier is visible.
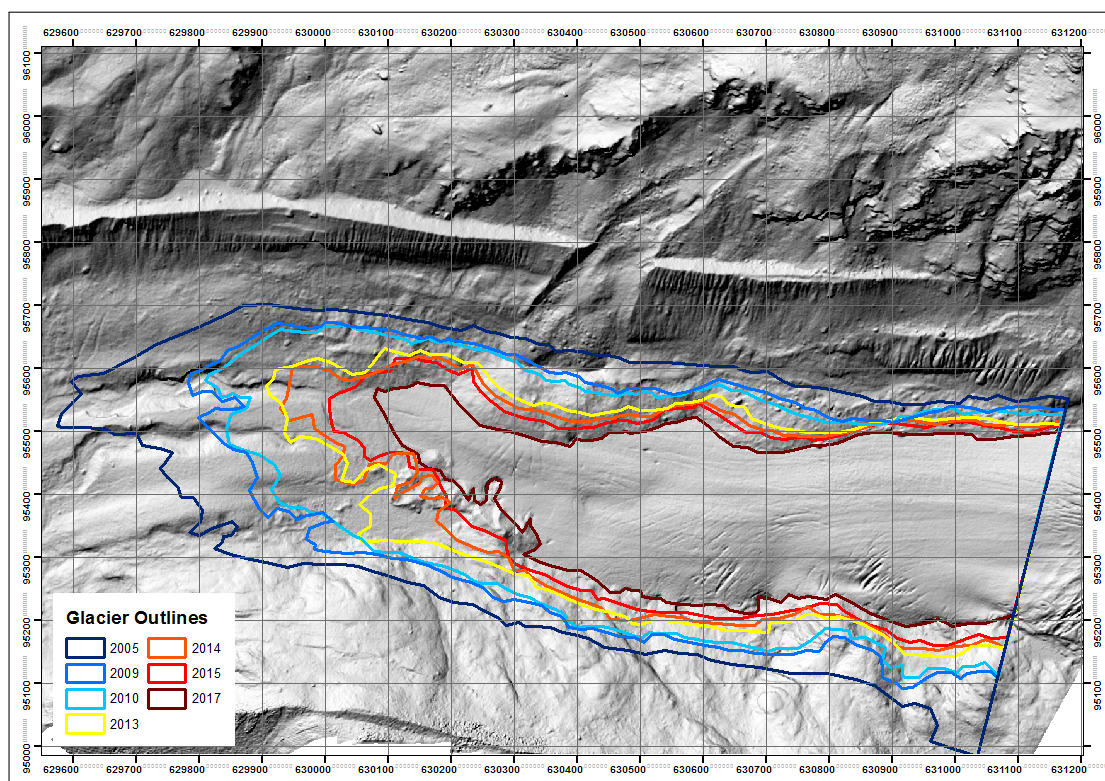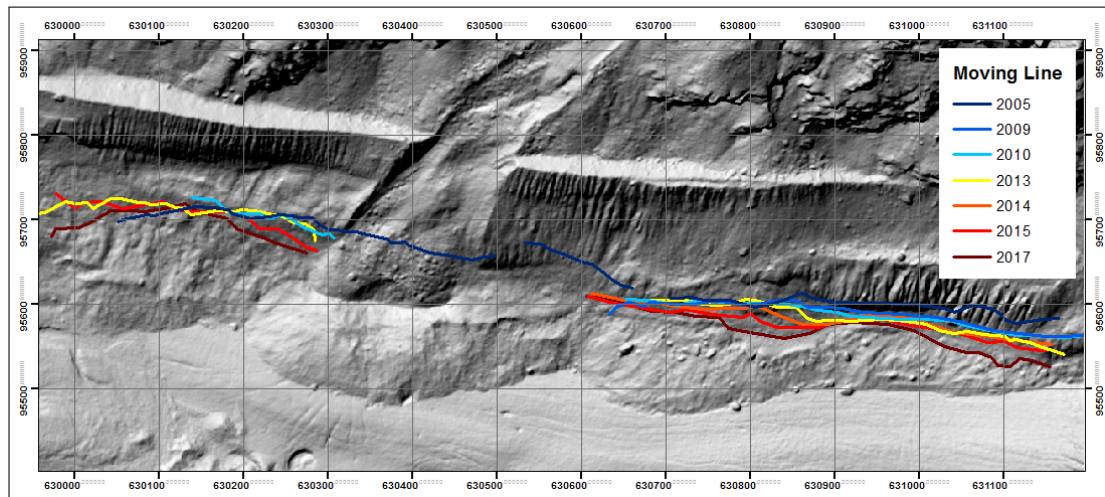

Figure 5.9: Moving Line for the different observation years (Background: Shaded relief of 2017)

5.3.4   Evolution of the Mound

Figure 5.10 shows the Mound for the different observation years (2013-2017). One can see a shifting of the whole feature towards the glacier middle, but also a increasing of the extent is detectable. The width is more or less stable for the all the observation years, it only slightly increases with time towards the glacier front (left).

Figure 5.10: Outlines of the Mound for the different observation years (Background: Shaded relief of 2017)

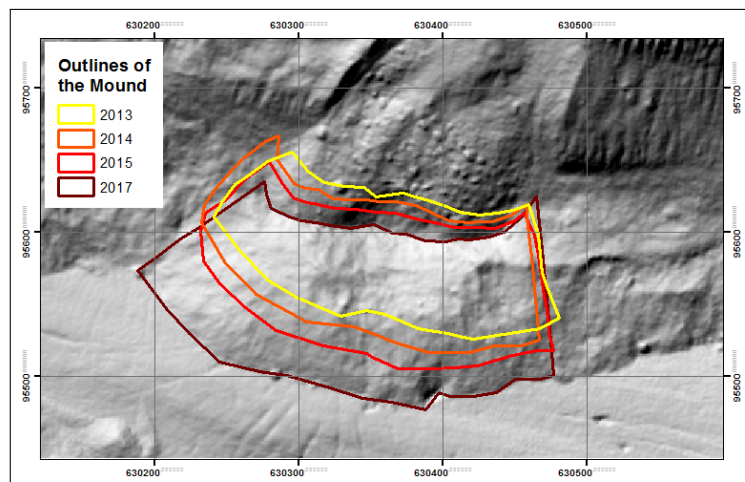## 5.4 Spatially discrete Analyses

The quantitative analyses can be divided into spatially discrete and distributed methods. The profile lines and the point tracking contribute to the spatially discrete analysis. Their results are shown in the following paragraphs, whereas the results of the distributed methods are covered in the next section 5.5.

5.4.1 Profile Lines

Eight Profiles through the right lateral moraine are set to investigate the evolution of the moraine at different locations. The Profiles A and B lie down-glacier from the landslide and Profile H up-glacier from it. The Profiles C to G cut partially or fully through the Slide-Area (Figure 3.2). The Profiles always start behind the moraine (glacier-averted side), go through the moraine to the middle of the glacier respectively the valley floor. The whole Profiles are shown in the Appendix Figures A.20-A.27), in the main text only selected Profiles and parts are visualized.

Profiles down-glacier from the landslide area (A & B)

Figure 5.11 shows the Moraine-Foot zone and part of the glacier respectively the valley floor along Profile A , which is lying down-glacier from the landslide. The kink such at 280m Profile Length in 2005 or at 400m Profile Length in 2015 mark the border between the Moraine-Foot zone and the Glacier. In 2017 such a kink is not visible as the glacier retreated behind the location of Profile A. Looking a bit closer at the Moraine-Foot zone (180m-350m) one can see that a surface lowering until 2013 occurs, whereas the elevation stays stable afterwards. Further, the surface lowering gets bigger towards the glacier. This can be a sign that there was dead-ice beneath the debris until 2013. In this part a surface lowering of ca. -1.5m/a for the periods 2005-2009 and 2009-2010 and a surface lowering of ca. -2.4m/a for the period 2010-2013 can be extracted from the elevation data (250m Profile Length). To compare on the glacier surface lowering from -5.5m/a to -7.4m/a occurred. The pattern of surface lowering that gets bigger towards the glacier can be seen also from 350m to 400m Profile Length and the years 2014 until 2017. Here, lowering rates of -1m/a to 2m/a can be observed, which implies that there is still ice beneath the debris.

In Profile B (Figure A.21, Appendix), which lies also down-glacier from the landslide, the surface lowering in the Moraine-Foot zone is smaller (-0.5m/a to -1.7m/a) than in Profile A, but also the surface lowering on the glacier is a bit smaller than in Profile A. An exception is the period 2015-2017 with an elevation loss of around -7.8m/a, which is higher. Further, one can see that in the Moraine-Foot zone the surface is lowering until 2017, which suggest that there is dead-ice present over the whole observation periods. Over the whole observation periods a surface lowering from 15-20m in the Moraine-Foot zone and from 60-70m on the glacier have occurred down-glacier from the landslide.
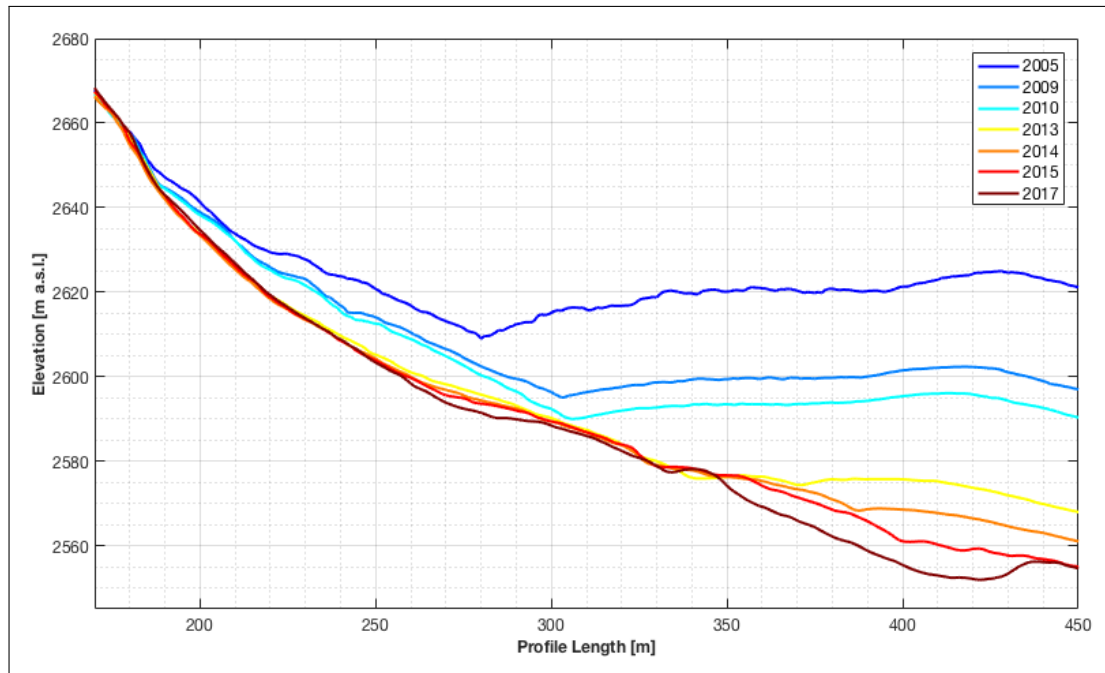
Figure 5.11: Elevation along Profile A for each observation year zoomed to the moraine-foot zone and the glacier

Profiles within the landslide area (C, D, E & F)

Profiles C, D, E and F go through the Slide-Area, in Figure 5.12 the lower part of the Slide-Area and the Mound are nicely recognizable, whereas in Figure 5.16 the upper part of the Slide-Area is shown. To achieve a better readability the elevation profile along Profile D (Figure 5.12) is once visible with all observation times (5.12a) and divided in 2005 to 2010 (5.12b) and in 2013 to 2017 (5.12c). Looking at the elevation profiles one can see the down-sliding of the landslide body as a bulge in the profiles. The kink, which marks the border between the Moraine-Foot zone and the Glacier, is visible in the first three profiles as the landslide have not reached it. The landslide body disturb the "normal" continuous surface lowering as seen in the previous profiles along the moraine flank. In the profiles 2013 to 2017 the landslide body almost stagnates in the front and the back slides further down. Since the profile of 2013 the Mound is established between the landslide body and the glacier. The Mound is limited by a channel towards the landslide body and by a kink, which marks the transition to the glacier. One can see that the Mound is shifted towards the glacier with time. The elevation difference between the Mound (top) and the glacier (highest point in the middle) ranges from 12-19m in 2013 towards 15-23m in 2017 depending on the profile location. This suggest that the surface lowering on the glacier is higher than on the mound.

(a) Elevation along Profile D (all observation times)

(b) 2005, 2009 and 2010

(c) 2013, 2014, 2015 and 2017
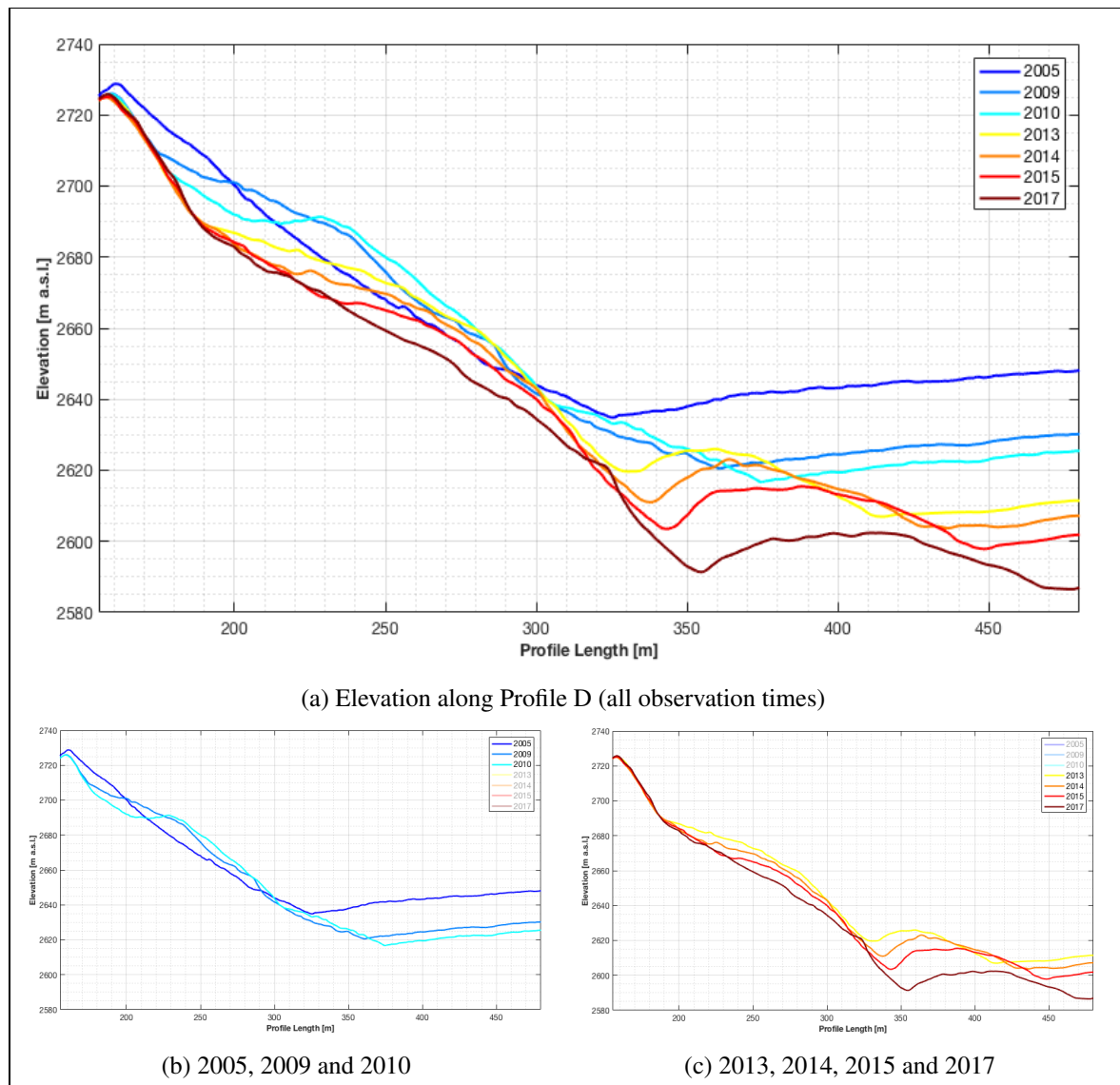
Figure 5.12: Elevation along Profile D for each observation year zoomed to the slide-area and the glacier

In the profiles the shifting of the mound towards the glacier is nicely visible and the magnitude of the shift along the profiles can be determined. To investigate the surface change on the Mound this shift has to be taken into account. Figures 5.13-5.15 show the elevation along the profiles starting at the channel. In Table 5.6 the corresponding shifts along the Profiles for each observation period is visible, which shows annual shifts ranging from 5 to 13m. Looking at the surface evolution of the Mound (Figures 5.13-5.15) one can see that a general lowering of the surface occurs from 2013 to 2017. Further, the Mound is getting extented towards the glacier due to the glacier shrinking and the pushing of the landslide. Along Profile C and D a collapse of the mound-top is recognizable as the top visible in 2013 and 2014 (also 2015 in Profile C) is removed in 2017 (and 2015). This evolution is not visible along Profile E as the general shape of the mound consistent over the observed time. Along Profile C the mean annual melting rates on the mound-top (20-50m) ranges from -2.34m/a (2013-2014) to -4.18m/a (2015-2017). Whereas along Profile E the mean annual melting rates are a bit higher for each observation period. The mean annual

melting rates on the mound-top (20-50m) along Profile D are -3.40m/a (2013-2014) and -6.85m/a (2015-2017). For the observation period 2013-2014 an elevation lowering of around 4m/a was observed on the glacier (see Section 5.4.1), which is more than on the Mound for the same period. For the observation period 2014-2015 it is the same. In the last observation period 2015-2017 the elevation lowering on the mound in Profiles C and E is smaller as the lowering on the glacier. Along Profile D the elevation change is almost the same as on the glacier (Figure 6.1).
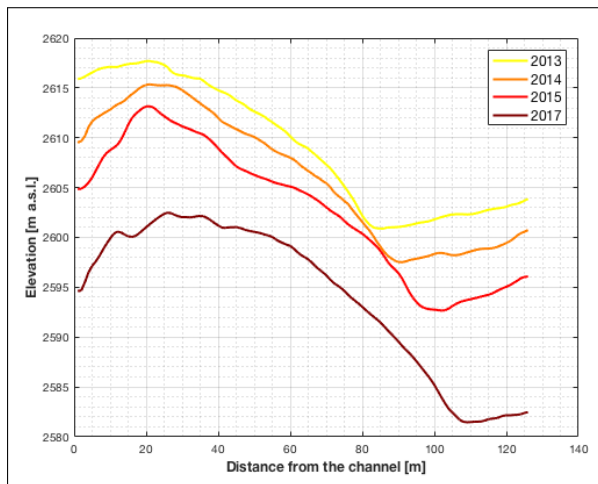
Figure 5.13: Profile C
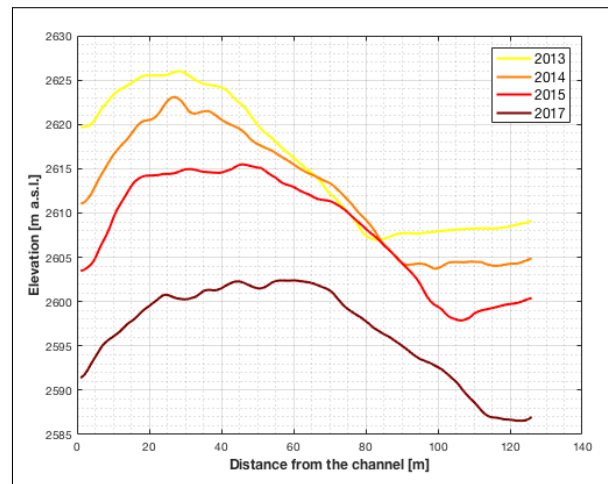
Figure 5.14: Profile D
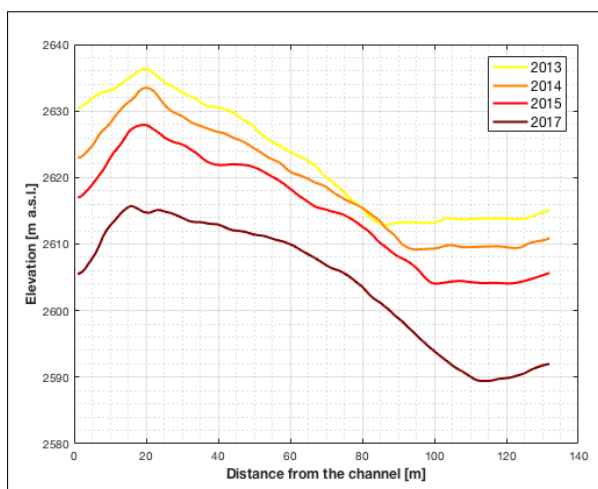
Figure 5.15: Profile E

	Profile C [m]	Profile D [m]	Profile E [m]
2013-2014	10	6	5
2014-2015	7	5	12
2015-2017	13	12	7
2013-2017	30	23	17

Table 5.6: Shift of the Mound

The upper part (release area of the landslide) of the elevation regime along Profile E is visible in Figure 5.16. One can see that the erosion (at this section) occurs in two steps. From 2005 to 2009/2010 the moraine top is removed, whereas the upper part of Profile E is less affected. From 2009/2010 towards 2013 material over the whole section (100m-450m Profile Length) is eroded. After 2013 the upper part stays stable. The maximum elevation loss occurred at the former moraine top with a loss of approximatly -30m from 2005 to 2017. Half of it got removed from 2005 to 2009/2010 and the other half from 2009/2010 to 2013.
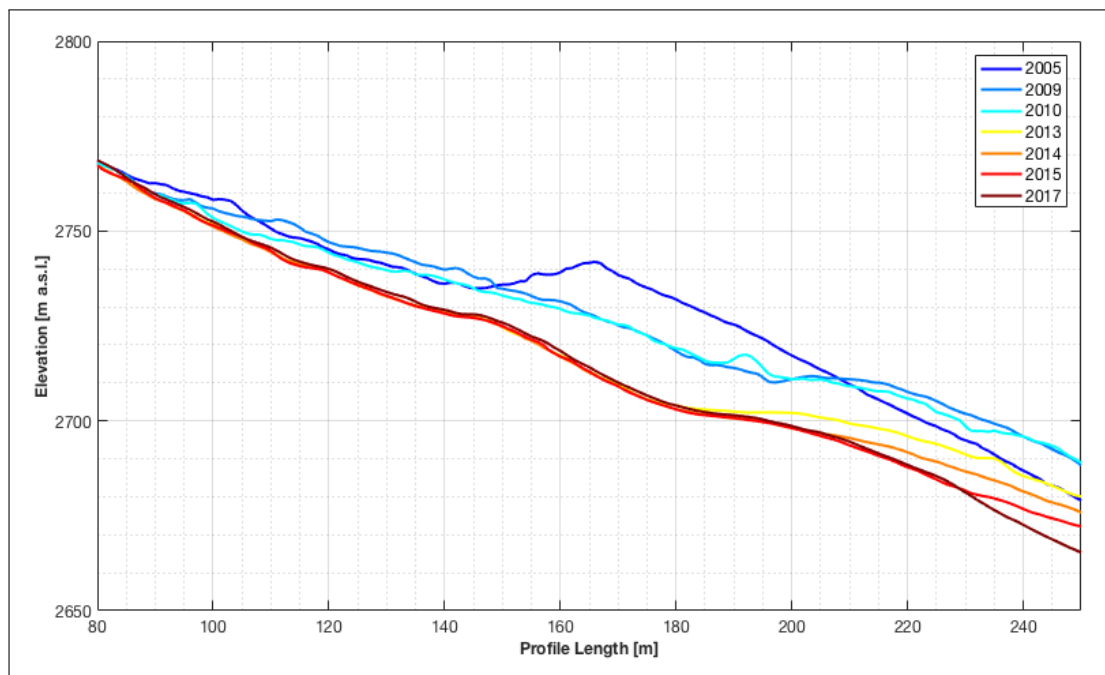
Figure 5.16: Elevation along Profile E for each observation year zoomed to the slide-area

Profile upglacier from the landslide area (H)

In Figure 5.17 one can see the elevation profile along Profile H for the Moraine-Foot zone and a part of the glacier. The border between the Moraine-Foot zone and the Glacier is visible as a kink in the elevation profile. Further, the formation of a terrace is recognizable (380m-390m Profile Length). Looking at the elevation developing one can see that a continuous surface lowering occurs in the Moraine-Foot zone and on the glacier. On the glacier a total surface lowering of approximately -46m is detectable between 2005 and 2017, whereby the annual elevation differences on the glacier vary from -3m/a to -4m/a for the early observation periods (until the period 2013-2014) to -5.5m/a for the last period.
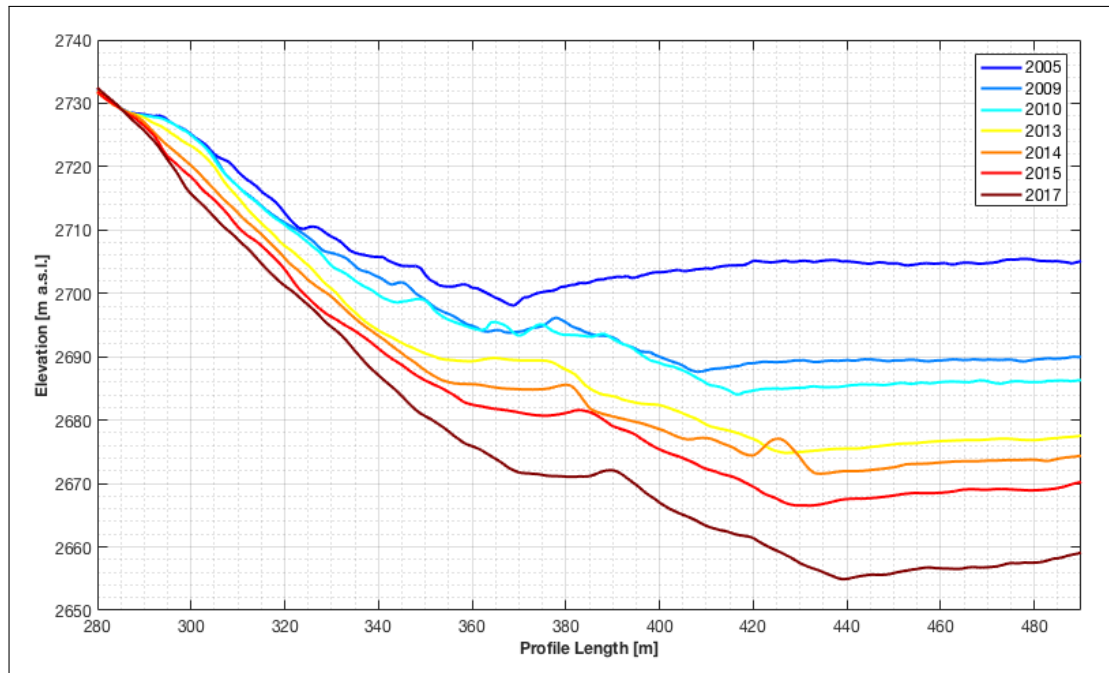
Figure 5.17: Elevation along Profile H for each observation year zoomed to the moraine-foot zone and the glacier

5.4.2 Point Tracking

In Figure 5.18 (up-right) one can see the two areas, in which large boulders are tracked over the different observation periods. In the maps left and low-right in Figure 5.18 the location of the boulder for each observation year is marked on the background of the shaded relief of 2017. On the map the position of 2016 is marked according to the available aerial photos, for the calculation of the direction and magnitude of the movement the observation period 2015-2017 is considered, in order to compare the data with the other analyses.
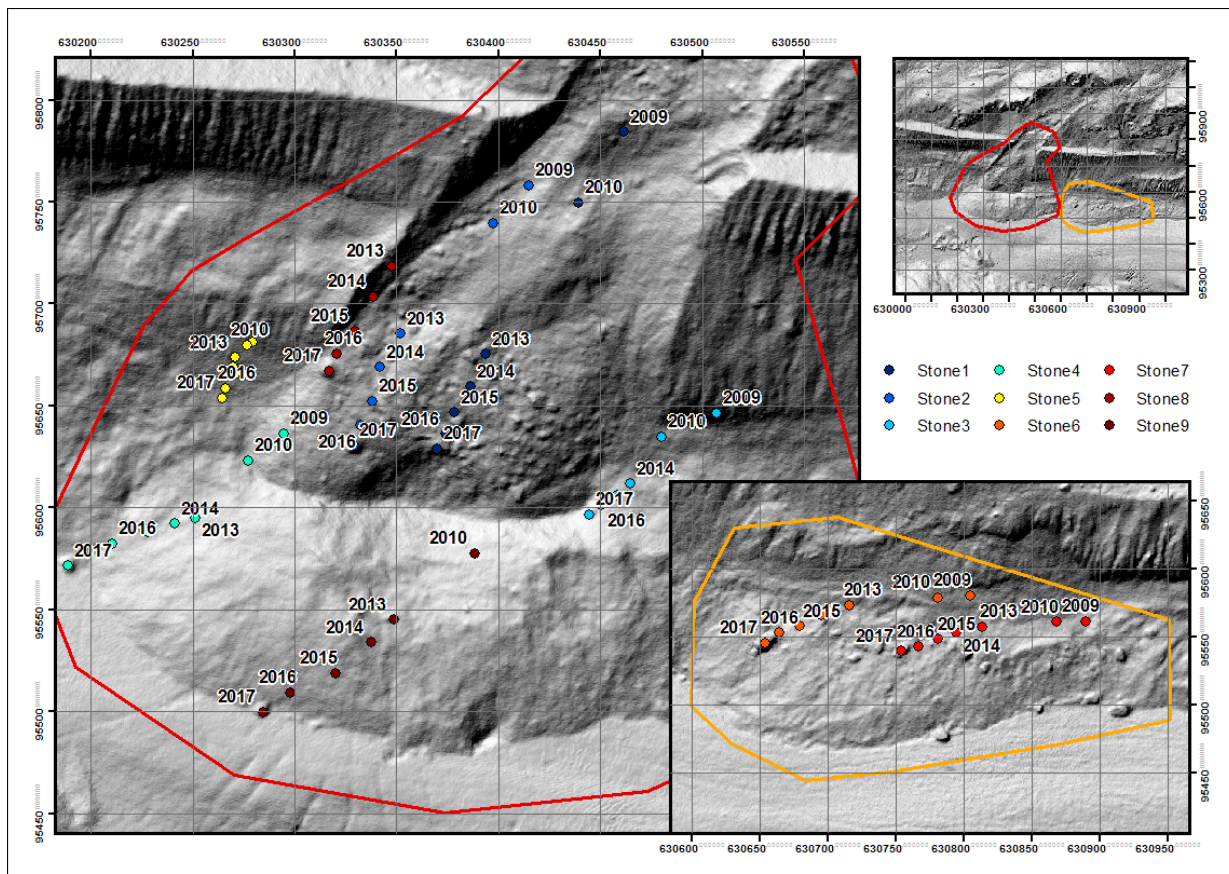
Figure 5.18: Map showing the position of the different tracked boulders for each observation year (Background: Shaded relief of 2017)

One can see that it was possible to track three stones within the Slide-Area (Stone 1, 2 & 8), two within the Mound (Stone 4 & 9) and four within the Moraine-Foot zone. Whereby two of the last-mentioned are beside the landslide (Stone 3 & 5) and two more up-glacier from it (Stone 6 & 7). Comparing the movement regimes in the two areas (red & orange) visually one can see that in the orange area the movement tends to be more west (along the moraine), whereas the movement in the red area is more South or southwest (perpendicular to the moraine). Table 5.7 shows the calculated directions for each stone and observation period. The visual observation can partially be confirmed. In general the stones in the red area moved southwest or South and in the orange area mostly west. Exceptional, Stone 4 in the red area is shifted in a western direction since 2013 and Stone 6 in the orange area is shifted southwest in the last two observation periods.

	2009 - 2010	2010 - 2013	2013 - 2014	2014 - 2015	2015 - 2017
Stone 1	SW	SW	SW	SW	SW
Stone 2	SW	SW	SW	S	S
Stone 3	SW	SW	SW	SW	SW
Stone 4	SW	SW	W	W	W
Stone 5	SW	SW	S	S	SW
Stone 6	W	W	W	SW	SW
Stone 7	W	W	W	W	W
Stone 8	-	-	SW	SW	SW
Stone 9	-	SW	SW	SW	SW

Table 5.7: Direction of the movement of the tracked boulders

Figure 5.19 shows the annual magnitude of the tracked boulders. Stone 3 and 5, which are not in the landslide area, show the smallest movements in all observation periods. An exception is the period 2009-2010, where a movement rate similar to the ones in the landslide could be determined for Stone 3. For all stones the largest movements can be determined for the observation period 2009-2010 respectively for the period 2014-2015, where no measurement for period 2009-2010 is taken. An exception is Stone 5, which shows the largest movement from 2015 to 2017.
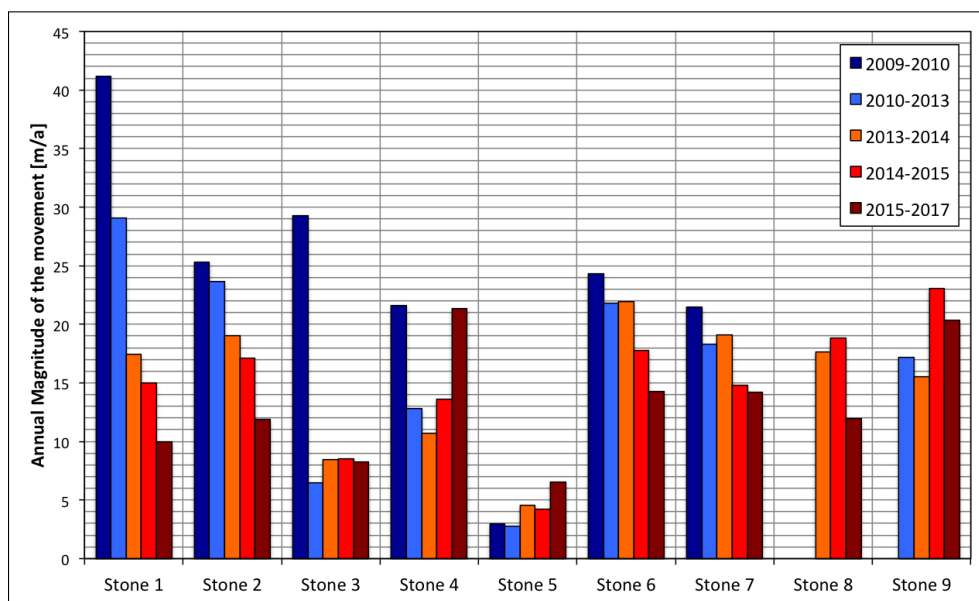
Figure 5.19: Annual magnitude of the movement of the tracked boulders

5.5   Spatially distributed Analyses

In the following the results of the spatially distributed analyses (DEM differences and image correlation) are addressed. This will be done according to the different zones (Slide-Area, Mound, Moraine-Foot zone (down- & up-glacier from the landslide) and Glacier). The results for the whole study area are shown in the Appendix. In Figures A.28-A.33 (Appendix A.6) the DEM differences for the whole study area are visible. Blue colors represent positive elevation changes and red colors negative ones. The areas with annual elevation changes between -0.39 and 0.4 m/a are represented transparent/with no color. Those areas are considered stable. Figures A.47-A.52 show the magnitude and direction of the determined horizontal movement for the whole study area. The direction of the movement is indicated through the orientation of the arrows and the magnitude of the movement through the color of the arrows. Displacements smaller than one meter are considered to be stable. The magnitudes of the displacement are classified in 5 classes from very small displacements (1-3m/a) to large displacements (>22m/a). Areas with no arrows are either stable (<1m horizontal movement) or the determined correlation-coefficients are insufficient.

5.5.1   Slide-Area

Observation Period 2005 - 2009

| (a) DEM Difference | (b) Image Correlation (CIAS) |

Figure 5.20: Slide-Area for the observation period 2005 - 2009

Figure 5.20 shows the results of the DEM difference (5.20a) and the image correlation (5.20b) for the observation period 2005-2009 zoomed to the Slide-Area. One can see that the outlines of the Slide-Area are clearly visible in the DEM difference, whereas it is only detectable in the upper part (behind the moraine-top) in the image correlation. Concerning the extent of the unstable terrain within the Slide-Area one can see that with both methods more or less the same area is classified as unstable. In the DEM difference two zones with surface lowering are visible, whereby the upper one represents the release area of the landslide and the lower one is located at the former moraine-top. Between the two zones with

surface lowering a zone with small surface lifting is visible, which can be explained by the temporary deposition of material as the material from the release area does not immediately completely slides down. The area with surface lifting on the moraine flank is the temporary deposition of the former moraine-top. These zones with lifting and lowering are also identifiable in the Profile lines (Figures 5.12 & 5.16). Overall, there is slightly more elevation loss than gain within the Slide-Area for this observation period resulting in a negative mean elevation change of -0.22m/a. The maximum elevation loss within the Slide-Area (Outlines 2009) is -4.7m/a and the maximum elevation gain is 3.01m/a. Within the image correlation neither a distinct direction nor length is detectable for the Slide-Area, which is visible in Figure A.54 showing the frequency of the detected movements.

Observation Period 2009 - 2010

(a) DEM Difference   (b) Image Correlation (CIAS)

Figure 5.21: Slide-Area for the observation period 2009 - 2010

In Figure 5.21 one can see the results for the DEM difference (5.21a) and the image correlation (5.21b) for the observation period 2009-2010 for the Slide-Area. Regarding the extent of the unstable terrain within the Slide-Area it is visible that with both methods more or less the same area is classified as unstable. Both methods show a stabilization of the most upper part of the Slide-Area. In the result of the DEM difference one can see the same two zones with surface lowering and lifting as in the first observation period, but their size have changed a bit. As in the first observation period the Slide-Area is dominated by elevation loss, which results in a mean elevation change of -0.89m/a with a maximum loss of 10.74m/a. Within the image correlation the Slide-Area can be divided from the movements on the moraine flank through higher magnitude of the movement (darker red colors) and partially by the direction of the movement (Arrows). A patch with the same direction (southwest) and very high magnitudes (>22m/a) of movement is detected in the Slide-Area. The area corresponds partially with a patch with high surface lowering. The two tracked boulders in the Slide-Area show large movements of 41.15m (Stone1) respectively 25.32m (Stone2) in a southwestern direction. However, only one of

the tracked boulders (Stone2) lies within the identified patch with large movements from the image correlation.

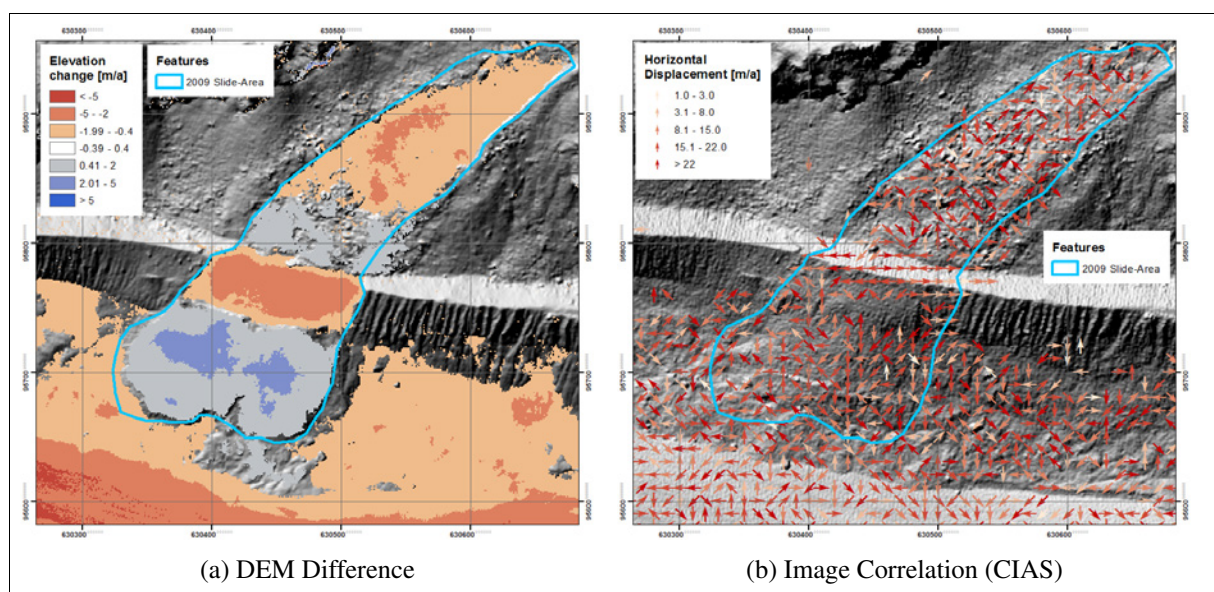**Observation Period 2010 - 2013**

(a) DEM Difference (b) Image Correlation (CIAS)

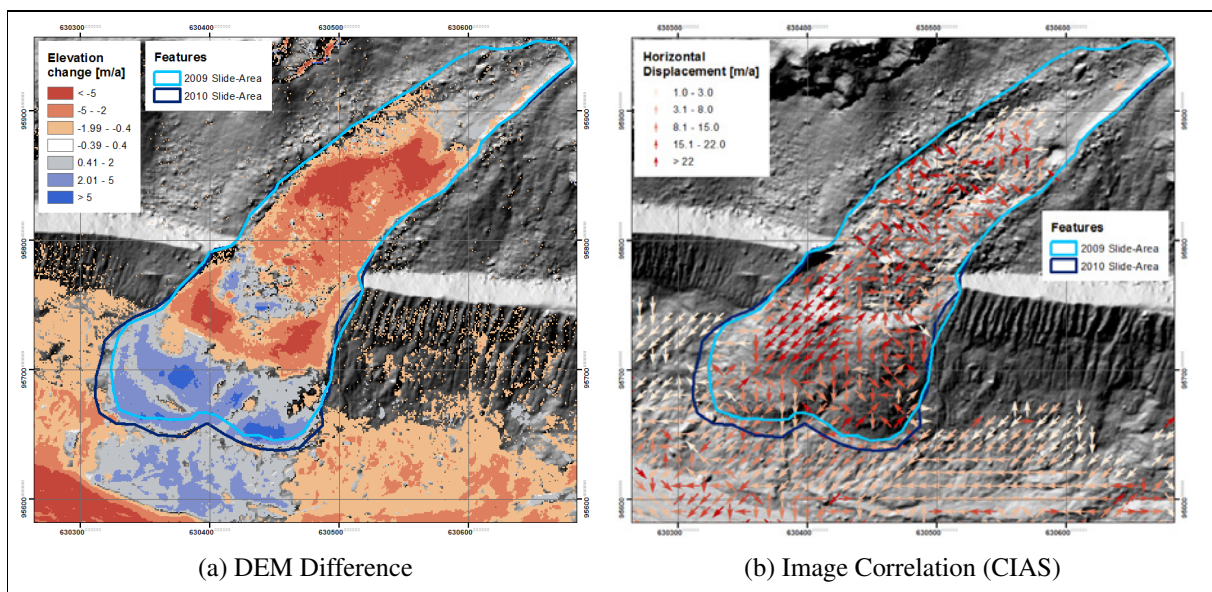Figure 5.22: Slide-Area for the observation period 2010 - 2013

The results of the DEM difference (5.22a) and the image correlation (5.22b) are shown in Figure 5.22 for the observation period 2010-2013. With both methods one can see that the extent of the unstable terrain within the Slide-Area slightly decreased towards the previous observation period. Further, it is visible that the annual magnitude of the determined surface changes (vertical and horizontal) are smaller than in the previous observation period. In the DEM difference one can see that the unstable part of the Slide-Area shows almost only surface lowering. The two zones with surface lifting have disappeared, only a very small part at the bottom of the Slide-Area is classified with a positive elevation change. The down-sliding of the material in the Slide-Area as well as the formation of the Mound during this observation period is good visible in the Profile lines 5.12. Only with the image correlation it is difficult to divid the Slide-Area from the movement of the Moraine-Foot zone as no distinct direction as well as no higher magnitudes of the movement are visible. However, the histogram with the frequency of the directions show a trend towards a southwest movement (Figure A.54). The two tracked boulders show a total horizontal displacement of 87.13m (29.04m/a) respectively 70.99m (23.66m/a) in a southwestern direction, which is in the same range as in the previous observation period.

Observation Period 2013 - 2014

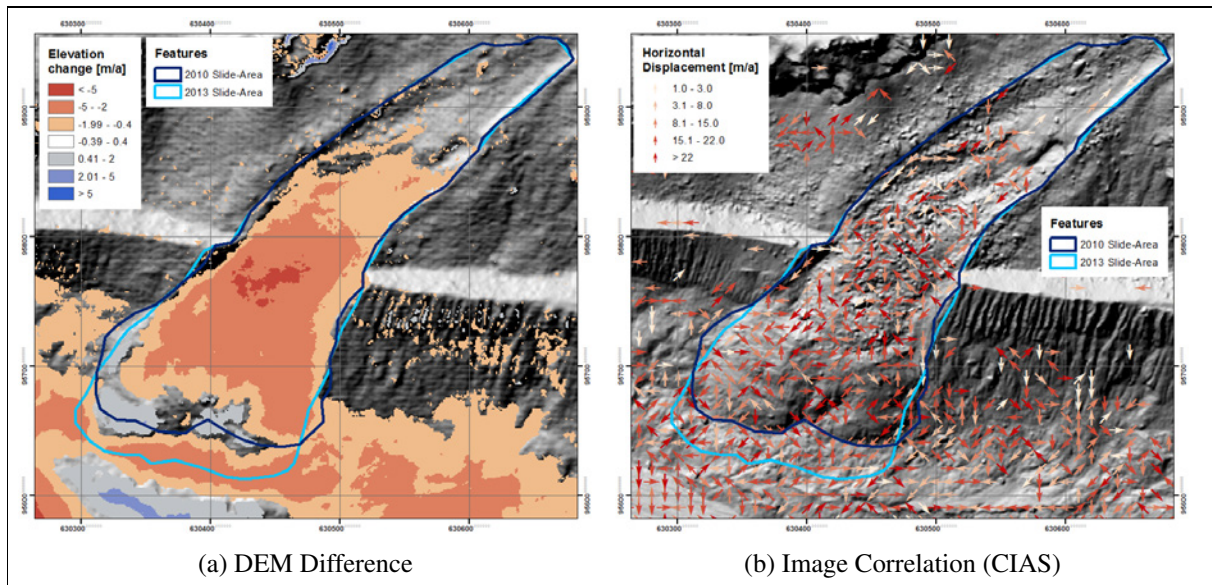(a) DEM Difference (b) Image Correlation (CIAS)

Figure 5.23: Slide-Area for the observation period 2013 - 2014

Figure 5.23 shows the results of the DEM difference (5.23a) and the image correlation (5.23b) for the observation period 2013-2014 zoomed to the Slide-Area. With both methods one can see that the extent of the unstable terrain is decreasing further. In this period only the part down from the former moraine-top is moving, which is also recognizable in the Profile Lines. Within the DEM difference one can see that surface lowering dominates within the Slide-Area resulting in a negative mean elevation change of -1.54m/a. The maximum negative elevation change is -8.26m/a. In the image correlation one can see that the magnitude of the movement in the landslide is higher than around it. Further, the movement direction within the Slide-Area is quite consistent resulting in a large patch with the southwest oriented movement with magnitudes higher than 15m/a. This patch corresponds with a high surface lowering in the DEM difference. On the other hand the tracked boulders show a decrease in the displacement (17.41m/a respectively 19.05m/a).

Observation Period 2014 - 2015

(a) DEM Difference   (b) Image Correlation (CIAS)

Figure 5.24: Slide-Area for the observation period 2014 - 2015

In Figure 5.24 one can see the results for the DEM difference (5.24a) and the image correlation (5.24b) for the observation period 2014-2015 for the Slide-Area. With both methods one can see that the extent of the unstable terrain within the Slide-Area is decreasing further. In the DEM difference a small patch with no or small positive elevation change is identifiable at the lower margin of the Slide-Area. This corresponds with the slipping-edge into the channel between the Slide-Area and the Mound. Among this one can see that only surface lowering has occurred in the Slide-Area and the magnitude of the lowering has decreased compared with the previous observation period. The mean elevation change declines to -1.30m/a. However, the maximum elevation loss stays high with -8.40m/a. Also in the magnitude of the horizontal movement (image correlation) is a decreasing visible, which corresponds with the measured displacements for the tracked boulders. Nevertheless, the magnitude of the movement is still higher than around the Slide-Area. The direction of the movement stays more or less similar than in the previous observation period. Only the right part of the Slide-Area changes towards a more south oriented movement comparing with the southwest direction from the pervious observation period. This is also visible in the histogram with the frequency of the directions (Figure A.54).
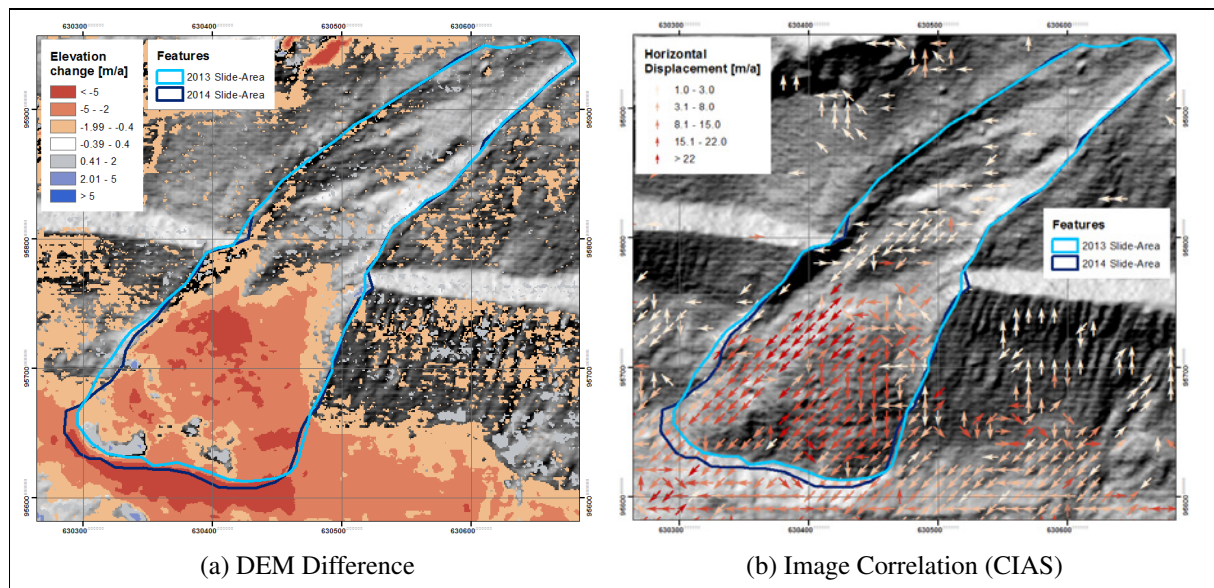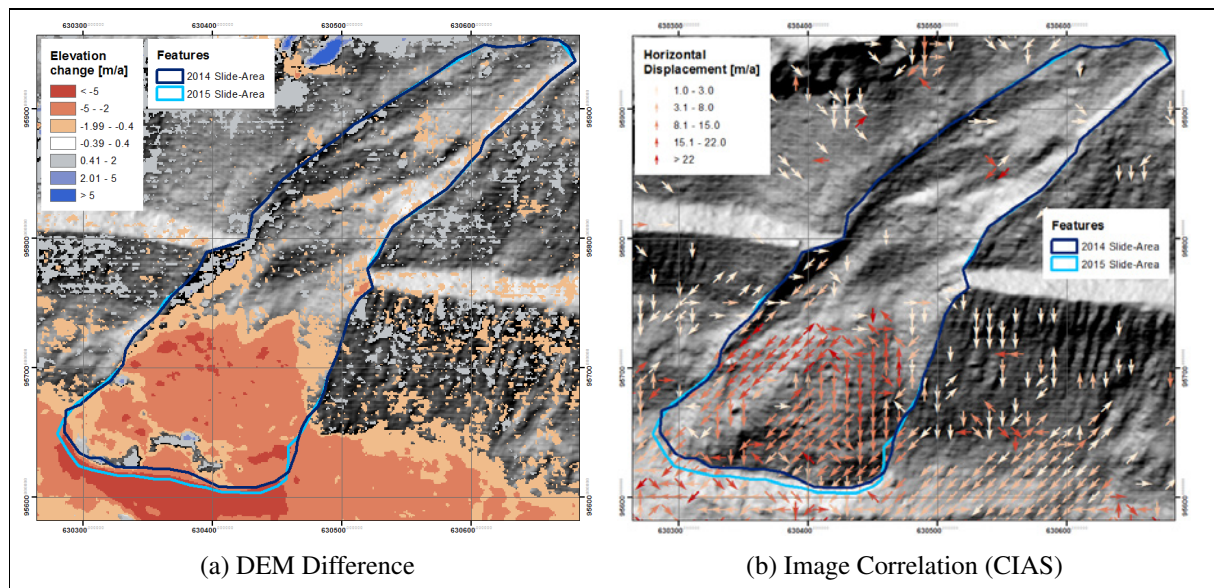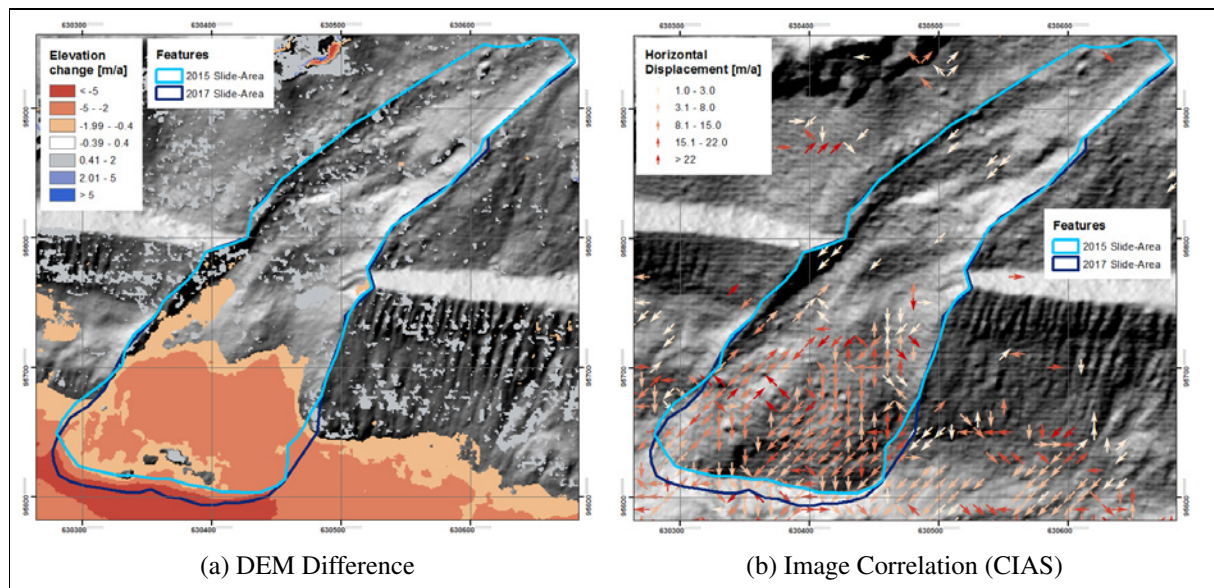
Observation Period 2015 - 2017

Figure 5.25: Slide-Area for the observation period 2015 - 2017

The results of the DEM difference (5.25a) and the image correlation (5.25b) is shown in Figure 5.25 for the observation period 2015-2017. With both methods one can see that the extent of the unstable terrain within the Slide-Area is decreasing further. As well as previously observed the magnitude of the changes decreases further in both methods. This corresponds with the displacement of the tracked boulders. The mean elevation change declines to -0.91m/a and the maximal elevation loss decreases to -4.73m/a. Even after the magnitude of the movement has decreased, it is still possible to distinguish the movement of the Slide-Area from the movement of the surrounding area. In the DEM difference a small patch with no or small positive elevation change is identifiable as in the previous observation period representing the slipping-edge in the channel between the Slide-Area and the Mound.

Volume Changes

For the Slide-Area the volume change respectively the volume budget can be calculated. Therefore, the elevation difference within the Slide-Area is classified into three groups: elevation loss, stable, elevation gain. For each group the volume change is calculated by sum up the elevation change multiplied by the pixel area for each group. For each observation period the extent of the Slide-Area is changing. The area consists to the Slide-Area increases from the first to the last observation period (Column 1 in Table 5.8), but also the composition to each of the three groups is changing, which is shown in Figure 5.26. Figures A.35-A.40 (Appendix) show the spatial distribution of the three groups within the Slide-Area. One can see that the area with volume gain is decreasing rapidly from 36% to 5%/7% from the period 2005-2009 to the period 2010-2013/2015-2017. Further, it is visible that with the decreasing area with volume gain the stable area is increasing. The area with volume loss stays more or less stable over the different observation periods.
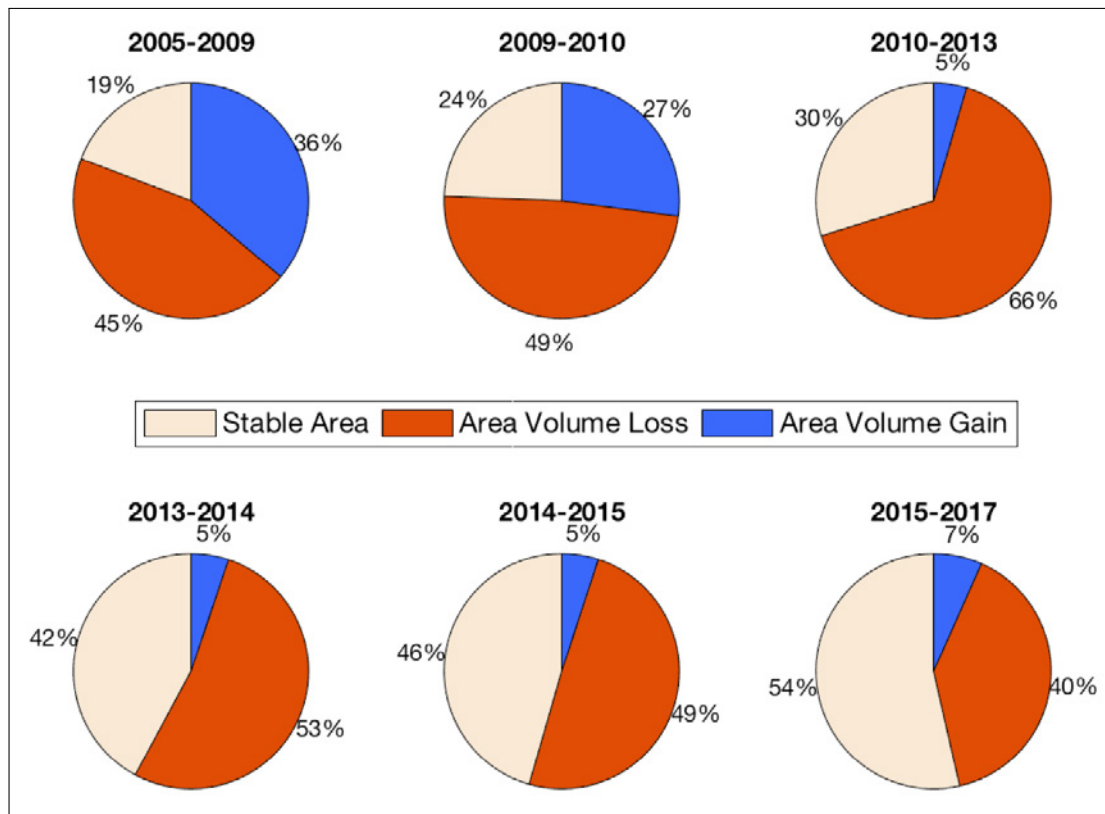
Figure 5.26: Proportion of the area used to calculate the Volume Budget (Slide-Area)

Looking at the total amount of the changing volume (Column 3 in Table 5.8) one can see that in the period 2009-2010 the volume is the highest with 87'745m^3/a and in the following the volume decreases continuously. The main part of this total unstable volume is contributed by volume loss (Percentages Column 4/6 in Table 5.8), especially since the period 2010-2013. The highest volume loss is determined for the period 2013-2014 with 72'511m^3/a in relation to only 1'843m^3/a volume gain for the same period. Regarding the volume budget (Column 6 in Table 5.8) one can see that it is negative for all observation periods. For the first observation period the budget is the least negative with -8'342m^3/a, whereas it is the most negative for the period 2013-2014 with -70'668m^3/a.

	Area [m^2]	Volume unstable [m^3/a]	Volume loss [m^3/a]	Volume gain [m^3/a]	Volume Budget [m^3/a]	Vol. Budget per Area [m^3/(a m^2)]
2005-2009	38'715	46'730	-27'536 (59%)	19'194 (41%)	-8'342	-0.22
2009-2010	41'175	87'745	-61'747 (70%)	25'998 (30%)	-35'749	-0.87
2010-2013	44'932	68'700	-66'892 (97%)	1'808 (3%)	-65'084	-1.45
2013-2014	45'661	74'354	-72'511 (98%)	1'843 (2%)	-70'668	-1.55
2014-2015	46'980	63'637	-61'804 (97%)	1'832 (3%)	-59'972	-1.28
2015-2017	49'319	52'840	-51'066 (97%)	1'774 (3%)	-49'292	-1.00

Table 5.8: Volume change within the Slide-Area (Outlines of the newer year were used)

5.5.2   Mound

Observation Period 2013 - 2014

(a) DEM Difference   (b) Image Correlation (CIAS)

Figure 5.27: Mound for the observation period 2013 - 2014

Figure 5.27 shows the results of the DEM difference (5.27a) and the image correlation (5.27b) for the observation period 2013-2014 zoomed to the Mound. In the DEM difference one can see that the Mound consists of two different zones: one with elevation lowering towards the Slide-Area and one with elevation rising towards the glacier. This zone of elevation rising is visible in Profiles C and D (Figure A.22 respectively 5.12), where the surface of 2014 is higher than the surface of 2013 (400m Profile Length) due to the shifting of the Mound towards the glacier. When correcting for this shift one can see that this elevation rising is not visible anymore (Figure 5.13) or very small as along Profile D (Figure 5.14). As a consequence this elevation gain does not fully origin from an accumulation of material, but through the transition from the glacier to the mound. In Figures 5.13-5.15 one can see that melting/surface lowering does occur with a mean elevation loss on the Mound-top (20-50m) of around -3.1m/a. In the image correlation one can see that mainly medium to high (8.1-22m/a) movements are detected. The direction of those movements is usually west or southwest visible through the detected patches and the frequency measure in Figure A.55. The direction as well as the magnitude of the detect movements corresponds with the tracked boulders. They show a displacement of 10.73m (Stone4) respectively 15.53m (Stone9) in western and southwestern direction.

Observation Period 2014 - 2015

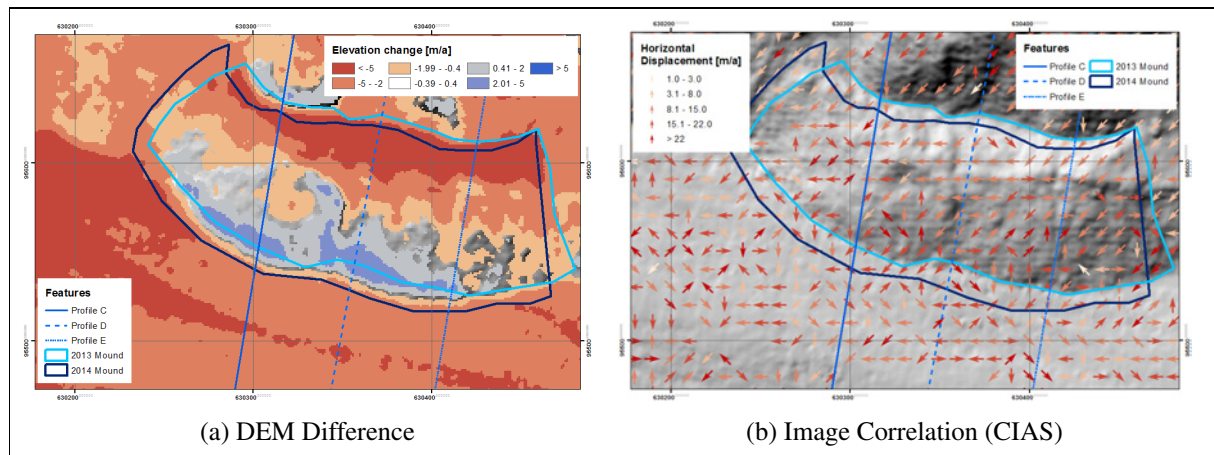(a) DEM Difference   (b) Image Correlation (CIAS)

Figure 5.28: Mound for the observation period 2014 - 2015

In Figure 5.28 one can see the results for the DEM difference (5.28a) and the image correlation (5.28b) for the observation period 2014-2015 for the Mound. Similar as in the period 2013-2014 a zone with elevation gain and a zone with elevation loss is identifiable, whereas the first-mentioned is smaller than in the previous period. The area with elevation loss does not only increases, but also the area with large surface lowering is bigger. A mean elevation loss around -4.5m/a is determinable along the Profiles for the mound-top (20-50m). Within the image correlation the magnitude of the movements is similar than in the previous observation period. On the other hand the displacement of the tracked boulders has increased to 13.59m (Stone4) respectively 23.07m (Stone9). Within the direction of the movement some patches with west or southwest movement are identified. Regarding the frequency of the directions one can see that southwest movement is detected the most followed by west direction (Figure A.55).

Observation Period 2015 - 2017

(a) DEM Difference

(b) Image Correlation (CIAS)
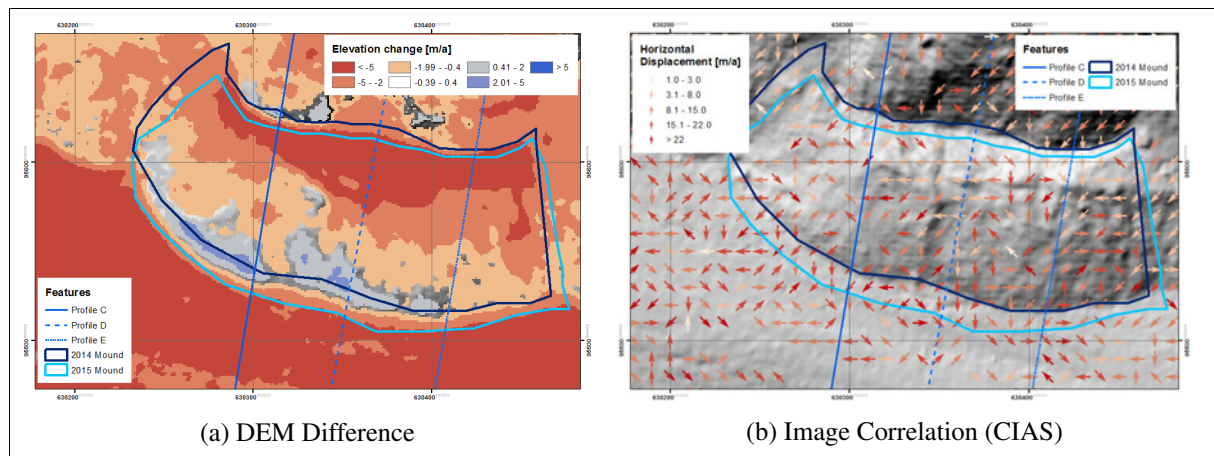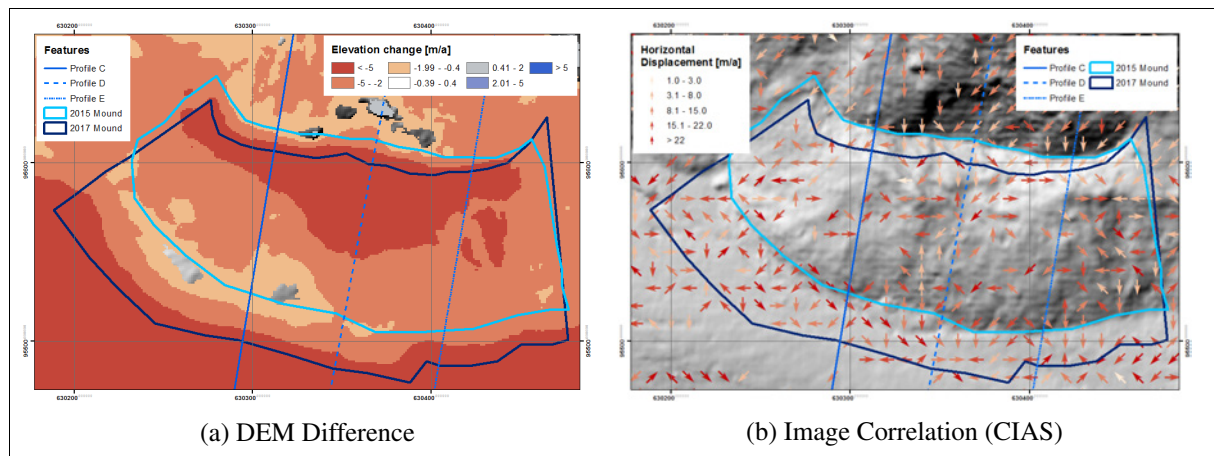
Figure 5.29: Mound for the observation period 2015 - 2017

The results of the DEM difference (5.29a) and the image correlation (5.29b) is shown in Figure 5.29 for the observation period 2015-2017 zoomed to the Mound. One can see that the area with elevation gain near the glacier margin, which is visible in the observation periods 2013-2014 and 2014-2015, is not detected anymore. Additionally, the area with large surface lowering increases further. On the Mound-top (20-50m) a mean elevation loss of -5.5m/a is detectable along the Profiles. Within the image correlation the magnitude of the movements show a slight decrease towards the previous observation period. One of the tracked boulders (near the margin) is displaced more than in the previous observation period (Stone4), whereas the other one shows a smaller displacement (Stone9). Within the direction of the movement no patches are detected on the Mound. Looking at the frequency of the individual direction one can see that southwest is the most frequent (Figure A.55).

5.5.3 Moraine-Foot zone down-glacier from the landslide

Observation Period 2005 - 2009

Considering the DEM difference (Figure 5.30a) and image correlation (Figure 5.30b) of the first observation period 2005-2009 one can see that the detected unstable terrain within the Moraine-Foot zone down-glacier from the landslide corresponds within both methods. In the DEM difference mainly small elevation loss is identified, whereas in the image correlation neither a distinct magnitude nor direction of the horizontal movement is recognizable.

(a) DEM Difference

(b) Image Correlation (CIAS)

Figure 5.30: Moraine-Foot zone down-glacier from the landslide for the observation period 2005 - 2009

Observation Period 2009 - 2010

In the observation period 2009-2010 both methods correspond in determining the unstable terrain as well as detecting a decrease in the extent (Figures 5.31a & 5.31b). As in the previous observation period small elevation loss is dominating within the down-glacier part of the Moraine-Foot zone. This surface lowering is also nicely visible in the Profile Lines (Figures A.20 & A.21). The elevation loss tends to increase towards the glacier margin. In the image correlation very small displacements in south or southwest direction dominates. The tracked boulder in this part of the study area show also a small movement of 2.97m in southwestern direction.

(a) DEM Difference

(b) Image Correlation (CIAS)

Figure 5.31: Moraine-Foot zone down-glacier from the landslide for the observation period 2009 - 2010

Observation Period 2010 - 2013

Regarding the DEM difference (Figure 5.32a) and the image correlation (Figure 5.32b) for the observation period 2010-2013 zoomed to the Moraine-Foot zone down-glacier from the landslide one can see that the detected unstable terrain corresponds with each other. The DEM difference shows a slight increase of the elevation loss visible by the increasing area with medium elevation loss. In the image correlation no distinct direction of the movement and no pattern in the magnitude of the movement is recognizable. The tracked boulder moves in a southern direction with 4.57m/a.

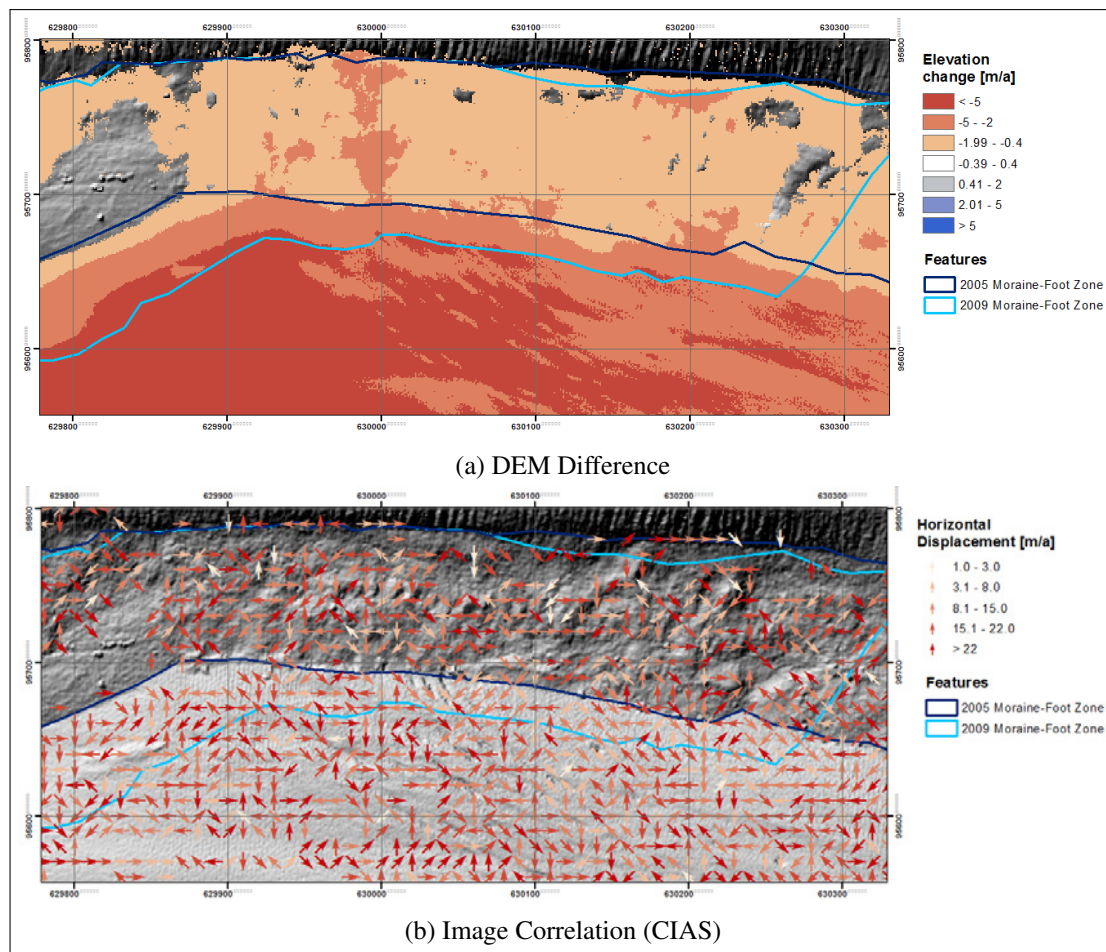(a) DEM Difference

(b) Image Correlation (CIAS)

Figure 5.32: Moraine-Foot zone down-glacier from the landslide for the observation period 2010 - 2013

Observation Period 2013 - 2014

In the observation period 2013-2014 the classified unstable terrain from the DEM difference and from the image correlation correspond with each other (Figures 5.33a & 5.33b). Within both methods the release of a small slide (below 630100/95800) is visible. In the DEM difference it is visible as a patch with high elevation loss followed downslope by a patch with small elevation gain. In the image correlation the release area is visible as a patch with high displacement in southern direction. The pathway and deposition show also medium to high displacements but chaotic in the direction. Among the small slide the pattern stays the same as in the previous observation periods with small to medium elevation loss and very small horizontal displacements in southern or southwestern direction. Further, a retreat of the unstable terrain with the glacier is visible compared with the last observation period.

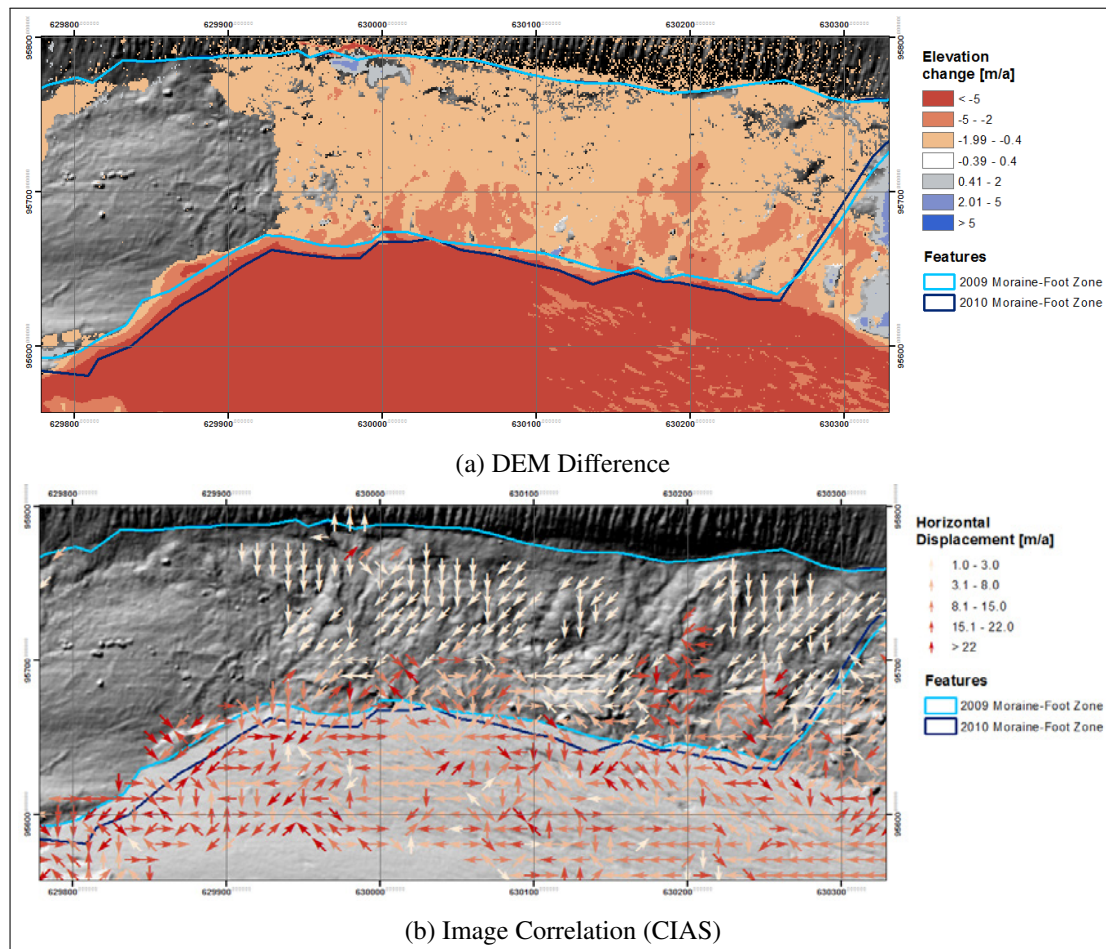(a) DEM Difference

(b) Image Correlation (CIAS)

Figure 5.33: Moraine-Foot zone down-glacier from the landslide for the observation period 2013 - 2014

Observation Period 2014 - 2015

Regarding the DEM difference (Figure 5.34a) and the image correlation (Figure 5.34b) for the observation period 2014-2015 of the Moraine-Foot zone down-glacier from the landslide one can see that the detected unstable terrain corresponds mostly with each other. In the DEM difference small to medium elevation loss are detected, also visible along Profile B (Figure A.21). Within the image correlation consists the detected unstable terrain mainly of a patch with small displacement in southwestern direction. This corresponds with the displacement of the tracked boulder in this area.
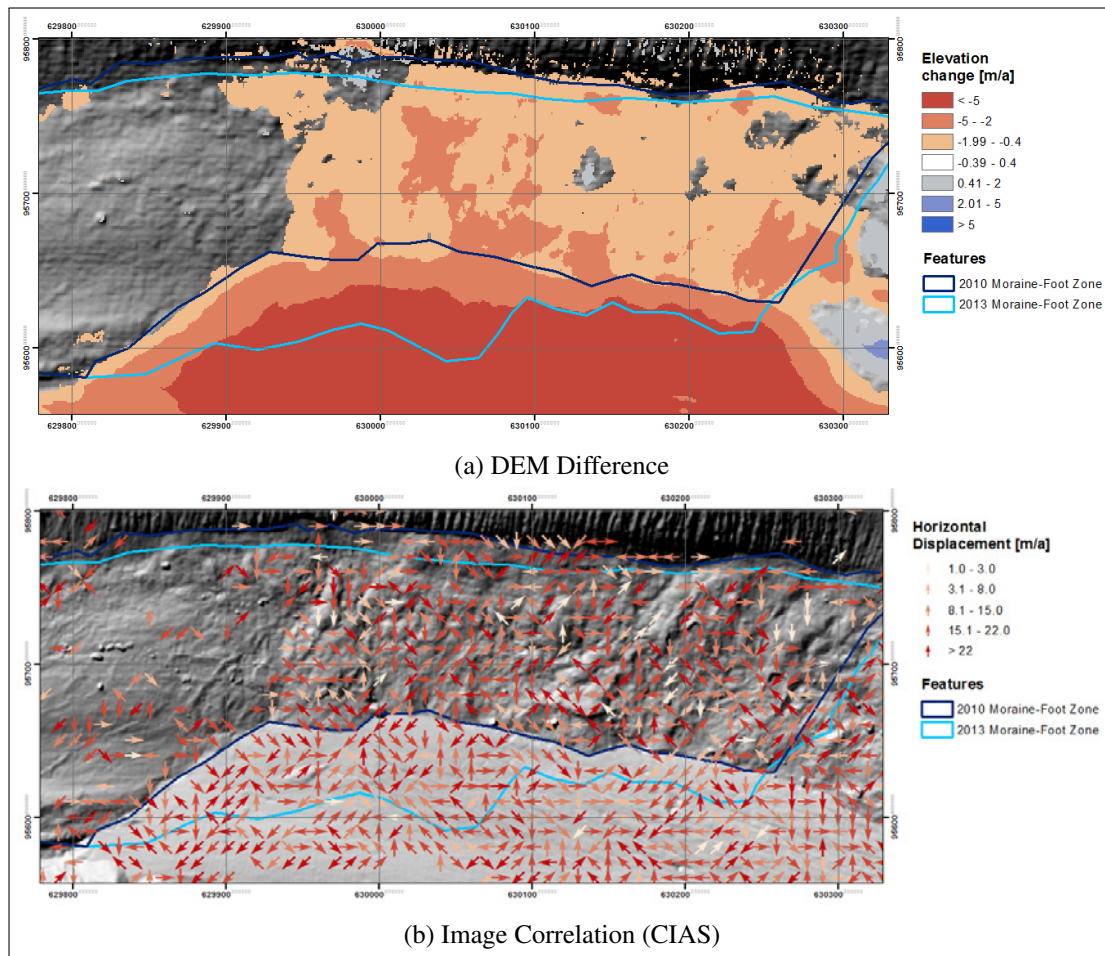

(a) DEM Difference

(b) Image Correlation (CIAS)
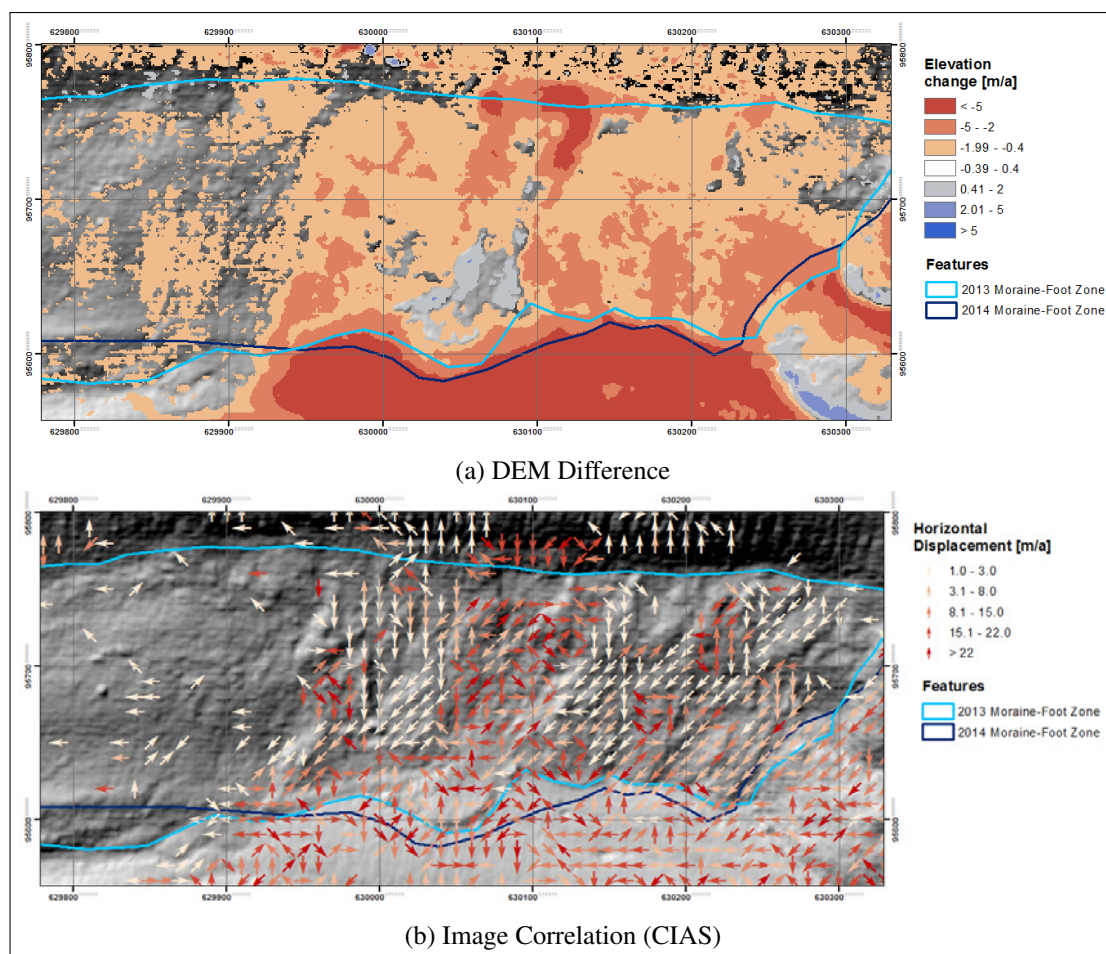
Figure 5.34: Moraine-Foot zone down-glacier from the landslide for the observation period 2014 - 2015

Observation Period 2015 - 2017

In the observation period 2015-2017 some small differences between the classified unstable terrain from the DEM difference and from the image correlation are visible (Figures 5.35a & 5.35b). However, a decrease in the unstable terrain is observable with the retreating glacier. In the DEM difference only elevation loss occurs with low and medium magnitudes, which is also visible along Profile B (Figure A.21). In the image correlation a patch with very small displacement in southwestern direction cates the eye. This patch corresponds with the small negative elevation change area.

(a) DEM Difference

(b) Image Correlation (CIAS)
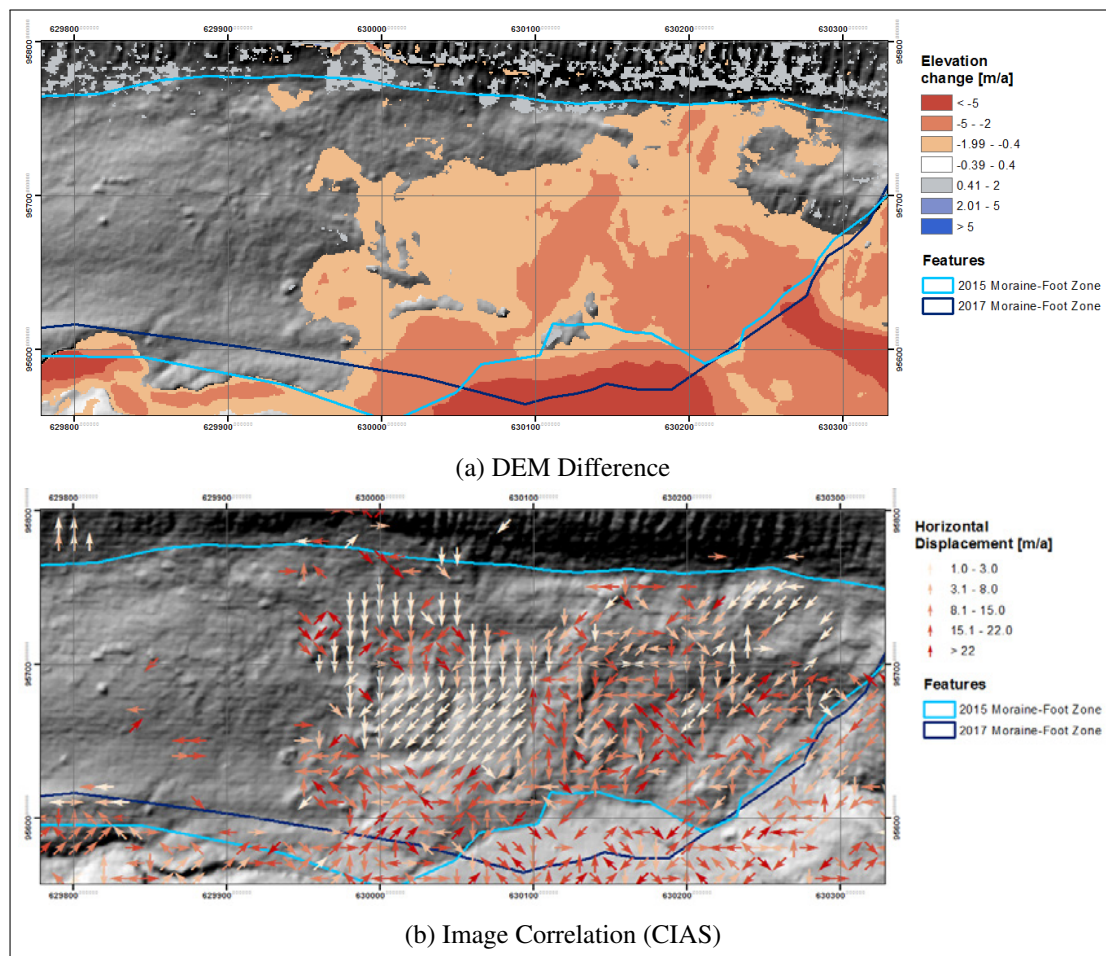
Figure 5.35: Moraine-Foot zone down-glacier from the landslide for the observation period 2015 - 2017

5.5.4 Moraine-Foot zone up-glacier from the landslide

Observation Period 2005 - 2009

The evolution of the up-glacier part of the Moraine-Foot zone differs from the down-glacier part. Starting with the first observation period one can see that the DEM difference (Figure 5.36a) and image correlation (Figure 5.36b) detect more or less the same area as unstable terrain. The DEM difference shows almost exclusively elevation loss with small or medium magnitude. Within the image correlation neither a distinct direction or magnitude is recognizable.

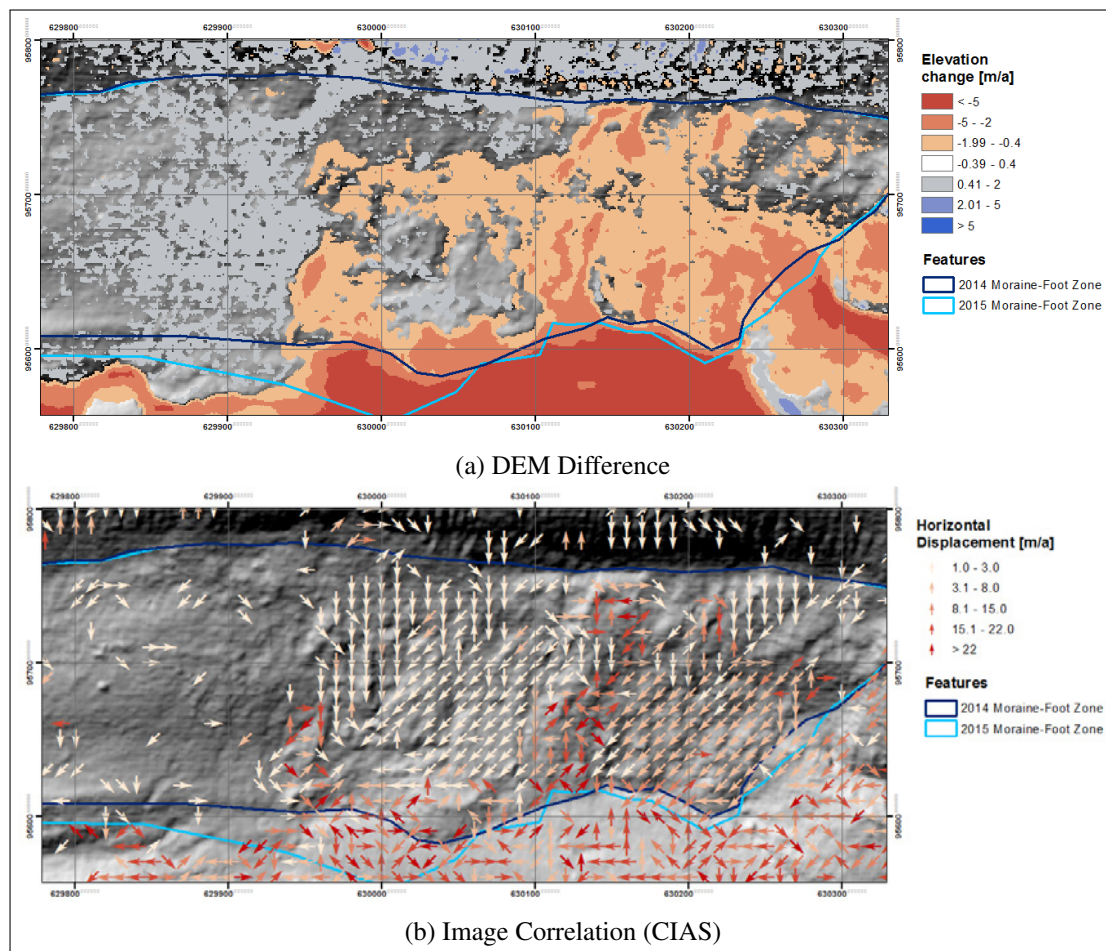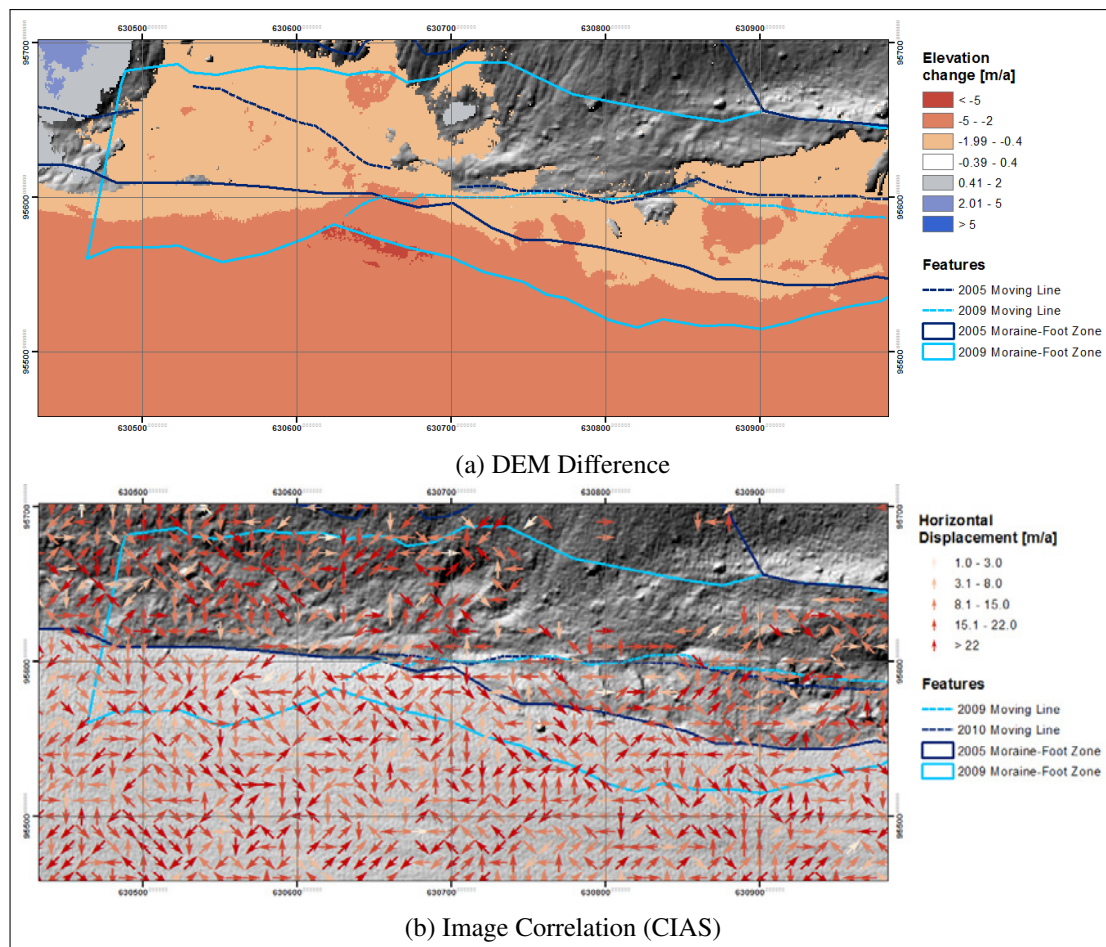(a) DEM Difference

(b) Image Correlation (CIAS)

Figure 5.36: Moraine-Foot zone up-glacier from the landslide for the observation period 2005 - 2009

Observation Period 2009 - 2010

In the observation period 2009-2010 the classified unstable terrain from the DEM difference and the image correlation corresponds with each other as in the first observation period (Figures 5.37a & 5.37b). In the DEM difference one can see a dark blue object (positive elevation change, below the point 630800/95600) followed up-glacier by a dark red object (negative elevation change). This is a large boulder, which moved from 2009 to 2010. The dark red represents the position in 2009 and the dark blue the position in 2010. Among that mainly small to medium elevation loss occurs. In the image correlation two dominant direction of the horizontal displacement are observable west and southwest. The south-west orientation of the movement is detected nearby the Slide-Area and between the Slide-Area and the glacier with low magnitudes. The west movement dominates on the bulge towards the glacier with magnitudes ranging from low to high. The Moving Line separates the two directions or the west-movement from the stable terrain. The two tracked boulders correspond with the findings of the image correlation, they show also a west orientation of the displacement and magnitudes of 24.33m (Stone6) respectively 21.49m (Stone7). The extent of the west movement is bounded by the Moving Line.

(a) DEM Difference

(b) Image Correlation (CIAS)

Figure 5.37: Moraine-Foot zone up-glacier from the landslide for the observation period 2009 - 2010

Observation Period 2010 - 2013

Regarding the DEM difference (Figure 5.38a) and the image correlation (Figure 5.38b) for the observation period 2010-2013 of the Moraine-Foot zone up-glacier from the landslide one can see that the detected unstable terrain corresponds mostly with each other. The DEM difference shows almost exclusively elevation loss with small or medium magnitude similar to the first observation period. Also similar to the first observation period no distinct direction or magnitude is recognizable in the image correlation. The tracked boulders show a bit smaller movements (magnitude and direction) as in the previous observation period with 21.77m/a (Stone6) respectively 18.29m/a (Stone7).

(a) DEM Difference

(b) Image Correlation (CIAS)
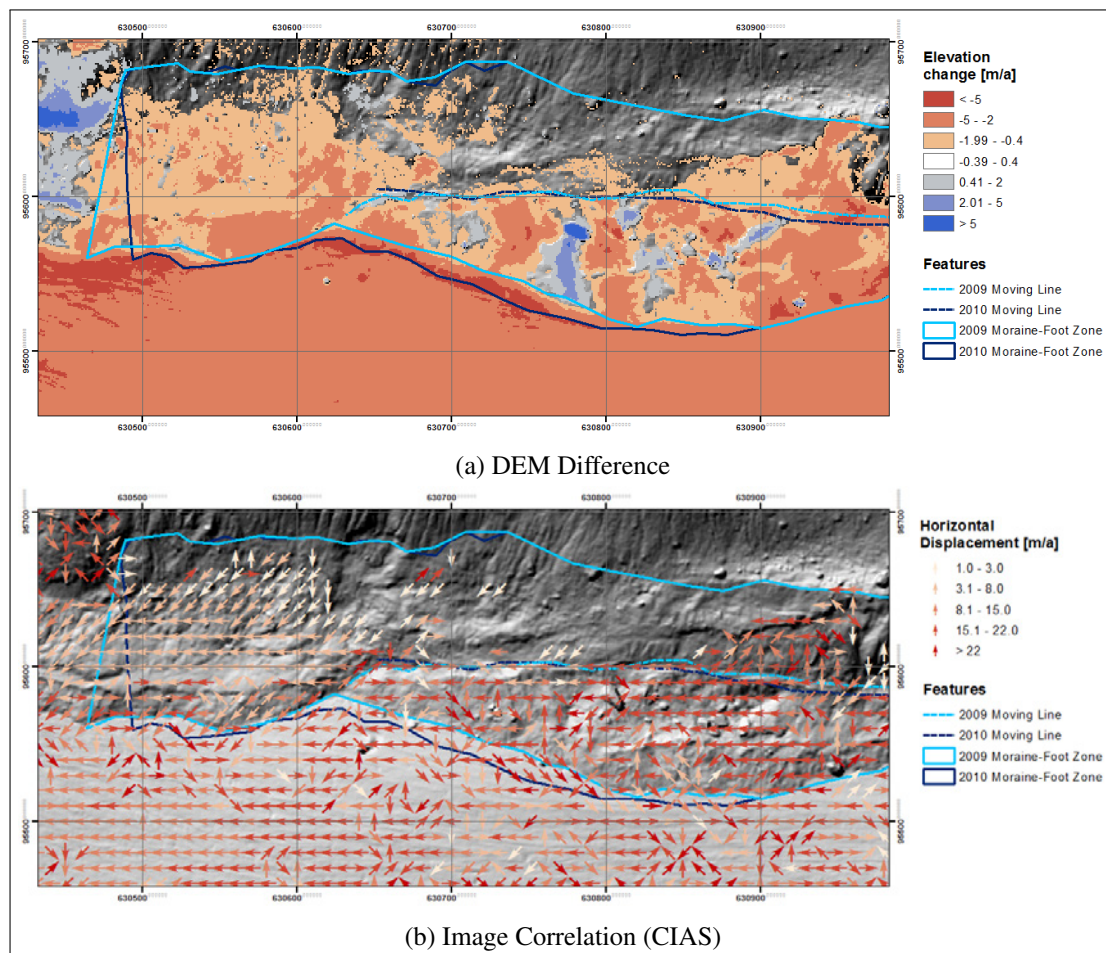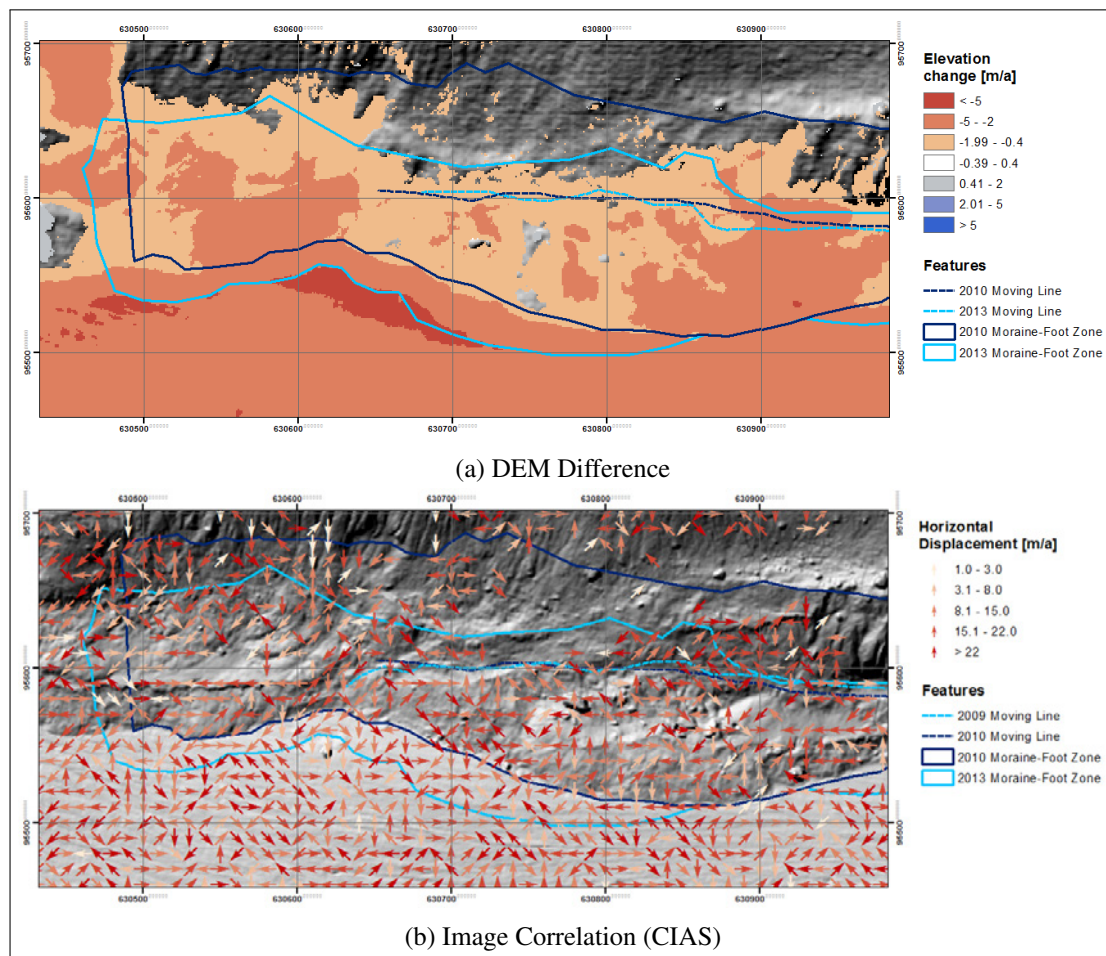
Figure 5.38: Moraine-Foot zone up-glacier from the landslide for the observation period 2010 - 2013

Observation Period 2013 - 2014

In the observation period 2013-2014 the classified unstable terrain from the DEM difference and the image correlation is more or less similar (Figures 5.39a & 5.39b). The DEM difference for this period and area is dominated by elevation loss with medium magnitude. This is also observable along the Profiles G and H (Figure A.26 & A.27). Further, the movement of a large boulder (below 630700/95600) is detectable as a dark red point followed down-glacier by a dark blue point. In the image correlation the same pattern as in the observation period 2009-2010 is also detectable in this period. The direction of the horizontal movement of the bulge is west, whereas the area near the Slide-Area is moving in southwestern direction. Thereby is the west-moving with a higher magnitudes than the southwestern one. The west-movement is again restricted by the Moving Line. The tracked boulders are still moving westwards with a similar magnitude as in the previous period.
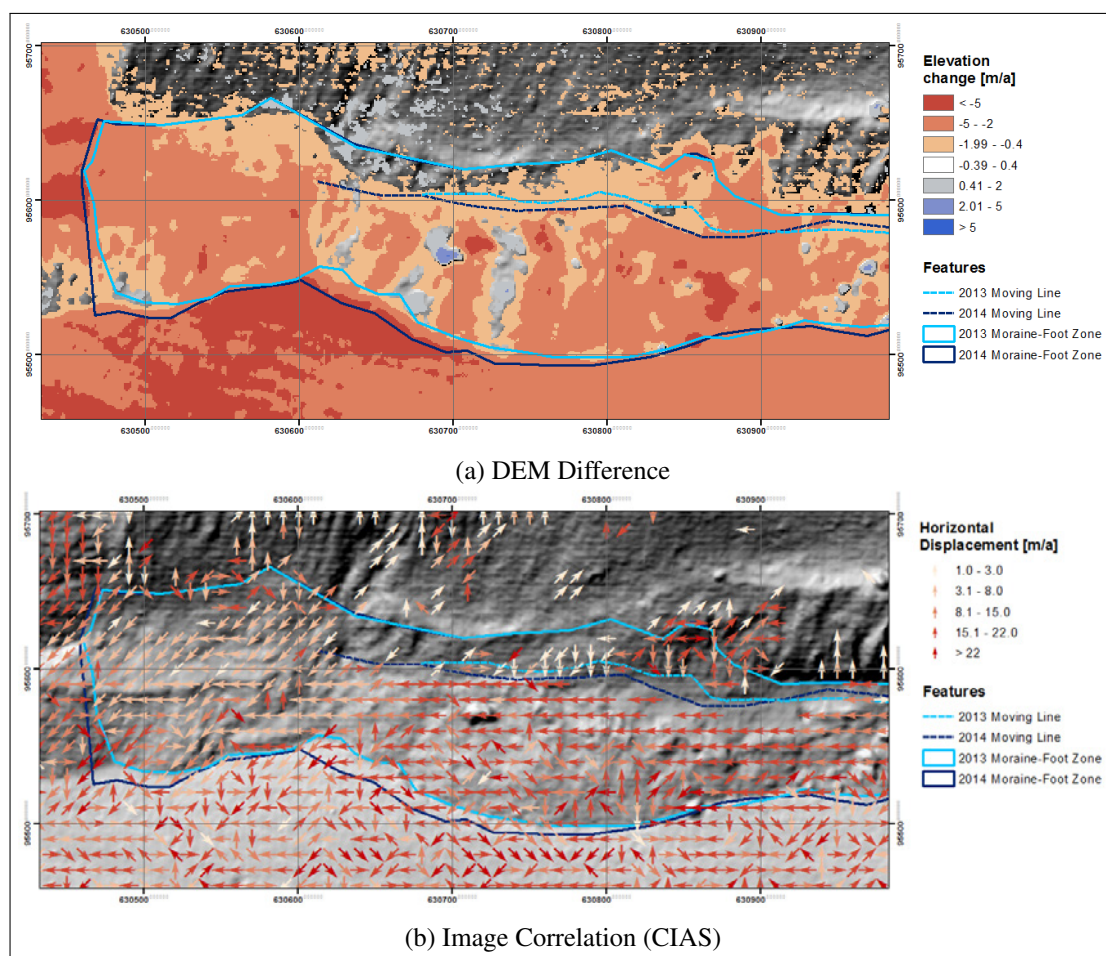

(a) DEM Difference

(b) Image Correlation (CIAS)

Figure 5.39: Moraine-Foot zone up-glacier from the landslide for the observation period 2013 - 2014

Observation Period 2014 - 2015

Regarding the DEM difference (Figure 5.40a) and the image correlation (Figure 5.40b) for the observation period 2014-2015 of the Moraine-Foot zone up-glacier from the landslide one can see that the detected unstable terrain corresponds mostly with each other. The DEM difference shows almost exclusively elevation loss with medium magnitude. The continuously elevation loss is also visible along the Profiles G and H (Figure A.26 & A.27). Further, the large boulder, which is moving, is recognizable again (below 630700/95600). In the image correlation the same pattern as in the observation periods 2009-2010 and 2013-2014 is detectable. On the one hand there is a southwestern displacement with a small magnitude near the Slide-Area and on the other hand there is the west movement of the area between the Moving line and the glacier (bulge) with higher magnitudes. In this observation period the west movement is less dominant than before. At the down-glacier end of the bulge a disturbance (chaotic structure) is observable. This can be caused through a decrease in the western movement, which is supported by the tracked boulders as their magnitude of displacement declines further and the orientation of the movement of one of the boulders turn to southwest.
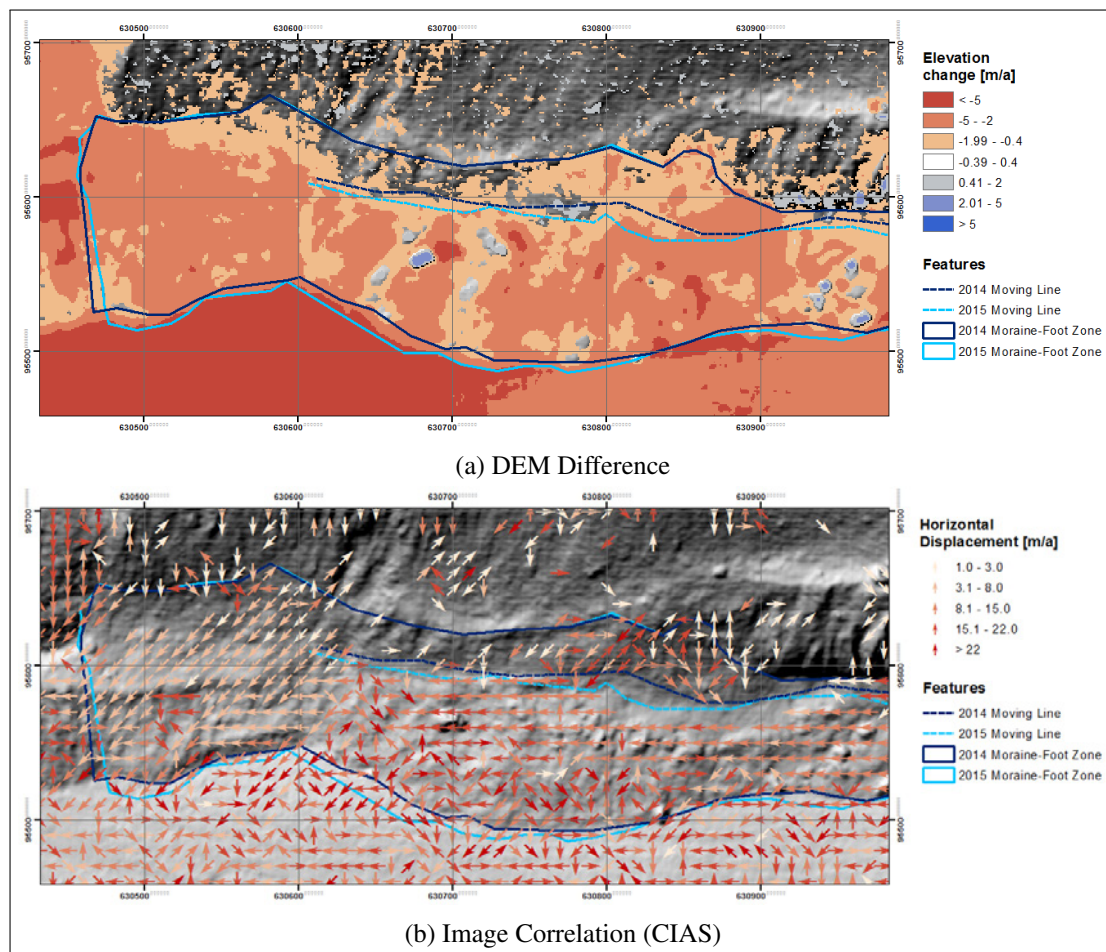

(a) DEM Difference

(b) Image Correlation (CIAS)

Figure 5.40: Moraine-Foot zone up-glacier from the landslide for the observation period 2014 - 2015

Observation Period 2015 - 2017

In the observation period 2015-2017 the classified unstable terrain from the DEM difference and the image correlation corresponds with each other (Figures 5.41a & 5.37b). The DEM difference for this period and area is dominated by elevation loss with medium magnitude, which is also observable along the Profiles G and H (Figure A.26 & A.27). The large boulder is visible as well as in the previous observation periods, but this time the newer position (2017) is marked as stable instead of a positive elevation change (middle of the square right/low of 630600/95600). In the image correlation the pattern from the previous observation periods is only partially recognizable within the last period. This is valid for the southwest displacement near the Slide-Area as well as for the west movement of the bulge. In what way this has a natural cause or originates from the image correlation itself (tends to be more chaotic in the more than one-year periods) is not determinable. However, the magnitude of the tracked boulders also decreases further.
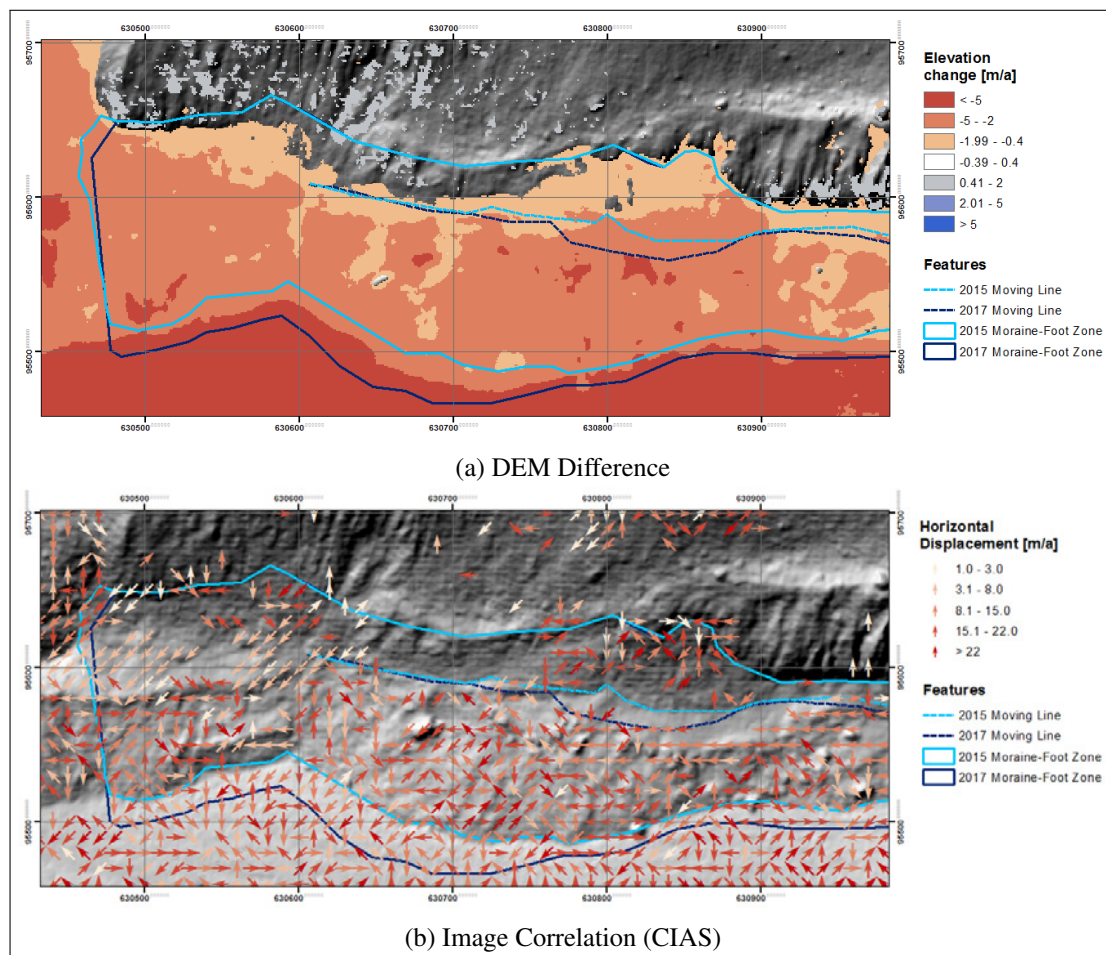

(a) DEM Difference

(b) Image Correlation (CIAS)

Figure 5.41: Moraine-Foot zone up-glacier from the landslide for the observation period 2015 - 2017

5.5.5   Glacier

For the glacier one can summarize the different observation period. In the DEM differences (Figures A.28-A.33) only high elevation loss are detectable in all observation periods. The front of the tongue shows surface lowering higher than -5m/a, whereas the area behind has lower values from -2–5m/a. In the first observation period a mean annual elevation change of -4.71m/a is determined, which increases to -7.1m/a in the last observation period. The highest maximum elevation loss have occurred in the period 2009-2010 with -15.89m/a and the lowest with -7.68m/a in the period 2005-2009. In the image correlation (Figures A.47-A.52) on the one hand a west movement with low to medium magnitudes is observable in the one-year periods (Figure A.53) and on the other hand a chaotic arrangement of the directions and the magnitudes in the other periods.

6. Discussion

6.1 Evolution from 2005 to 2017

Findelengletscher has retreated since the Little Ice Age (maximum around 1850) like most glaciers in the Alps (Fischer et al., 2015; Rastner et al., 2016). In this period its length has decreased about -3.53km until 2010 (Rastner et al., 2016) and another 250m until 2017. The general decrease is interrupted by two periods with thickness gain and advance of the glacier, lastly in the late 1980s (GlaciologicalReports, 2017; Rastner et al., 2016). The glacier recession has left two large lateral moraines, which are now flanking the glacier and his foreland (Joerg et al., 2012; Lukas et al., 2012; Ruff, 2015). According to the presented moraine formation theory of Lukas et al. (2012) (see Section 3.1.3) it is assumed that the moraine is partially containing buried-ice. This is the basis of this master thesis, where the evolution of the glacier and the right lateral moraine since 2005 is scoped.

After the field visiting and the first qualitative sighting of the data three respectively four zones are defined according to which the study area is analyzed. The zones Slide-Area and Mound are linked to the first research question, whereas the zones Glacier and Moraine-Foot zone contributes to the second research question. In the following the changes of the zones and within the zones are discussed on the basis of the applied methods. Afterwards, the findings are summarized.

6.1.1 Evolution of the Landslide (Slide-Area)

Within the first observation periods the occurrence of the landslide can be detected visually in the shaded reliefs as well as in the DEM differences and the image correlation. The released material does not suddenly moves downslope, it is more a sliding down from year to year. This slowly sliding is observable visually in the shaded reliefs as well as in the DEM Differences. The qualitative evaluation of the shaded reliefs and pictures show that the whole landslide body consists of two parts, which can be differentiated according to their color. Thereby, is the movement of the 'brown' material (hillsope material) a bit faster than the one of the 'grey' material (moraine material), which results in the brown material rolling on the grey during the observation periods. The material between the down-sliding landslide and the glacier is blocked by the glacier, which leads to the compression and uplifting of the area, visible through an elevation gain in the period 2009-2010. Afterwards the material gets pushed on the glacier leading to the formation of the Mound firstly visible in 2013. In what way it is a pushing on the glacier or just the retreat of the glacier leading to this feature, is not clearly determinable with the available data. However, it can be assumed that the formation of the mound is caused by both processes. In the same manner it cannot be explained how the channel is formatted and why it is persistent over the time.

Within the release area of the landslide a stabilization with time is recognizable visually in the shaded reliefs as well as in the DEM Differences and the image correlation. In the last observation period (2015-2017) only the part below the former moraine-top is still active. In some parts the moraine material got eroded down to the bedrock, especially in the Eastern part of the landslide (Figure 3.8). Further, one can see a decrease in the magnitude of the movement after 2014 detectable in the elevation change as well as in the image correlation. The dominant direction of the determined (horizontal) displacements is southwest or south, which seems reasonable as the moraine flank and the hillslopes are exposed in those directions.

The determination of a reasonable sediment budget for the landslide is very difficult as the extent of the area is changing with time and due to ice-containment of the moraine, which leads to elevation loss through ice melting. The most total moving volume is observed for the period 2009-2010 with almost 88'000m^3/a, whereas it is the lowest for the first observation period with almost 47'00m^3/a. For the first two observation period the volume loss and the volume gain are at the same level (59%:41% and 70%:30%) comparing with the further observation periods, where 97% of the total volume is a volume loss.

In the recently deglaciated area of the grosser Aletschgletscher (also Canton Wallis Switzerland) a landslide is under surveillance, which was triggered by the glacier retreat and the resulting debuttressing. There the whole rock flank, on which the LIA moraine lies, is moving. The estimated volume of the active landslide is several magnitudes larger than the small landslide at the Findelengletscher (Kos et al., 2016), but it shows the possible dimension of instabilities in recently deglaciated areas.

Landslides, which break through the lateral moraine or sediments overspilling are important regarding the sediment budget and cascade in a proglacial landscape (Carrivick and Heckmann, 2017; Cossart and Fort, 2008). The moraine acts as a barrier for the sediments, which are eroded and accumulated behind it. The breaching of the moraine leads to a sudden input of a large amount of sediments (Figure 2.6) (Cossart and Fort, 2008). In this context, small landslide can have a major impact on the sediment transfer into the proglacial area, from where debris flows and other hazards can originate.

6.1.2 Evolution of the Mound

The Mound is firstly recognizable in the shaded relief of 2013. In the following it moves towards the glacier middle continuously. On the one hand through the pushing of the landslide and on the other hand through the retreating of the glacier. Since his formation it can be delimited from the landslide by a channel. Along the Profiles a maximum total shift of 30m from 2013 to 2017 of the channel/mound is observed. According to this shift the DEM differences have to be analyzed with caution because elevation changes are caused by surface changes through melting as well as through the shifting of the surface. However, in Figures 5.13-5.15, which show the elevation along the Profiles C-E corrected for the shift, one can see that surface lowering caused by ice melting occur. The melt rates increases with time ranging from roughly -3m/a for the period 2013-2014 to roughly -5m/a for the period 2015-2017. Compared with the glacier the melting on the Mound is smaller, which seems reasonable due to the debris cover (Benn and Evans, 2010; Nicholson and Benn, 2006).

The field work in summer 2017 confirmed the first assumption that the mound consist of ice. Whether it is a mixture of ice and debris or an ice body with debris cover could not be determined and was not

part of this thesis. With the digging at selected locations debris thickness from 10cm to at least 50cm are detected. The field visiting also showed that at the slope towards the channel clean ice is exposed and forms ice cliffs (Figure A.1). Such ice cliffs are a major source of ice loss on debris covered glaciers (Benn et al., 2012; Pellicciotti et al., 2015). This can explain the high negative elevation change in this area. According to the field visits (Figure A.3) the Mound looks somehow like a small-scale hummocky moraine with the moundy and irregular topography (Benn and Evans, 2010). Also showing typical phenomena for ice-cored moraines like the fall sorting or the building of sinkholes (Kjær and Krüger, 2001; Schomacker, 2008).

The Mound moves in a western and southwestern direction, which seems reasonable comparing with the digitalized outlines of the different years and the tracking of large boulders. The image correlation shows a decrease in the magnitude of the movement with time, whereas the tracked boulders indicate an increase in the displacement (from 13m/a to 22m/a).

6.1.3   Evolution of the Moraine

Visually, the right lateral moraine is signed by intense gullying in the upper part and by debris deposits in the lower part (Moraine-Foot zone). This pattern is typical for paraglacial re-working as reported by various studies (Ballantyne, 2002; Ballantyne and Benn, 1994; Curry et al., 2006) and makes it possible to divid the moraine in a top and foot zone. The conducted analyses show that the top zone (gullies) is stable over the short time scale of this study, which suggest that the evolution of the gullying occurs on a longer time scale. Schiefer and Gilbert (2007) investigated the morphodynamic of a proglacial landscape in British Colombia (Canada) from 1947 to 1997. They also identified the gullying as the most noticeable change, but additionally mention short-time events like the occurrence of some small, discrete landslides and the transition of ice-cored moraines to kettle features.

The observed small elevation loss and horizontal displacement in the moraine-foot zone down-glacier from the landslide can be explained by the continuous melting of the buried-ice beneath the debris. Lukas et al. (2012) reported the occurrence of such buried-ice within this area. The extent of it can be estimated from the down sliding of the debris on the ice-debris horizon, which sometimes exposes the buried-ice (Bennett and Evans, 2012; Lukas et al., 2012). Such small slides are also observable during the observation period of this thesis. Such slides causes the accumulation of debris at the base of the sidewalls (Lane et al., 2017). If no buried-ice would be present, this leads to the reduction of the slope at the base as it is reported for the paraglacial re-working by Curry et al. (2006) or Ballantyne and Benn (1994). The retreat of the unstable terrain with the glacier retreat also suggest that the observed movements are mainly caused by the melt of the buried-ice. Further, the magnitude of the horizontal displacements are in the same range as the one for creeping ice-features like rockglaciers (Kääb, 2002).

In the Moraine-Foot zone up-glacier from the landslide the qualitative analyses showed a line (Moving Line) dividing somehow this zone. The quantitative analyses confirm this observation partially. Within the DEM difference the line is not recognizable, whereas it is in the image correlation. Especially, in the one-year time periods one can see that the area between the glacier margin and the Moving Line shows a distinct western movement, so the same direction as the glacier. The tracking of some large boulders confirm this mainly west-orientation of the horizontal movement. However, in the result from the tracked boulders a downslope movement towards the glacier (southwest) can also be detected. This

probably origins from the higher spatial resolution of the shaded relief (1m) compared to the image correlation (10m). This west movement can be explained when assuming that under the debris in this area is still active glacier ice causing the formation of a debris cover glacier part. In the last two observation periods this west movement is not that dominant anymore, especially towards the landslide, which suggest a decrease in the glacier flow (see Section 6.1.4). Further, the magnitude of the west movement decreases towards the Slide-Area/Mound in all the one-year time periods. Probably the landslide interferes the west movement causing a slowing down through the more weight.

For future studies it can be interesting to track evolution of this debris covered glacier part to catch the moment it stagnates and may transform to an ice-cored moraine deposit as observed down-glacier from the landslide. Further, one can look in the past and investigate if such a debris covered glacier part once already exist along the lateral moraine.

As already mentioned above, the lateral moraine acts as a barrier for the sediments eroded and accumulated behind it. The overspilling or breaching of the moraine lead to a sudden input of a large amount of sediments into the proglacial area (Figure 2.6) (Cossart and Fort, 2008). The deposits of such events can dam the proglacial streams causing the proglacial lakes vulnerable to a sudden outburst. This represents a great danger for settlements and infrastructure down-valley from the proglacial area (Kos et al., 2016).

6.1.4   Evolution of the Glacier

When looking only at the evolution of the glacier the most obvious change is the shrinking of the glaciated area (Figure 5.5). Between 2005 and 2017 a retreat of 500m in length and one of 200m in width was observable.

The annual elevation change determined by the difference between the different DEMs can be compared with the measured elevation change at an ablation stake. Stake 6 (Figure 4.1) belong to the measurement network of the Findelengletscher and as such the ablation/elevation change have been determined for each year. To compare these measurements with the DEM differences one have to calculate the mean for the non one-year periods (Table A.1 in the Appendix). Figure 6.1 shows the comparison of the measured and the calculated annual elevation change. One can see that for the observation periods 2005-2009, 2013-2014 and 2015-2017 the annual elevation change calculated with the DEM difference is bigger (more negative) than the measured melting at the stake. The differences between the two methods range from 0.56 to 1.77m/a for those periods. For the other observation periods (2009-2010, 2010-2013 and 2014-2015) the melting at the stake is bigger than the elevation loss determined through the DEM difference. For those periods the difference between the methods span from 1.94 to 2.64m/a, which is a bit bigger than for the other way around. The highest melting/elevation loss is determined at the stake in the period 2014-2015 with -8.04m/a, the smallest melting/elevation loss is measured also at the stake in the period 2005-2009 with -3.05m/a. With the DEM difference the biggest elevation loss is observable for the period 2015-2017 with -7.5m/a and the smallest for the period 2009-2010 with -4m/a. The difference between both methods lies in the generation method. The surface of a glacier changes due to mass loss or gain (ablation/accumulation) and because of the glacier dynamics (glacier motion). The first refers to the ablation rate and the second to the rate at which ice is refilled from up-glacier. With the geodetic method (DEM differences) the mass change (surface, internal and basal) is determined, whereas

the glaciological method examines the surface mass change and the glacier dynamic (Bennett and Evans, 2012; Cuffey and Paterson, 2010; Fischer et al., 2011). Therefore, either internal or basal volume loss occurs or the glacier dynamic (flow) varies within the different observation periods.

Regarding the horizontal movements determined by the image correlation no trend in the magnitude of the detected displacements is visible, but a distinct western direction of the displacements is recognizable. A surface velocity around 15m/a seems in a reasonable range as Cuffey and Paterson (2010) report a surface velocity of 15m/a for the Storglaciären (Mountain Glacier in Sweden). Rossini et al. (2018) investigated the glacier tongue of the Morteratschgletscher with an UAV and found flow velocities up to 8m for a three month observation period.
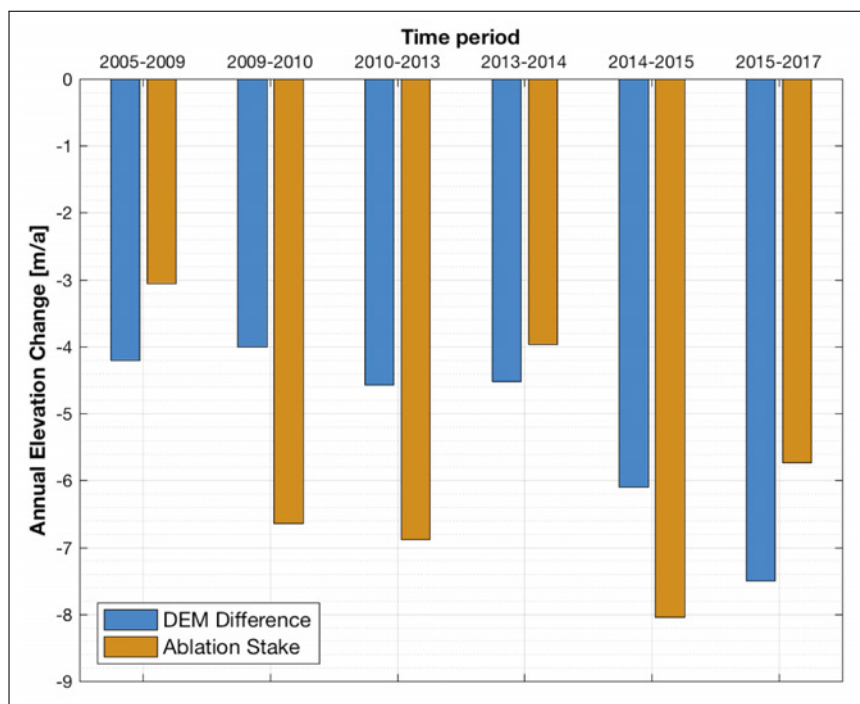
Figure 6.1: Comparison between the annual melting/elevation change at the location of stake 6

6.1.5 Synthesis

On the basis of the above discussed results it is reasonable to partially revise the in advance defined zones. On the one hand the observed patterns within the zones landslide (Slide-Area), glacier and mound are consistent, whereas on the other hand the moraine-foot zone shows different changing regimes. Therefore, the moraine-foot zone is divided into three Zones (A-C). The rest of the moraine (the top with the gullies) is Zone D (Figure 6.2).

The Glacier is the clean-ice body, which is characterized by a continuous shrinking visible through the loss in length and width as well as in the DEM differences. The direction of the horizontal movement is west. The Landslide is spatial detectable by his scar and deposition. His evolution is a continuous down-sliding towards the glacier. The lower part is still active, whereas the upper part has been stabilized after a few years. The formation of the Mound is caused by the down-sliding of the landslide and by the retreat of the glacier. It consist of ice and debris. Among some ice cliffs towards the landslide,

the Mound is completely debris covered. Therefore, the highest surface lowering occurs at the location of those ice cliffs. The Moraine is divided into the Zones A to D. The Zone A represents areas with dead-ice beneath the moraine material. The exact extent is hard to determine, which is indicated by the dashed line. The zone shows continuous elevation loss with higher magnitudes towards the glacier. In the horizontal movement one can see small displacements down the slope. Sometimes, this pattern is interrupted by some very small landslides released from Zone B or D. Zone B shows surface changes originating from the down falling or rolling of debris due to gravity on the one hand and on the other hand the outwashed material from Zone D is partially deposited in it. The Zone C represents a debris-covered part of the glacier. The horizontal movements go along with the glacier in western direction with speeds ranging from 3m/a to 22m/a. Further, a continuous surface lowering is detected with smaller magnitudes than on the glacier. The Zone D contains the steep gullies, which incise this upper part of the moraine. Over the time-scale of this thesis this zone is more or less stable.
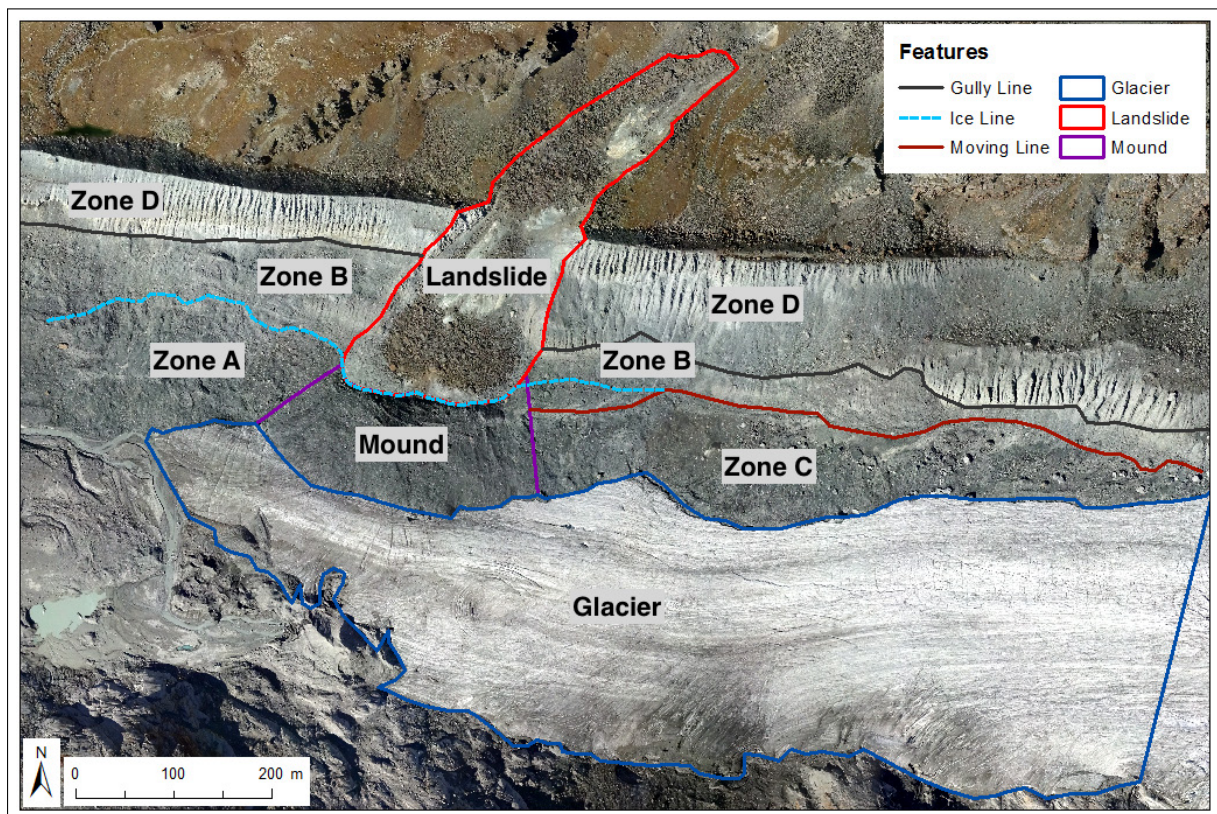
Figure 6.2: Classification of the study area according to the patterns in the performed analyses (Background: orthophoto 2017)

6.2   Evolution in 2017 (RQ3)

For answering research question 3 about the short-time evolution of the glacier-landslide system, the installed ablation stakes are considered. On one hand the ablation on the mound and on the glacier is conducted and on the other hand the stakes on the mound are measured with the dGPS to determine their movement within the field campaign period (13th July and 21st September 2017).

6.2.1   Melting

The ablation measurements show a clear difference between the melting on the mound (melting beneath a debris cover) and the melting on the glacier (bare ice). Over the whole field campaign (70 days) the melting get reduced up to 78% (30cm debris cover) towards the melting on the bare ice. At a debris cover of 15cm the melt decreases to the half towards the melt on the bare ice. At the same debris thickness the higher melting rates are measured at the stake on the mound top towards the one on the flank. On the bare ice a melt of 4.05m is determined for the three month period (July-September). Rossini et al. (2018) investigated the Morteratschgletscher also for a three month period (July-September) in 2016 and detected a mean melt of 4.1m.

Regarding the two time periods (13th Jul - 23rd Aug & 23rd Aug - 21st Sept) one can see that the melting rates for the first observation period are higher for all ablation stakes. This can be explained on the one hand by the longer time span, but also the air temperature is higher during this period, which favors melting. The mean air temperature between the 13th July and the 23rd August is 8.97°C versus 4.83°C for the second period (23rd Aug - 21st Sept).

Comparing the measured melting (Table 5.1) with the elevation difference measured with the dGPS (Table 5.3) the similar trend with the highest elevation loss/melting at Stake 1 and the smallest at Stake 3 is measured. This correlates with the debris thickness at the stake locations (Figure 6.3). For Stake 4 the measured melting is higher than the elevation lowering by measured with the dGPS, wheres it is the other way around for the other Stakes. The differences between the dGPS and the Stakes vary from 0.32m (Stake 1) to 0.68m (Stake 3), which can originate from measurement uncertainties. Probably mostly through tilting of the ablation stake as the biggest difference occurred at the Stake, which was tilted the most.

Figure 6.3 shows the relation between the observed melting over the whole measurement period and the debris thickness at the stakes together with a theoretical relation between melting and debris cover and a potential curve fitting to the measurements at the debris covered stakes. In theory the melt under a debris cover is indirectly proportional to debris thickness with the product of the temperature gradient and thermal conductivity determining the numerator of the fraction (see Section 2.1.4, Equation 2.8) (Nicholson and Benn, 2006). For the data in this thesis the best fitting value for this product is 0.35, which is shown as the dotted line in Figure 6.3. This value is found experimentally.
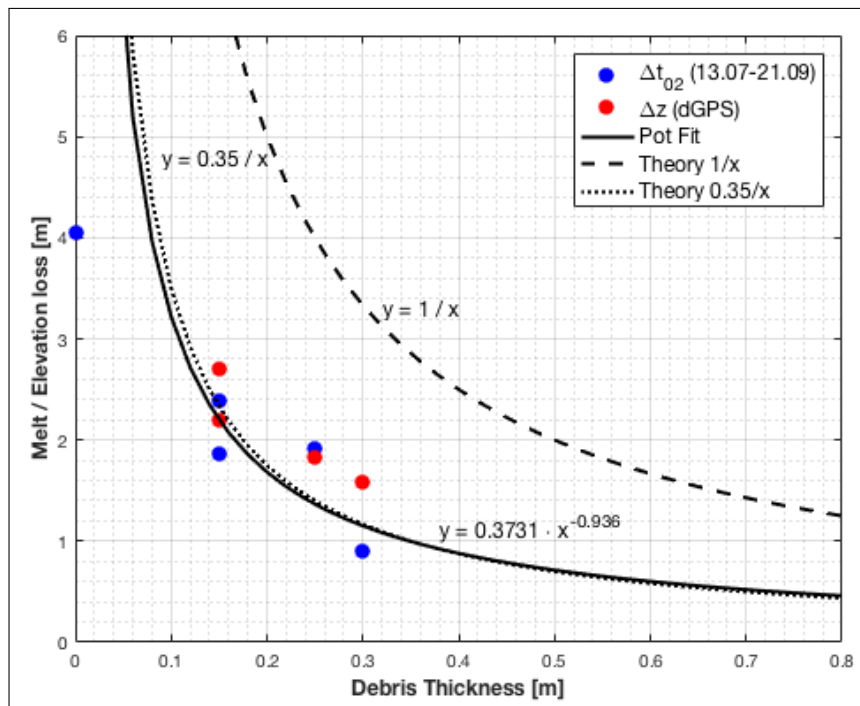
Figure 6.3: Relation between the Debris Thickness and the measured Melting (blue dots) over the whole observation period with the theoretical curve (dotted & dashed) and a potential fitting (the measurement on bare-ice is excluded from the fitting). Red dots represent the elevation loss measured with the dGPS

At the study site of Findelengletscher no ablation measurements beneath a debris cover have been yet measured, this means no comparison with other data is possible. Nevertheless, it is possible to compare the melting on the bare ice for the field campaign with measurement within the past years at Stake 6 (Part of the Findelengletscher measurement network). Therefore, ablation measurements at Stake 6 over the summer are extracted from the network data and are shown in Table 6.1. Observation periods with at least 50 days are considered and the melt per day is calculated in order to compare the data. It

Year	Days	Melt [m]	Melt/Day [m/d]
2007	65	-2.28	-0.035
2008	77	-3.10	-0.040
2009	54	-2.84	-0.053
2016	52	-3.37	-0.065
*2017	70	-4.05	-0.058

Table 6.1: Summer-Melt at Stake 6 over the similar time period for other years (*Measured at Stake 5))

is visible that the measurement from this summer are in the same range (melt per day) as in the years 2014 and 2016 and as such a bit higher than in the years 2007 and 2008. This indicates the evolution towards higher melting rates.

6.2.2 Movement

The measurements with the dGPS (on the 13th July and 21st September) showed a western or southwestern movement of the stakes. Within the horizontal displacement no trend with location of the stake or the debris thickness is detectable, whereas a the vertical displacement is smaller with thicker debris cover (Table 5.3).

6.3   Uncertainty Assessment and Suitability of the Methods

6.3.1   Uncertainty Assessment

Digital Elevation Models

The uncertainties within the DEMs used in this study are described by the mean elevation difference MED (systematic uncertainty), the standard deviation STDV (stochastic uncertainty) and the standard error SE (stochastic uncertainty) over stable terrain. The systematic uncertainty is further described by the residual shift vectors after the co-registration (Bolch et al., 2011; Rastner et al., 2016; Zemp et al., 2013).

The analysis of the systematic uncertainties show a maximum systematic error smaller than plus/minus 0.5m for the MED as well as for the residual shift vectors (-0.45m MED and -0.49m shift vectors; Table 5.5). For the period 2015-2017 the shift vectors are higher than plus/minus 0.5m, therefore the DEM from 2017 has been shifted according to the determined shift vectors. After iteration 4 a sufficient accuracy has been achieved. Among the period 2015-2017 the systematic errors are not corrected as they are clearly smaller than the pixel size.

The stochastic uncertainties are described by the standard deviation and the standard error. The STDV over stable terrain ranges from 0.23 to 0.59m and the SE from 0.01 to 0.03m (Table 5.5). For the calculation of the standard error a threshold distance of 10m is used, where the autocorrelation gets insignificant (Bossard, 2014). Koblet et al. (2010) on the other hand used a threshold distance of 100m, which would result in a magnitude higher standard error values as determined in this thesis. This suggest that the stochastic uncertainties are underestimated with the SE. On the other hand the STDV leads to an overestimation because it does not take the averaging over large-scale area into account (Berthier et al., 2007; Bossard, 2014). Therefore, it has to be assumed that the stochastic uncertainty lies between the values of the SE and the STDV.

Image Correlation

The image correlation (CIAS) is performed with the shaded reliefs derived from the DEMs. Therefore, the uncertainties in the image correlation originate from the DEMs (shaded reliefs) itself and the quality of the image correlation. The applied image correlation is suitable to detect horizontal displacements in range of the pixel size of the input data (Debella-Gilo and Kääb, 2011; Kääb, 2002; Kääb and Vollmer, 2000). The challenge by applying the image correlation is to find the parameter settings that are able to find matches on smooth terrain (glacier and vegetated areas) as well as on rough terrain (moraine). To assess the quality of the determined horizontal movements the Signal-to-Noise ration (SNR) is calculated as the ration between the maximum correlation and the average correlation. The SNR-values are classified into three groups (insufficient, sufficient and good) and are graphically shown in Figures A.41-A.46.

6.3.2 Suitability of the methods

In this section the applied methodological approach is discussed by looking at the potentials and limitations of the used methods. Further, the problems and potential improvements for this particular study are addressed.

Digital Elevation Models (DEMs)

Multi-temporal DEMs are commonly used to study landform changes, especially in glacial and periglacial systems (Abermann et al., 2010; Fischer et al., 2011; Müller et al., 2014b). DEMs can be generated with a variety of techniques like laser scanning or photogrammetry. Each generation method has his advantages and disadvantages, which will not be discussed in this thesis as more the application of the DEMs is scoped. In order to compare different DEMs with each other they have to be aligned to each other (Co-Registration). In this thesis the method introduced by Nuth and Kääb (2011) is applied. However, the application of the co-registration shows some limits. Firstly, only one (geo-location of the data) of the three potential biases over stable terrain identified by Nuth and Kääb (2011) is determined with in this thesis, whereas the other two biases are not investigated (elevation dependent and sensor specific biases). Further, the applied co-registration method cannot correct non-linear tilts between the DEMs. Secondly, the result of the co-registration strongly depends on the definition of the stable terrain. Ideally, it should be equally distributed over the study area, including different aspects and the slope should be steeper than 5° (Nuth and Kääb, 2011; Rastner, 2015). However, it has been difficult to fulfill this conditions because of the limited stable terrain as the investigation area is quite small and dominated by two aspect directions. The applied co-registration show no need for correcting shifts except for the period 2015-2017 (Table 5.4, Section 5.2.2). However, when looking at the DEM differences (Figures A.28-A.33, Appendix) one can see that in the periods 2013-2014 and 2014-2015 unusual areas (compared with the other observation periods) are classified as unstable. The observed pattern implies that the data of 2014 are the reason for it. Therefore, the DEM difference between 2013 and 2015 (Figure A.34) is considered here to confirm this. In this period those areas are classified as stable, which means that the data of 2014 are the reason for this pattern. Regarding the systematic uncertainties for the period 2014-2015 one can see that the mean annual elevation difference (MED) as well as the residual shifts (Δy and $\overline{dh}$) are quite high, only the periods 2005-2015 and 2015-2017 show higher values. This implies that the accuracy of the DEM difference 2014-2015 is not that good as the one for 2013-2015, which shows smaller values.

Furthermore, some limitations interpreting DEM differences can occur especially in proglacial areas. Detected elevation changes can either be caused by erosion/deposition, horizontal shifts or degradation/aggradation of ice. Additionally, those processes can overlay each other, which makes it even harder to identify geomorphological processes from DEM differences. Especially for calculating sediment budgets these leads to problems (Carrivick and Heckmann, 2017; Ruff, 2015). One possibility to address for these problems is to classify the DEM Difference with the local or focal standard deviation. Theoretically, ice melt should be dividable from erosion through a homogeneous pattern (Carrivick and Heckmann, 2017).

Image Correlation (CIAS)

The image correlation Software CIAS provides a user-friendly opportunity to determine horizontal movements from grey-scale orthoimages or shaded reliefs. The software has been applied to a variety of fea-

tures like glaciers, rockglaciers and landslides (Kääb, 2002). With CIAS horizontal displacements with in range of the pixel size of the input data are detectable, whereas for sub-pixel other algorithms should be used. The accuracy of image correlation does not depend on the precision of the applied algorithm, but mainly on the terrain properties on which the algorithm is used (Kääb, 2002; Kääb and Vollmer, 2000). The parameters of the image correlation (reference block, test area size and grid size) have to be chosen according to the expected maximum shift and the characteristics of the surface. The last-mentioned is challenging in this study as the surface of the area of interest consist of smooth terrain (glacier and vegetated areas) as well as rough terrain (moraine, debris). To improve the input data some filters can be applied in advance for a better contrast in the shaded reliefs (Kääb, 2002; Kääb and Vollmer, 2000).

During the analyses of the DEM differences and the image correlation a difference between the laser data (2005, 2009 and 2010) and the photogrammetry data (2013, 2014, 2015 and 2017) are observable. The laser data show less noise in the to be considered stable terrain on the hillslopes compared with the photogrammetry data. This can originate from shadow effects during the acquiring of the (aerial) photos or from the coarser resolution of the aerial photos than the laser point cloud (Kääb, 2005a; Müller et al., 2014b)

7. Conclusion and Outlook

7.1 Conclusion

This Master's thesis investigated the evolution of a moraine-breaching landslide in the recently deglaciated area of the Findelengletscher. The aim was describe and quantify the evolution of the landslide and the one of the glacier and the moraine in relation to the landslide. To achieve these goals a multi-temporal Digital Elevation Models (DEMs) with a resolution of one meter were used. The uncertainty assessment showed that the systematic and stochastic uncertainties are in the subpixel range, which enables the study of such a small scale area. Further, the melting rates between from the landslide affected glacier part and the bare glacier are compared with each other over one summer. Therefore, some glaciological field measurements were conducted during this time period.

RQ1: How is the evolution of the landslide since the occurrence?
The landslide is firstly recognizable in 2009. The active part of the landslide is clearly visible within the DEM difference as well as within the image correlation for each observation period. The movement of the landslide body is a continuous down-sliding towards the glacier. After the initial release, the upper part of the landslide area has been stabilized, whereas the lower part is still active. However, the horizontal and vertical displacements have decreased with time. The maximal vertical as well as the maximal horizontal change are detected between 2009 and 2010 with -10m/a respectively 33m/a.

Since 2013 a mound between the glacier and the landslide is visible. In the following years he gets shifted towards the glacier middle continuously. Along the profiles a maximum total shift of the channel of 30m from 2013 until 2017 can be observed. The surface lowering on the mound is increasing during the observation periods to around 5.5m/a in the last period, which is less than on the glacier. The difference in the elevation loss leads to height gain of the mound towards the glacier of 3-5m from 2013 to 2017. The highest elevation loss occurs, where clean ice (ice cliffs) are visible. Regarding the horizontal movements the mound is displaced in west and southwest direction with small or medium magnitudes (3.1-15m/a). In contrast to the surface lowering is the magnitude of the horizontal displacement decreasing with time.

RQ2: How is the evolution of the glacier and the moraine in relation to the landslide?
The extent of the glacier is good detectable in the DEM differences as zone with medium to high elevation loss (>-2m/a), whereby the frontal part shows the highest surface lowering. From 2005 to 2017 the glacier have retreated about 500m and have lost about 200m of his width. On the glacier tongue mean elevation change is declining from -4.71m/a towards -7.10m/a from 2005 to 2017.

The lateral moraine can be divided into two zones: a top zone (gullies) and a foot zone (zone between gullies and glacier). First-mentioned is not investigate as the initial analyses showed no or only small changes over the covered observation periods, whereas the foot zone evolve during this time. In the Moraine-Foot zone down-glacier from the landslide the unstable area is retreating with the glacier. The extent of the unstable area detected by the DEM differences correspond with the image correlation. Both methods show a continuous surface lowering respectively down sliding/creeping. The elevation loss is higher in the lower part near the glacier due to the melting of dead-ice. In the Moraine-Foot zone up-glacier from the landslide the qualitative analyses showed a line (Moving Line) dividing somehow this zone. In the image correlation one can see that this line corresponds with the extent of the westwards movement of the lower part of the moraine-foot zone. This implies that the underlying ice is still connected with the glacier and flows with it. Between the Moving line and the upper extent of the Moving-Foot zone the similar evolution as down-glacier from the landslide are observable. The western movement of the bulge is decreasing during the observation periods starting with more than 20m/a for the period 2009-2010 declining to 13m/a for the last period.

RQ3: How does the landslide affect the glacier in relation to melting and moving?
During the field campaign (13th July - 21st September) the ablation on the mound and on the glacier have been measured with ablation stakes. On the glacier a melt of 4.05m is determined, whereas the melt on the mound is reduced due to the debris cover. A debris cover of 15-25cm thickness leads to half of the melt compared with the one on bare ice. For a debris thickness of 30cm a reduction of 78% have been observed. Further, the position of the ablation stakes on the mound are measured with the dGPS in the beginning and in the end of the field campaign. The results show a southwest or west orientation of the movement with magnitudes ranging from 1.92 to 2.26m. Within the horizontal movement no trend with the debris thickness is observable.

This study showed the usability of multi-temporal DEMs to investigate geomorphological changes. The good data coverage of the investigation area made it possible to follow the evolution of the landslide, the lateral moraine and the glacier. However, while working with the remote sensing data, the conducted fieldwork and sighting of the area helped to understand the observed patterns.

The on-going glacier recession leave a landscape of unconsolidated glacial sediments vulnerable to be re-worked by geomorphological processes. The a sudden, down-stream evacuation of those sediments can be dangerous for settlements and other infrastructure. Therefore, it is important to understand the evolution and the included processes within such recently deglaciated areas. Until today only little is known about the evolution of the lateral moraines and the hillslopes of those landscapes, most of the proglacial studies focused on the proglacial stream network as this evacuates the sediments. However, Cossart and Fort (2008) and Carrivick and Heckmann (2017) showed that the connectivity of the stream network with the hillslopes is also important to determine sediment budgets and cascades.

7.2 Outlook

This study opens the possibilities for further research. First of all one could continue to track the evolution of the identified features, which is possible if the good data coverage of the Findelengletscher goes on. Especially, the future of the mound seems to be an interesting question. Regarding the ice content of the mound and the moraine some Ground-Penetrating radar investigations might bring some clearance to the extent and thickness of it. Concerning the evolution of the glacier it will be interesting to see if the glacier tongue collapse at a certain point in time as a depression in the glacier surface on the left side was observable in 2017. Further, it would be interesting to see how the evolution of the mound changed the hydrological system of the glacier.

In a broader spectrum it would be interesting to compare the evolution of Findelengletscher surrounding with the evolution around other glaciers. With the on-going climate change glaciers will further retreat and exposing new landscapes. According to the hazard potential of those areas it is crucial to assess their stability and evolution to may estimate the hazard potential for settlements and infrastructure. Recording and quantifying is the starting point to may be able to model and predict the evolution of those landscapes.

Bibliography

Abermann, J., Fischer, A., Lambrecht, A., and Geist, T., (2010). On the potential of very high-resolution repeat DEMs in glacial and periglacial environments. *Cryosphere*, 4(1):53–65.

Agisoft LLC. Agisoft PhotoScan Pro, (2018). Available at: `http://www.agisoft.com`. [Accessed on: 2018-04-05].

Albertz, J., (2009). *Einführung in die Fernerkundung. Grundlagen der Interpretation von Luftbildern und Satellitenbildern*. Wissenschaftliche Buchgesellschaft (WBG), Darmstadt, 4th edition.

Ballantyne, C. K., (2002). Paraglacial geomorphology. *Quaternary Science Reviews*, 21(18-19):1935–2017.

Ballantyne, C. K., (2003). Paraglacial Landsystems. In Evans, D. J., editor, *Glacial Landsystems*, chapter Chapter 17, pages 432–461. Arnold, London.

Ballantyne, C. K. and Benn, D. I., (1994). Paraglacial Slope Adjustment and Resedimentation Following Recent Glacier Retreat, Fabergstolsdalen, Norway. *Arctic and Alpine Research*, 26(3):255–269.

Benn, D. I. and Evans, D. J., (2010). *Glaciers and Glaciation*. Hodder Education, Oxon, 2nd edition.

Benn, D. I., Kirkbride, M. P., Owen, L. A., and Brazier, V., (2003). Glaciated Valley Landsystems. In Evans, D. J., editor, *Glacial Landsystems*, chapter Chapter 15, pages 372–406. Arnold, London.

Benn, D. I., Bolch, T., Hands, K., Gulley, J., Luckman, A., Nicholson, L. I., Quincey, D., Thompson, S., Toumi, R., and Wiseman, S., (2012). Response of debris-covered glaciers in the Mount Everest region to recent warming, and implications for outburst flood hazards. *Earth-Science Reviews*, 114 (1-2):156–174.

Bennett, G. L. and Evans, D. J., (2012). Glacier retreat and landform production on an overdeepened glacier foreland: The debris-charged glacial landsystem at Kvíárjökull, Iceland. *Earth Surface Processes and Landforms*, 37(15):1584–1602.

Berthier, E., Arnaud, Y., Kumar, R., Ahmad, S., Wagnon, P., and Chevallier, P., (2007). Remote sensing estimates of glacier mass balances in the Himachal Pradesh (Western Himalaya, India). *Remote Sensing of Environment*, 108(3):327–338.

Blair, R., (1994). Moraine and Valley Wall Collapse due to Rapid Deglaciation in Mount Cook National Park , New Zealand. *Mountain Research and Development*, 14(4):347–358.

Bolch, T., Pieczonka, T., and Benn, D. I., (2011). Multi-decadal mass loss of glaciers in the Everest area (Nepal Himalaya) derived from stereo imagery. *Cryosphere*, 5(2):349–358.

Bossard, T., (2014). *Evaluation of swissALTI 3D with airborne laser scanning data for applications in glaciology. Master's thesis.* Master's thesis, University of Zurich.

Burrough, P. A. and McDonnell, R., (2005). *Principles of Geographical Information Systems.* Oxford University Press, Oxford.

Carrivick, J. L. and Heckmann, T., (2017). Short-term geomorphological evolution of proglacial systems. *Geomorphology*, 287:3–28.

Church, M. and Ryder, J., (1972). Paraglacial sedimentation: a consideration of fluvial processes conditioned by glaciation. *Geological Society of America*, 83:3059–3071.

Cogley, J., Hock, R., Rasmussen, L., Arendt, A., Bauder, A., Braithwaite, R., Jansson, P., Kaser, G., Möller, M., Nicholson, L., and Zemp, M., (2011). Glossary of Glacier Mass Balance and Associated Terminology. In *IACS Contribution No.2 UNESCO-IHP Paris*, volume 86, page 114, (2011). Available at: `unesdoc.unesco.org/images/0019/001925/192525e.pdf`.

Cossart, E. and Fort, M., (2008). Sediment release and storage in early deglaciated areas: Towards an application of the exhaustion model from the case of Massif des Écrins (French Alps) since the Little Ice Age. *Norsk Geografisk Tidsskrift*, 62(2):115–131.

Cuffey, K. M. and Paterson, W., (2010). *The Physics of Glaciers.* Elsevier Ltd, 4th edition.

Curry, A. M., Cleasby, V., and Zukowskyj, P., (2006). Paraglacial response of steep, sediment-mantled slopes to post-'Little Ice Age' glacier recession in the central Swiss Alps. *Journal of Quaternary Science*, 21(3):211–225.

Debella-Gilo, M. and Kääb, A., (2011). Sub-pixel precision image matching for measuring surface displacements on mass movements using normalized cross-correlation. *Remote Sensing of Environment*.

Deems, J. S. and Painter, T. H., (2006). Lidar measurements of snow depth: accuracy and error sources. In *Proceedings of the international snow sicence workshop*, number August 2014, pages 1–6, (2006).

ESRI. ArcGIS, (2017). Available at: `http://www.esri.com/arcgis/about-arcgis`. [Accessed on: 2017-12-03].

Fischer, L., Eisenbeiss, H., Kääb, A., Huggel, C., and Haeberli, W., (2011). Monitoring topographic changes in a periglacial high-mountain face using high-resolution DTMs, Monte Rosa East Face, Italian Alps. *Permafrost and Periglacial Processes*, 22(2):140–152.

Fischer, M., Huss, M., and Hoelzle, M., (2015). Surface elevation and mass changes of all Swiss glaciers 1980-2010. *Cryosphere*, 9(2):525–540.

GlaciologicalReports, (2017). *The Swiss Glaciers. Yearbooks of the Cryospheric Commision of the Swiss Acadamy of Sciecnes (SCNAT)*. Labratory of Hydraulics, Hydrology and Glaciology (VAW) of ETH Zürich.

GLAMOS. Schweizerisches Gletschermessnetz, (2018). [Accessed on: 2018-03-28].

Heckmann, T., Mccoll, S., and Morche, D., (2016). Retreating ice: Research in pro-glacial areas matters. *Earth Surface Processes and Landforms*, 41(2):271–276.

Heid, T. and Kääb, A., (2012). Evaluation of existing image matching methods for deriving glacier surface displacements globally from optical satellite imagery. *Remote Sensing of Environment*, 118:339–355.

Hock, R., (2005). Glacier melt: a review of processes and their modelling. *Progress in Physical Geography*, 29(3):362–391.

Hubbard, B. and Glasser, N., (2005). *Field Techniques in Glaciology and Glacial Geomorphology*. Wiley, Chichester.

Hugenholtz, C. H., Whitehead, K., Brown, O. W., Barchyn, T. E., Moorman, B. J., LeClair, A., Riddell, K., and Hamilton, T., (2013). Geomorphological mapping with a small unmanned aircraft system (sUAS): Feature detection and accuracy assessment of a photogrammetrically-derived digital terrain model. *Geomorphology*, 194:16–24.

Huss, M., (2013). Density assumptions for converting geodetic glacier volume change to mass change. *The Cryosphere Discussions*, 7(1):219–244.

Huss, M., Zemp, M., Joerg, P. C., and Salzmann, N., (2014). High uncertainty in 21st century runoff projections from glacierized basins. *Journal of Hydrology*, 510:35–48.

IPCC, (2013). Observations: Cryosphere. *Climate Change 2013: The Physical Science Basis. Contribution of Working Group I to the Fifth Assessment Report of the Intergovernmental Panel on Climate Change*, pages 317–382.

Joerg, P. C. and Zemp, M., (2014). Evaluating volumetric glacier change methods using airborne laser scanning data. *Geografiska Annaler, Series A: Physical Geography*, 96(2):135–145.

Joerg, P. C., Morsdorf, F., and Zemp, M., (2012). Uncertainty assessment of multi-temporal airborne laser scanning data: A case study on an Alpine glacier. *Remote Sensing of Environment*, 127: 118–129.

Kääb, A., (2002). Monitoring high-mountain terrain deformation from repeated air- and spaceborne optical data: Examples using digital aerial imagery and ASTER data. *ISPRS Journal of Photogrammetry and Remote Sensing*, 57:39–52.

Kääb, A., (2005a). *Remote Sensing of Mountain Glaciers and Permafrost Creep*. Phd thesis, University of Zurich.

Kääb, A., (2005b). Remote sensing of mountain environments. In *Proceedings second and third GLOCHAMORE workshop*, pages 92–99. UNESCO publications, (2005b).

Kääb, A. and Vollmer, M., (2000). Surface Geometry, Thickness Changes and Flow Fields on Creeping Mountain Permafrost: Automatic Extraction by Digital Image Analysis. *Permafrost and periglacial processes*, 11:315–326.

Kjær, K. H. and Krüger, J., (2001). The final phase of dead-ice moraine development: Processes and sediment architecture, Kötlujökull, Iceland. *Sedimentology*, 48(5):935–952.

Koblet, T., Gärtner-Roer, I., Zemp, M., Jansson, P., Thee, P., Haeberli, W., and Holmlund, P., (2010). Reanalysis of multi-temporal aerial images of Storglaci??ren, Sweden (1959- 99) - Part 1: Determination of length, area, and volume changes. *Cryosphere*, 4(3):333–343.

Kociuba, W., (2017). Assessment of sediment sources throughout the proglacial area of a small Arctic catchment based on high-resolution digital elevation models. *Geomorphology*, 287:73–89.

Kos, A., Amann, F., Strozzi, T., Delaloye, R., von Ruette, J., and Springman, S., (2016). Contemporary glacier retreat triggers a rapid landslide response, Great Aletsch Glacier, Switzerland. *Geophysical Research Letters*, 43(24):12,466–12,474.

Lane, S. N., Bakker, M., Gabbud, C., Micheletti, N., and Saugy, J. N., (2017). Sediment export, transient landscape response and catchment-scale connectivity following rapid climate warming and Alpine glacier recession. *Geomorphology*, 277:210–227.

Lilesand, T. M., Kiefer, R. W., and Chipman, J. W., (2008). *Remote Sensing and image interpretation*. Wiley, Hoboken, 6th edition.

Lukas, S., Graf, A., Coray, S., and Schlüchter, C., (2012). Genesis, stability and preservation potential of large lateral moraines of Alpine valley glaciers - towards a unifying theory based on Findelengletscher, Switzerland. *Quaternary Science Reviews*, 38:27–48.

Machguth, H., Eisen, O., Paul, F., and Hoelzle, M., (2006). Strong spatial variability of snow accumulation observed with helicopter-borne GPR on two adjacent Alpine glaciers. *Geophysical Research Letters*, 33(13):1–5.

Maisch, M., Wipf, A., Denneler, B., Battaglia, J., and Benz, C., (2000). *Die Gletscher der Schweizer Alpen: Gletscherhochstand 1850, Aktuelle Vergletscherung, Gletscherschwundszenarien.* vdf Hochschulverlag AG an der ETH Zürich, Zurich, 2nd edition.

Micheletti, N., Lane, S. N., and Chandler, J. H., (2015). Application of archival aerial photogrammetry to quantify climate forcing of alpine landscapes. *Photogrammetric Record*, 30(150):143–165.

Müller, J., Gärtner-Roer, I., Kenner, R., Thee, P., and Morche, D., (2014a). Sediment storage and transfer on a periglacial mountain slope (Corvatsch, Switzerland). *Geomorphology*, 218:35–44.

Müller, J., Gärtner-Roer, I., Thee, P., and Ginzler, C., (2014b). Accuracy assessment of airborne photogrammetrically derived high-resolution digital elevation models in a high mountain environment. *ISPRS Journal of Photogrammetry and Remote Sensing*, 98:58–69.

Nicholson, L. and Benn, D. I., (2006). Calculating ice melt beneath a debris layer using meteorological data. *Journal of Glaciology*, 52(178):463–470.

Nuth, C. and Kääb, (2011). Co-registration and bias corrections of satellite elevation data sets for quantifying glacier thickness change. *Cryosphere*, 5(1):271–290.

Otto, J.-C., Schrott, L., Jaboyedoff, M., and Dikau, R., (2009). Quantifying sediment storage in a high alpine valley (Turtmanntal, Switzerland). *Earth Surface Processes and Landforms*, 34:1726–1742.

Paul, F., Bolch, T., Kääb, A., Nagler, T., Nuth, C., Scharrer, K., Shepherd, A., Strozzi, T., Ticconi, F., Bhambri, R., Berthier, E., Bevan, S., Gourmelen, N., Heid, T., Jeong, S., Kunz, M., Lauknes, T. R., Luckman, A., Merryman Boncori, J. P., Moholdt, G., Muir, A., Neelmeijer, J., Rankl, M., VanLooy, J., and Van Niel, T., (2015). The glaciers climate change initiative: Methods for creating glacier area, elevation change and velocity products. *Remote Sensing of Environment*, 162:408–426.

Pellicciotti, F., Stephan, C., Miles, E., Herreid, S., Immerzeel, W. W., and Bolch, T., (2015). Mass-balance changes of the debris-covered glaciers in the Langtang Himal, Nepal, from 1974 to 1999. *Journal of Glaciology*, 61(226):373–386.

Rastner, P., (2015). Co-Registration Tutorial. Technical report.

Rastner, P., Joerg, P. C., Huss, M., and Zemp, M., (2016). Historical analysis and visualization of the retreat of Findelengletscher, Switzerland, 18592010. *Global and Planetary Change*, 145:67–77.

Reznichenko, N. V., Davies, T. R., and Alexander, D. J., (2011). Effects of rock avalanches on glacier behaviour and moraine formation. *Geomorphology*, 132(3-4):327–338.

Rossini, M., Di Mauro, B., Garzonio, R., Baccolo, G., Cavallini, G., Mattavelli, M., De Amicis, M., and Colombo, R., (2018). Rapid melting dynamics of an alpine glacier with repeated UAV photogrammetry. *Geomorphology*, 304:159–172.

Ruff, A., (2015). *Spatio-temporal quantication of geomorphological processes in the recently deglaciated area surrounding the Findelengletscher*. Master's thesis, University of Zurich.

Sailer, R., Bollmann, E., Hoinkes, S., Rieg, L., Sproß, M., and Stötter, J., (2012). Quantification of geomorphodynamics in glaciated and recently deglaciated terrain based on airborne laser scanning data. *Geografiska Annaler, Series A: Physical Geography*, 94(1):17–32.

Schiefer, E. and Gilbert, R., (2007). Reconstructing morphometric change in a proglacial landscape using historical aerial photography and automated DEM generation. *Geomorphology*, 88(1-2):167–178.

Schomacker, A., (2008). What controls dead-ice melting under different climate conditions? A discussion. *Earth-Science Reviews*, 90(3-4):103–113.

SenseFly. eBee Drone, (2017). Available at: `https://www.sensefly.com/`. [Accessed on: 2017-10-30].

Shulmeister, J., Davies, T. R., Evans, D. J., Hyatt, O. M., and Tovar, D. S., (2009). Catastrophic landslides, glacier behaviour and moraine formation - A view from an active plate margin. *Quaternary Science Reviews*, 28(11-12):1085–1096.

Slaymaker, O., (2011). Criteria to Distinguish Between Periglacial, Proglacial and Paraglacial Environments. *Quaestiones Geographicae*, 30(1):85–94.

Smithson, P., Addison, K., and Atkinson, K., (2008). *Fundamentals of Physical Environment*. Routledge, London, 4th edition.

Sold, L., Huss, M., Hoelzle, M., Andereggen, H., Joerg, P. C., and Zemp, M., (2013). Methodological approaches to infer end-of-winter snow distribution on alpine glaciers. *Journal of Glaciology*, 59: 1047–1059.

Staines, K. E., Carrivick, J. L., Tweed, F. S., Evans, A. J., Russell, A. J., Jóhannesson, T., and Roberts, M., (2015). A multi-dimensional analysis of pro-glacial landscape change at Sólheimajökull, Southern Iceland. *Earth Surface Processes and Landforms*, 40(6):809–822.

Strahler, A. and Strahler, A., (2009). *Physische Geographie*. Ulmer, Stuttgart, 4. edition.

Sugden, D., (1994). Glacier. In *The Dictionary of Physical Geography*, page 226.

Swisstopo. REFRAME, (2017a). Available at: `https://www.swisstopo.admin.ch/de/karten-daten-online/calculation-services/reframe.html`. [Accessed on: 2017-11-15].

Swisstopo. GPS-Messverfahren, (2017b). Available at: `https://www.swisstopo.admin.ch/de/wissen-fakten/geodaesie-vermessung/messverfahren/gps-messverfahren.html`. [Accessed on: 2017-11-15].

Uhlmann, B., Jordan, F., and Beniston, M., (2013a). Modelling runoff in a Swiss glacierized catchment-part I: Methodology and application in the Findelen basin under a long-lasting stable climate. *International Journal of Climatology*, 33(5):1293–1300.

Uhlmann, B., Jordan, F., and Beniston, M., (2013b). Modelling runoff in a Swiss glacierized catchment-Part II: Daily discharge and glacier evolution in the Findelen basin in a progressively warmer climate. *International Journal of Climatology*, 33(5):1301–1307.

University of Oslo. Image Correlation Software - CIAS, (2017). Available at: `http://www.mn.uio.no/geo/english/research/projects/icemass/cias/`. [Accessed on: 2017-12-04].

USGS. Landslide Types and Processes, (2004). Available at: `https://pubs.usgs.gov/fs/2004/3072/fs-2004-3072.html`. [Accessed on: 2018-01-04].

Varnes, D., (1978). Slope movement types and processes. In Schuster, R. and Krizek, R., editors, *Landslides-Analysis and control: National Research Council*, chapter Chapter 2, pages 11–33. Washington, D.C.

Wehr, A. and Lohr, U., (1999). Airborne laser scanning: an introduction and overview. *ISPRS Journal of Photogrammetry & Remote Sensing*, 54:68–82.

Westoby, M. J., Brasington, J., Glasser, N. F., Hambrey, M. J., and Reynolds, J. M., (2012). 'Structure-from-Motion' photogrammetry: A low-cost, effective tool for geoscience applications. *Geomorphology*, 179:300–314.

WGMS. World glacier monitoring service, (2018). [Accessed on: 2018-01-24].

Zemp, M., Haeberli, W., Bajracharya, S., Chinn, T. J., Fountain, A. G., Hagen, J. O., Huggel, C., Kääb, A., Kaltenborn, B. P., Karki, M., and Others, (2007). Glaciers and ice caps. Part I: Global overview and outlook. Part II: Glacier changes around the world. *UNEP: Global outlook for ice & snow.*, pages 115–152.

Zemp, M., Thibert, E., Huss, M., Stumm, D., Rolstad Denby, C., Nuth, C., Nussbaumer, S. U., Moholdt, G., Mercer, A., Mayer, C., Joerg, P. C., Jansson, P., Hynek, B., Fischer, A., Escher-Vetter, H., Elvehøy, H., and Andreassen, L. M., (2013). Reanalysing glacier mass balance measurement series. *Cryosphere*, 7(4):1227–1245.

Zepp, H., (2011). *Geomorphologie - eine Einführung*. Schöningh, Paderborn, 5th edition.

A. Appendix

A.1 Field Measurements and Photographs 2017

Figure A.1: Ice cliff on the mound with the clean-ice exposed to the moraine (2017)

Figure A.2: Channel between the mound and the landslide (2017)

Figure A.3: Surface of the mound (2017)
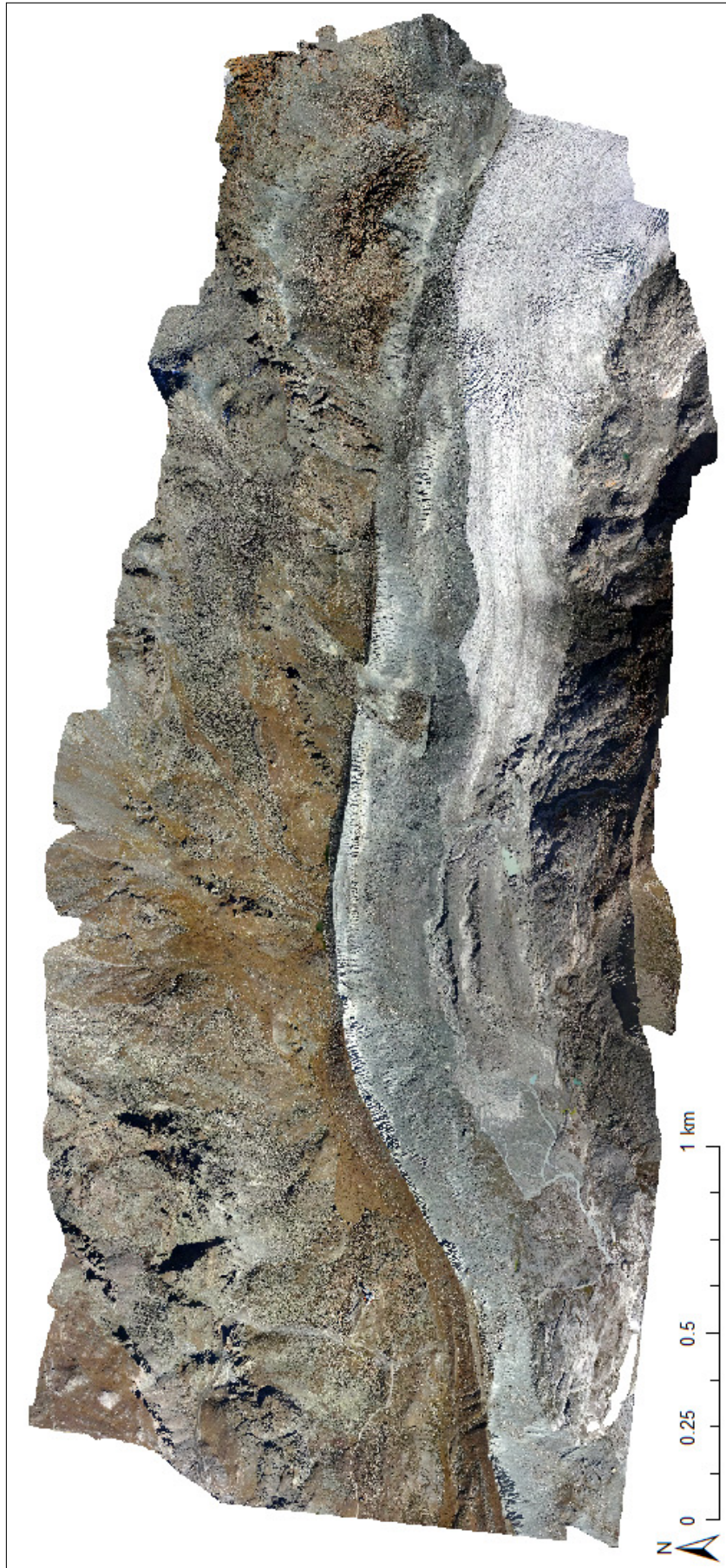
Figure A.4: Orthophoto of 2017
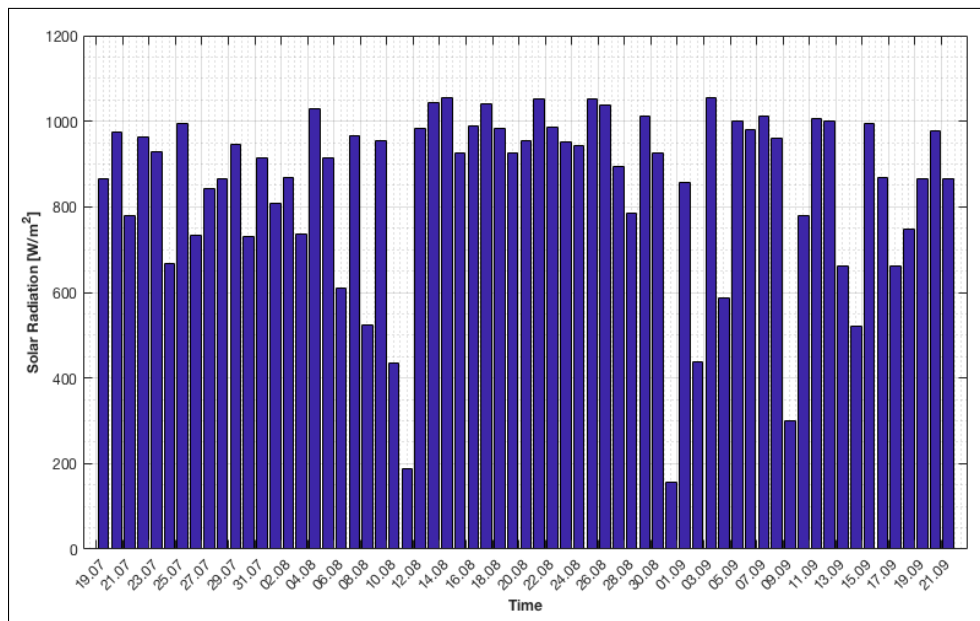
Figure A.5: Daily max solar radiation during the Field Campaign

A.2   Ablation Measurements Findelengletscher

Time Period	Measured Melt [m]	Mass Balance [m w.e.]	Time Period	Measured Melt [m]	Mass Balance [m w.e.]
2004 - 2005	-4.60	-4.14	2011 - 2012	-6.68	-6.01
2005 - 2006	-4.40	-3.96	2012 - 2013	-5.54	-4.91
2006 - 2007	-1.68	-1.51	2010 - 2013	-6.88	-6.20
2007 - 2008	-3.55	-3.20	2013 - 2014	-3.96	-5.16
2008 - 2009	-2.55	-2.30	2014 - 2015	-8.04	-7.23
2005 - 2009	-3.05	-2.74	2015 - 2016	-4.62	-4.16
2009 - 2010	-6.64	-5.97	2016 - 2017	-6.83	-6.15
2010 - 2011	-8.52	-7.67	2015 - 2017	-5.73	-5.16

Table A.1: Measured Melting and Mass Balance at stake 6 (Fi-200 from the Findelen-Measurement-Network)

A.3 Shaded Reliefs of the Study Area
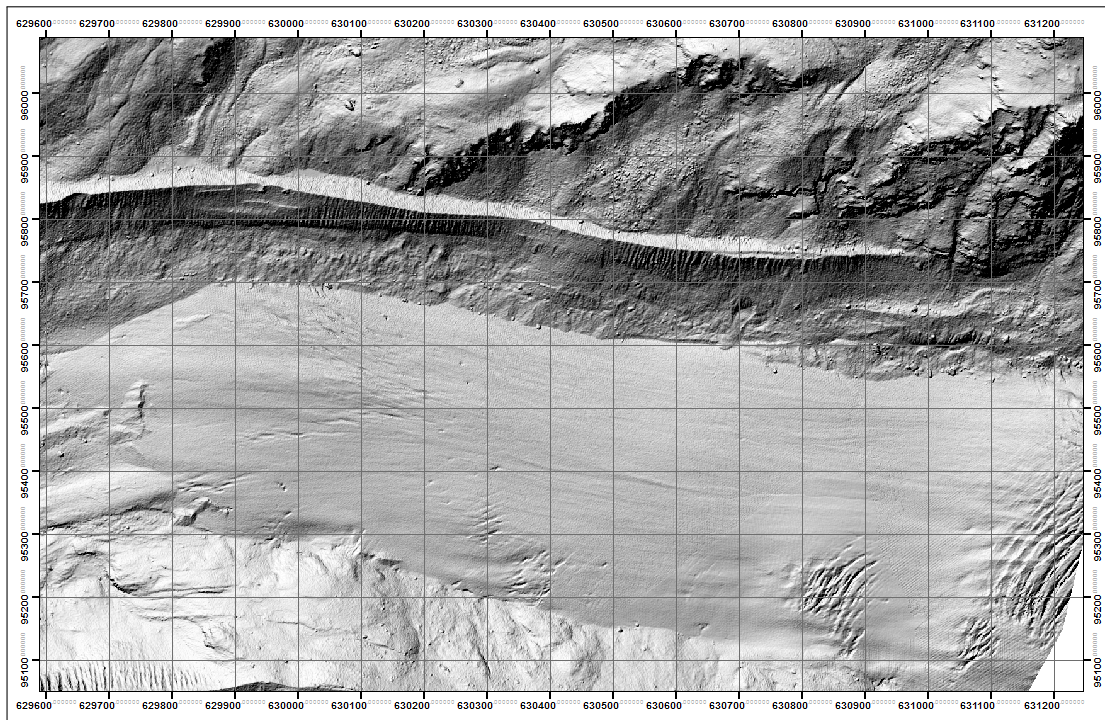
Figure A.6: Shaded Relief of 2005
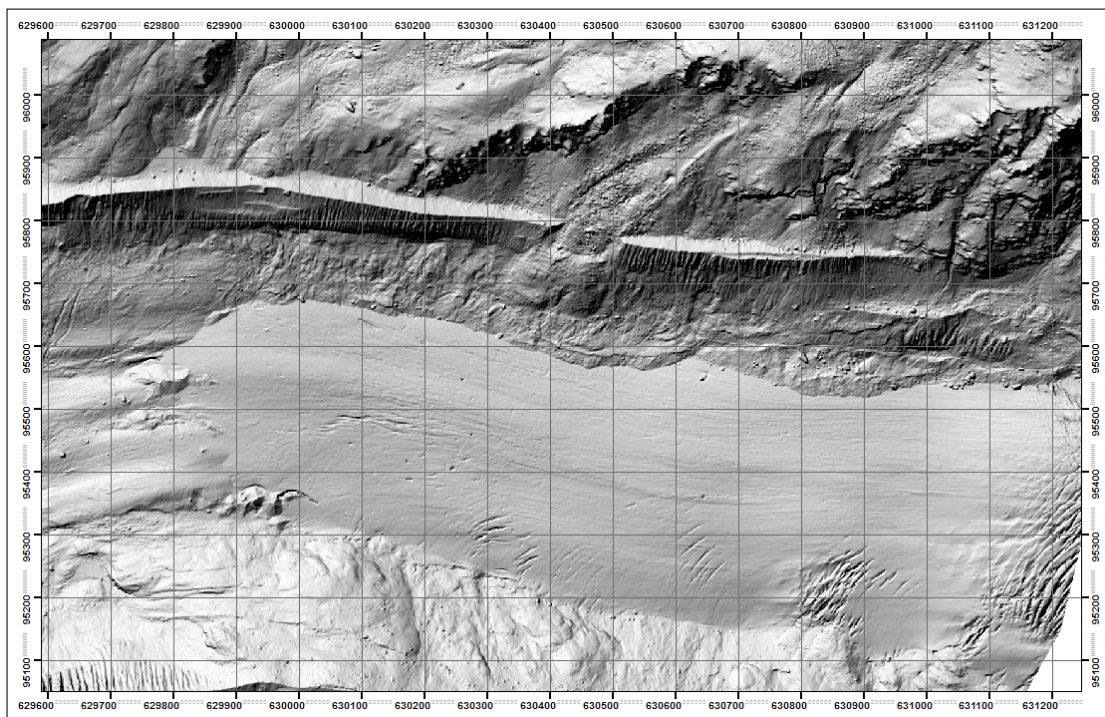
Figure A.7: Shaded Relief of 2009
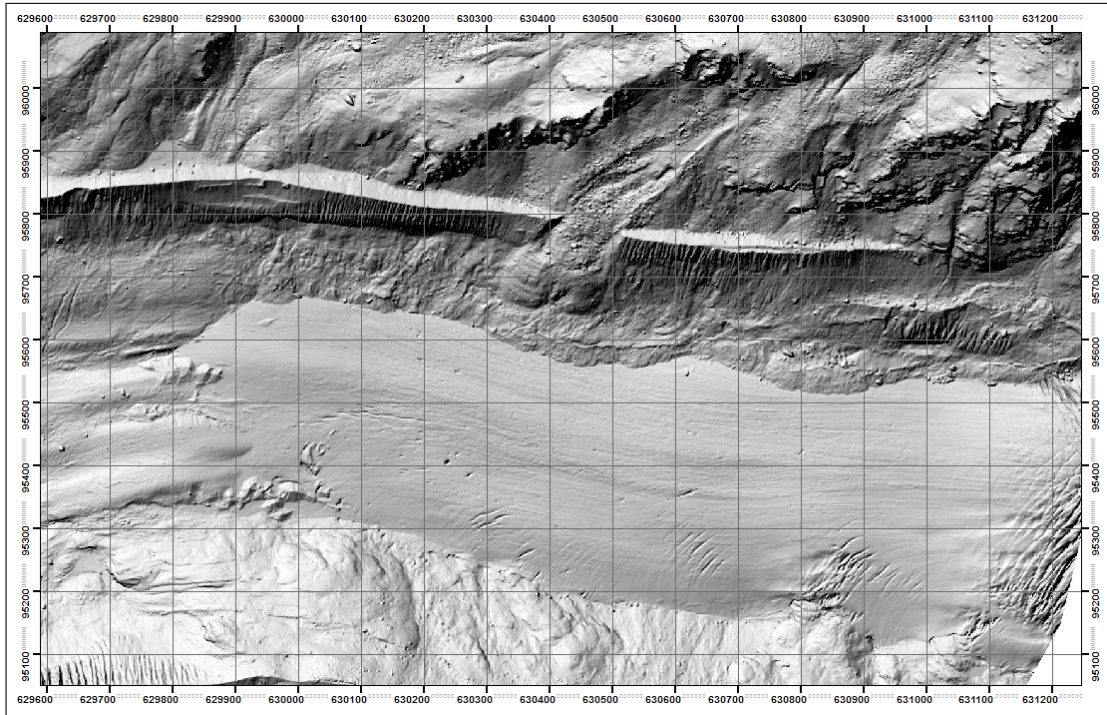
Figure A.8: Shaded Relief of 2010
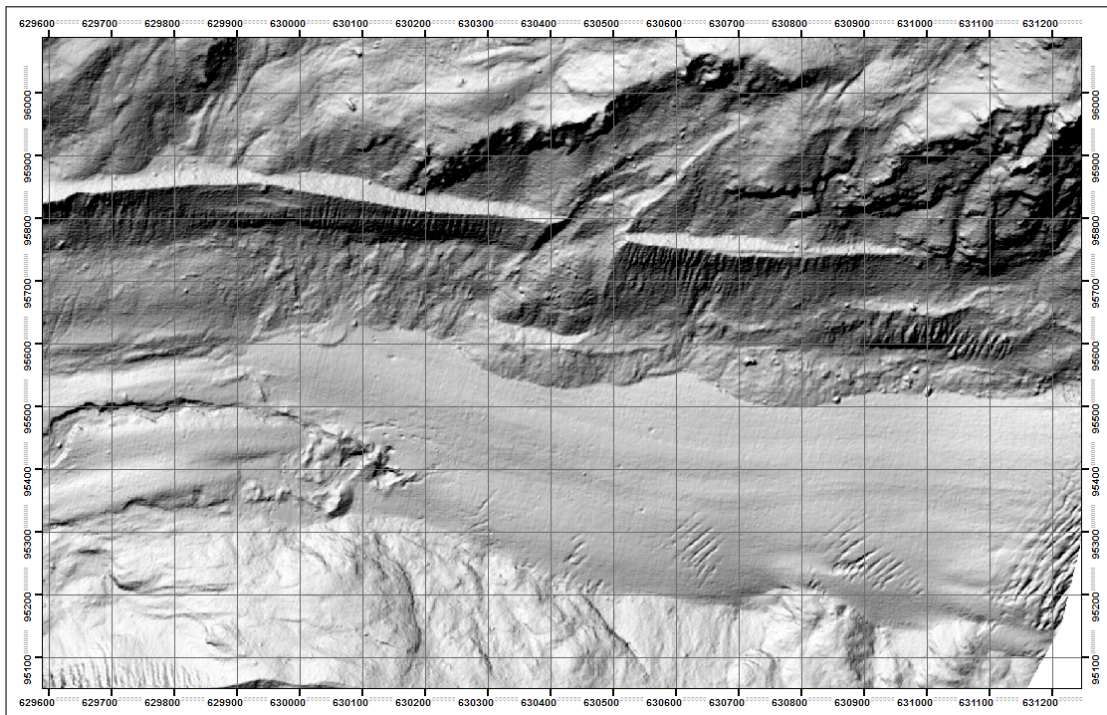
Figure A.9: Shaded Relief of 2013
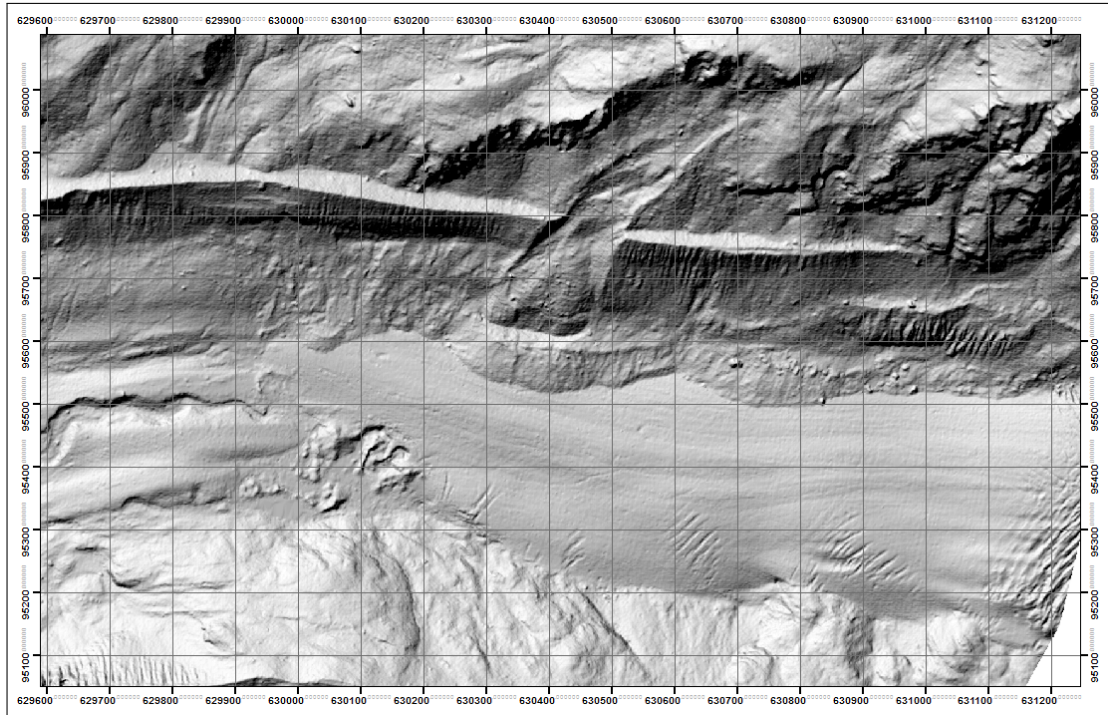
Figure A.10: Shaded Relief of 2014
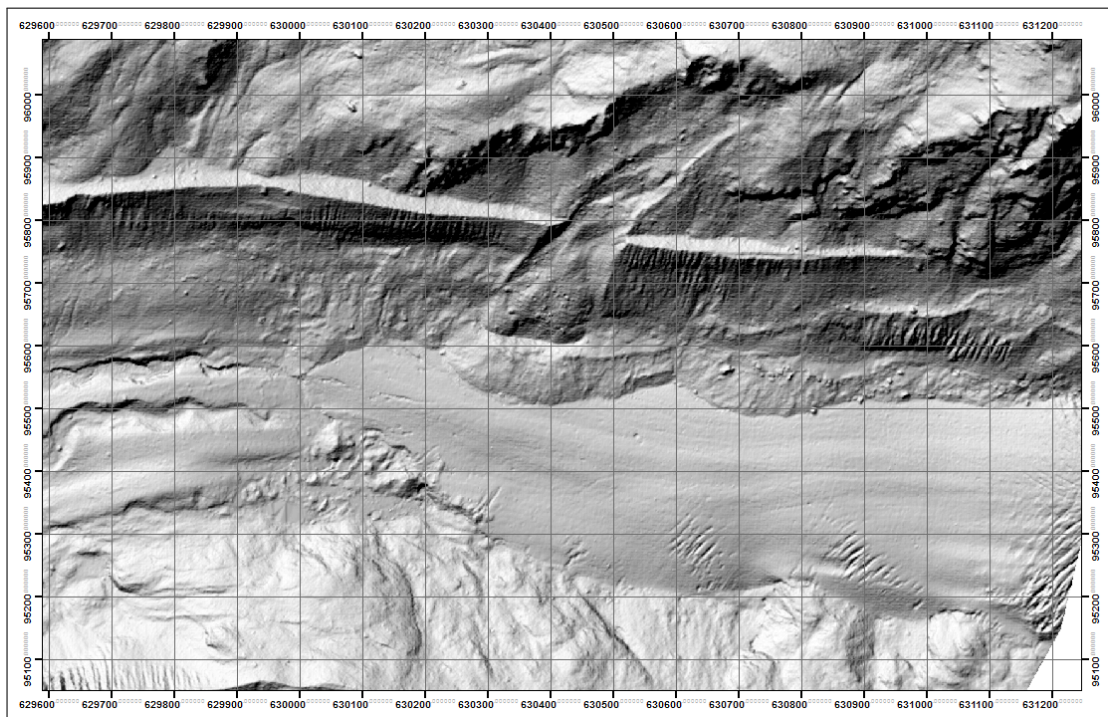
Figure A.11: Shaded Relief of 2015
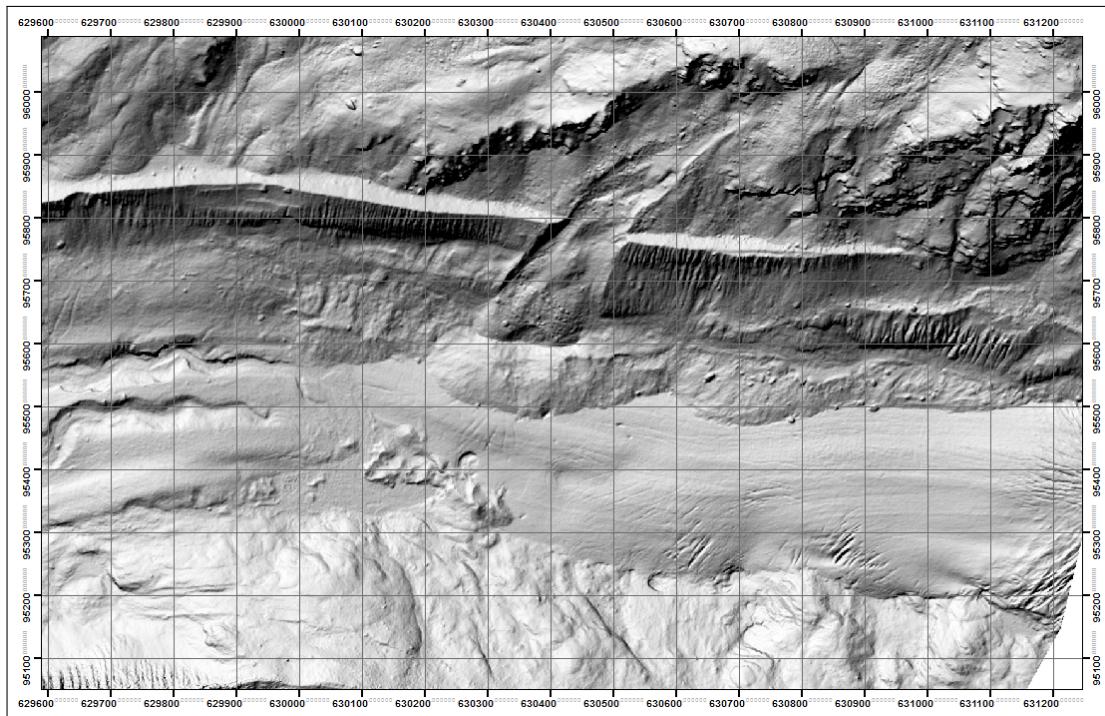
Figure A.12: Shaded Relief of 2017

A.4 Zones for the different years
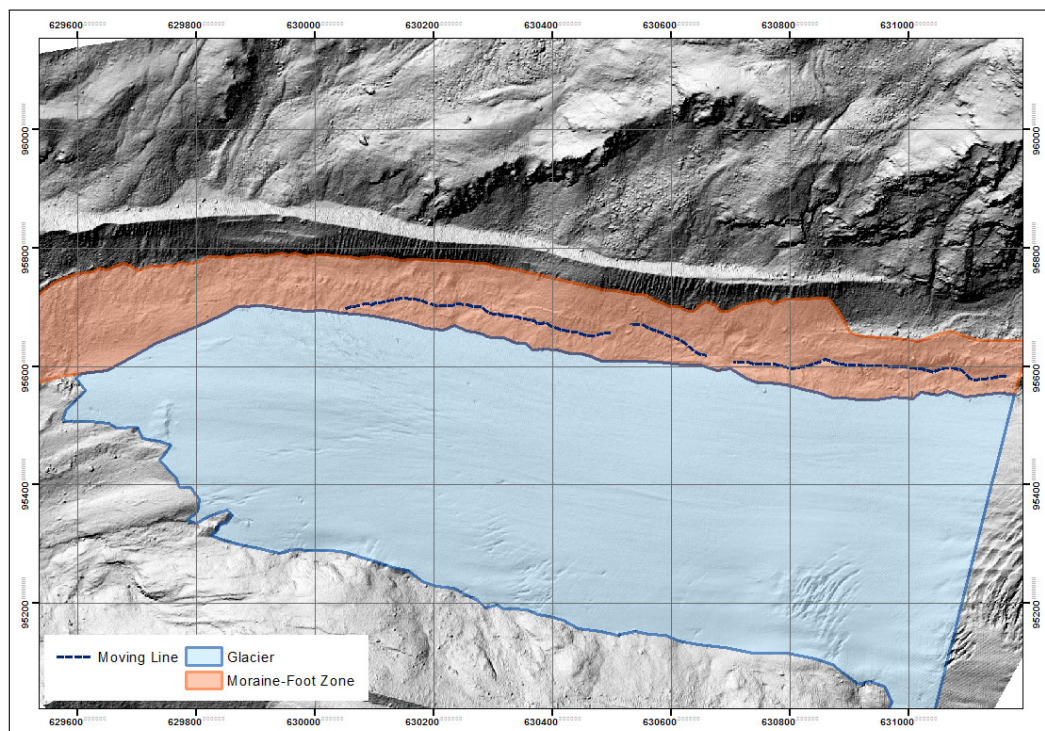
Figure A.13: Shaded Relief of 2005 with the Glacier and the Moraine-Foot Zone
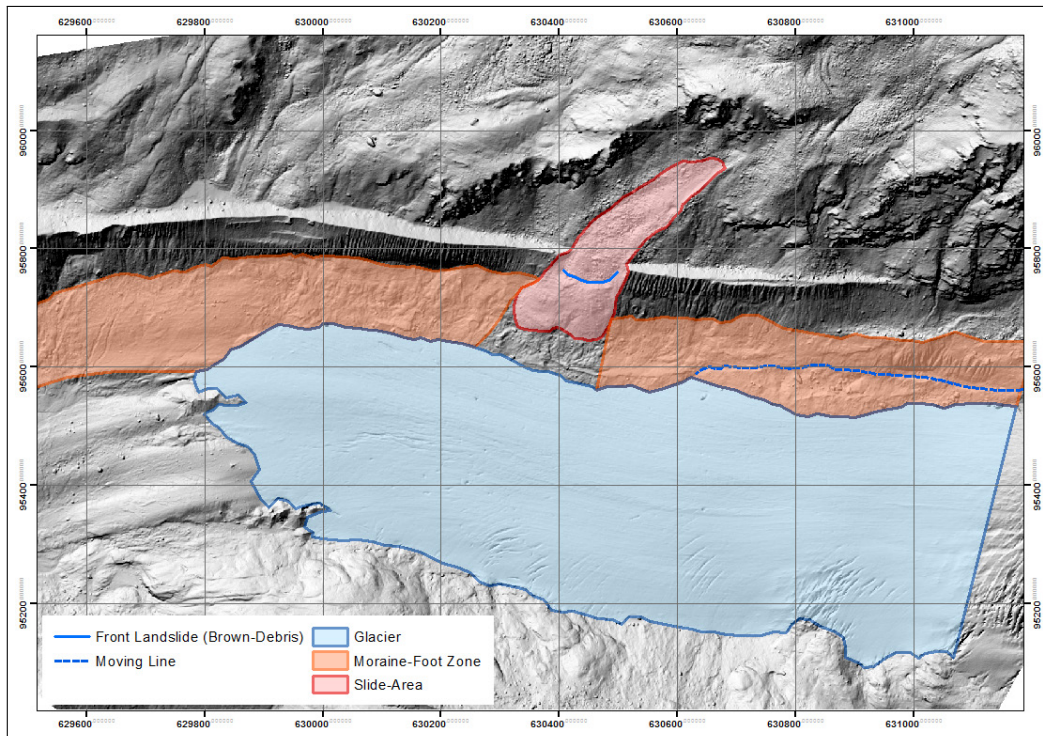
Figure A.14: Shaded Relief of 2009 with the Glacier, the Moraine-Foot Zone and the Slide-Area
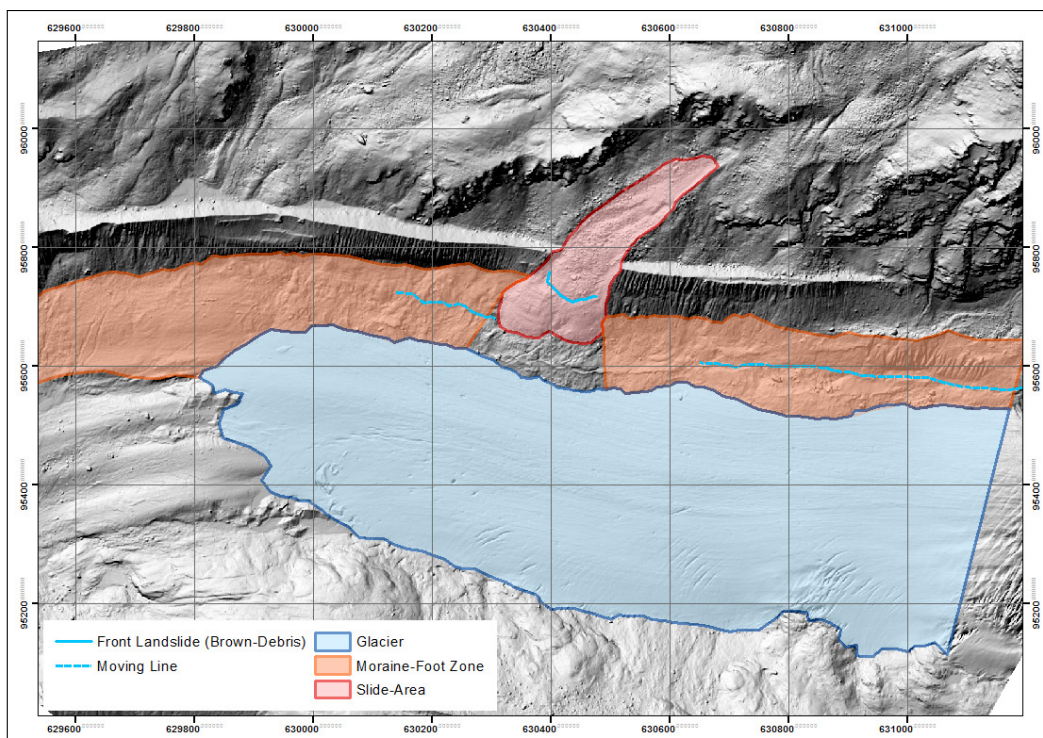
Figure A.15: Shaded Relief of 2010 with the Glacier, the Moraine-Foot Zone and the Slide-Area
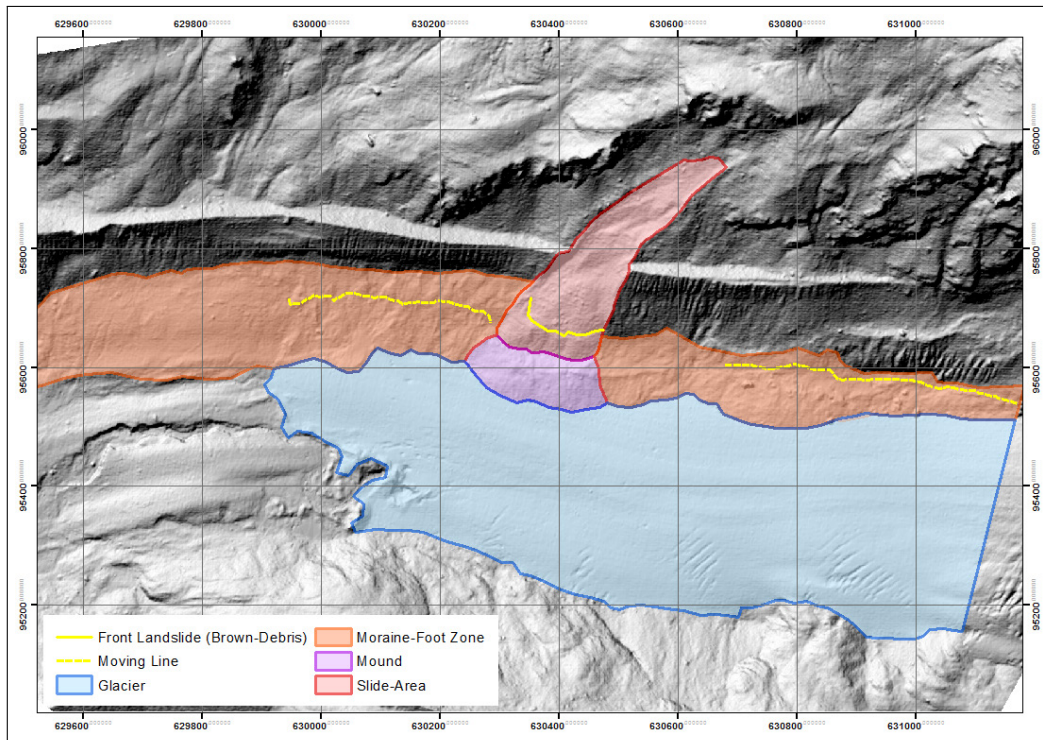
Figure A.16: Shaded Relief of 2013 with the Glacier, the Moraine-Foot Zone, the Mound and the Slide-Area
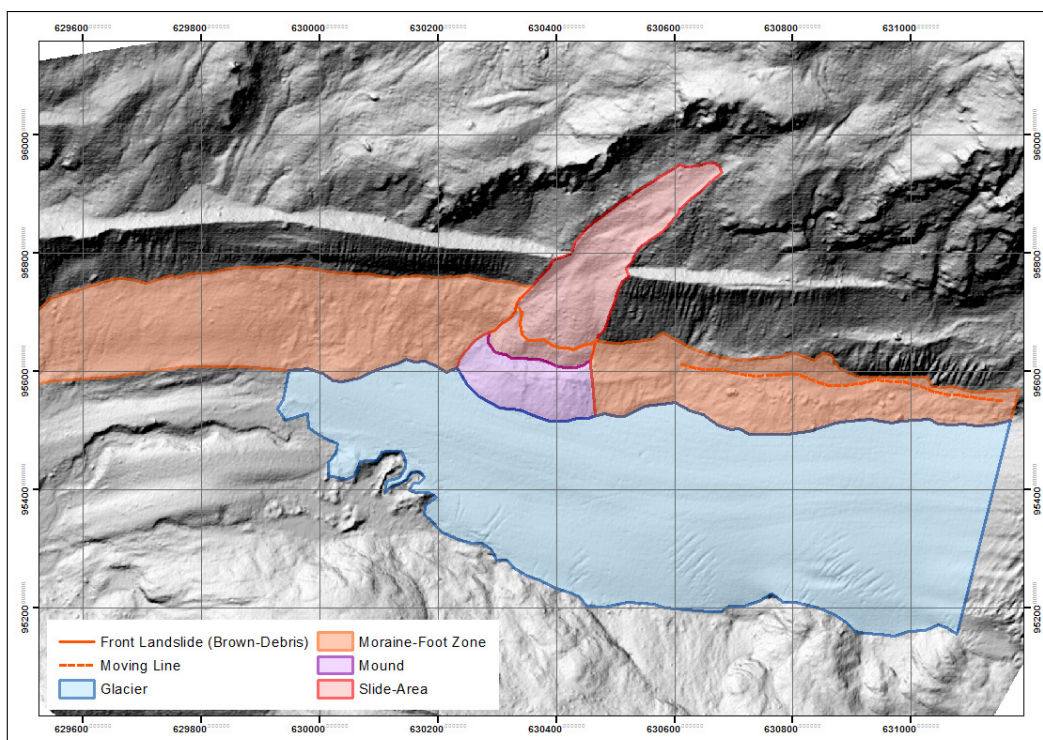
Figure A.17: Shaded Relief of 2014 with the Glacier, the Moraine-Foot Zone, the Mound and the Slide-Area
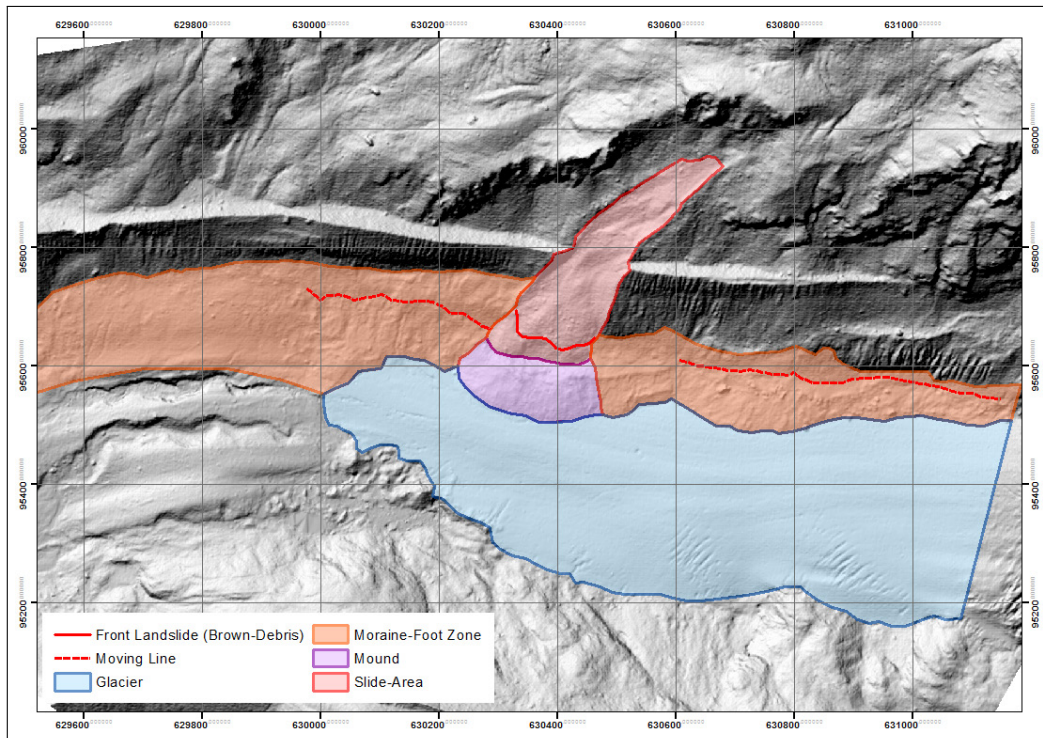
Figure A.18: Shaded Relief of 2015 with the Glacier, the Moraine-Foot Zone, the Mound and the Slide-Area
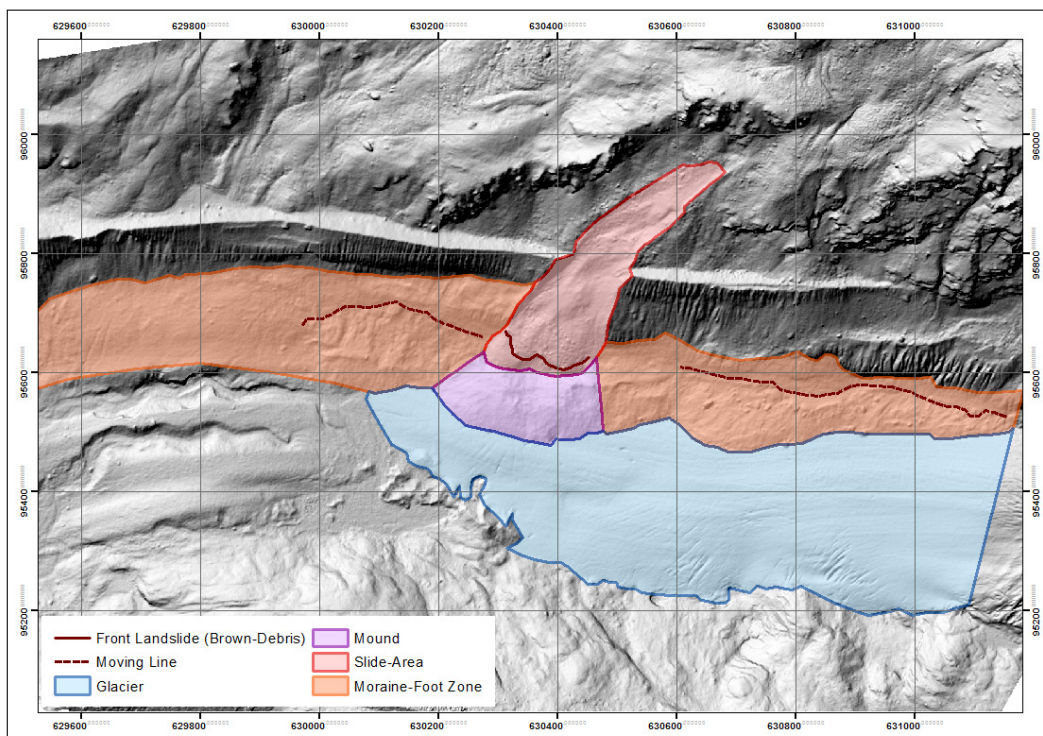
Figure A.19: Shaded Relief of 2017 with the Glacier, the Moraine-Foot Zone, the Mound and the Slide-Area

A.5 Profile Lines
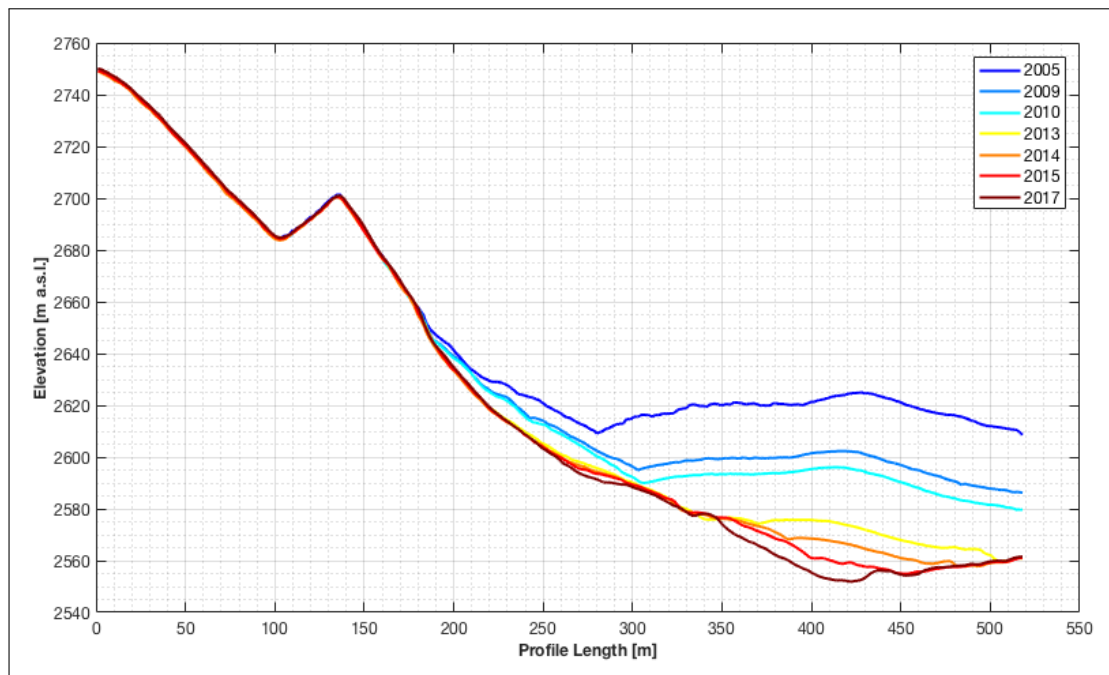
Figure A.20: Elevation along Profile A for each observation year
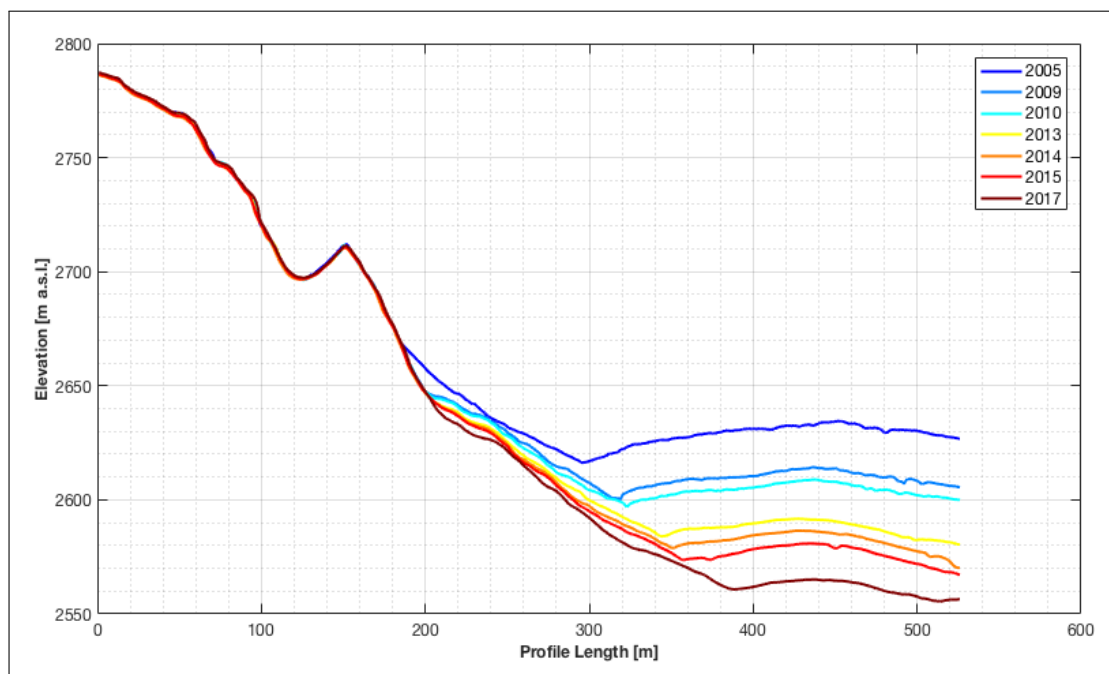
Figure A.21: Elevation along Profile B for each observation year
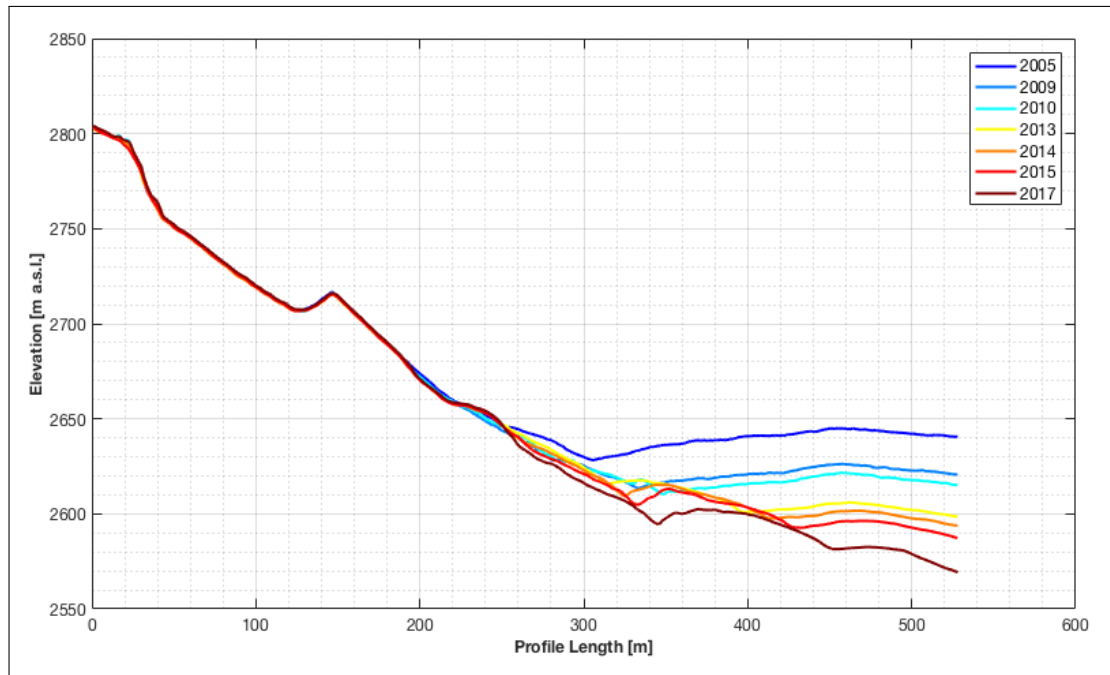
Figure A.22: Elevation along Profile C for each observation year
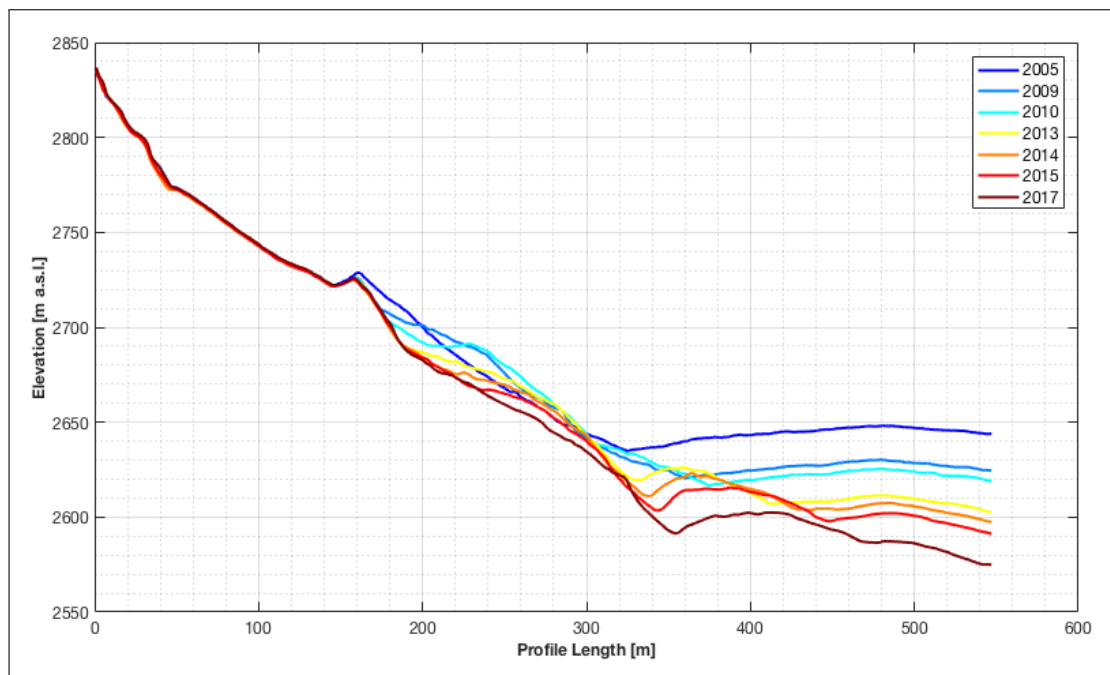
Figure A.23: Elevation along Profile D for each observation year
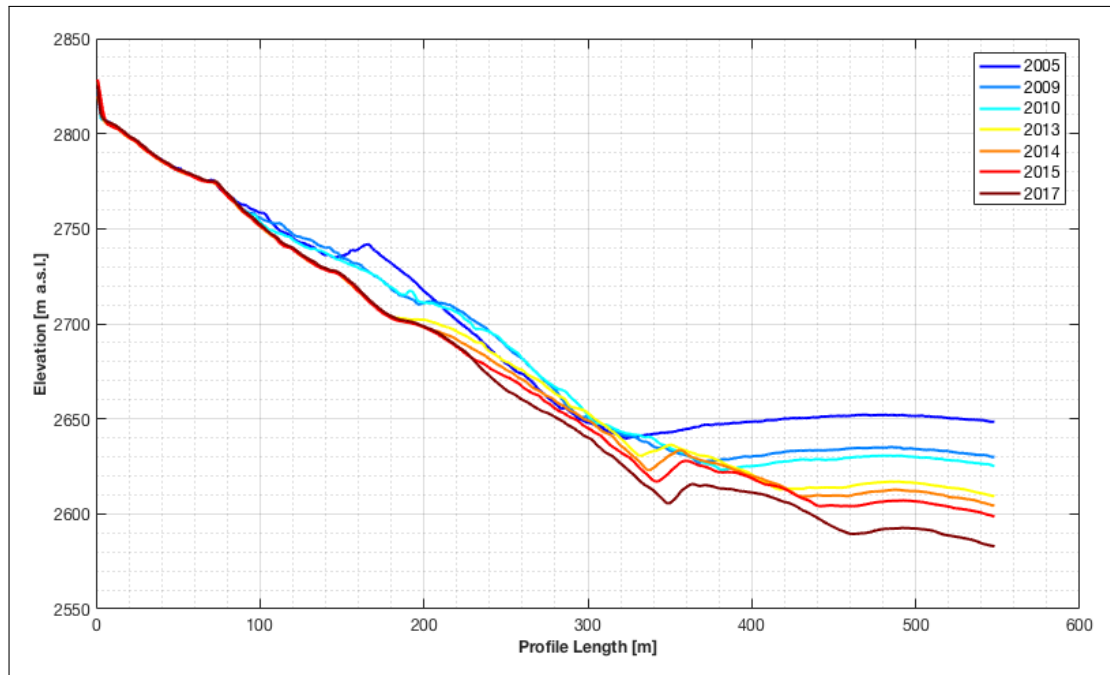
Figure A.24: Elevation along Profile E for each observation year
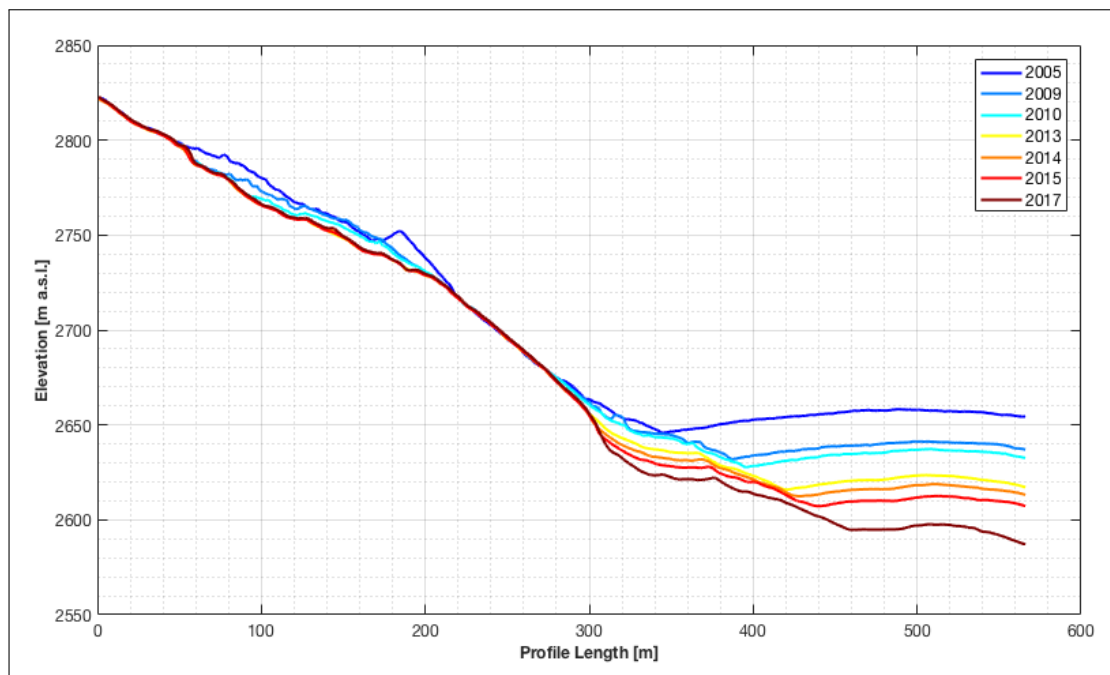
Figure A.25: Elevation along Profile F for each observation year
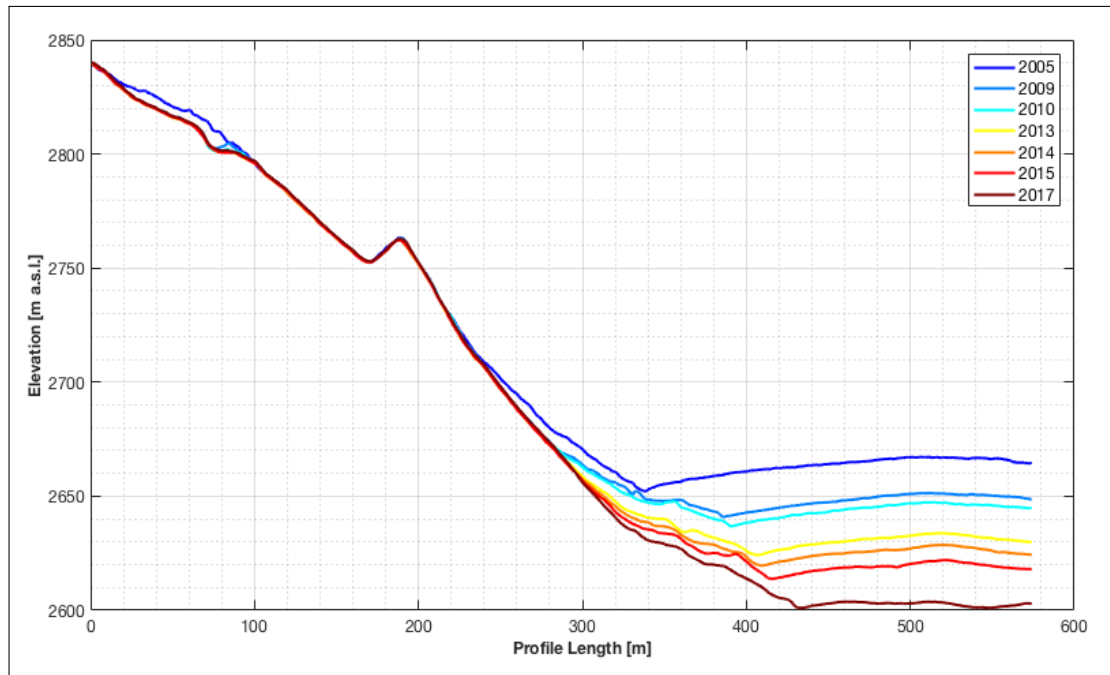
Figure A.26: Elevation along Profile G for each observation year
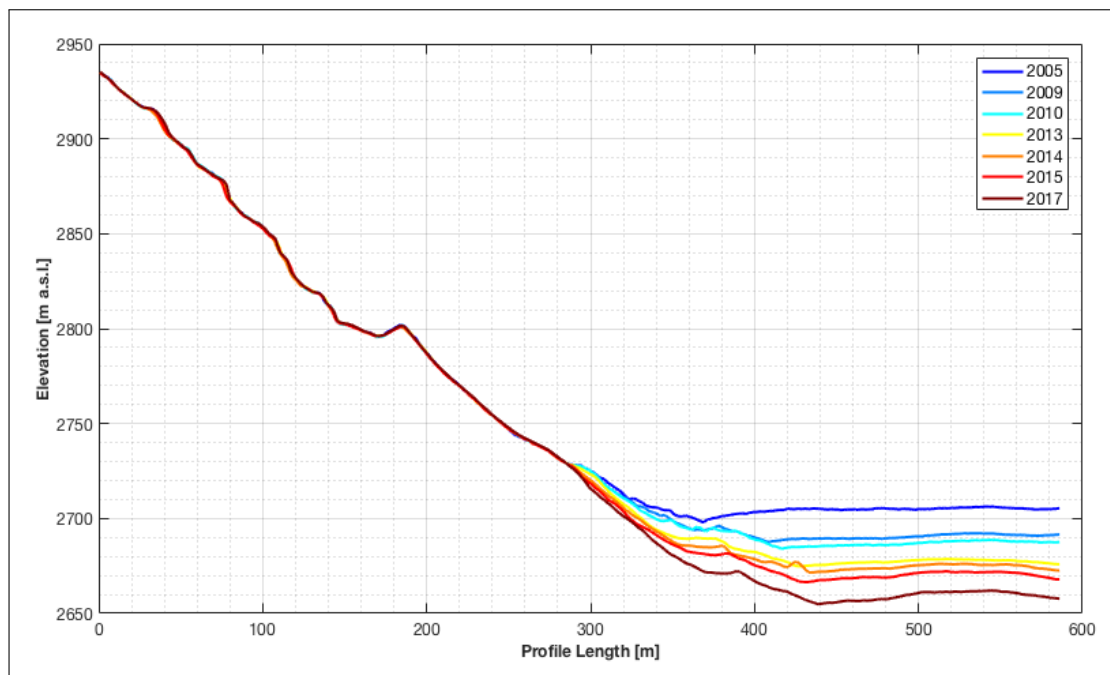
Figure A.27: Elevation along Profile H for each observation year

A.6 Elevation Differences
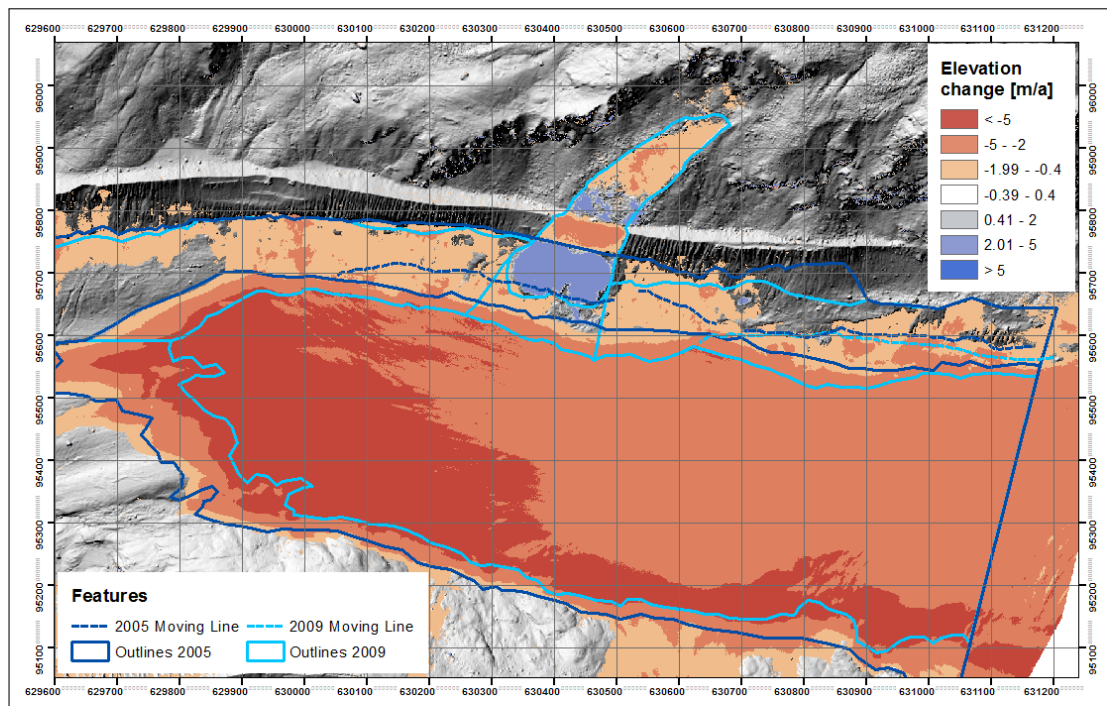
Figure A.28: Elevation change 2005-2009
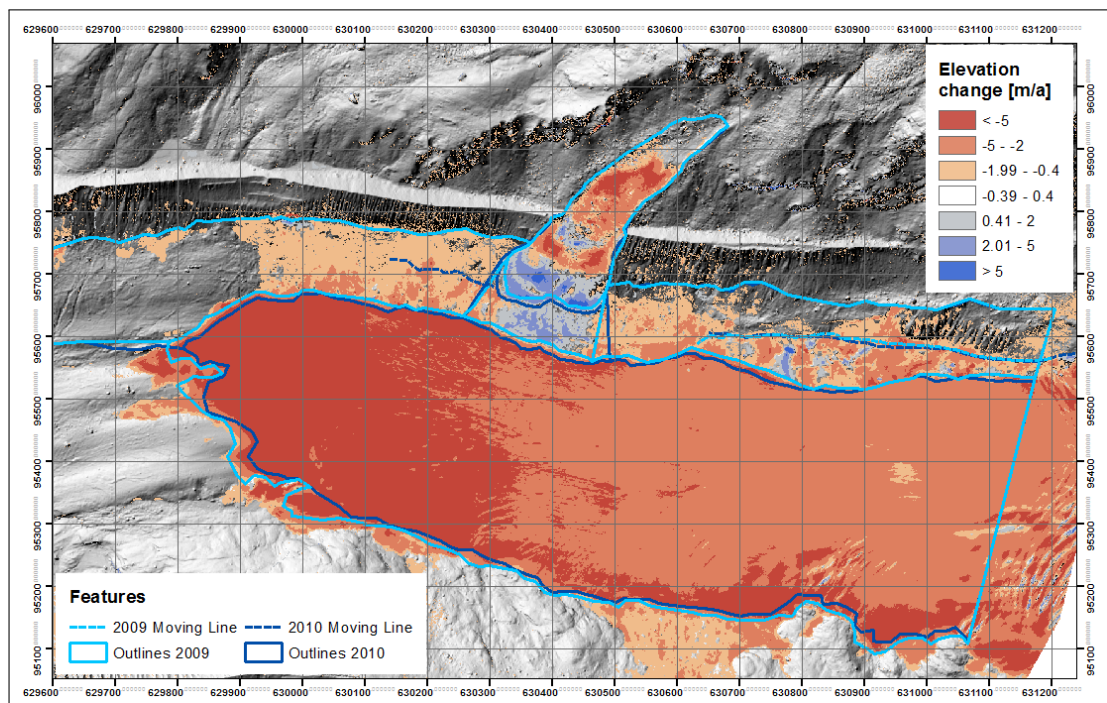
Figure A.29: Elevation change 2009-2010
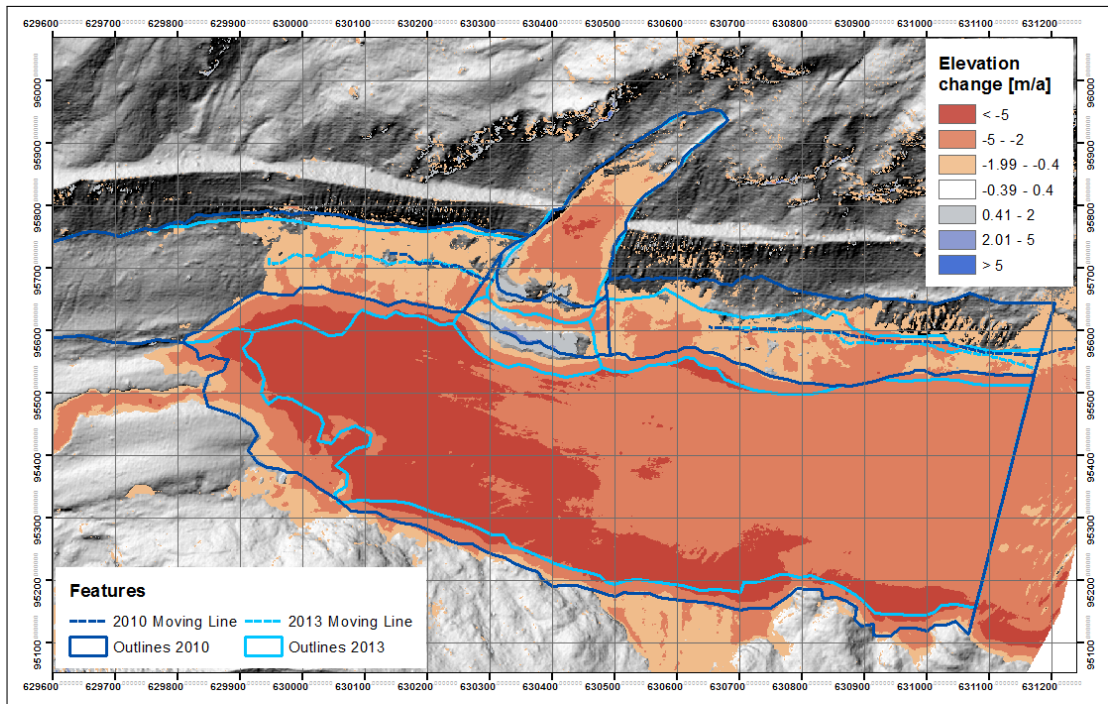
Figure A.30: Elevation change 2010-2013
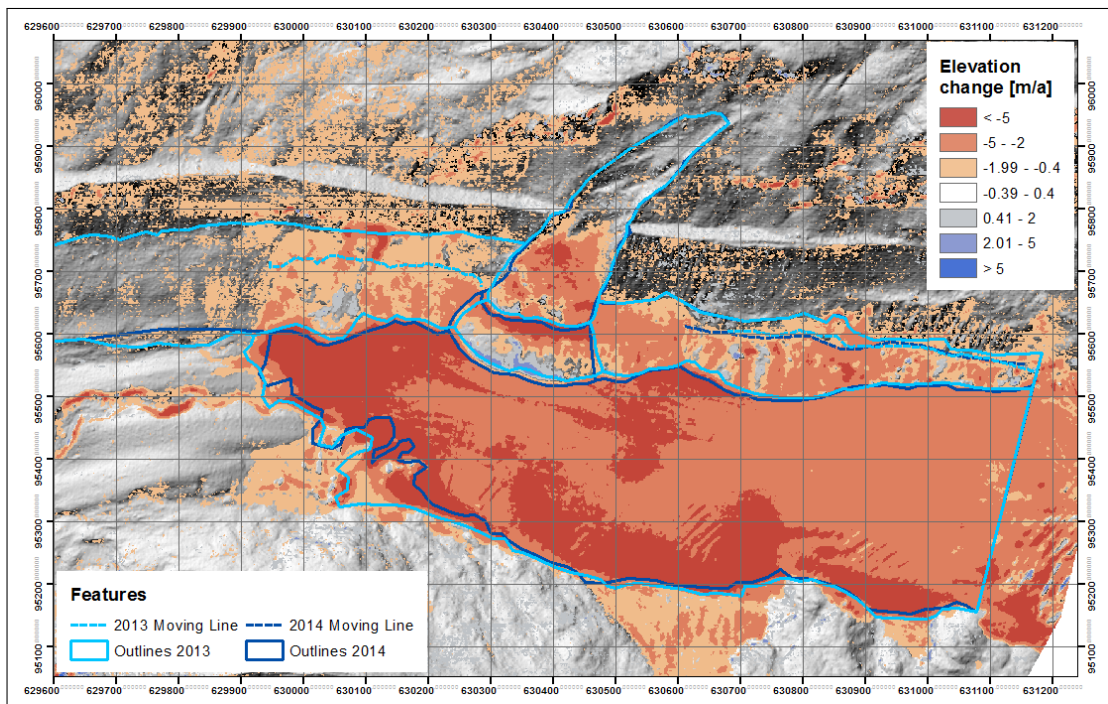
Figure A.31: Elevation change 2013-2014
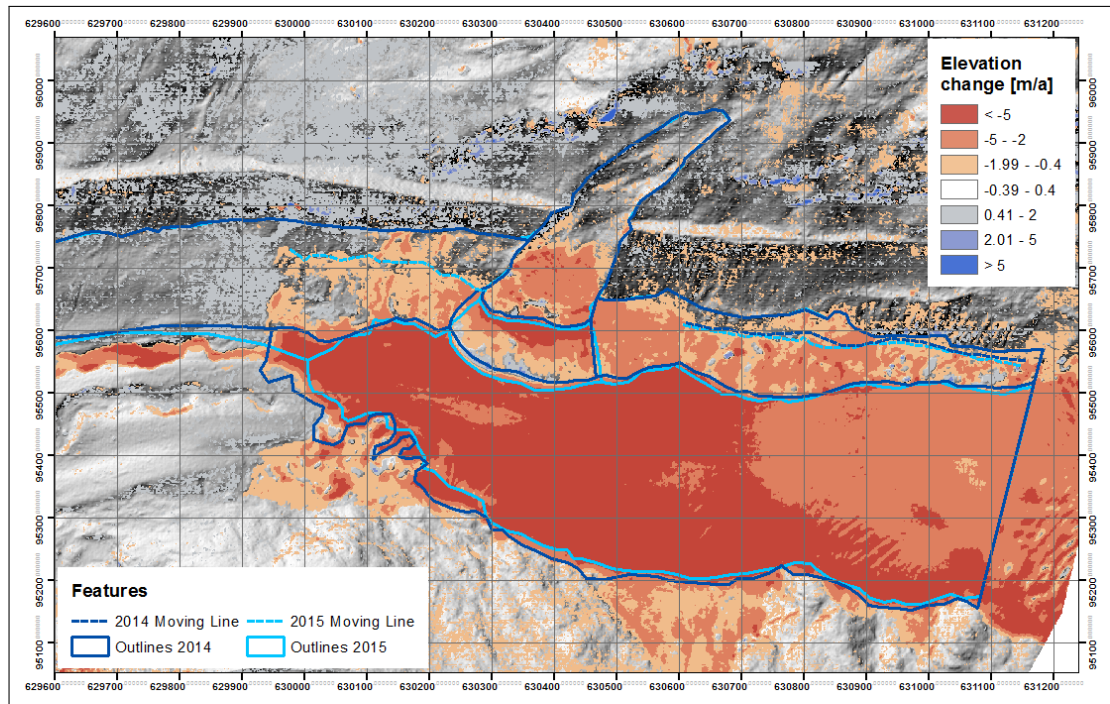
Figure A.32: Elevation change 2014-2015
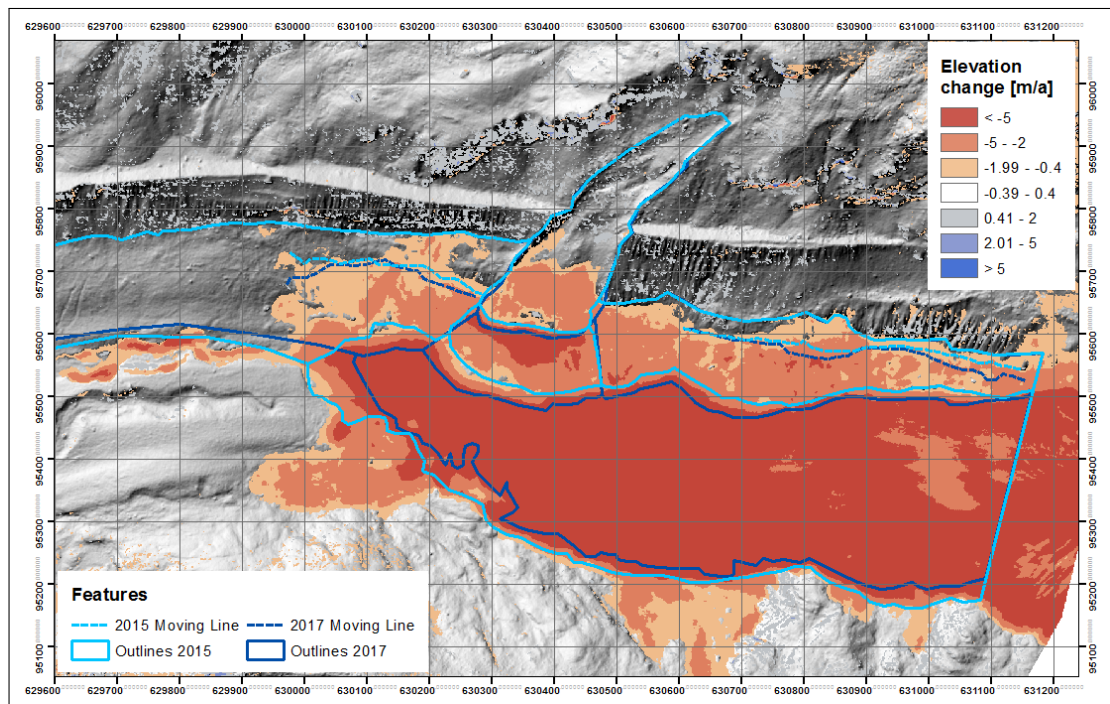
Figure A.33: Elevation change 2015-2017
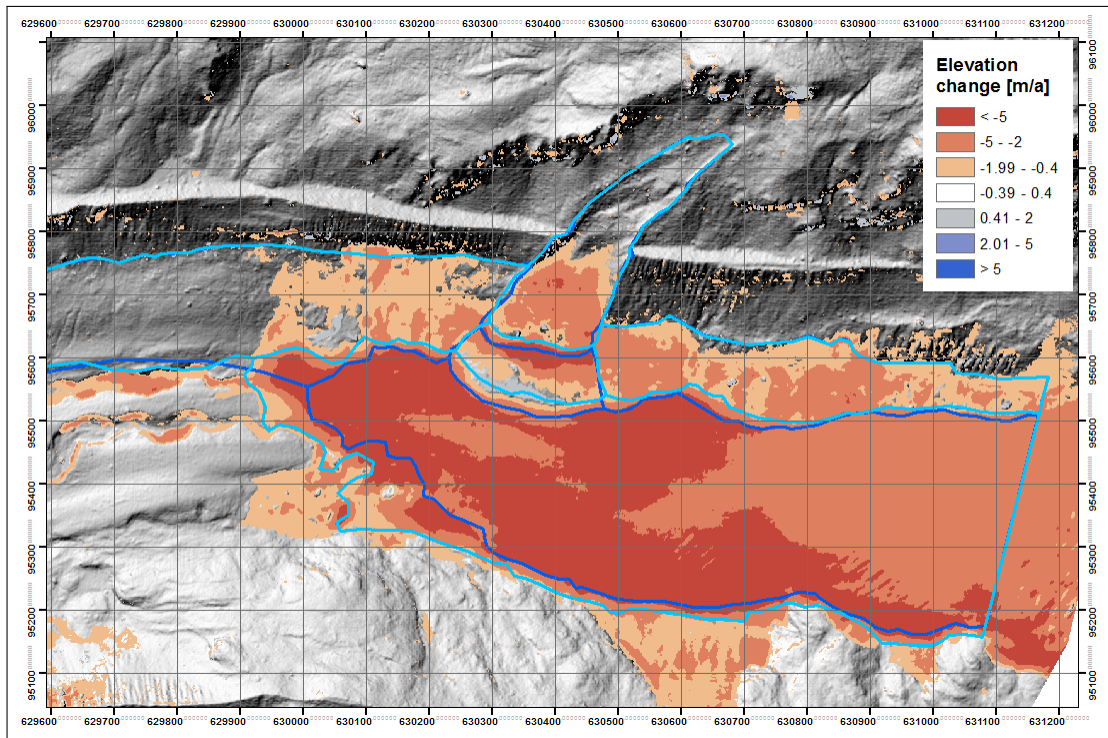
Figure A.34: Annual elevation change from 2013 to 2015

A.7 Volume Change
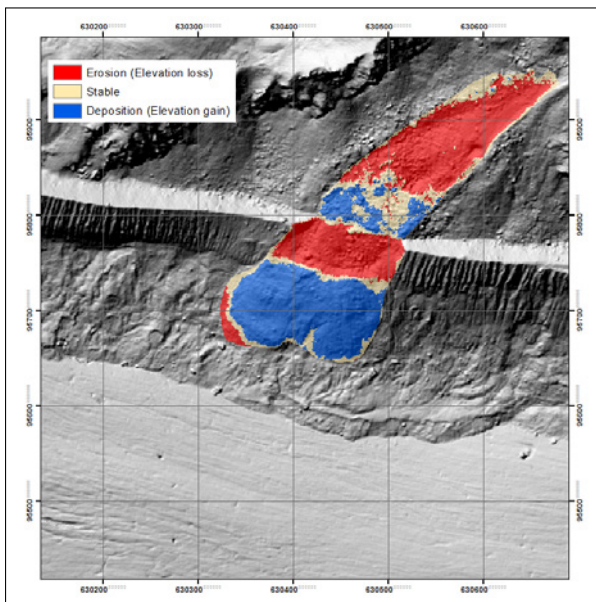
Figure A.35: Area for volume change 2005 - 2009
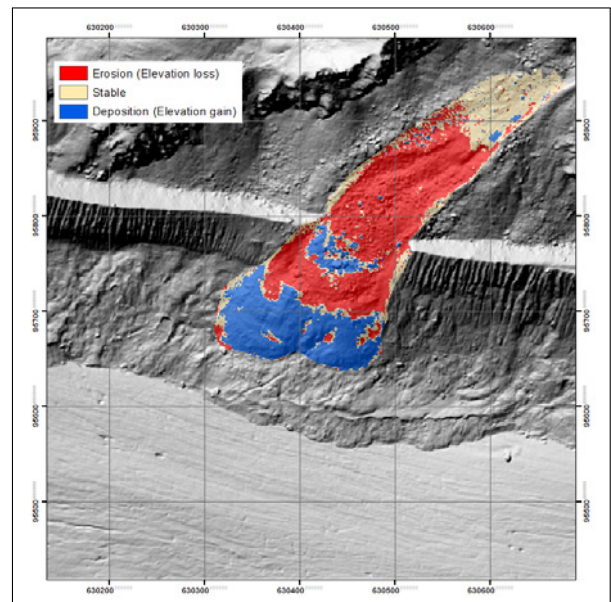
Figure A.36: Area for volume change 2009 - 2010
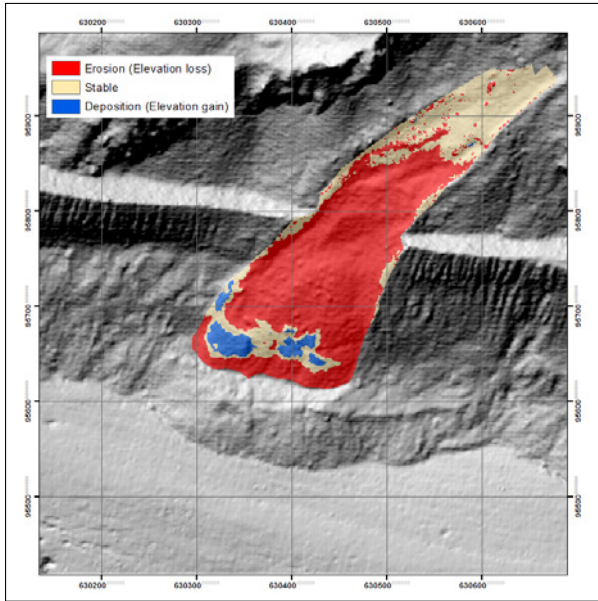
Figure A.37: Area for volume change 2010 - 2013
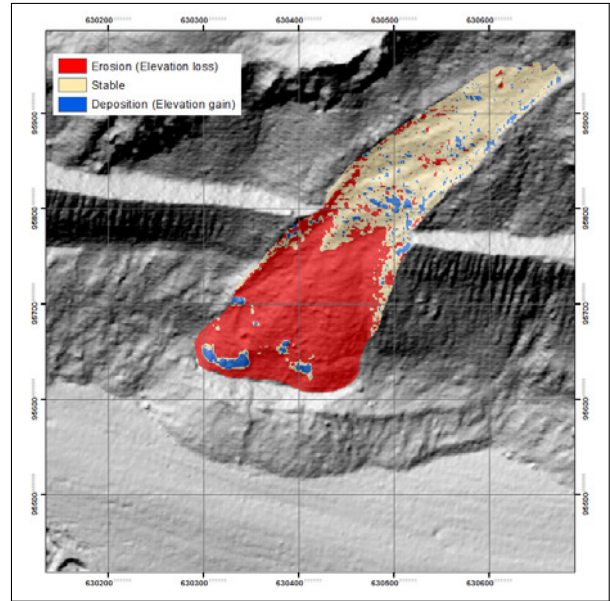
Figure A.38: Area for volume change 2013 - 2014
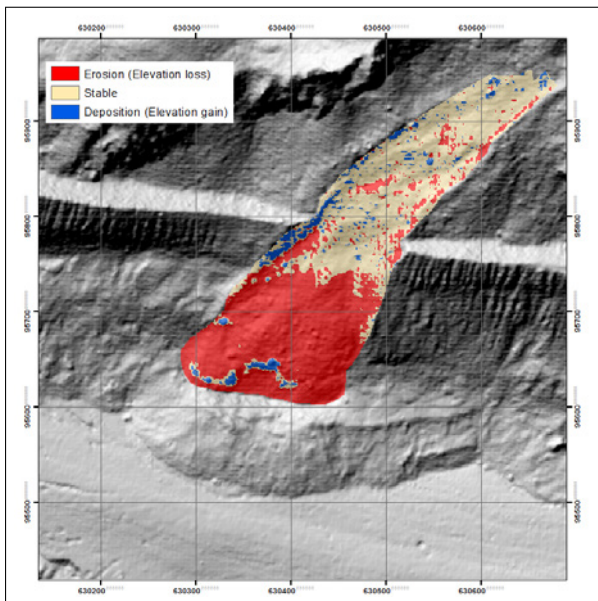
Figure A.39: Area for volume change 2014 - 2015
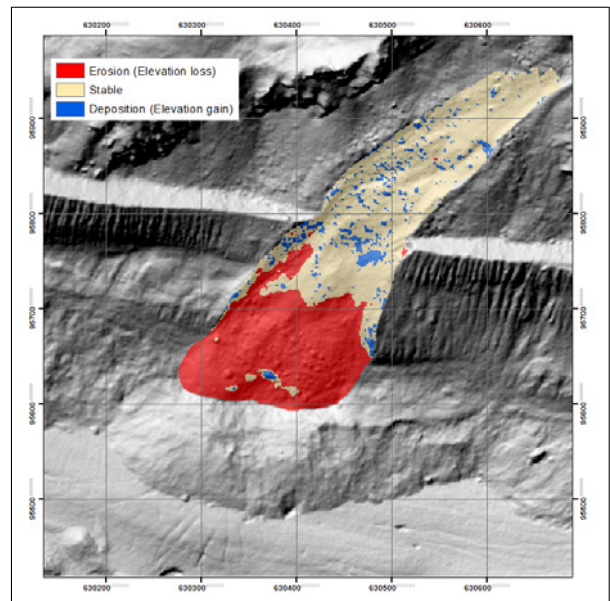
Figure A.40: Area for volume change 2015 - 2017

A.8   Point Tracking

	Time Period	Δx[m]	Δy[m]	Horizontal Shift [m]	Direction [°]
Stone 1	2009 to 2010	-22.09	-34.73	41.15	212.46
	2010 to 2013	-45.64	-74.22	87.13	211.59
	2013 to 2014	-7.14	-15.88	17.41	204.22
	2014 to 2015	-7.94	-12.7	14.98	212.01
	2015 to 2016	-4.37	-10.72	11.57	202.17
	2016 to 2017	-4.37	-7.14	8.37	211.43
Stone 2	2009 to 2010	-17.33	-18.45	25.32	223.2
	2010 to 2013	-45.64	-54.37	70.99	220.01
	2013 to 2014	-9.92	-16.27	19.05	211.37
	2014 to 2015	-3.97	-16.67	17.13	193.39
	2015 to 2016	-5.95	-11.91	13.31	206.56
	2016 to 2017	-3.18	-9.92	10.42	197.74
Stone 3	2009 to 2010	-26.86	-11.71	29.30	246.44
	2010 to 2013	-9.92	-16.67	19.40	210.76
	2013 to 2014	-5.56	-6.35	8.44	221.19
	2014 to 2015	-6.54	-5.49	8.54	229.97
	2015 to 2016	-7.83	-5.08	9.34	237.03
	2016 to 2017	-5.72	-4.45	7.24	232.13
Stone 4	2009 to 2010	-17.30	-12.96	21.62	233.16
	2010 to 2013	-25.82	-28.36	38.36	222.32
	2013 to 2014	-10.37	-2.75	10.73	255.14
	2014 to 2015	-12.91	-4.23	13.59	251.85
	2015 to 2016	-17.78	-5.50	18.61	252.80
	2016 to 2017	-21.59	-10.80	24.14	243.44

Stone 5	2009 to 2010	-2.67	-1.3	2.97	244.12
	2010 to 2013	-5.72	-6.14	8.39	222.95
	2013 to 2014	-1.06	-4.45	4.57	193.39
	2014 to 2015	1.27	-4.02	4.22	162.47
	2015 to 2016	-4.87	-6.56	8.17	216.57
	2016 to 2017	-1.67	-4.64	4.93	199.75
Stone 6	2009 to 2010	-24.26	-1.87	24.33	265.59
	2010 to 2013	-65.09	-5.56	65.32	265.12
	2013 to 2014	-20.64	-7.54	21.97	249.93
	2014 to 2015	-15.88	-7.94	17.75	243.43
	2015 to 2016	-15.08	-4.76	15.82	252.47
	2016 to 2017	-10.32	-7.54	12.78	233.84
Stone 7	2009 to 2010	-21.48	-0.28	21.49	269.24
	2010 to 2013	-54.77	-3.57	54.89	266.27
	2013 to 2014	-18.65	-3.97	19.07	257.99
	2014 to 2015	-13.89	-5.16	14.82	249.62
	2015 to 2016	-14.29	-5.56	15.33	248.75
	2016 to 2017	-12.70	-3.18	13.09	255.96
Stone 8	2013 to 2014	-9.13	-15.08	17.63	211.18
	2014 to 2015	-8.73	-16.67	18.82	207.65
	2015 to 2016	-9.13	-11.11	14.38	219.40
	2016 to 2017	-3.97	-8.73	9.59	204.44
Stone 9	2010 to 2013	-39.95	-32.54	51.53	230.83
	2013 to 2014	-10.85	-11.11	15.53	224.31
	2014 to 2015	-17.46	-15.08	23.07	229.18
	2015 to 2016	-22.23	-9.79	24.29	246.23
	2016 to 2017	-13.49	-9.26	16.37	235.54

Table A.2: Horizontal Displacement of the tracked boulders

A.9 Image Correlation (CIAS)
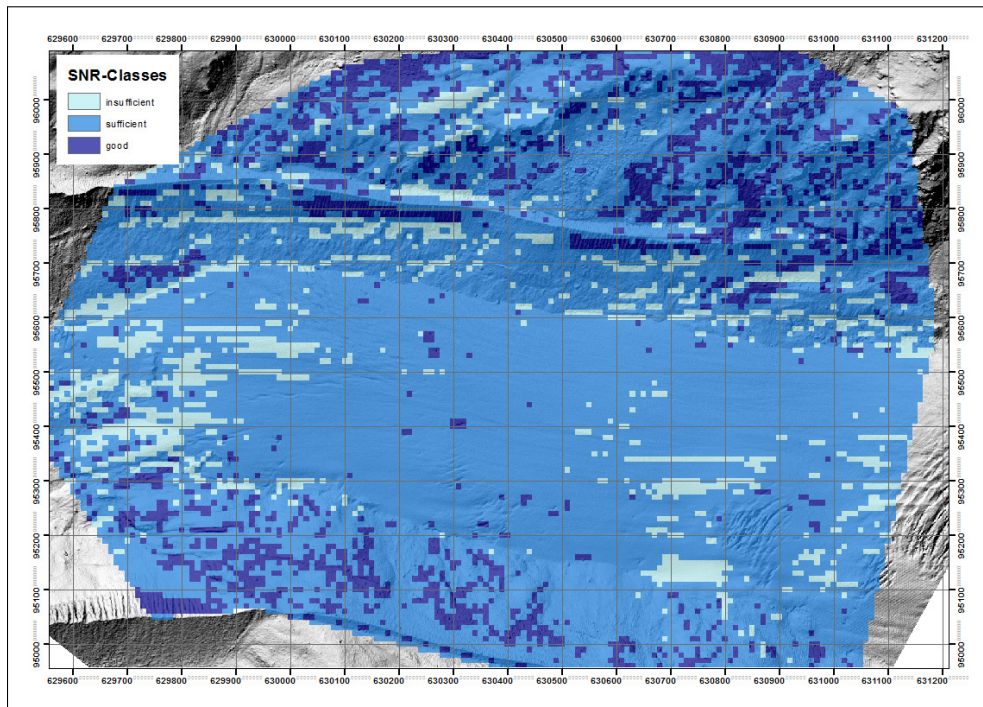
Figure A.41: Signal-to-Noise ratio between 2005 and 2009
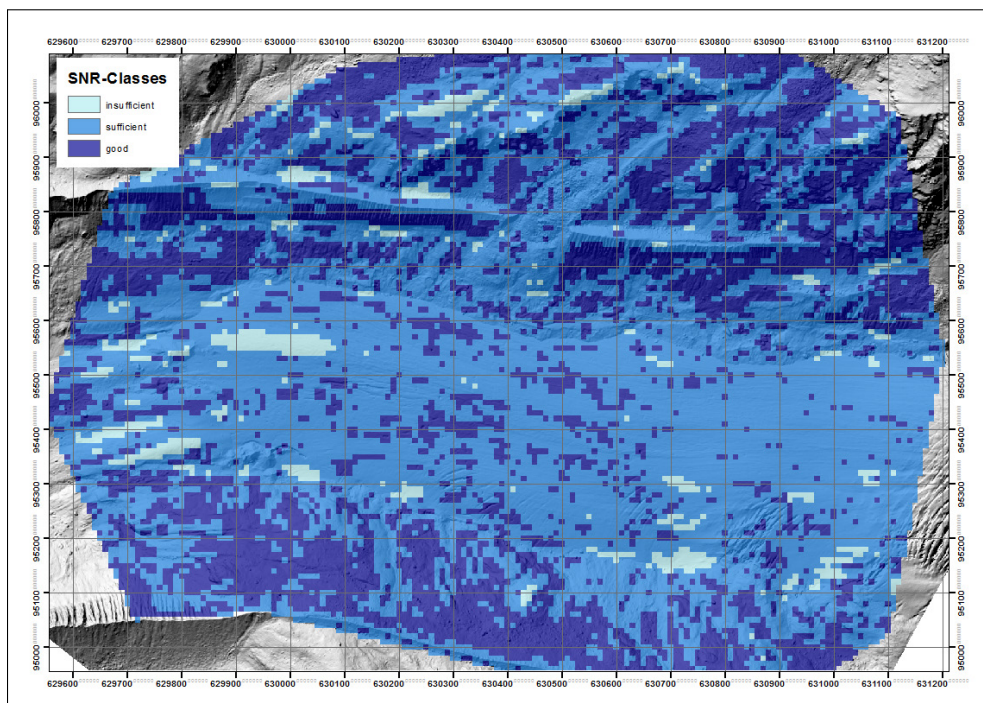
Figure A.42: Signal-to-Noise ratio between 2009 and 2010
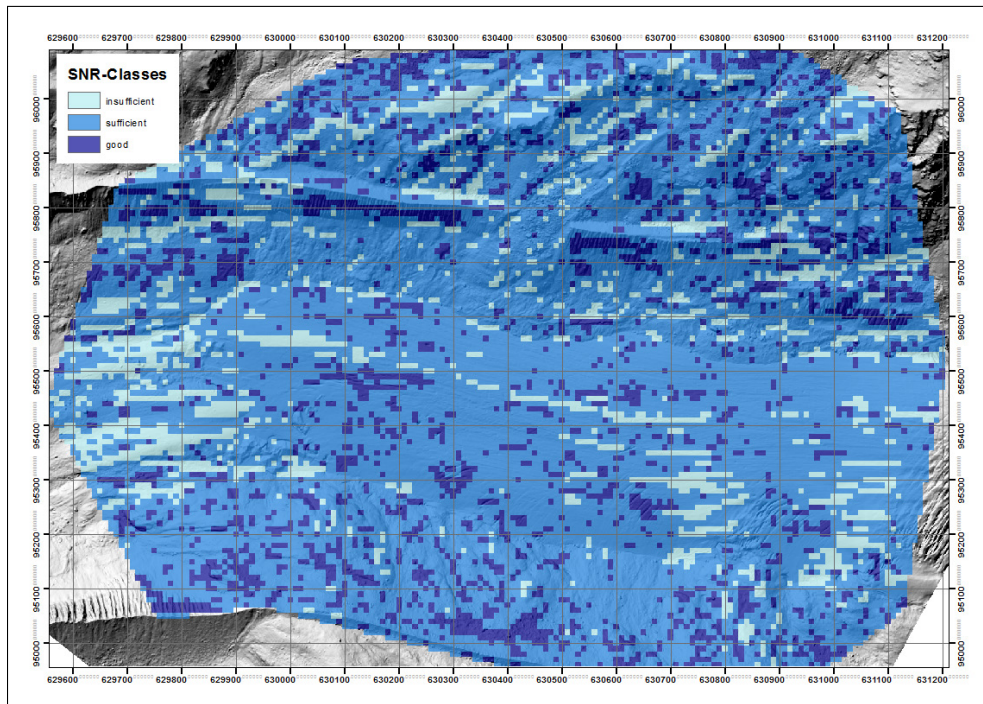
Figure A.43: Signal-to-Noise ratio between 2010 and 2013
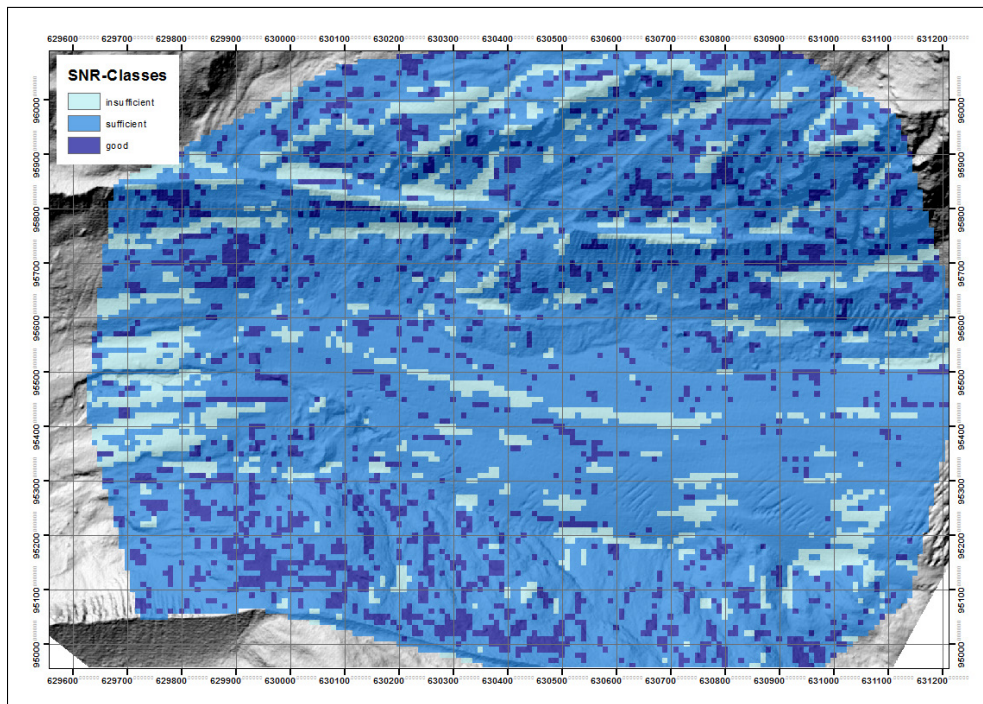

Figure A.44: Signal-to-Noise ratio between 2013 and 2014
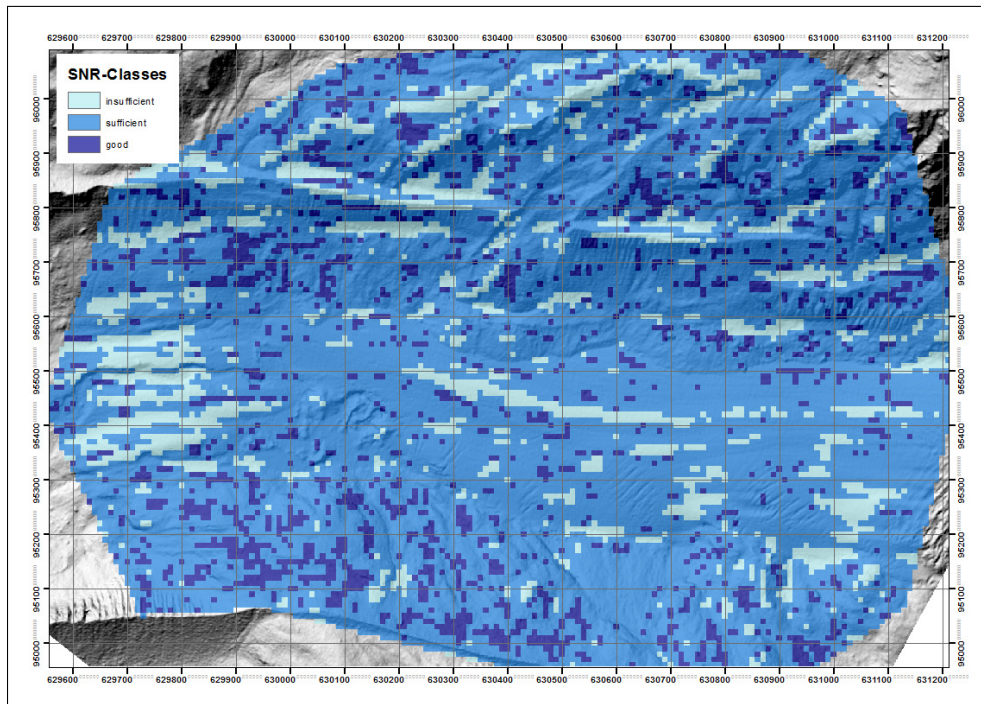
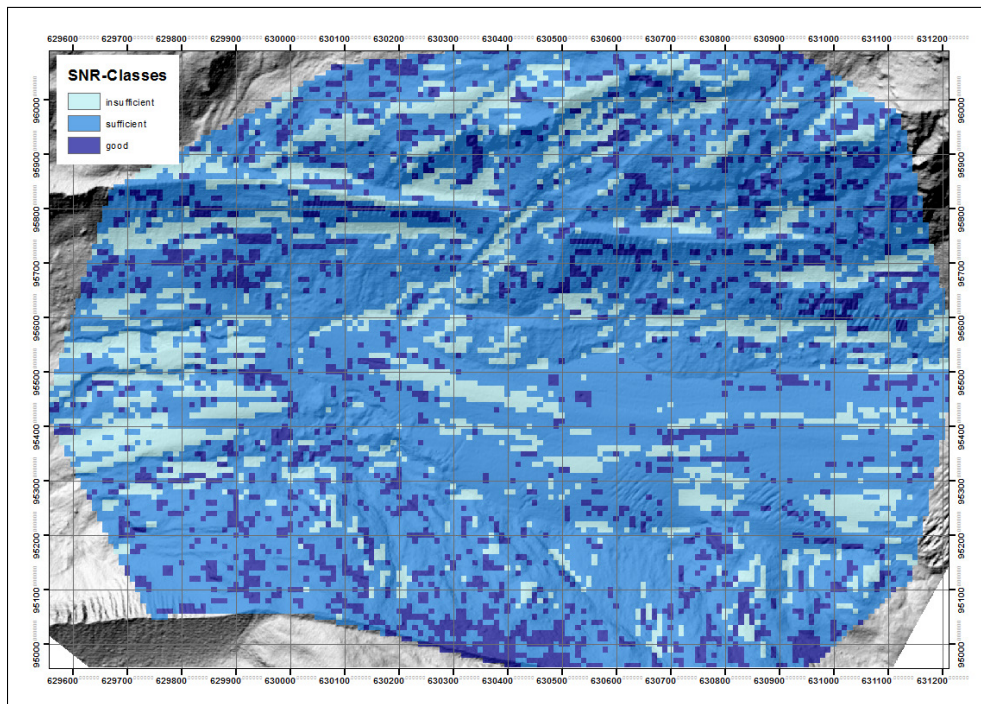Figure A.45: Signal-to-Noise ratio between 2014 and 2015

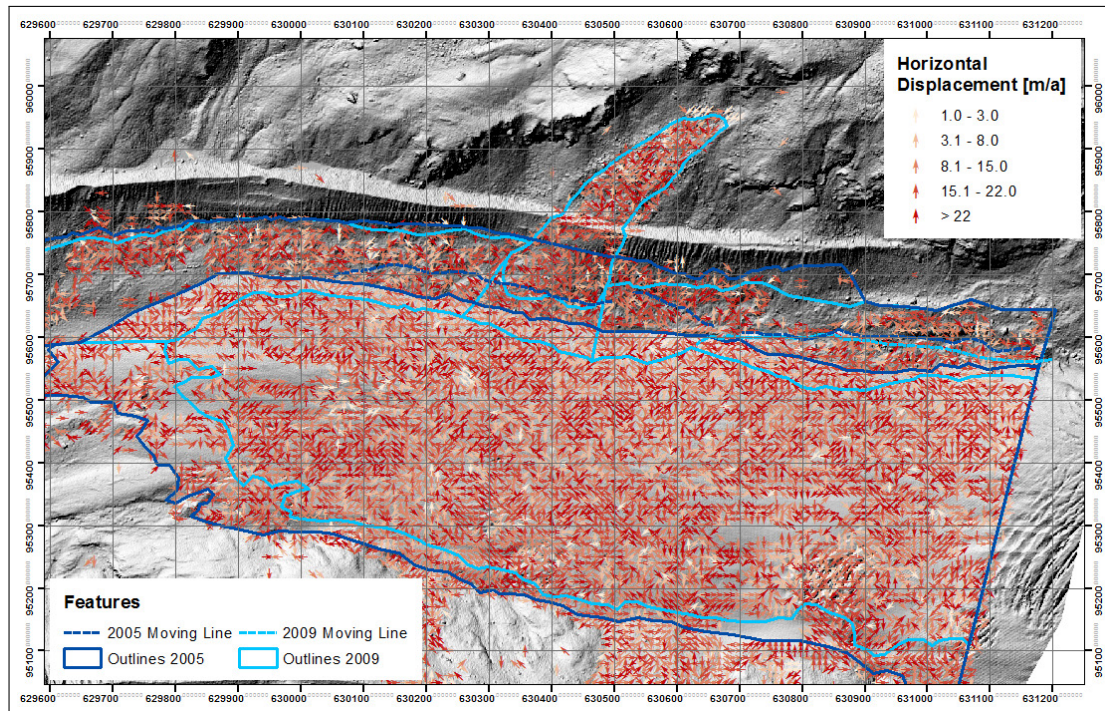Figure A.46: Signal-to-Noise ratio between 2015 and 2017

Figure A.47: Annual horizontal movement between 2005 and 2009 (Arrow = orientation of the displacement, color = magnitude of the displacement)
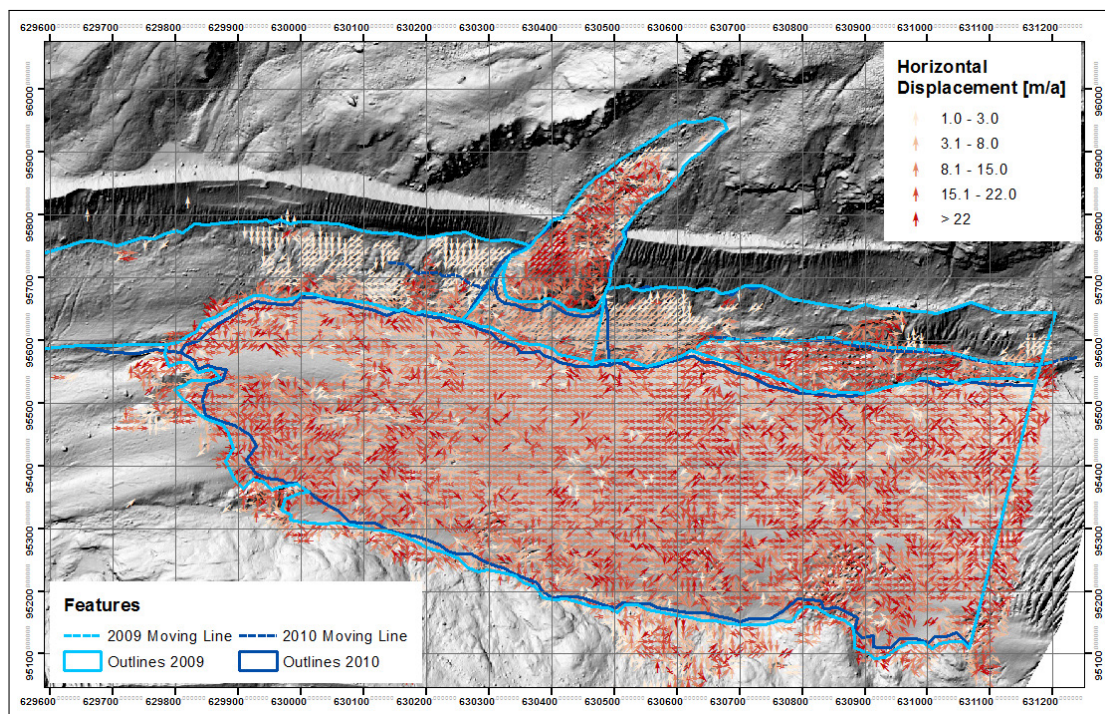
Figure A.48: Horizontal movement between 2009 and 2010 (Arrow = orientation of the displacement, color = magnitude of the displacement)
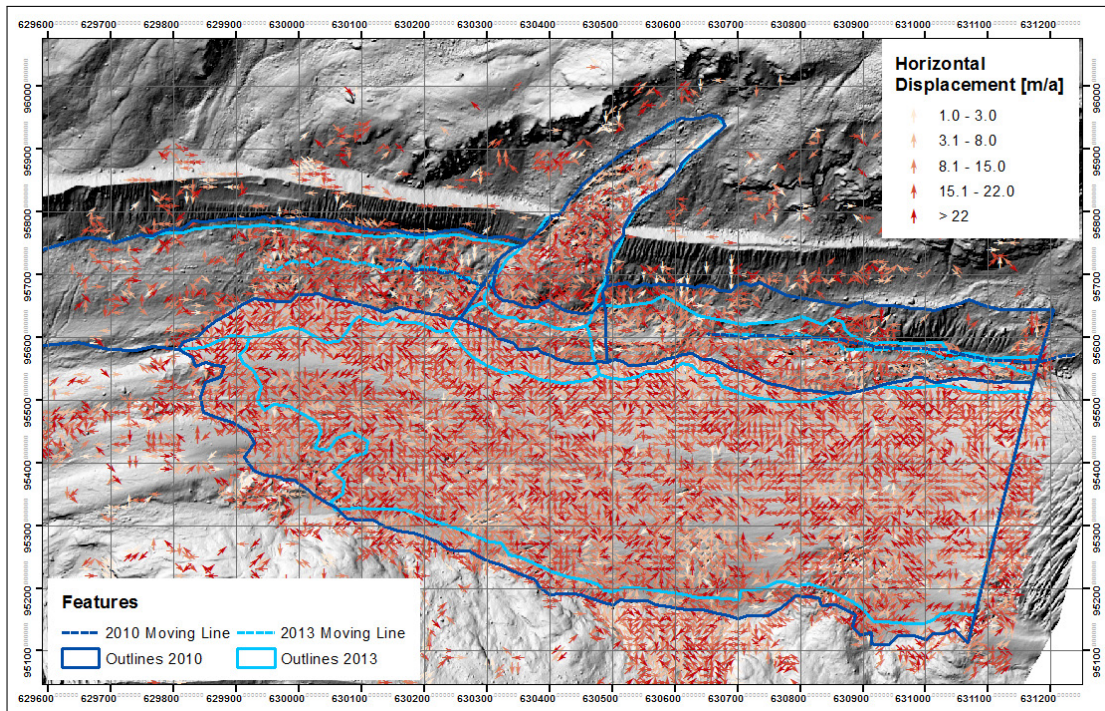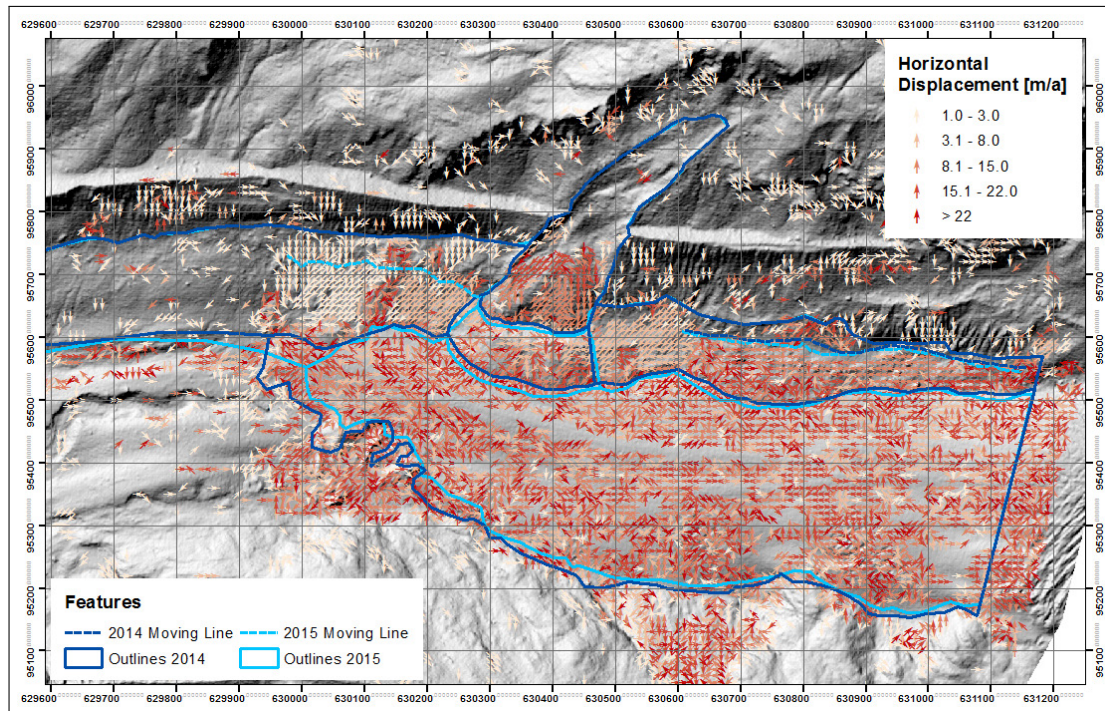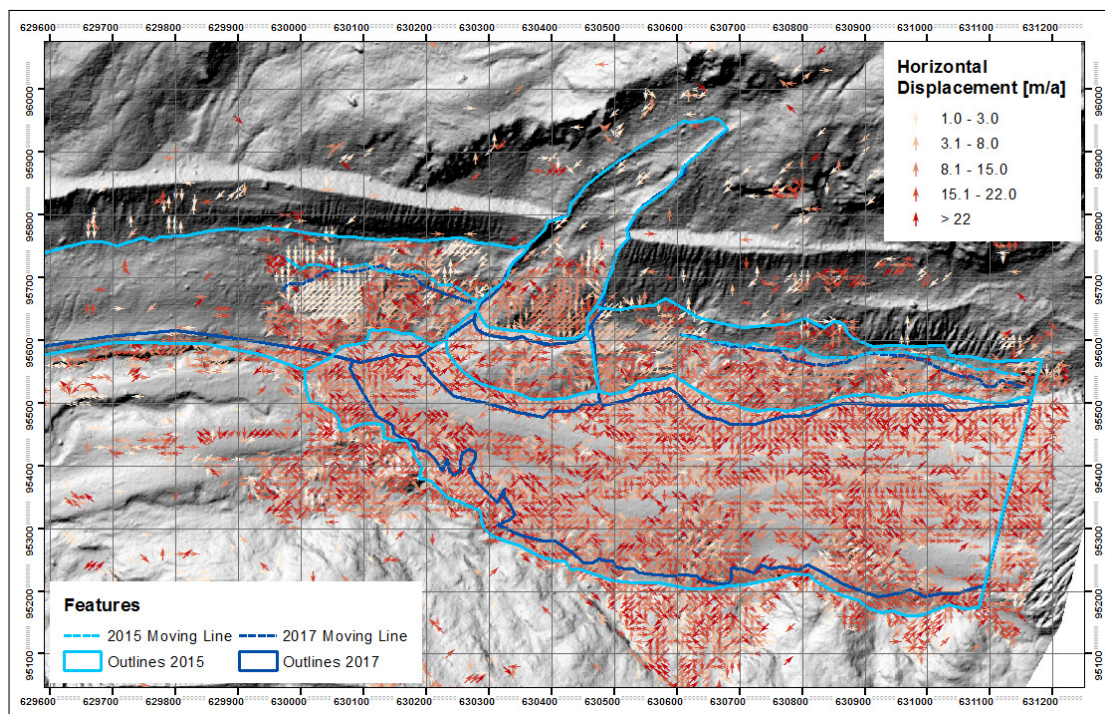
Figure A.49: Annual horizontal movement between 2010 and 2013 (Arrow = orientation of the displacement, color = magnitude of the displacement)
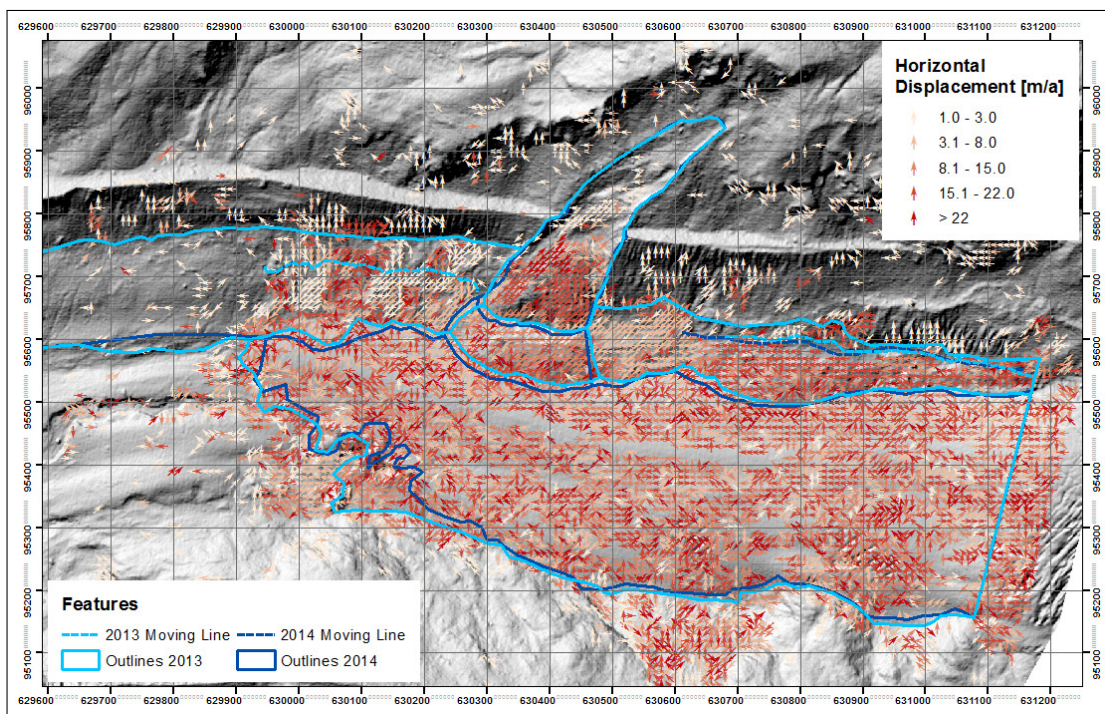
Figure A.50: Horizontal movement between 2013 and 2014 (Arrow = orientation of the displacement, color = magnitude of the displacement)

Figure A.51: Horizontal movement between 2014 and 2015 (Arrow = orientation of the displacement, color = magnitude of the displacement)

Figure A.52: Annual horizontal movement between 2015 and 2017 (Arrow = orientation of the displacement, color = magnitude of the displacement)
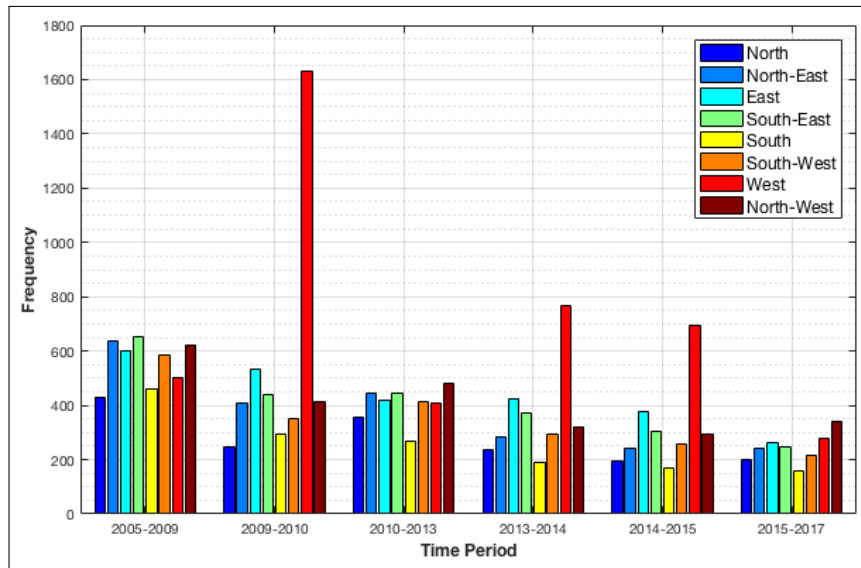
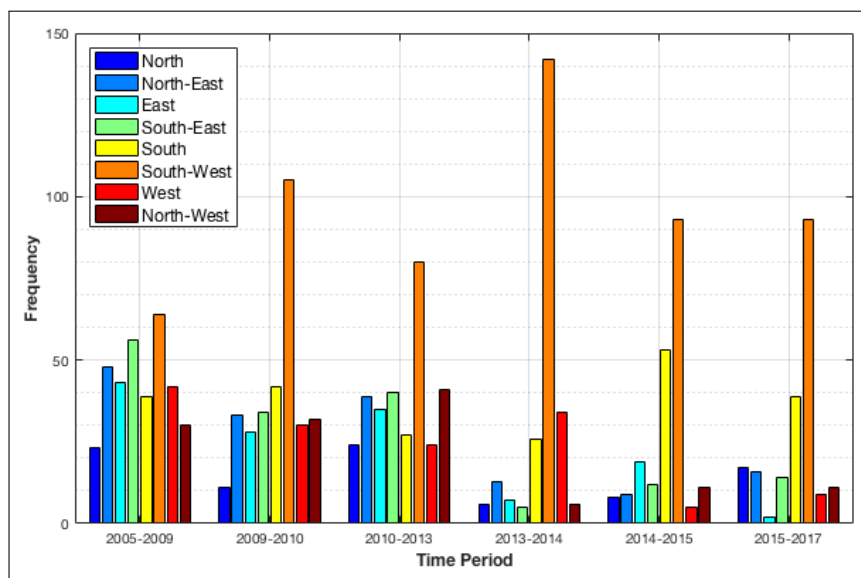Figure A.53: Direction of the movement within the Glacier Area

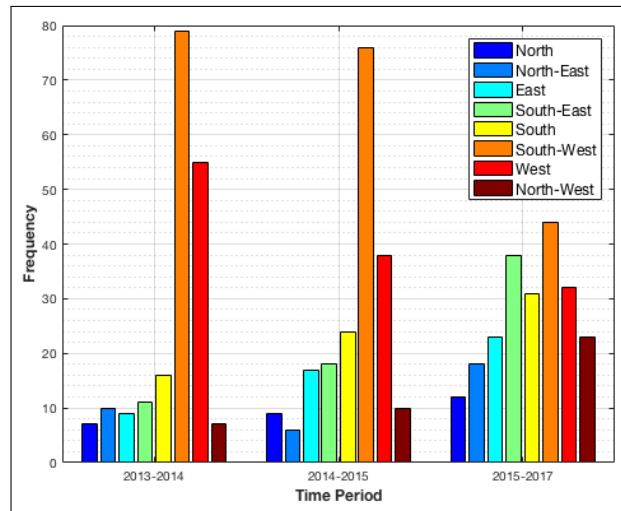Figure A.54: Direction of the movement within the Slide Area

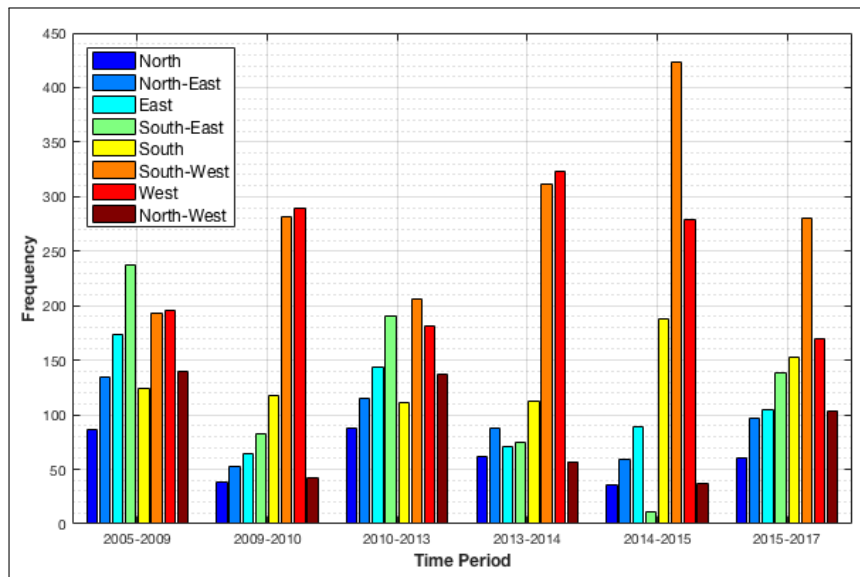Figure A.55: Direction of the movement within the Mound

Figure A.56: Direction of the movement within the Moraine-Foot Zone

Personal declaration

I hereby declare that the submitted thesis is the result of my own, independent work. All external sources are explicitly acknowledged in the thesis.

Zurich, 30. April 2018

Christine Schärer